

Cover Page



Universiteit Leiden



The handle <http://hdl.handle.net/1887/25721> holds various files of this Leiden University dissertation.

Author: Klooster, Ronald van 't

Title: Automated image segmentation and registration of vessel wall MRI for quantitative assessment of carotid artery vessel wall dimensions and plaque composition

Issue Date: 2014-05-07

Automated Image Segmentation and Registration of Vessel
Wall MRI for Quantitative Assessment of Carotid Artery Vessel
Wall Dimensions and Plaque Composition

Ronald van 't Klooster

Automated Image Segmentation and Registration of Vessel Wall MRI for Quantitative Assessment of Carotid Artery Vessel Wall Dimensions and Plaque Composition

Ronald van 't Klooster

ISBN: 978-90-5335-845-0

Printed by Ridderprint BV

About the cover: The front cover shows a carotid artery bifurcation including the lumen (red), the outer vessel wall (green) and different plaque lesions (calcium: orange, lipid: yellow, hemorrhage: blue). The background of the cover is composed of images of a multi-sequence MRI vessel wall protocol.

© 2014, Ronald van 't Klooster, Leiden, The Netherlands. All rights reserved. No part of this publication may be reproduced or transmitted in any form or by any means, electronic or mechanical, including photocopying, recording, or any information storage and retrieval system, without prior permission in writing from the copyright owner.

Automated Image Segmentation and Registration of Vessel Wall MRI for Quantitative Assessment of Carotid Artery Vessel Wall Dimensions and Plaque Composition

Proefschrift

ter verkrijging van

de graad van Doctor aan de Universiteit Leiden,

op gezag van Rector Magnificus prof.mr. C.J.J.M. Stolker,

volgens besluit van het College voor Promoties

te verdedigen op woensdag 7 mei 2014

klokke 15:00 uur

door

Ronald van 't Klooster

geboren te Laren

in 1981

Promotiecommissie

Promotores: Prof. dr. ir. B. P. F. Lelieveldt
Prof. dr. ir. J. H. C. Reiber

Co-promotor: Dr. ir. R. J. van der Geest

Overige leden: Prof. dr. H. J. Lamb
Prof. dr. M. J. A. P. Daemen
Academic Medical Center, Amsterdam
Prof. dr. ir. A. van der Steen
Erasmus MC, University Medical Center, Rotterdam



This work was carried out in the ASCI graduate school.
ASCI dissertation series number 305.

The research described in this thesis was performed within the framework of CTMM, the Center for Translational Molecular Medicine (www.ctmm.nl), project PARISk (grant 01C-202), and supported by the Dutch Heart Foundation (DHF-2008T094).

Financial support by the Dutch Heart Foundation for the publication of this thesis is gratefully acknowledged.

Financial support for the publication of this thesis was kindly provided by:

- ASCI research school,
- Bontius Stichting inz. Doelfonds beeldverwerking,
- Library of the University of Leiden,
- Medis medical imaging systems bv, Leiden,
- Pie Medical Imaging BV, Maastricht.

Contents

1	General introduction	1
1.1	Atherosclerosis of the carotid artery	2
1.2	Magnetic resonance imaging	4
1.3	Image derived measures of atherosclerosis	7
1.4	Manual image analysis	7
1.5	Automated image analysis	8
1.6	Thesis overview	10
2	Automatic lumen and outer wall segmentation of the carotid artery using deformable 3D models in MR angiography and vessel wall images	13
2.1	Introduction	15
2.2	Materials and methods	16
2.3	Results	22
2.4	Discussion	23
3	Carotid wall volume quantification from MRI using deformable model fitting and learning-based correction of systematic errors	29
3.1	Introduction	31
3.2	Methods	32
3.3	Data specific preprocessing	35
3.4	Experiments	38
3.5	Results	40
3.6	Discussion	47
3.7	Conclusion	47
4	Automated registration of multispectral MR vessel wall images of the carotid artery	49
4.1	Introduction	51
4.2	Materials and methods	53
4.3	Experiments and results	56
4.4	Discussion	62
4.5	Appendix: 1.5T optimized settings applied to 3.0T data	68
5	Visualization of local changes in vessel wall morphology and plaque progression in serial carotid artery MRI	71
5.1	Introduction	73
5.2	Methods	73

5.3	Results	75
5.4	Discussion	77
5.5	Conclusion	77
6	Automated versus manual in vivo segmentation of carotid plaque MRI	79
6.1	Introduction	81
6.2	Materials and methods	81
6.3	Results	84
6.4	Discussion	86
6.5	Conclusions	90
7	Agreement and reproducibility of automated atherosclerotic carotid artery plaque classification using optimized 3d morphological and intensity features in MR vessel wall images	91
7.1	Introduction	93
7.2	Materials and methods	94
7.3	Results	101
7.4	Discussion	106
8	Evaluation of multicontrast MRI including fat suppression and inversion recovery spin echo for identification of intra-plaque hemorrhage and lipid core in human carotid plaque using the mahalanobis distance measure	109
8.1	Introduction	111
8.2	Materials and methods	112
8.3	Results	116
8.4	Discussion	122
8.5	Conclusions	126
9	An objective method to optimize the MR sequence set for carotid plaque classification using automated image segmentation	127
9.1	Introduction	129
9.2	Materials and methods	130
9.3	Results	133
9.4	Discussion	136
10	Summary and conclusions	139
10.1	Summary	139
10.2	Conclusion	141
10.3	Future directions	142
	Samenvatting en conclusies	145
	References	151
	Publications	165
	Acknowledgments	167
	Curriculum Vitae	169

Chapter 1

General introduction

1.1 Atherosclerosis of the carotid artery

Atherosclerosis is the primary cause of heart disease and stroke. These cardiovascular diseases (CVD) are the leading cause of death in the Western world and accounted for 29% of all deaths in 2010 in The Netherlands. Other major causes of death in The Netherlands are cancer (31%) and chronic lower respiratory disease (10%) [1]. Due to an increased use of evidence-based medical therapies and due to changes in risk factors in the population attributable to lifestyle and environmental changes a decline of 65% in CVD deaths was achieved from 1950 to 2011. Additionally, the duration of hospital admission was almost halved in the period from 1994 to 2010. In 2007, the cost of CVD in the Netherlands was 9,3% of the total healthcare budget [2].

Atherosclerosis is a progressive systemic disease which, at an early stage, is characterized by the accumulation of lipids, inflammatory cells, and scar tissue in the vessel wall of large arteries, and, at a later stage, by the formation of plaque lesions inside the vessel wall [3] (Fig. 1.1). Initially, the vessel accommodates for the expanding lesions inside the vessel wall by an enlargement of the outer wall (outward remodeling) [4]. When the plaque burden exceeds the capacity of the artery to remodel outward, inward remodeling, reduction of the lumen size, occurs causing narrowing of the vessel lumen [5]. In case of severe narrowing, a stenosis, the artery can be occluded blocking the blood stream.

Over time, lesions can progress into larger, complicated plaques. Atherosclerotic plaques are separated into two categories: stable and unstable plaque, the latter also called vulnerable plaque. Stable plaques consist of a thick fibrous cap, which is the layer of extracellular matrix separating the lesion from the arterial lumen, and are rich in extracellular matrix and smooth muscle cells. Vulnerable plaques are rich in macrophages and foam cells and the fibrous cap is usually weak and prone to rupture [6]. In patients with vulnerable plaques, rupture of the thin fibrous cap causes the plaque contents to enter the vessel lumen possibly causing myocardial infarction or stroke.

Individuals who develop atherosclerosis tend to develop it in a number of different

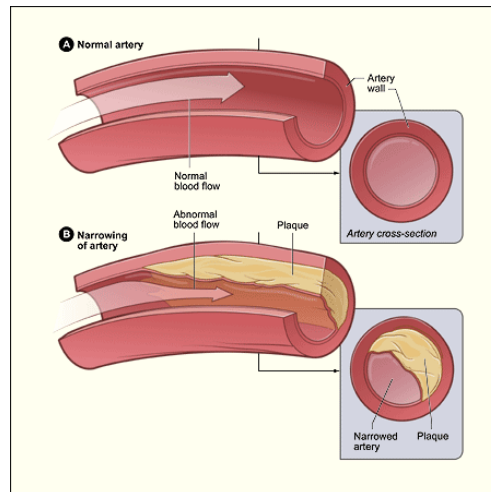


Figure 1.1: a) normal artery, b) buildup of atherosclerotic plaque inside the vessel wall causes narrowing of the lumen. (image from commons.wikimedia.org)

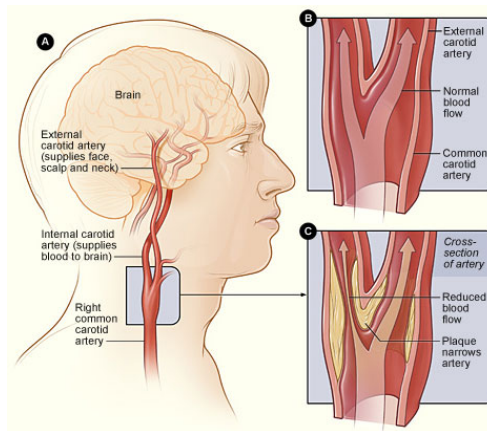


Figure 1.2: a) Overview of the common, internal and external carotid artery in the head and neck, b) cross-section of a normal carotid artery bifurcation, c) carotid bifurcation with plaque buildup and reduced blood flow (image from commons.wikimedia.org).

types of arteries including the carotid artery. This artery is located in the neck and supplies the head and neck with oxygenated blood. Inside the neck, the common carotid artery (CCA) bifurcates into the internal carotid artery (ICA) and the external carotid artery (ECA) (Fig. 1.2). The ICA runs deeper towards the skull supplying the brain with blood. The ECA runs closer to the skin and splits into numerous branches that supply the neck and face. The bifurcation is a common site for atherosclerosis and the buildup of atherosclerotic plaque can narrow the lumen of the CCA and ICA, decreasing blood flow to the brain, or a plaque can rupture causing its contents and blood clots to travel through the circulation to blood vessels in the brain. As the vessel gets smaller, the particles can get stuck inside the vessel restricting blood flow to parts of the brain. A disruption in blood flow, an ischemia, causing a shortage of oxygen and glucose in areas in the brain, can result in temporary loss of vision, difficulty speaking, and weakness, numbness or tingling, usually on one side of the body. This ischemia can be either temporary, yielding a transient ischemic attack (TIA), or permanent resulting in a stroke. A TIA doesn't generally cause permanent brain damage but is considered as a serious warning sign of stroke.

Symptoms of atherosclerosis in the carotid artery are narrowing of the lumen, a thickened vessel wall and the presence of atherosclerotic plaques. There are often no signs of atherosclerosis in the carotid artery until the occurrence of a TIA or stroke. Diagnostic procedures for carotid artery atherosclerosis are a physical examination and several tests using noninvasive imaging techniques. During physical examination a stethoscope is used to listen to the arteries in the neck. If an abnormal sound is heard over an artery, it may reflect turbulent blood flow which could indicate a stenosis. Non invasive imaging techniques for diagnosis of atherosclerosis include duplex ultrasound imaging, computerized tomography angiography (CTA), magnetic resonance angiography (MRA), and magnetic resonance imaging (MRI) [7]. Duplex ultrasound uses high-frequency sound waves to generate real-time images of the structure of the carotid artery. The static images can show the degree of a stenosis and the presence of plaque lesions, the dynamic images can be used to detect and quantify a stenosis based on the speed of the blood through the blood vessel. CTA uses a CT-scanner and the administration of contrast agent to gen-

erate a 3D image of the arterial structure which can accurately depict stenosis. Similarly, MRA aims to depict blood inside the body and is used for the evaluation of carotid artery stenosis. The application of multiple MRI contrast weightings enables the identification and classification of individual plaque components [8]. A more detailed description of the diagnosis of atherosclerosis of the carotid artery by MRA and MRI is given in the next section. Other, invasive, imaging techniques are conventional angiography, digital subtraction angiography, intravascular ultrasound and optical coherence tomography. These techniques require the administration of a contrast medium or the use of a catheter, are time consuming and include the risk of complications.

Different options are available to treat atherosclerosis. These options include lifestyle changes, medication, and surgery. Life style changes involve following a healthy diet to reduce high blood pressure or high blood cholesterol and to maintain a healthy weight, an increase in physical activity, quit smoking, and managing stress. Medication includes drugs to lower the cholesterol level or blood pressure and medicines to prevent blood clots from forming. In case of severe atherosclerosis, surgical procedures to treat carotid artery disease are carotid endarterectomy (CEA) or carotid artery stenting. In a CEA procedure, an incision is made on the side of the neck, then the carotid artery is opened and atherosclerotic plaque buildup on the inside of the carotid artery wall is surgically removed, restoring normal blood flow to the brain. Carotid artery stenting is a minimally invasive procedure performed through catheter techniques. Using catheters a small balloon is inflated in the narrowed area of the carotid artery opening the artery for improved blood flow. A stent is then inserted into the newly-opened area to help keep the artery from narrowing or closing again.

Stroke, often caused by carotid atherosclerosis, results in considerable morbidity, and mortality, and costs. Prevention is essential. Patient symptomatology and degree of luminal stenosis are currently the main grounds to perform CEA. However, many patients undergo CEA with its attendant risks without taking advantage, whereas in other patients, with a low to moderate degree of stenosis, CEA is probably incorrectly withheld [7]. Therefore, the focus has changed from stenosis evaluation towards the assessment of vulnerable plaque as morphological features of the plaque itself other than the degree of luminal narrowing may be important to identify patients at high risk of stroke. Advances in carotid MRI have enabled the noninvasive assessment of a wide-range of parameters associated with atherosclerotic disease [9]. Moreover, these parameters are possible candidate biomarkers which can be used to evaluate new treatment methods or outcome of clinical trials.

1.2 Magnetic resonance imaging

The key advantage of MRI over US and CTA is that MRI has the ability to characterize morphological, structural, and compositional features of atherosclerotic plaque in vivo [9, 10]. Additionally, MRA provides 3D images of the vessel lumen, allowing detection and quantification of a luminal stenosis. Furthermore, MRI is noninvasive, does not involve ionizing radiation, and can be repeated serially to track progression or regression [11]. Drawbacks of MRI are long scanning times and the high cost of the MRI system.

Imaging and plaque characterization of carotid arteries is relatively simple compared to other major arteries such as the coronary or the femoral arteries. The carotid arteries are superficial and not subject to significant motion of moving organs [12]. Most imaging

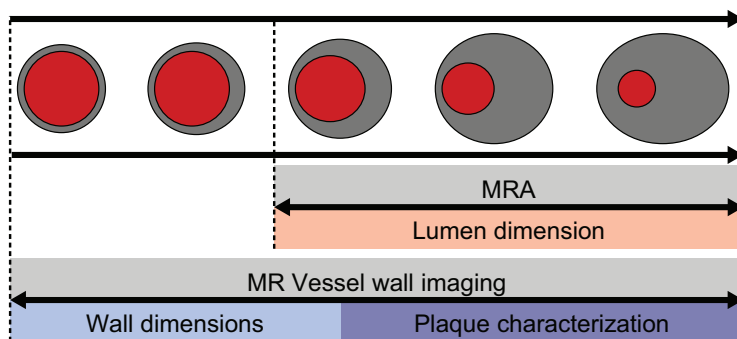


Figure 1.3: Schematic representation of atherosclerotic disease progress in relation to magnetic resonance imaging techniques and extractable metrics.

of the vessel wall by MRI has been performed on 1.5T scanners using a carotid coil resulting in a voxel size in the order of $0.4 \times 0.4 \times 3$ mm. More recent studies are performed using a 3.0T scanner enabling increased image quality and resolution (e.g. $0.3 \times 0.3 \times 2$ mm). Because the carotid arteries are superficial structures, the use of an MR phased array surface coil has shown to be extremely effective. Coil usage provides higher resolution and higher signal to noise ratio reducing scanning time [13].

A typical MRI protocol to study the status of atherosclerosis in the carotid artery consists of the application of multiple MR sequences. First a survey scan, generally a fast sequence, is used to get an anatomical overview of the area of interest. Based on this scan, the carotid artery of interest is identified and further sequences are planned in which the imaging volume is centered on the area of interest (e.g. the bifurcation, the atherosclerotic plaque, or the stenosed area). Optionally a TOF or MRA is acquired to enable stenosis assessment. Subsequently, several additional vessel wall acquisitions are planned and acquired to obtain information about the vessel wall morphology and plaque composition. These vessel wall images are usually scanned perpendicular to the carotid artery and typically have a high resolution in-plane (0.2 - 0.4 mm) and a much lower through-plane resolution (2 - 3 mm). As illustrated in Figure 1.3, the analysis of both the MRA and vessel wall images allows the assessment of lumen and vessel wall dimensions as well as characterization of the plaque components. The duration of a multi-sequence MRI protocol, depending on the number of sequences, can be between 20 and 60 minutes.

Imaging pulse sequences for vascular MRI can be divided into bright blood and dark blood sequences. In bright blood, flow signal enhancement techniques are used to visualize flowing blood while in black blood imaging the signal of the flowing blood is eliminated. Bright blood techniques are used in Phase Contrast MRA and 3D time-of-flight (TOF) to visualize the lumen and stenosis evaluation in the carotid artery. Quantification of lumen size is difficult due to limitations of MRA imaging such as slow blood flow near the vessel wall and irregular blood flow patterns in the bifurcation. Both effects can result in unwanted signal loss. The TOF imaging technique can show specific contrast features which, in conjunction with black blood imaging, can be helpful in identifying certain plaque components [13]. Alternatively, contrast-enhanced MRA can be used in which an MRI contrast agent is injected and images are acquired during the first pass of the agent through the arteries. The use of contrast-enhanced MRA is more complex, but does result in images of higher quality than regular MRA or TOF imaging.

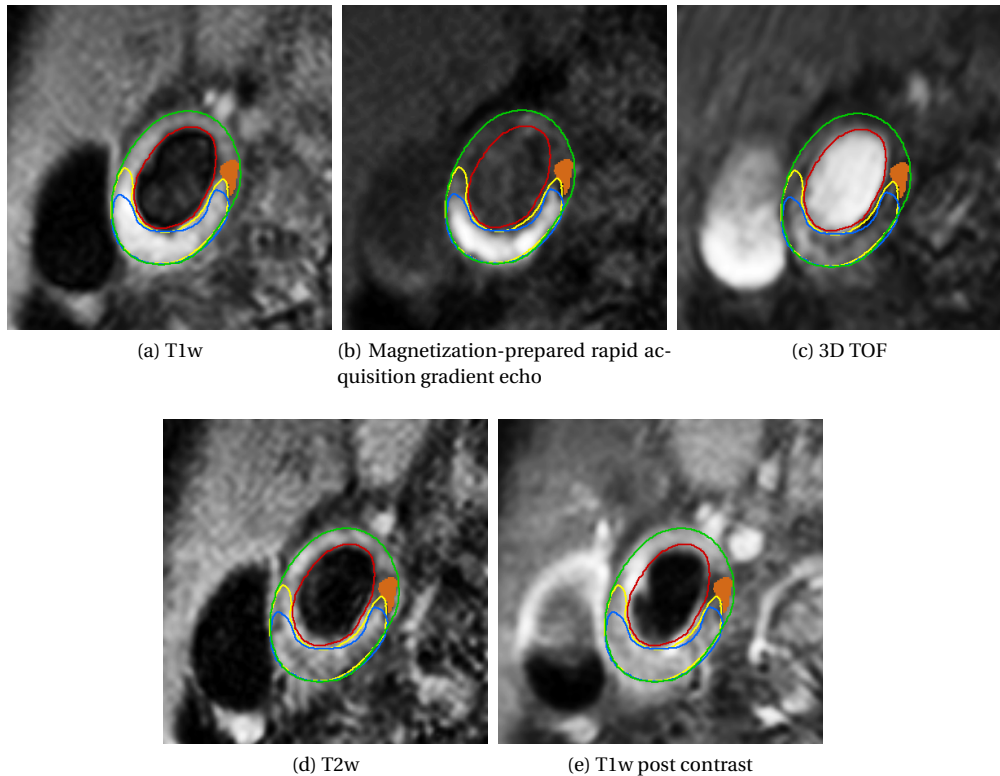


Figure 1.4: Images from a 3.0T multi-sequence MRI protocol including manual segmentations (orange = calcification, yellow = lipid-rich necrotic core, blue = presence of intraplaque hemorrhage).

Black blood imaging techniques are used to create multiple contrast weightings with the common goal to visualize the vessel wall. Based on these contrast weightings, individual components inside the plaque can be identified. Common black blood sequences are T1-, T2-, and proton density (PD) weighted image contrasts, where T1w and PDw images are especially helpful for evaluation of vessel wall morphology and show good contrast for fibrous matrix and lipid core [13]. Often a second T1w sequence is acquired after administration of gadolinium-based contrast agent which improves the reproducibility and quantification of the lipid-rich necrotic core [9]. Another approach is to develop sequences which are tailored to identify a specific plaque component. Examples are magnetic resonance direct thrombus imaging [14], magnetization-prepared rapid acquisition gradient echo [15], and diffusion-weighted magnetic resonance imaging for the detection of lipid-rich necrotic core [16]. A multi-contrast approach with bright and dark blood sequences enables comprehensive characterization of individual plaque components. An example is shown in Figure 1.4.

1.3 Image derived measures of atherosclerosis

Application of an extensive multi-contrast MRI protocol allows the assessment of morphological, structural and plaque composition features. MRA techniques provide information about the vessel lumen enabling stenosis detection and quantification. MRI vessel wall imaging provides detailed information of the vessel wall and can be used to quantify morphological features such as average, minimum and maximum vessel wall thickness, vessel wall area, vessel wall volume and derived metrics such as eccentricity or plaque index. Plaque index, also referred to normalized wall index, is the ratio between vessel wall volume against the volume of the whole vessel (lumen and vessel wall volume). Structural features of the plaque are the status of the fibrous cap and the presence of an ulceration. Individual plaque components, such as calcification, lipid, intraplaque hemorrhage (IPH), and loose matrix can be identified and quantified using multi-contrast vessel wall images. Volumes of different tissue components inside the plaque can be measured and also the type of plaque according to the AHA classification [17], which is a derived measure based on the plaque composition, can be obtained.

Measurement of vessel wall dimensions can be used to detect early onset of atherosclerosis and follow-up measurements of vessel wall dimensions can be used as an endpoint in clinical trials assessing the effect of pharmacological treatment of systemic atherosclerosis [18]. The fibrous cap status and cap thickness may identify patients at risk for stroke, which may lead to better patient selection for surgical intervention [19]. The vulnerability of an atherosclerotic plaque, the risk to rupture, can be assessed by evaluating the size of the plaque and its composition [20].

1.4 Manual image analysis

The current practice in clinical research to derive atherosclerotic features from the multi-contrast vessel wall imaging data is manual processing of the images. Several processing steps, such as lumen boundary detection, outer wall boundary detection, multi-contrast image registration, and plaque segmentation, are needed for a complete analysis of all image data. A common workflow to analyze the image data is as follows:

1. One of the contrast-weightings is defined as reference. Usually this is an image with clear depiction of the vessel wall, in most studies a T1w image is used.
2. In case the other contrast weightings were acquired at a different resolution or geometry, these contrast weightings are processed to match the resolution and geometry of the reference image using multiplanar reconstruction.
3. The lumen boundary and outer wall boundary are manually delineated in the reference image and copied to the other sequences.
4. To correct for possible patient movement while scanning, the other MR sequences are manually aligned to the reference image by applying a combination of through-plane translation of the complete image stack and in-plane translations for the individual image slices. The expert takes into account the appearance of the images and uses the lumen and outer wall contours as a reference.

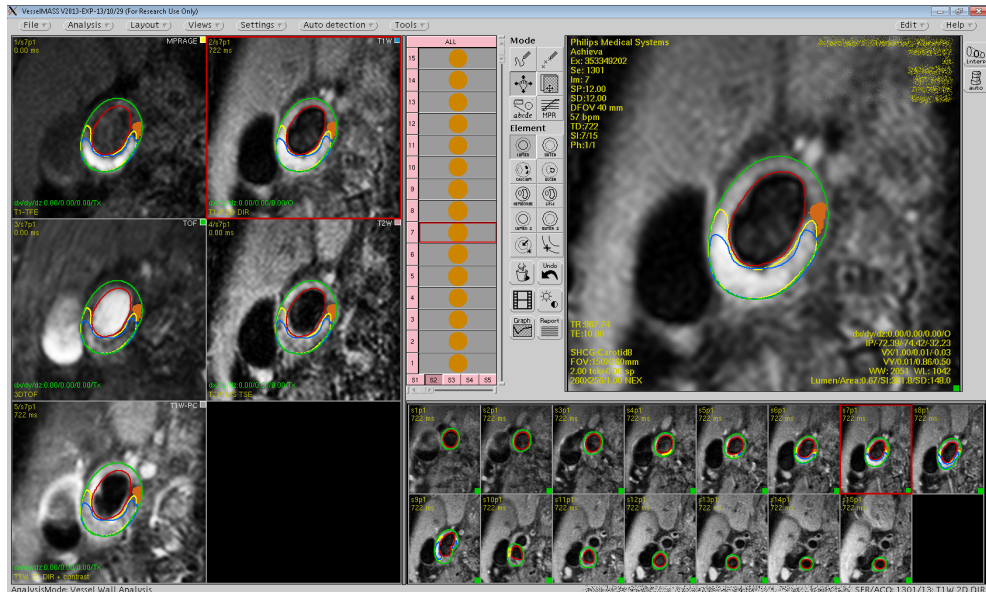


Figure 1.5: Screenshot of the software program VesselMass which can be used for manual segmentation of the multi-sequence MRI images.

- Once all images are aligned, regions of plaque can be identified and characterized by evaluating the relative signal intensities in the available imaging sequences. Various schemes for plaque classification have been reported for different imaging protocols, which can be used to identify regions of calcification, lipid core, IPH, ulceration, loose matrix and fibrous tissue [19, 21–24]. Alternatively, histological information can be used to aid to segmentation of the different plaque components.

The manual image analysis results in an aligned set of vessel wall images including manual segmentation of the vessel wall and plaque components (e.g. Fig. 1.4). All measures described in the previous section can be extracted from the manual segmentation. To perform the manual image analysis a software program is used which contains functionally to view, align and segment the images. An example of such a software program is VesselMass [25], see Fig. 1.5.

Finally, serial MRI is used to assess progression or regression of atherosclerosis by comparing vessel wall volume, presence and volume of atherosclerotic plaque components over time. Serial MRI is used to study the natural progression of atherosclerosis [26], effectiveness of drug therapy [27, 28], and the immediate and long-term effects of IPH on plaque progression in the carotid artery [29].

1.5 Automated image analysis

Manual image analysis is, due to the large amount of image data, a time-consuming procedure and is subject to inter- and intra-observer variation. Consequently, computerized segmentation, registration and classification techniques are being investigated to overcome these limitations. The application of computerized methods is a difficult task due

to the nature and quality of the vessel wall images, the difficulty of obtaining a gold standard and variation in scan protocols between scanners and medical centers. Imaging of the carotid vessel wall requires sub-millimeter resolution which is achieved at the expense of signal-to-noise ratio and is subject to image artifacts due to blood flow and physiologic motion and intensity inhomogeneity caused by the use of surface coils [30]. A gold standard is often not available as the acquisition of a gold standard, such as histology, requires the patient to undergo surgery. In practice, manual segmentation, which suffers from inter- and intra-observer variation, is used as a surrogate gold standard. Another challenge is introduced by the variation in scan protocols between different scanners and hospitals. A method developed on a set of MR images from one scanner, might perform poorly on other images because of differences in contrast between the images. Especially methods for the classification of plaque components, which heavily rely on image contrast, are hindered by variation in scan protocols. Therefore, robust computerized methods are needed which can cope with these challenges and are applicable to a wide range of MR images.

In the past, different steps of the manual segmentation process have been automated. Automated segmentation methods for lumen and outer wall boundary segmentation have been investigated. Reported methods range from interactively guiding a segmentation algorithm [31,32] to approaches requiring one user interaction per image slice [25] or one interaction to start the complete segmentation process [33,34]. Often an MRA or TOF image is used to perform a rough segmentation of the lumen contours which are then copied to a vessel wall sequence in which the lumen contours are refined. Subsequently the outer wall boundary contour is detected with the aid of the information of the lumen contour. More recent methods focus on detecting the lumen and outer wall boundary contours simultaneously [35,36].

Automated image registration methods have been developed to align the multi-contrast vessel wall images, the fourth step in the manual analysis process. Image registration was mainly performed in 2D ignoring any patient movement in the through-plane direction [37–40]. More recent studies applied image registration in 3D allowing for translation and rotation in all three directions [41,42]. In most studies, a region of interest around the carotid artery, based on the lumen and outer wall boundaries, was used and image similarity metrics based on correlation, mutual information, or gradients in the image were used.

The final step in the analysis is the identification and classification of plaque components. Several methods for automated classification of plaque components in the carotid artery have been described in literature, the majority employing statistical pattern recognition techniques [25,37,38,43]. Commonly a supervised classifier, which is trained on features and classes extracted from example data, is employed to classify unseen image data into different plaque components. Characteristic features are signal intensities and edge information from the multi-contrast MR images, and morphological features such as local vessel wall thickness and distance to the lumen or outer boundary of the vessel wall. Before the extraction of signal intensity features, the MR images are normalized to enabling inter-subject comparison. Preferable the classifier is trained on a training set and tested on a independent test set. In case the size of the dataset is too small, cross validation techniques, e.g. leave-one-patient-out, are used.

Currently, no computerized methods have been proposed to aid the comparison of baseline and follow-up scans of serial MRI studies.

1.6 Thesis overview

The main goal of this thesis is to develop methods for automated segmentation, registration and classification of the carotid artery vessel wall and plaque components using multi-sequence MR vessel wall images. Automated analysis seeks to overcome the drawbacks of manual segmentation in terms of accuracy, objectivity, reproducibility and time. The new methods will be clinically validated on patient data and compared to existing methods where possible.

The structure of the remaining part of this thesis is as follows. First, automated segmentation of the lumen and outer boundary is discussed. Then, automated image registration is applied to align multi-sequence images and scans of multiple time points. The third part focuses on several challenges related to the automated classification of plaque components. Finally, we conclude the thesis by providing the summary, the conclusion and a future outlook. A detailed overview of the next chapters:

In **chapter 2** a new method for automated segmentation of the lumen and outer wall boundaries in MR vessel wall studies of the common carotid artery was developed and validated. This new segmentation method was developed using a 3D deformable vessel model requiring only one single user interaction by combining 3D MR angiography and 2D vessel wall images.

Chapter 3 presents a method for carotid vessel wall volume quantification from MRI which combines lumen and outer wall segmentation based on deformable model fitting, described in **chapter 2**, with a learning-based segmentation correction step to correct for systematic differences between the automated segmentation method and manual annotations by the expert.

In **chapter 4**, we introduced automated image registration techniques to correct for possible patient movement within one scanning session. Furthermore, in **chapter 5**, image registration was used to align scans from serial MRI studies to enable visual assessment of local changes in vessel wall thickness and progression or regression of different plaque components over time.

In **chapter 6**, pattern recognition techniques were introduced to automatically detect and quantify atherosclerotic plaque components based on in vivo MR imaging data of the carotid artery in a multicenter study. A supervised classifier was trained using image features from four MR sequences and morphological features from a training group of 20 patients. The classifier was applied to a testing group of 40 patients and results were compared with the manual segmentation.

In **chapter 7**, we investigated the effect of new morphological features, image normalization methods and the composition of the training data for automated plaque classification and evaluated the reproducibility of automated classification versus manual segmentation.

Chapters 8 and 9 focus on the evaluation of MR-sequences and the trade-off between scan duration and automated image segmentation performance. In **chapter 8** the image contrast between different plaque components in several high field MR sequences are evaluated using the Mahalanobis distance measure. In **chapter 9** an objective method to optimize the MR sequence set for plaque classification in carotid vessel wall images using automated image segmentation is presented.

Chapter 10 provides discussions for each of the previous chapters. In each chapter a new method was developed and the improvements over existing methods are discussed

as well as directions for further research. Finally, a general conclusion is drawn and suggestions for future work are given.

Chapter 2

Automatic lumen and outer wall segmentation of the carotid artery using deformable 3D models in MR angiography and vessel wall images

This chapter was published in:

R. van 't Klooster, P. J. H. de Koning, R. A. Dehnavi, J. T. Tamsma, A. de Roos, J. H. C. Reiber, R. J. van der Geest. Automatic lumen and outer wall segmentation of the carotid artery using deformable three-dimensional models in MR angiography and vessel wall images, *Journal of Magnetic Resonance Imaging*, Volume 35, Issue 1, Pages 156–65, 2012.

Abstract

Purpose: To develop and validate an automated segmentation technique for the detection of the lumen and outer wall boundaries in MR vessel wall studies of the common carotid artery.

Materials and methods: A new segmentation method was developed using a three-dimensional (3D) deformable vessel model requiring only one single user interaction by combining 3D MR angiography (MRA) and 2D vessel wall images. This vessel model is a 3D cylindrical Non-Uniform Rational B-Spline (NURBS) surface which can be deformed to fit the underlying image data. Image data of 45 subjects was used to validate the method by comparing manual and automatic segmentations. Vessel wall thickness and volume measurements obtained by both methods were compared.

Results: Substantial agreement was observed between manual and automatic segmentation; over 85% of the vessel wall contours were segmented successfully. The interclass correlation was 0.690 for the vessel wall thickness and 0.793 for the vessel wall volume. Compared with manual image analysis, the automated method demonstrated improved interobserver agreement and inter-scan reproducibility. Additionally, the proposed automated image analysis approach was substantially faster.

Conclusion: This new automated method can reduce analysis time and enhance reproducibility of the quantification of vessel wall dimensions in clinical studies.

2.1 Introduction

Atherosclerosis is a progressive disease which, at an early stage, is characterized by vessel wall thickening causing outward remodeling, then narrowing of the lumen, and at a later stage by the formation of plaque lesions inside the vessel wall [3]. In patients with unstable plaques, the thin fibrous cap can rupture causing the plaque contents to enter the vessel lumen causing a stroke. Therefore, accurate assessment of the vessel wall dimensions and composition of the vessel wall is essential for identifying patients at risk. The 3.0 Tesla (T) MRI offers high-resolution noninvasive imaging of the vessel wall of the carotid artery. For quantitative assessment of the vessel wall morphology and plaque composition, contours describing the boundaries of the vessel wall are needed [38]. Vessel wall thickness measurements have been shown to correlate well with ultrasound (US) intima media thickness measurements (IMT) [33, 44, 45]. IMT has emerged as a marker for cardiovascular disease and has been used as an endpoint in clinical trials assessing the effect of pharmacological treatment of systemic atherosclerosis [46, 47]. In turn, MRI is also used in clinical trials [48, 49], but compared with US, it offers the advantage that it can provide a 3D image of the vascular structure instead of a 2D image that is dependent on the angle of insonation [45]. Other advantages of MRI over US are lower measurement variability [45], enabling smaller sample sizes and potentially shorter study duration in clinical trials.

Currently, quantitative assessment of the vessel wall dimensions is based on manual tracing of the lumen and outer wall boundaries, which is timeconsuming and subject to inter- and intra-observer variation. Consequently, computerized segmentation techniques have been developed to overcome these limitations. Reported methods range from interactively guiding a segmentation algorithm [31, 32] to approaches requiring one user interaction per imaging section [25] or one interaction to start the complete segmentation process [33, 34]. Despite the advances in automated vessel wall contour detection techniques, further improvements are needed to improve the accuracy, robustness and speed of automated quantitative vessel wall analysis. Further improvements might be accomplished by applying 3D registration and segmentation techniques, instead of 2D methods that process each slice independently of all other slices.

Accordingly, the purpose of this study was to develop a highly automated 3D image segmentation technique for the detection of the lumen and outer wall boundaries in MR vessel wall imaging studies of the common carotid artery.

We present an automatic segmentation method that uses combined Time of Flight (TOF) MRA and vessel wall images to segment the vessel wall using deformable 3D tube models. The combination of the two types of images potentially decreases user interaction, and increases segmentation performance. By using a 3D approach, the image segmentation can take advantage of information in neighboring slices in case there is little image information in a slice, and in case of isotropic 3D datasets, the method can gain full advantage of the extra available image information. The performance of this new method is evaluated by comparing the automatic segmentations with manual segmentations of carotid vessel wall imaging studies of 45 subjects. In addition, inter-observer variability, as well as inter-examination reproducibility were investigated for both manual and automated assessment of vessel wall parameters.

2.2 Materials and methods

Subjects

Forty-five adult subjects (56% male; 19-79 years old; mean age = 52 years) underwent a carotid MRI on a 3T scanner (Achieva; Philips, Best, The Netherlands). A variation of cardiovascular risks was present in the group, but none of the subjects had symptoms of cardiovascular disease. Ten subjects, randomly chosen from the group of 45 subjects, were imaged twice, at baseline (T_0) and at a maximum of 28 days later (T_1), resulting in a total of 55 MR studies. The subjects were imaged in the supine position with the neck positioned at the isocenter of the magnet. In all subjects the left carotid artery was examined.

MR image acquisition

A scan protocol was applied, which was tailored to obtain a series of oblique axial slices perpendicular to the course of the left common carotid artery starting at the level of the flow divider and ending in the common carotid artery, as previously described by Alizadeh Dehnavi et al [50]. Automated vessel wall contour detection was based on processing of the TOF-MRA survey scan and high resolution vessel wall images. The TOF-MRA was acquired with the following parameters: 20 contiguous transversal slices, fast gradient-echo sequence, acquired pixel size = 1 mm x 1.23 mm x 5.0 mm, field of view (FOV) = 300 mm, echo time (TE) = 3.8 ms, repetition time (TR) = 7.7 ms, and flip angle = 20°. The parameters for the vessel wall images, a black-blood sequence, were: an electrocardiograph triggered dual IR spoiled segmented k-space FGRE sequence, 8 slices, no slice gap, acquired pixel size = 0.46 mm x 0.46 mm x 2 mm, reconstructed pixel size = 0.27 mm x 0.27 mm x 2 mm, FOV = 140 mm, TE = 3.6 ms, TR = 12 ms, and flip angle = 45°. The black-blood sequence was optimized to achieve maximum contrast between the carotid wall and the vessel lumen.

Automatic image segmentation

The automated segmentation algorithm is initialized by specifying the artery of interest in the MRA image of the neck area. This image provides a global overview of the arterial structure and allows users to easily identify the artery segment by manually indicating a proximal and a distal point in one of the image slices or on the maximum intensity projection of the 3D volume. Based on these two points, the following five steps are performed automatically, resulting in a segmented vessel wall in the vessel wall images: (1) Detection of the arterial lumen in the MRA image; (2) Transfer and registration of the MRA lumen segmentation to the vessel wall images; (3) Refinement of the lumen boundary in the vessel wall images; (4) Estimation of initial outer wall boundary; (5) Detection of the outer wall boundary in the vessel wall images.

In steps 1, 3, and 5, a segmentation algorithm based on the fitting of a 3D cylindrical NURBS surface is used.

3D Cylindrical NURBS surface segmentation applied to carotid arteries

A 3D Cylindrical NURBS surface is used to model the anatomy of vascular structures [51, 52] (Fig. 2.1). This model possesses several advantageous properties, such as local control of shape and the flexibility to describe both simple and complex objects. The surface is

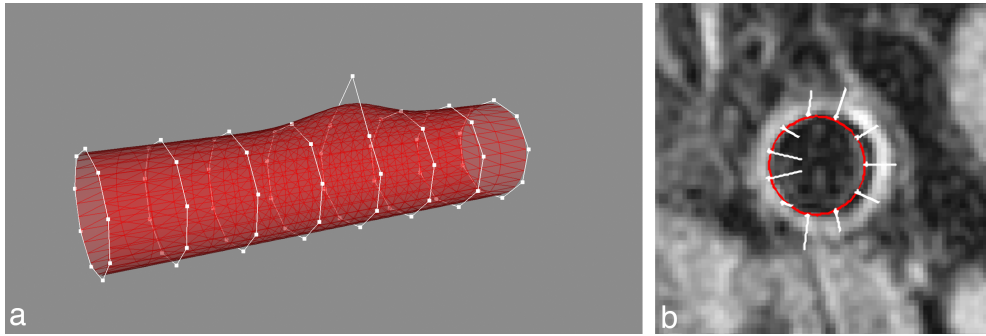


Figure 2.1: a) Cylindrical NURBS surface (red tube) with local change in shape enforced by two control points (white points, the control points are connected by straight lines for illustrative purpose). b) The 2D vessel wall image example showing image forces (white lines) acting on the control points (white points) and the corresponding lumen contour (red).

defined by several spatially distributed control points. Increasing the number of control points allows the creation of more complex surfaces. By moving the control points (see Fig. 2.1b), the surface can be relocated. For this application, the surface is relocated to fit the underlying image data by iteratively moving the control points such that the surface is moved toward edges in the image.

In this study, a tube model is initialized by creating multiple rings with control points positioned perpendicular to the detected vessel axis. For each ring, the diameter and number of control points must be specified. The fitting of the surface to the image data is performed by iteratively moving the control points. The movement of a control point is derived from image forces acting on nearby surface points. The closer the surface point is to the control point, the more influence it has on the control point. In each iteration, an image force is calculated at each surface point. This image force is the desired movement to move the surface point to the structure of interest, for example, an edge, in the image. The image force at each surface point is calculated as follows and is illustrated in Figure 2.2: (i) A signal intensity (SI) profile along the surface normal, centered at the surface point is obtained. The SI values are obtained by 3D linear interpolation of the image information. (ii) The SI profile is analyzed by detecting the strongest edge in a particular direction. The direction can either be positive, from low to high SI values, or negative, from high to low SI values. If the direction is not set, the strongest edge is selected. (iii) The image force vector for that surface point is then proportional to the distance of the strongest edge with respect to the center of the SI profile multiplied by the surface normal.

The exact influence of the surface points on a control point can be calculated analytically from the description of the NURBS surfaces [53]. The closer the surface point is located to a control point, the more influence it has on the control point. At the end of each iteration, the image forces acting on the surface points are applied to the control points. Finally the position of the control points in each ring is constrained in such a way that the ordering of the points remains unchanged and a minimum distance between control points is enforced. The fitting algorithm can be adapted to a specific situation by changing the width of the SI profile and by selecting a positive or negative edge direction. The SI profile width represents the search range for edges in the image. If the initial tube

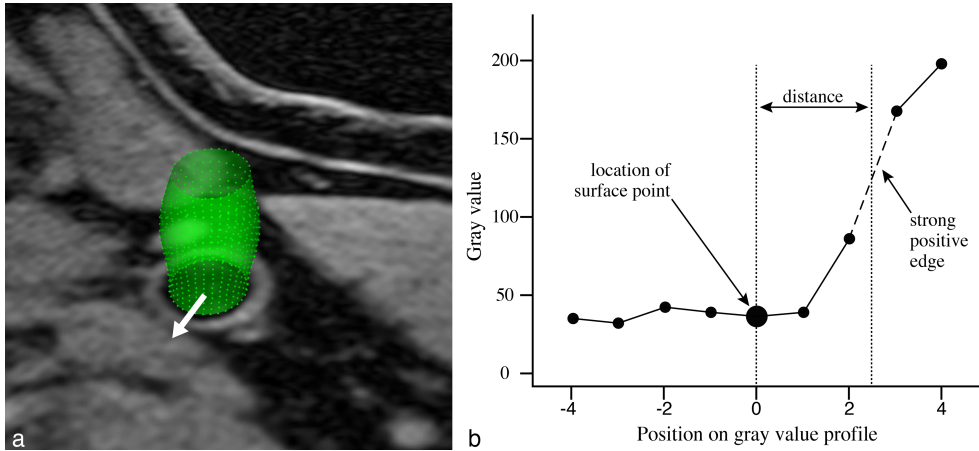


Figure 2.2: a) Intermediate result of fitting the lumen tube. The green points are the surface points, the white arrow shows the signal intensity (SI) profile along the surface normal. b) SI profile corresponding to the white arrow and detection of the strongest positive edge.

surface is expected to be far from the final segmentation, a large SI profile width has to be chosen.

Detection of the arterial lumen in the MRA image

The automatic image segmentation is initialized by the manual selected proximal and distal point specifying the artery segment of interest. Subsequently, a 3D curve inside the arterial lumen and an estimation of the lumen diameter between the indicated points is found using Wavefront propagation based on fast marching level sets [51, 54, 55]. A tube model is initialized by generating rings with control points perpendicular to the curve and fitted to the image data. Each ring was centered on the curve and the diameter was set to the estimated lumen diameter obtained before. During the fitting, the control points were allowed to move in 3D space, the width of the SI profile was set to 2 mm, the number of iterations was 50 and the surface was fitted to edges in the image which are bright inside the vessel model and dark outside.

Transfer and registration of the MRA lumen segmentation to the vessel wall images

The 3D MRA lumen segmentation is transferred to the 2D vessel wall slices by intersecting the tube model with the vessel wall slices based on their known geometrical relation. Subsequently, a 2D lumen contour is extracted for each vessel wall slice. Direct transfer of the tube model to the vessel wall images is not possible because the locations of the control points do not correspond with the 2D slices. Also, the higher resolution of the vessel wall images requires the usage of more control points to accurately describe the lumen boundary. To compensate for possible patient motion during the scanning of the different sequences, an automatic registration step is applied before the transfer of the MRA lumen segmentation to ensure that the extracted lumen contours are correctly aligned to the lumen boundaries in the vessel wall images.

The automatic registration is based on the assumption that the lumen boundary is a dominant circular structure in the vessel wall image near the transferred MRA lumen contour. A Hough transform, which is an image processing algorithm that can be used to detect circular structures, was applied to the vessel wall images to generate an image that has high signal intensities at the center of circular structures. Subsequently, the 3D MRA lumen tube was translated and rotated to include the highest responses from the Hough transform inside the tube. Least squares optimization was used to find the best fit resulting in a 3D tube which is registered to the vessel wall images. In case this registration step was deemed unsuccessful, the user was able to correct the registration.

Refinement of the lumen boundary in the vessel wall images

The set of registered lumen contours was used to initialize a new tube model in the vessel wall images. In each vessel wall slice, a ring with control points was created by placing the control points equidistantly on the registered contour. The tube model is fitted to the image data with the constraint that the control points were only allowed to move within the image slice. The width of the SI profile was set to 2 mm, the number of iterations was 50 and the surface was fitted to edges in the image which are dark inside the vessel model and bright outside. The result of this step is the lumen tube.

Estimation of the initial outer wall boundary

The lumen tube is intersected by the vessel wall slices and for each slice a 2D contour is extracted. An estimate of the outer wall boundary is found by dilating these contours from 0.5 to 2.0 mm in steps of 0.05 mm. For each step, the average edge strength under the contour was calculated, taken into account an edge direction from bright to dark. The dilated contour with the strongest average edge strength was selected as the initial outer wall boundary for that slice. This process was repeated for every slice resulting in an estimation of the outer wall boundary.

Detection of the outer wall boundary in the vessel wall images

The outer wall is detected in a similar manner as was done for the lumen boundary. Because the initial outer wall boundary is estimated at the position of the expected outer boundary, the SI profile width was limited to 1 mm. The tube surface is fitted to edges in the image which are bright inside the vessel model and dark outside. An example of the fitting of the outer tube is given in Figure 2.3.

The final segmentation of the vessel wall is defined by the lumen tube and the outer tube and is used to derive various quantitative carotid vessel wall parameters, described below.

Manual image analysis

All images were manually analyzed using the VesselMASS software package [25], by an experienced radiologist (M_1). Ten scans, the T_0 group, were analyzed by a second radiologist (M_2). Each observer independently traced the lumen and outer wall boundaries of the vessel wall in the axial slices of the black-blood sequence. The obtained contours from observer M_1 were used as the gold standard.

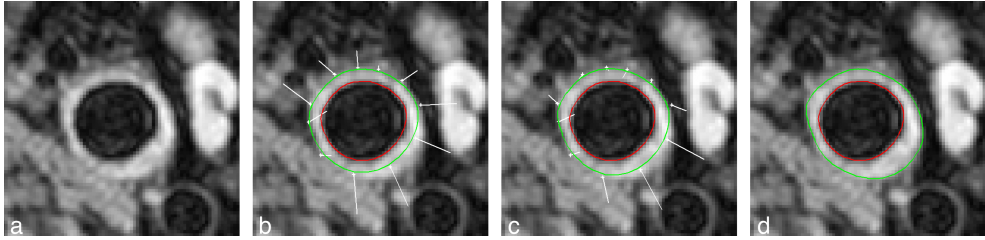


Figure 2.3: Model fitting process for the outer vessel wall shown in 2D. a) T1W image slice. b) First iteration showing the image forces that act on the control points (white). c) Intermediate result. d) The final result after 50 iterations.

Automatic image analysis procedure

The same set of images was analyzed with the automatic image segmentation method. To study the effect of initialization on the segmentation result, two users (A_1 and A_2) independently analyzed the T_0 subset of 10 carotid arteries with the automatic image segmentation algorithm. The automatic image segmentation method was implemented in C++ and all analyses were performed on a standard PC with a quad-core processor running at 2.4 GHz (Intel Q6600) and 4 GB of RAM. For both the manual and automatic image analysis, the duration of the analysis was recorded.

Definition of quantitative parameters

Vessel wall thickness and volume measurements

The vessel wall thickness (VWT) was derived automatically by first determining the centerline between the lumen and outer contour in each vessel wall slice. Then 100 chords connecting the lumen and outer wall contour were equidistantly sampled perpendicular to that centerline. For each slice, the median of the length of these 100 chords was calculated, and the average of the measurements of all slices resulted in the VWT. The user was able to visualize the individual VWT measurement chords in 3D by color mapping the VWT on the segmentation of the lumen (Fig. 2.4) enhancing visual inspection of the vessel structure. The vessel wall volume (VWV) was calculated by summing the vessel wall area in each slice and then multiplying that sum by the slice thickness.

Contour comparison metric

To compare the performance of the automatic segmentations with the reference standard in more detail, the degree of similarity (DoS) was calculated for the contours in each analyzed image slice [56]. The DoS is defined as the percentage of points that is similar between two contours. The number of sample points per contour was 100, obtained by equidistant sampling. Pairs of corresponding points are assumed to be similar if the distance between two points does not exceed a certain threshold. The threshold was chosen to be 0.27 mm, which is similar to the reconstructed pixel size (0.27 x 0.27 mm). An example is given in Figure 2.5. Similar points are interpreted as successfully segmented, while dissimilar points need adjustments to match the expert segmentation. The DoS allows evaluating the lumen and outer contours independent of each other.

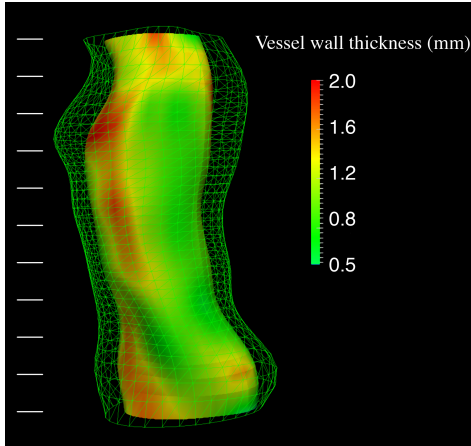


Figure 2.4: Final vessel wall segmentation showing the lumen with the vessel wall thickness color-coded on it, the outer wall (green wireframe) and slice levels (white lines).

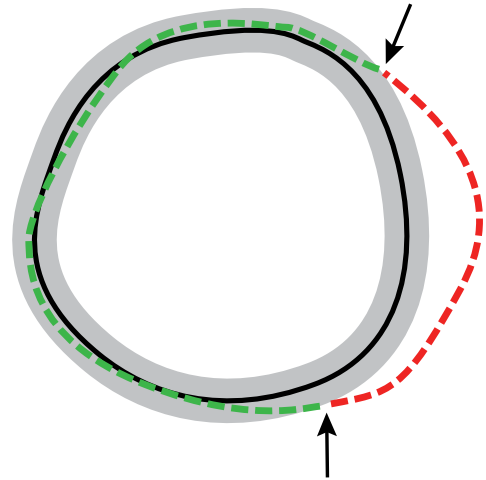


Figure 2.5: Example of a degree of similarity of 73%. The solid line is the reference contour; the grey band shows the 0.27 mm margin. The dashed line represents the computed contour. A total of 73% of the solid line coincides with the dashed line.

Comparison and statistical analysis

Automatic versus manual segmentation

The performance of the automatic segmentation method was quantified by calculating the DoS between the automatic segmented and manual contours. The agreement between both methods was evaluated by calculating the mean, standard deviation and intraclass correlations including 95% confidence intervals for the VWT and VWV found by manual and automatic segmentation. A paired t-test was performed to assess whether the means of both methods differed. Bland-Altman plots [57] for both parameters were generated to investigate the limits of agreement between automated and manual analysis. A P-value smaller than 0.05 was considered significant.

Interobserver agreement and reproducibility

To estimate the interobserver agreement, ten subjects were analyzed twice, each time by a different observer; this was done for both the manual segmentation as well as the automatic segmentation method. Bar plots were used to evaluate the variability between different observers and also the DoS was determined. To assess reproducibility, intraclass correlations including 95% confidence intervals between the time points T_0 and T_1 were determined for the VWT and VWV.

Table 2.1: Comparison between the automatic and manual segmentation using one manual and one automatic observer.

Manual vs. automatic [$n = 45$]		
	Mean of differences \pm SD	ICC [CI]
VWT (mm)	0.12 ± 0.21 ($P < 0.01$)	0.690 [0.500-0.817]
VWV (mm^3)	45.39 ± 80.16 ($P < 0.01$)	0.793 [0.682-0.892]

VWT = vessel wall thickness; VWV = vessel wall volume; SD = standard deviation; P , P value of t-test; ICC = intraclass correlation; CI = confidence interval.

Table 2.2: Interobserver analysis using two manual and two automatic observers.

Inter-observer analysis [$n = 10$]				
	M_1 vs. M_2		A_1 vs. A_2	
	Mean of differences \pm SD	ICC [CI]	Mean of differences \pm SD	ICC [CI]
VWT (mm)	-0.04 ± 0.05 ($P = 0.02$)	0.975 [0.904-0.994]	0.01 ± 0.03 ($P = 0.24$)	0.986 [0.945-0.997]
VWV (mm^3)	-7.51 ± 18.69 ($P = 0.41$)	0.985 [0.942-0.996]	0.95 ± 4.61 ($P = 0.53$)	0.999 [0.996-0.998]

VWT = vessel wall thickness; VWV = vessel wall volume; SD = standard deviation; P , P value of t-test; ICC = intraclass correlation; CI = confidence interval.

2.3 Results

Automated versus manual segmentation

The time needed to automatically segment the TOF-MRA and vessel wall images of one subject was approximately 18 s after indicating the artery of interest. Indication of the artery of interest was completed within 30 s by the user. A manual analysis took on average 12 min including visual identification of the artery of interest. The average DoS for 45 studies was 96.2% ($\pm 5.4\%$) for the lumen contour and 75.3% ($\pm 17.7\%$) for the outer contour, which is an average of 85.7% for both contours. The DoS values indicate better performance of the automatic segmentation for the lumen than for the outer contour. The systematic error, standard deviations, P-value of the paired t-test and intraclass correlations, including 95% confidence intervals, for the quantitative measurements are given in Table 2.1. The automatic segmentation algorithm shows substantial agreement [58] for both the quantification of VWT and VWV.

Bland-Altman analysis for the quantitative parameters is given in Figure 2.6. The figures show a small but significant underestimation, as indicated by the paired t-test, of the VWT and VWV of respectively 10.5% and 11.9% by the automatic segmentation method. A significant upward trend is observed for the VWT ($r = 0.65$; $P < 0.001$) and VWV ($r = 0.67$; $P < 0.001$).

Interobserver agreement and reproducibility

Bias of the mean, standard deviations of the difference, and intraclass correlations between the two pairs of observers (M_1 and M_2 , A_1 and A_2) and the multiple time points (T_0 , T_1) are given in Tables 2.2 and 2.3.

The intraclass correlations between different observers show that the analysis reproducibility of the automated segmentation method is higher than the manual segmentation. The DoS of the lumen and outer contour for manual experts was 97.8% and 92.3%, these numbers were higher for the automatic observers (A_1 and A_2); 99.8% for the lumen

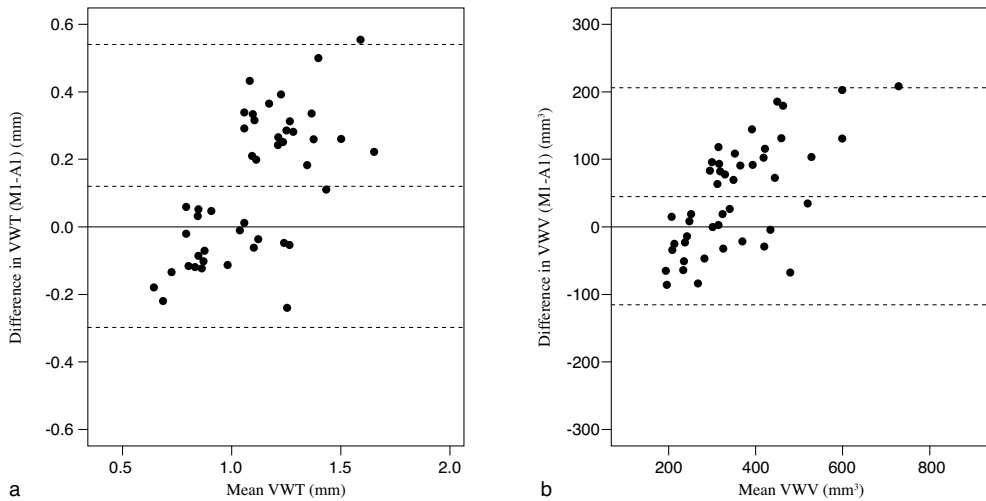


Figure 2.6: Bland-Altman plots showing the comparison between the manual and automatic segmentation for (a) vessel wall thickness (VWT) and (b) vessel wall volume (VWV).

Table 2.3: Scan-rescan analysis using one manual and one automatic observer.

	Scan-rescan analysis [$n = 10$]			
	T_0 vs. T_1 (M_1)		T_0 vs. T_1 (A_1)	
	Mean of differences \pm SD	ICC [CI]	Mean of differences \pm SD	ICC [CI]
VWT (mm)	-0.06 ± 0.11 ($P = 0.13$)	0.830 [0.457-0.955]	-0.02 ± 0.06 ($P = 0.12$)	0.940 [0.780-0.985]
VWV (mm^3)	-12.82 ± 24.62 ($P = 0.44$)	0.976 [0.908-0.994]	-3.62 ± 21.10 ($P = 0.60$)	0.983 [0.934-0.996]

VWT = vessel wall thickness; VWV = vessel wall volume; SD = standard deviation; P , P value of t-test; ICC = intraclass correlation; CI = confidence interval.

contour and 99.0% for the outer contour. No significant bias was found in both clinical measures for the automated method, contrary to the VWT as measured by the manual observers (Table 2.2). Figure 2.7 shows a smaller bias and variation of the VWT and VWV measurement with the automatic segmentation method. These results indicate a lower interobserver variability when compared with the manual segmentation method.

Finally, inter-scan reproducibility was assessed by correlating the clinical measurements found on T_0 and T_1 (see Table 2.2). The intraclass correlations for both metrics were higher for the automated segmentation method. Figure 2.7 shows a smaller bias and variation for the automatic segmentation method indicating better reproducibility of the automatic method.

2.4 Discussion

In this study, a 3D method was presented for automated segmentation of the vessel wall of the common carotid artery in combined MRA and vessel wall images. To our knowledge this is the first approach using a true 3D model which can be applied to both isotropic and nonisotropic image data. Comparison of the automated method with manual segmentation shows substantial agreement, with slight underestimation and a proportional error of the vessel wall thickness and volume. Compared with manual image analysis,

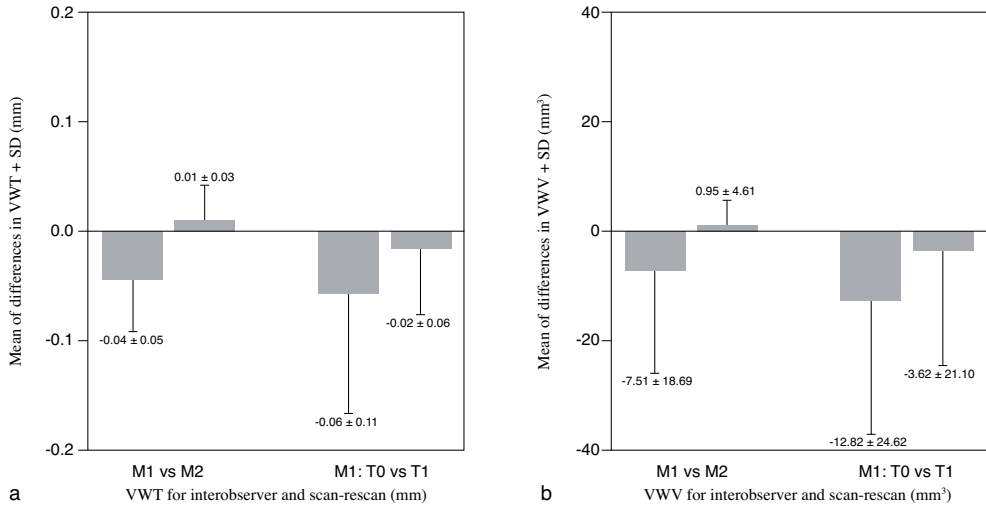


Figure 2.7: Bar plots showing interobserver variation and intra-scan reproducibility of (a) vessel wall thickness (VWT), (b) vessel wall volume (VWV).

the automated method demonstrated improved interobserver agreement and inter-scan reproducibility. Additionally, the proposed automated image analysis approach was substantially faster.

The performance of the automatic segmentation method is similar to existing methods which are all based on a 2D approach. In line with previous research, automated segmentation of outer contours was shown to be more difficult than lumen contours. Based on visual inspection, Underhill et al [33] report that 100% and 93% of the lumen and outer contours were successfully segmented, respectively. However, the detected contours were not compared with an independent manual reference. In our study, we used the DoS to compare the automated segmentation results with the manual reference. Using this stricter metric, 96.2% of the lumen contour was successfully segmented while this was 75.3% for the outer contour. The results of our repeatability study show a smaller variability for measurement of the VWT compared with the method developed by Underhill et al.

Adame et al [25] presented a different automated analysis approach, which requires one user interaction per slice. First, the outer wall is detected by fitting an ellipse to the image data, and then the lumen contour is found by clustering. Comparison of our results with this method is not straightforward, because different quantitative measures are used and our scores are based on a subject level and not on a slice level. However, our method requires less user interaction and the shape of the outer contour is not constrained to an ellipse.

In a more recent study [34], it was shown that a decrease in user interaction and an increase in segmentation performance can be accomplished by combining the MRA and VWI images. Our method uses a similar workflow but the registration and segmentation methods are 3D, instead of 2D.

Although image quality varied between and within subjects (Figs, 2.8,2.9,2.10), no images were excluded from the evaluation and no manual corrections were applied to any

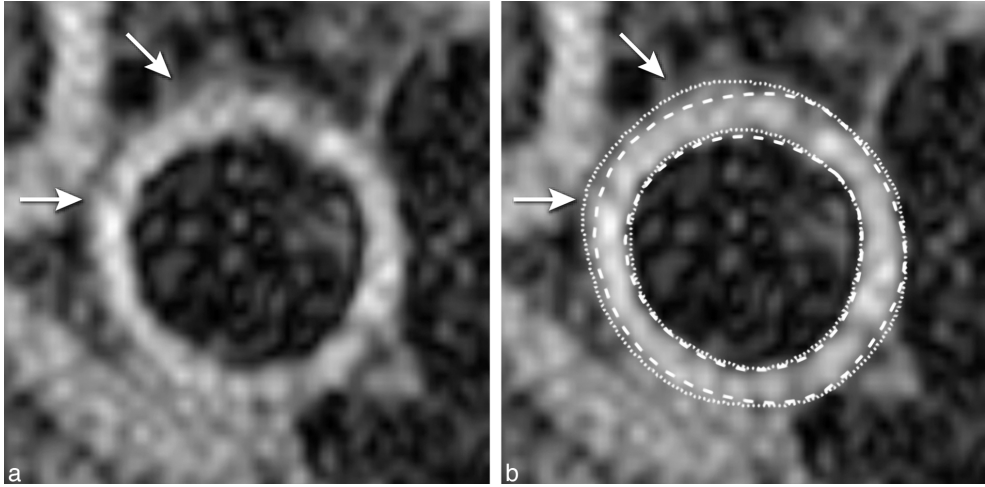


Figure 2.8: Example where the outer contour was fitted on the strongest edge, indicated by the arrows, but the manual contour was not drawn on the strongest edge (dotted = manual, striped = automatic).

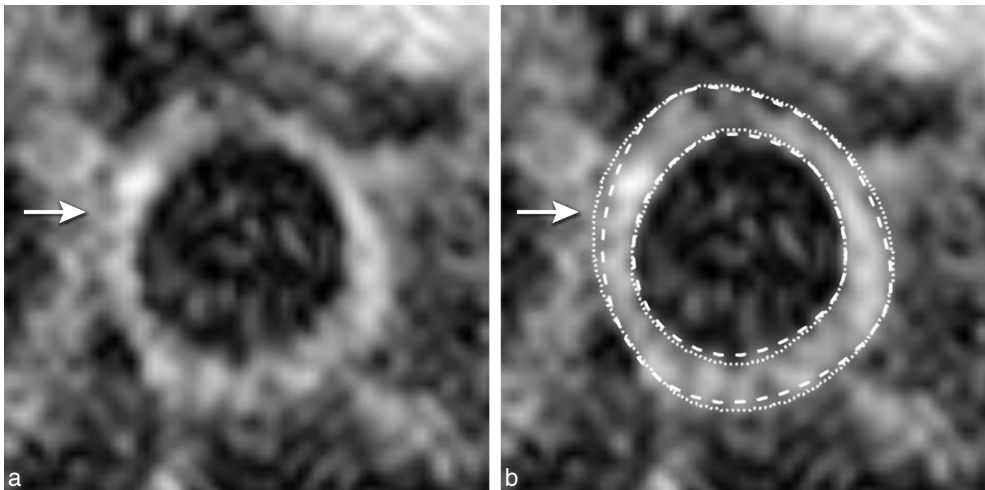


Figure 2.9: Example of weak edge information at the outer boundary (indicated by the arrow). The automatic contour is not attracted by an image edge, although the manual expert extrapolates the vessel in these areas (dotted = manual, striped = automatic).

of the automatically detected contours. The reported results, therefore, provide a realistic view on the practical applicability of the proposed analysis method.

Compared with other methods, our method requires minimal user interaction and has the advantage that it extracts 3D image information instead of acting independently on each vessel wall slice, which is the case for the existing segmentation methods.

Most of the disagreement in VWT and VWV was caused by small deviations in the segmentation of the outer wall. Small disagreements can be explained by the difference be-

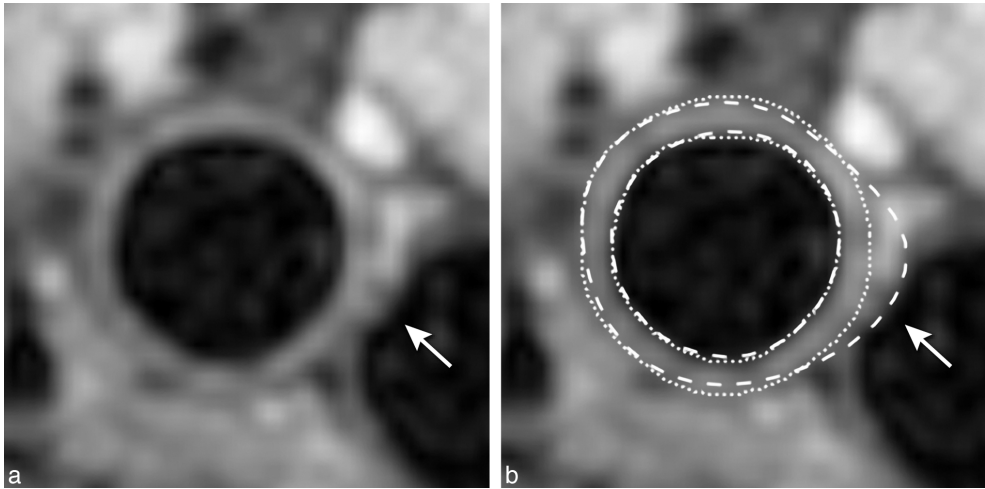


Figure 2.10: Incorrect segmentation of the outer vessel wall as indicated by the arrow. The outer tube is fitted to a strong edge which does not correspond to outer vessel wall (dotted = manual, striped = automatic).

tween the automatic and manual segmentation method. While the automatic method is designed to fit the tube surface on the strongest edge, a manual observer delineates the vessel wall based on its visual perception, which is subjective and also depends on the window/level setting of the display. This means that the observer does not necessarily draw on the strongest edge, an example can be seen in Figure 2.8; the strongest edge is not at the location of the outer boundary. The lumen boundary has a sharp edge in the image and is less sensitive to this effect. The outer boundary, especially for the more thickened vessels, is much more affected, explaining both the observed underestimation and proportional error in the quantification of the vessel wall dimensions.

Areas in the image with low image contrast are another source of errors. In those areas, an observer delineates the contours based on his experience and how it should look like, while the automatic segmentation either does not change its initial shape because there is no image force guiding the algorithm (Fig. 2.9), or the tube might be attracted by edges from nearby structures (Fig. 2.10). In our approach, image information from neighboring slices is taken into account to improve situations where edges are weak or missing.

This study is subject to several limitations. The presented automated method is dependent on the availability of a 3D MRA series. In this study, a Time of Flight MRA image is used to identify the artery of interest. In case this image is not available, the lumen center can also be detected directly in the vessel wall images. However, we did not investigate the impact on the performance when a MRA image is not present. Also the user interaction will become more complex because no global overview of the arterial structure is present and the artery of interest has to be indicated in the vessel wall slices.

In this study, the common carotid artery was analyzed. The 3D model can be adapted to support a bifurcating structure [59] including the internal carotid artery, however, obtaining good quality black blood vessel wall images in the carotid bifurcation is technically more challenging [60]. The shape of the carotid artery changes rapidly in the bifurcation and partial volume effect is very likely to appear when using a slice thickness of over 1

mm. Isotropic 3D imaging of the bifurcation might overcome this problem.

The next step in the development and validation of this method is to address the observed underestimation and trend. The manual expert does not always draw the outer boundary on the maximum edge, especially in cases with higher VWT, but uses another criterion. A potential solution is to change the calculation of the image forces for the segmentation of the outer wall. Outer contours drawn by different manual observers should be analyzed to get insight in the average SI profile of the outer boundary. Then the calculation of the image forces can be adapted by taking that average SI profile into account.

In conclusion, quantification of the vessel wall dimensions is an important tool in the research of atherosclerosis. Using automated segmentation reduces the processing time of the analysis and provides reproducible results. Even if manual corrections are needed in some images, the analysis time is still shorter than doing a complete manual segmentation. An additional advantage is the visualization of the 3D segmentation results. Different visualizations of the vessel wall can provide more insight in the condition of the artery because local shape and characteristics like asymmetry are more easily assessed. This study was performed with 2D vessel wall slices, but developments of MR pulse sequences are directed toward true 3D imaging [44, 60–62]. In that case, manual segmentation of the image data becomes impractical due to the size of the dataset, while the presented method is already able to analyze isotropic image data.

Acknowledgments

This study was funded by the Dutch Technology Foundation STW, which is the applied science division of NWO, and the Technology Programme of the Ministry of Economic Affairs.

Chapter 3

Carotid wall volume quantification from magnetic resonance images using deformable model fitting and learning-based correction of systematic errors

This chapter was published in:

K. Hameeteman, R. van 't Klooster, M. Selwaness, A. van der Lugt, J. C. M. Witteman, W. J. Niessen, S. Klein. Carotid wall volume quantification from magnetic resonance images using deformable model fitting and learning-based correction of systematic errors, *Physics in Medicine and Biology*, Volume 58, Pages 1605–1623, 2013.

Abstract

We present a method for carotid vessel wall volume quantification from Magnetic Resonance Imaging (MRI). The method combines lumen and outer wall segmentation based on deformable model fitting with a learning-based segmentation correction step. After selecting two initialization points, the vessel wall volume in a region around the bifurcation is automatically determined. The method was trained on 8 datasets (16 carotids) from a population based study in the elderly for which one observer manually annotated both the lumen and outer wall. Evaluation was done on a separate set of 19 datasets (38 carotids) from the same study for which two observers made annotations. Wall volume and normalized wall index measurements resulting from the manual annotations were compared to the automatic measurements. Our experiments show that the automatic method performs comparably to the manual measurements. All image data and annotations used in this study together with the measurements are made available through the website <http://ergocar.bigr.nl>.

3.1 Introduction

The prevalence of cardiovascular diseases (CVD) is rising and heart disease is the leading cause of death in the western world, claiming approximately one out of every five lives [63]. Atherosclerosis, a disease of the vessel wall, is the primary cause of cardiovascular disease. Atherosclerotic wall thickening in the carotid arteries can cause a narrowing or total occlusion of the lumen. Atherosclerotic plaque that does not cause occlusion may still lead to clinical events because of rupture and development of thromboembolism, which may subsequently lead to cerebral ischemia [64]. Consequently, much research is aimed at finding parameters that describe the plaque, and which can be used to improve risk stratification and for monitoring the progression of atherosclerotic disease. One of those parameters is the size of the plaque and its relation to the size of the vessel.

Magnetic Resonance Imaging (MRI) is an important means to monitor and quantify the state of the vessel wall and lumen. Several studies have shown the possibility to visualize the vessel lumen and outer wall on MRI [50, 65–69]. Annotation of both the lumen border and the outer vessel wall is a laborious task. Therefore, several researchers have proposed automatic wall segmentation methods e.g. [18, 31]. Although calculating the volume of the vessel wall is straightforward once a segmentation is made, a comparison between automatic and manual wall volume measurements has, to the best of our knowledge, not yet been done.

In this paper we present an automatic method to measure carotid wall volume from MR images. The contribution is five-fold:

1. The automatic method combines a deformable model approach [18] with a learning-based postprocessing step, in which systematic segmentation errors of the deformable model fitting are corrected. The idea behind this segmentation correction was developed by Wang et al [70]. However, whereas the method described in [70] was designed for brain structure segmentation, we modified it such that it can handle vessel-shaped structures.
2. An intensity inhomogeneity correction method is designed to compensate for the nonuniform sensitivity pattern of the RF surface coils.
3. A training set of eight subjects with manual annotations is used to exhaustively optimize a number of algorithm parameters.
4. The final algorithm is evaluated on a different set of 19 subjects, and the automatic results are compared with manual vessel wall volume measurements and inter-observer variability.
5. All image data used in this study together with the manual and automatic measurements are made available through the website <http://ergocar.bigr.nl> (user/pwd: reviewer/PMBVesselWall).

The remainder of this paper is organized as follows. Firstly, Section 3.2 explains the deformable model fitting and learning-based segmentation correction, and the wall volume quantification. Section 3.3 describes the image data and the preprocessing steps. Section 3.4 describes the experiments that were conducted to optimize the parameters of the method and to evaluate the wall volume quantification. The results of the experiments are given in Section 3.5. Discussion and conclusion are given in Sections 3.6 and 3.7 respectively.

3.2 Methods

Deformable model fitting

The method described by Van 't Klooster et al [18] was used to create an initial segmentation of the lumen and outer wall. This method requires a MR Angiography (MRA) image and a Black Blood (BB) image. The MRA image is used to obtain a robust initial segmentation of the carotid lumen. This segmentation is copied to the BB image and based on this initialization, the lumen and outer wall are segmented. The MRA and BB images are assumed to be co-registered (see Section 3.3). The only required user input consists of two initialization points. Based on these, the method fully automatically fits a deformable surface model of the lumen and the outer wall to the image data. Below, a brief description of this method is given which is summarized in Figure 3.1. For further details we refer to [18].

The method starts with a two-point initialization: one in the common carotid artery (CCA) and one in the internal carotid artery (ICA). These two points are used to initialize a wavefront propagation [51] in the MRA image which results in an approximate centerline with an associated lumen diameter estimate (green curve in frame 1 of Figure 3.1) at each centerline position. This centerline together with the diameters is used to initialize a NURBS surface [51] (blue surface lines in frame 2). The method then performs an optimization step in which the boundaries of the NURBS surface are more precisely fit to the lumen boundaries in the MRA image by searching for the maximum gradient magnitude in an intensity profile with a specified length (dL_{MRA}) perpendicular to the lumen surface (frame 3 shows the location of a profile and frame 4 the corresponding intensities along the profile; frame 5 shows an update of the initial contour). Only those edges are selected which have a high value (bright) inside the model and a low value (dark) outside the model. This optimization step is performed for a given number of iterations (nL_{MRA}).

The lumen NURBS surface found in the MRA image is used to initialize the lumen segmentation in the BB image (frame 6). Here, the same optimization of the surface fit to the lumen boundary is performed as in the MRA image (frame 7 and 8), using again a specified length (dL_{BB}) of the intensity profile and number of iteration steps (nL_{BB}). The edge direction in this step is set from dark inside the model to bright outside the model.

The estimated lumen surface is expanded and used to initialize the search for the outer wall. This is done in the same manner as for the BB lumen segmentation, by searching for the maximum gradient magnitude in an intensity profile with a specified length (dW_{BB}) for a number of iterations (nW_{BB}). For this segmentation step, the edge direction is set from bright inside the model to dark outside the model.

Learning-based correction of systematic errors

Using a deformable model to acquire an automatic segmentation limits the precision of the final segmentation to the flexibility of the used (NURBS) model. In areas where there is a sudden change in the shape of the vessel, this may lead to errors. Also, the deformable model approach described in the previous section was originally designed and optimized for one particular set of images. To compensate for the limitation of the deformable model and to adjust for the differences in image characteristics when using a different scanner, surface coil, and/or different MR acquisition parameter settings, we propose to use a post-processing step in which the segmentation is tailored to a new set of images. The idea behind this method was developed by Wang et al [70]. We will refer to this method as the

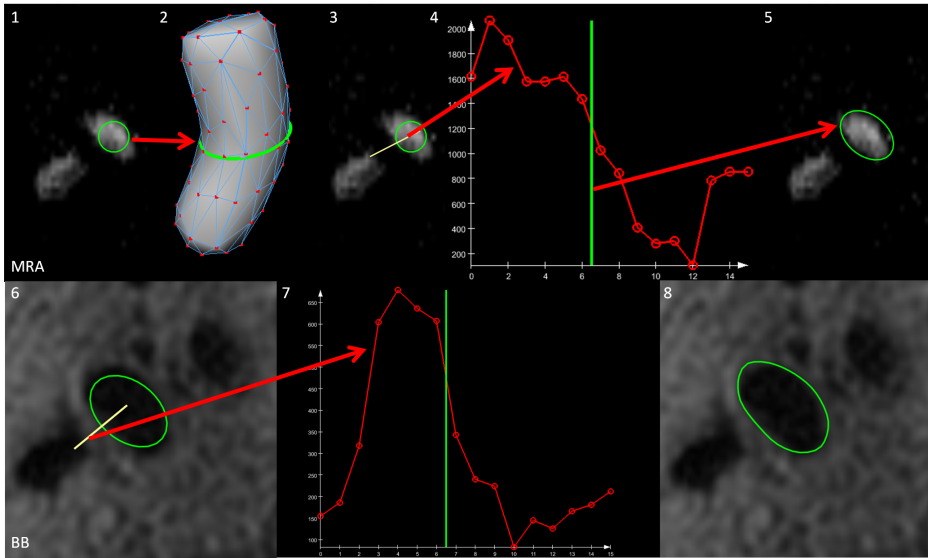


Figure 3.1: Graphical summary of the deformable model fitting method. An MRA segmentation based on wavefront propagation (1) is used to initialize a NURBS surface (2), which is fit to the lumen boundary by searching for a maximum gradient magnitude (4) along an intensity profile (3). The resulting segmentation is used as initialization in the BB image (6) where it is optimized (7,8) in the same manner as is done in the MRA image.

Learning-Based Segmentation Correction (LBSC) method. As the LBSC method was designed for brain structure segmentation, we modified it to be able to handle vessel structures. We will refer to this modified method as the Learning-Based Vessel Segmentation Correction (LBVSC) method.

The LBSC method uses a ground truth segmentation (in our case manual annotations) to train a classifier that modifies a binary segmentation made by a host segmentation method (in our case the result from the deformable model fitting described in Section 3.2). The LBSC method classifies all voxels in a region of interest (ROI), which is created by dilating the host segmentation. For each voxel, a feature vector is computed, consisting of:

- all image values in a $5 \times 5 \times 5$ neighborhood of the voxel in the MR image (125 features)
- all values in a $5 \times 5 \times 5$ neighborhood of the voxel in the host segmentation (125 features)
- x, y and z coordinate of the voxel relative to the center of mass of the host segmentation (3 features)
- product of the neighborhood and coordinate features ($3 * (125 + 125)$ features)

This leads to a total of 1003 features. The LBSC method trains a classifier on the difference between the host segmentation and the manual annotation. It thus learns to correct the errors made by the host segmentation. AdaBoost is chosen as classifier, which combines many weak classifiers (regression stumps) into a single strong classifier [71]. The

AdaBoost classifier has previously been shown to be successful in the context of medical image segmentation [72, 73].

For our application, a number of modifications are proposed: We use the signed distance to the host segmentation's border and the z-index as spatial features. Since the carotid artery is roughly perpendicular to the transversal plane, this latter feature is an approximation of the position along the centerline. For elongated structures like vessels, these two spatial features seem more appropriate than the distance to the center of mass. In addition to these spatial features we used the intensity of the BB image and its gradient magnitude. Instead of using a $5 \times 5 \times 5$ neighborhood we used a $7 \times 7 \times 3$ neighborhood. The effect of this neighborhood size, ($fL_x \times fL_y \times fL_z$ and $fW_x \times fW_y \times fW_z$ for the lumen and outer wall feature neighborhood respectively) on the segmentation accuracy was determined experimentally (see Section 3.4). Thus the two spatial features of the LBVSC method are:

- signed distance to the boundary host segmentation (1 feature)
- relative z-index (1 feature)

The 441 appearance features are the $7 \times 7 \times 3$ neighborhood voxels of:

- the host segmentation (i.e. 0 or 1) (147 features)
- the BB image (147 features)
- the gradient magnitude of the BB image (147 features)

Similar to the LBSC method we also used the product of the spatial and appearance features as additional features ($2 * (147 + 147 + 147) = 882$, leading to a total of $2 + 441 + 882 = 1325$ features).

Since most errors in the host segmentation are near the boundary of the segmentation, our LBVSC method only classifies the voxels within a ROI around this boundary. This region is defined by a morphological dilation minus an erosion of the binary host segmentation using a spherical kernel with radius rL_{dilation} and rL_{erosion} for the lumen and rW_{dilation} and rW_{erosion} for the outer wall segmentation. The binary host segmentation of the outer wall includes the lumen area.

When the classifier is trained on the difference between the host segmentation and the manual annotation (as in the original LBSC method), only the voxels that are not correctly segmented in the host segmentation get a negative label. If the host segmentation has large overlap with the manual annotation, this leads to many positive samples and only a few negative samples. To prevent this unequal class sizes we trained the AdaBoost classifier directly on the label from the manual annotation, which leads to a better balance between the classes. To make the classification tractable, only half of the randomly selected voxels within the ROI are used as samples.

Whereas the output of the deformable model fitting described in Section 3.2 is smooth, the output of the LBVSC method may have holes or isolated voxels. Therefore a morphological closing with a kernel radius of 2 voxels is applied to the output of the LBVSC method and isolated voxels are removed using connected components analysis.

Vessel wall volume quantification

The vessel wall volume V_{wall} is quantified in a region of 25 mm in the transversal direction centered at the bifurcation. The bifurcation point is manually annotated and defined as the first transversal plane on which two separate lumens (one of the ICA and one of the External Carotid Artery (ECA)) are visible. In cases where part of the evaluation region falls outside the scan range, the evaluation region is restricted by the image boundaries.

Application of the LBVSC method results in a binary mask for the lumen and the outer wall. The difference of these two masks is defined as the vessel wall. The vessel wall volume is computed by voxel counting and multiplying the result with the volume of one voxel.

Besides the volume, a clinically used parameter to quantify the vessel wall V_{wall} is the Normalized Wall Index (NWI) which is defined as:

$$\text{NWI} = \frac{V_{\text{wall}}}{V_{\text{lumen}} + V_{\text{wall}}} \quad (3.1)$$

where V_{lumen} is the volume of the vessel lumen. Bigger plaques thus lead to a higher NWI.

3.3 Data specific preprocessing

Data description

The image data of this study is taken from a prospective, population-based study among subjects aged 45 years and older. This study has been described in detail elsewhere [74]. All participants having a maximum intima-media thickness of more than 2.5 mm (determined using Ultra Sound [75]) in at least one carotid artery were invited for a carotid MRI exam. In total, 1072 participants were scanned.

MRI of the carotid arteries was performed on a 1.5-T MR scanner (Signa Excite, GE Healthcare, Milwaukee, USA) with a bilateral phased-array surface coil. To reduce motion artifacts, subjects were stabilized in a custom-designed head holder. The total scanning time was about 30 minutes in which, among others, the following sequences were acquired (see [75] for acquisition details):

- Proton density weighted Fast Spin Echo Black-blood (BB)
- Phase Contrast sequence which consists of an image showing flow in any direction (PC), a magnitude image (PCMag) and 3 images for the flow in the x, y and z direction.

The PC is used as MRA image for the deformable model fitting (see Section 3.2) and the PCMag image is used to register the PC image to the BB image (see Section 3.3). Figure 3.2 shows an example slice of each of these MR sequences.

Inhomogeneity correction

The bilateral phased-array surface coils cause severe intensity inhomogeneity within the neck. The sensitivity near the skin is much higher than in the middle of the neck. Figure 3.3c shows a typical example of the intensity profile across the neck in a BB image. Many popular intensity inhomogeneity correction methods have strong assumptions on

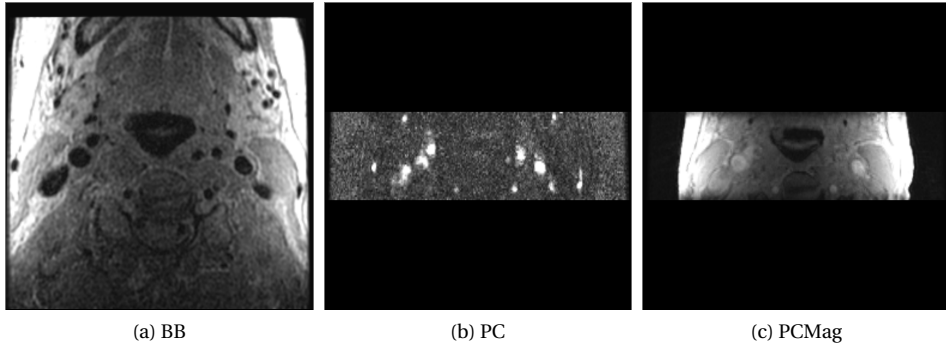


Figure 3.2: Example slice near the bifurcation of the three different MR sequences used in this study.

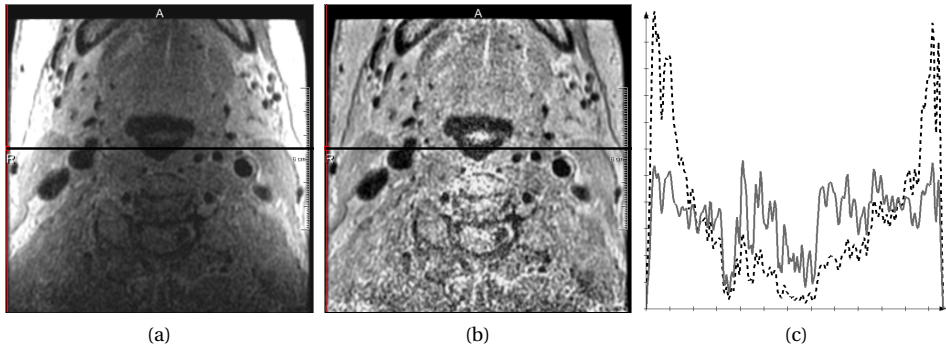


Figure 3.3: Example of the intensity inhomogeneities caused by a surface coil (a), the same image after applying the LEMS method (b) and the intensity profiles of the black line in the original (black, dashed line) and the corrected (gray, solid line) image (c).

the distribution of the modeled bias field. For example, N3 [76] and N4 [77] assume the distribution of the bias field intensities to be log-normal. Other methods like the one proposed by [78] and [79] assume a slowly varying bias field. These methods do not result in a satisfactory correction of the intensity inhomogeneities in the case of phased-array surface coils. The method proposed by [80], called Local Entropy Minimization with a bicubic Spline model (LEMS), was designed to deal with inhomogeneities caused by phased array surface coils.

The original LEMS method was designed for 2D images. To ensure a smooth bias field across slices, we extended the method to 3D with the following modifications.

LEMS tries to identify the voxels that do not have any signal as they cannot be used to estimate the bias field. We estimated the background voxels using the whole 3D image. Furthermore, the 2D slice based estimation of the bias field is smoothed in the slice direction using Gaussian blurring with a σ of 3 slices.

This way a spatially smooth bias field is obtained as can be seen in Figure 3.4.

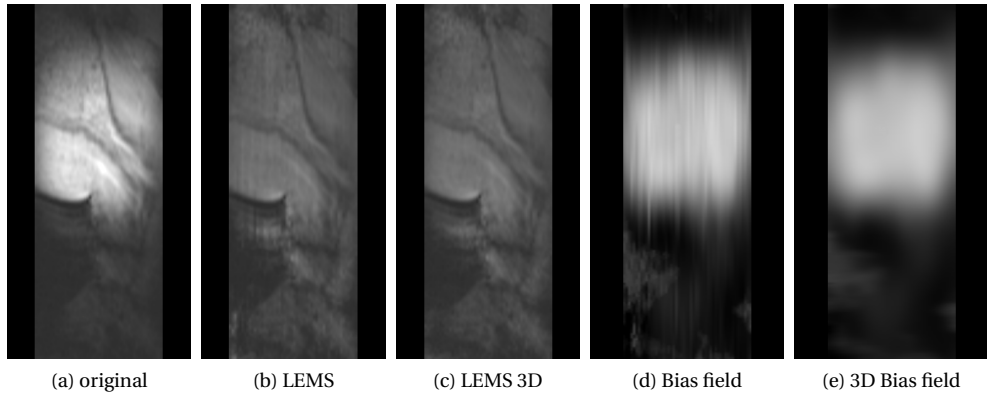


Figure 3.4: Inhomogeneity correction using LEMS and smoothing the estimated correct field. Sagittal slice of (a) the original BB image, (b) after correction using standard LEMS (c), using LEMS with smoothed bias field, (d) estimated bias field of the standard LEMS method and (e) estimated bias field with smoothing in the slice direction.

Because the LEMS method uses a multiplicative bias field model, the correction is performed by dividing the original image by the estimated bias field. This can lead to very large intensity values in the corrected image in regions where the estimated bias field has small values. The registration between the BB and MRA image (see Section 3.3) is hampered by a few extremely high intensity values within the image, therefore the highest 1% of the intensities of the corrected image are clamped. Figure 3.3a and 3.3b show an example of the BB image before and after inhomogeneity correction, respectively, and the effect of the correction on the intensity profile can be seen in Figure 3.3c.

Registration

As stated in Section 3.3, the complete MRI exam takes approximately 30 min. Although the position of the head of the subjects is stabilized using a head-holder, they still have the ability to move their body, which can cause twisting of the neck. Moreover, cardiac and breathing motion can also lead to displacement of the arteries in the neck. This motion leads to small mis-registrations between the different sequences. The lumen and vessel wall segmentation method described in Section 3.2 requires a registered BB and MRA image. We perform an intensity-based registration method to align the images. The PC image contains very little anatomical information as can be seen in Figure 3.2b and is therefore not very well suited for an intensity based registration. The PCMag image (shown in Figure 3.2c) which is simultaneously acquired with the PC image contains much more anatomical information. Therefore the PCMag image was registered to the BB image and the resulting deformation was applied to the PC image.

The registration first performs a rigid registration step to compensate for global displacements. Because the BB image and the PCMag image contain different anatomical regions, a mask was used for both the fixed and the moving image to indicate the regions where there should be overlapping information. The rigid registration was followed by a B-Spline registration [81] using mutual information as similarity metric [82]. For the

optimization we used an adaptive stochastic gradient descent optimizer [83]. The registration was performed in a multi-resolution framework with three resolution levels and was achieved using the ITK [84] based registration toolbox `elastix` [85].

3.4 Experiments

For the experiments, 27 subjects were randomly selected from the full database. This evaluation set was split in a training set of 8 subjects and a test set of 19 subjects. The training set was used to optimize the parameters of the deformable model fitting (dL_{MRA} , nL_{MRA} , dL_{BB} , nL_{BB} , dW_{BB} and nW_{BB}) and the LBVSC method ($rL_{dilation}$, $rL_{erosion}$, $rW_{dilation}$, $rW_{erosion}$, $fL_x \times fL_y \times fL_z$ and $fW_x \times fW_y \times fW_z$). The test set was used to evaluate the vessel wall volume and NWI quantification.

Manual annotations

On the complete set of 27 subjects the lumen and outer wall of both the left and the right carotid artery were annotated manually by observer 1 (ob1). On the test set observer 2 (ob2) performed the same annotations. The manual annotation started with an accurate definition of the centerline, after which longitudinal contours along this centerline were drawn in a curved planar reformatted image for both the lumen and the outer wall. These longitudinal contours were used to create cross-sectional contours perpendicular to the centerline. The cross-sectional contours were then adjusted to fit the lumen and the outer wall. More details on the annotation process can be found in [86]. The manual annotations were converted into binary masks for calculating the Dice [87] overlap coefficient and using the masks in the LBVSC step. The mask generation was achieved by fitting a surface through the contour points using variational interpolation [88] and voxelizing this closed surface. The mask of the outer wall contains everything within the outer wall including the lumen.

The manual annotations of the ICA do not incorporate the external part in the bifurcation region. Because the automatic method does not differentiate between ICA and ECA in the bifurcation region, the automatic segmentation may cover a larger part of the lumen area within the bifurcation region. This larger automatic segmentation is not wrong, but would result in errors during the evaluation because the manual ground truth does not contain the ECA. To make sure that this does not influence the evaluation results, the ECA region of the bifurcation was masked out and no evaluation was done in that region.

Parameter optimization

Surface distance

Since there is no ground truth definition in the MRA sequence, the values of profile length dL_{MRA} and the number of iterations nL_{MRA} were chosen such that the resulting segmentation visually provided a good initialization for the BB lumen segmentation.

For the parameter optimization of the deformable model fitting in the BB image, a distance measure was computed between the NURBS surface and the manual contours. First, the surface was intersected with the MPR plane (perpendicular to the centerline) in which the contours were drawn. This created a contour for the automatic segmentation.

Then the symmetric average Euclidean distance between the manual and automatic contours was calculated. This distance was calculated for all manual contours and the average was computed for each carotid. The average over all carotid segmentations in the training set (denoted by $\delta L_{\text{surface}}$ and $\delta W_{\text{surface}}$ for the lumen and outer wall segmentation, respectively) was used as optimization objective.

The dL_{BB} , nL_{BB} , dW_{BB} and nW_{BB} parameters were selected by an exhaustive search, minimizing $\delta L_{\text{surface}}$ and $\delta W_{\text{surface}}$. First the lumen parameters were optimized and then the outer wall parameters. The value of dL_{BB} was optimized between 5 and 25 mm in steps of 2 mm. The number of iterations nL_{BB} was optimized over the following set: {5,10,15,25,50,75,100,150}. The outer wall parameter dW_{BB} was optimized between 5 and 15 mm in steps of 2 mm and nW_{BB} over the following set: {0,1,2,3,5,7,10,25,50,75}. Each combination of profile length and number of iterations was tested, leading to 88 lumen experiments and 60 outer wall experiments.

Learning-based vessel segmentation correction

The influence of the neighborhood size of the features, $fL_x \times fL_y \times fL_z$ and $fW_x \times fW_y \times fW_z$, on the resulting segmentation was determined for the following values: 3x3x3, 5x5x3, 5x5x5, 7x7x3, 7x7x5, 7x7x7, 9x9x3, 9x9x5, 9x9x7, 9x9x9. For each of these feature neighborhoods the optimal combination of rL_{dilation} and rL_{erosion} , and rW_{dilation} and rW_{erosion} was determined. These LBVSC parameters were optimized with respect to the Dice overlap of the resulting segmentation with the manual segmentation. For each combination of neighborhood size dilation and erosion radius, a new classifier was trained. As the training of each classifier took several hours, performing cross-validation on the training set would take too much time. Therefore each classifier was trained on the complete training set and the evaluation of the resulting segmentation was also performed on the complete training set. This may lead to an overestimation of the performance of the LBVSC method. This is of minor importance, since these experiments are only meant to optimize the dilation and erosion parameters, and the true performance will be evaluated on the test set (see Section 3.5). The dilation and erosion radii were varied over the interval [0,9] mm in steps of 1 mm. The AdaBoost classifier was trained using 400 iterations.

Evaluation on test set

The algorithm was evaluated on the 38 carotids of the 19 datasets in the test set. We evaluated the final segmentation of the lumen and the outer wall by calculating the Dice coefficient for each. This evaluation was done both without the segmentation correction step, and applying the original LBVC method and our modification, the LBVSC method. The significance of the difference caused by applying the segmentation correction methods was tested using a paired t-test.

The vessel wall volumes and NWI from the manual annotations were computed in the same way as for the automatic segmentation (see Section 3.2). This was done for both observers that annotated the test set.

The manual and automatic wall volumes were compared by calculating the average difference between the two volumes, the average difference of the NWI and the standard deviation of these two difference measures. Also the Pearson and intra-class correlation [89] coefficient were calculated.

		dL_{BB} (mm)										
		5	7	9	11	13	15	17	19	21	23	25
nL_{BB}	5	0.84	0.77	0.73	0.70	0.69	0.69	0.71	0.90	0.91	0.92	0.93
	10	0.76	0.62	0.54	0.51	0.50	0.50	0.51	0.72	0.73	0.74	0.74
	15	0.70	0.54	0.46	0.44	0.43	0.43	0.45	0.66	0.66	0.66	0.67
	25	0.65	0.47	0.40	0.39	0.39	0.39	0.42	0.63	0.63	0.64	0.65
	50	0.70	0.53	0.49	0.46	0.45	0.43	0.46	0.52	0.63	0.71	0.87
	75	0.68	0.52	0.48	0.45	0.46	0.45	0.48	0.56	0.78	0.82	0.94
	100	0.67	0.50	0.48	0.45	0.46	0.47	0.49	0.59	0.78	0.92	0.96
	150	0.65	0.50	0.47	0.45	0.47	0.47	0.51	0.64	0.80	1.30	0.96

Table 3.1: Average surface distance $\delta L_{\text{surface}}$ for the various settings of profile length dL_{BB} and the number of iterations nL_{BB} used in the BB lumen segmentation. The minimum value is shown in bold font.

In these evaluations on the test set both observers were compared to each other and to the automatic method.

The influence of the number of training sets for the LBVSC method was determined by increasing this number from 10 until 18 in steps of 2. Because for the eight datasets in the training set no manual segmentations of the second observer was available, we only used the manual annotations of the first observer for evaluation. For each training set size (10, 12, 14, 16 and 18 datasets) 10 different random selections of the 38 data sets were made and the results of these 10 experiments were averaged. Just as in the other evaluations on the test set we calculated the Dice coefficient between the automatic segmentation of the lumen and the outer wall.

3.5 Results

Parameter optimization

Deformable model fitting

The PC MRA images used in this study have a lower contrast compared to the TOF images used in [18]. Especially in the bifurcation area the optimization of the MRA lumen surface generated a small or “half moon” shaped vessel surface leading to a bad initialization for the BB lumen segmentation. To handle this problem we drastically reduced the number of iterations, nL_{MRA} , to 1 and kept the profile length dL_{MRA} to the minimum of 5 voxels. This gives the NURBS surface less freedom to adjust and results in a more circular cross-section of the segmented lumen.

Table 3.1 and 3.2 show the results of the optimization experiments for the lumen and outer wall parameters respectively. The bold, most red cell indicates the optimal value, i.e the minimal average surface distance $\delta L_{\text{surface}}$ and $\delta W_{\text{surface}}$. We did not perform any experiments using a profile length of less than 5 mm as this would require the estimation of a gradient on less than 3 voxels.

		dW_{BB} (mm)					
		5	7	9	11	13	15
nW_{BB}	0	0.54	0.54	0.54	0.54	0.54	0.54
	1	0.52	0.51	0.50	0.50	0.50	0.50
	2	0.51	0.50	0.49	0.49	0.49	0.49
	3	0.49	0.49	0.50	0.54	0.58	0.62
	5	0.48	0.50	0.57	0.67	0.75	0.84
	7	0.49	0.53	0.66	0.81	0.93	1.05
	10	0.51	0.61	0.82	1.02	1.19	1.34
	25	0.62	0.90	1.27	1.59	1.87	2.11
	50	0.74	1.12	1.55	1.95	2.28	2.57
75	0.81	1.23	1.69	2.11	2.50	2.83	

Table 3.2: Average surface distance $\delta W_{\text{surface}}$ for the various settings of the profile length dW_{BB} and the number of iterations nW_{BB} used in the BB outer wall segmentation. The minimum value is shown in bold font.

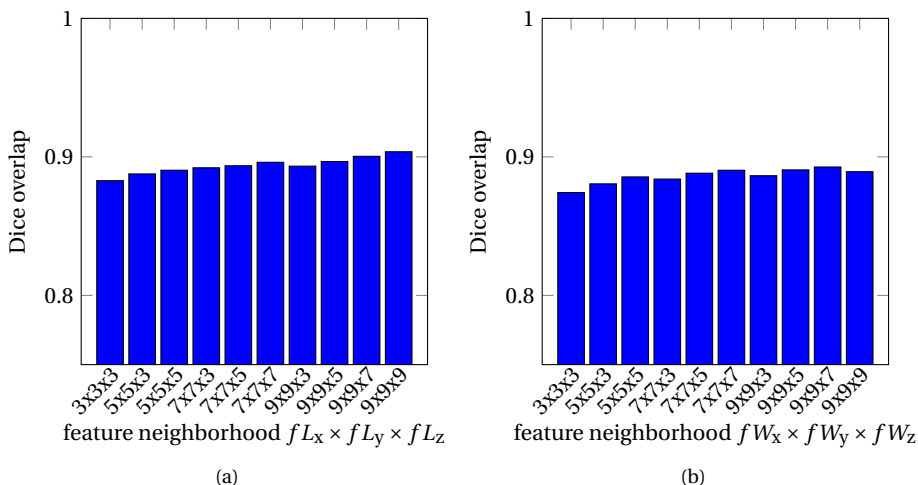


Figure 3.5: Influence of the feature neighborhood size on the final Dice overlap with the manual segmentation for (a) the lumen and (b) the outer wall.

Learning-based vessel segmentation correction

Figure 3.5 shows for each neighborhood size the maximum Dice overlap (obtained with optimum settings of the erosion and dilation parameters, which may be different for each neighborhood size). As can be seen from Figure 3.5 the influence of the feature neighborhood size on the segmentation accuracy is relatively small for both lumen and outer wall. As the computational costs increase significantly with a growing feature neighborhood we chose a neighborhood size of $7 \times 7 \times 3$, which is computationally feasible and accounts for the anisotropic voxel size.

Table 3.3 and 3.4 show the Dice overlap values for the $7 \times 7 \times 3$ feature neighborhood size for different combinations of dilation and erosion radii, rL_{dilation} , rL_{erosion} , and rW_{dilation}

and rW_{erosion} for the lumen and outer wall, respectively. The maximum Dice coefficients are shown in bold font. The values for a dilation and erosion with zero radius show the Dice overlap without applying the LBVSC method. The tables for the other feature neighborhood sizes can be found on the website <http://ergocar.bigr.nl> (user/pwd: reviewer/PMBVesselWall). In both Table 3.3 and 3.4 the value for zero dilation and erosion

		rL_{erosion} (voxels)									
		0	1	2	3	4	5	6	7	8	9
rL_{dilation} (voxels)	0	78.9	80.4	80.6	80.8	80.8	80.8	80.8	80.7	80.8	80.8
	1	85.1	84.7	85.0	85.2	85.2	85.2	85.2	85.2	85.1	85.1
	2	86.2	85.7	86.0	86.1	86.1	86.2	86.1	86.2	86.2	86.2
	3	87.2	86.8	87.1	87.1	87.1	87.2	87.2	87.2	87.2	87.2
	4	88.2	87.9	88.1	88.0	88.1	88.1	88.0	88.1	88.2	88.2
	5	88.6	88.5	88.8	89.1	88.9	89.1	88.8	88.9	88.8	88.8
	6	88.8	88.3	88.9	88.6	88.7	88.6	88.7	88.9	89.0	89.0
	7	88.8	88.0	88.3	88.7	88.6	88.9	88.8	88.7	88.9	88.9
	8	88.5	87.7	88.2	88.5	88.3	88.5	88.5	88.5	88.5	88.5
	9	88.2	87.6	87.9	88.0	88.1	88.1	88.3	88.2	88.1	88.0

Table 3.3: Average lumen Dice overlap values of the final segmentation for various sizes of the region around the host segmentation border which is defined by the dilation rL_{dilation} and erosion rL_{erosion} radius. The maximum value is in bold font. The value for zero dilation and erosion is the Dice overlap value for the uncorrected segmentation.

		rW_{erosion} (voxels)									
		0	1	2	3	4	5	6	7	8	9
rW_{dilation} (voxels)	0	81.3	82.2	82.3	82.4	82.3	82.3	82.4	82.3	82.4	82.4
	1	85.5	85.6	85.5	85.5	85.5	85.6	85.5	85.6	85.5	85.4
	2	86.4	86.4	86.4	86.4	86.4	86.4	86.4	86.4	86.5	86.4
	3	87.2	87.3	87.3	87.3	87.3	87.3	87.3	87.3	87.1	87.3
	4	87.8	87.9	88.0	87.9	87.9	87.9	88.0	87.9	87.9	88.0
	5	88.3	88.3	88.3	88.2	88.3	88.3	88.3	88.3	88.3	88.2
	6	88.2	88.2	88.1	88.2	88.2	88.1	88.3	88.3	88.1	88.1
	7	87.8	87.9	87.9	87.9	87.9	87.9	88.1	88.0	88.0	88.1
	8	87.8	87.7	87.4	87.8	87.7	87.9	87.9	87.6	87.7	87.5

Table 3.4: Average outer wall Dice overlap values of the final segmentation for various sizes of the region around the host segmentation border which is defined by the dilation rW_{dilation} and erosion rW_{erosion} radius. The maximum value is in bold font. The value for zero dilation and erosion is the Dice overlap value for the uncorrected segmentation.

is the smallest. On the training set the LBVSC method improved the segmentation result of the deformable model fitting: with any setting of rL_{dilation} , rL_{erosion} , rW_{dilation} and rW_{erosion} the results was better than $rL_{\text{dilation}} = rL_{\text{erosion}} = 0$ or $rW_{\text{dilation}} = rW_{\text{erosion}} = 0$.

Lumen		Outer wall	
parameter	value	parameter	value
nL_{MRA}	1	nW_{BB}	5
dL_{MRA}	5	dW_{BB}	5
nL_{BB}	25	$fW_x \times fW_y \times fW_z$	$7 \times 7 \times 3$
dL_{BB}	13	$rW_{dilation}$	5
$fL_x \times fL_y \times fL_z$	$7 \times 7 \times 3$	$rW_{erosion}$	7
$rL_{dilation}$	5		
$rL_{erosion}$	5		

Table 3.5: Optimal lumen and outer wall method parameters

	Lumen					Outer wall				
	No correction	LBSC	p-value	LBVSC	p-value	No correction	LBSC	p-value	LBVSC	p-value
ob1-ob2	0.90	0.90	–	0.90	–	0.90	0.90	–	0.90	–
ob1-auto	0.83	0.84	0.45	0.86	0.03	0.85	0.86	0.02	0.87	< 0.01
ob2-auto	0.84	0.83	0.64	0.84	0.86	0.83	0.85	0.11	0.86	0.01

Table 3.6: Dice overlap between the different measurements of the test set without segmentation correction and using the LBSC and LBVSC method.

Optimal parameters

Table 3.5 summarizes the optimal method parameters for both the lumen and the outer wall segmentation.

Evaluation on test set

The average Dice similarity coefficients for the lumen and outer wall are listed in Table 3.6. The average Dice overlap between the automatic segmentation and both observers is comparable to the Dice between the two observers. The overlap with the first observer is higher, which is expected as the automatic method was trained using the segmentations of this observer. The LBSC method only improved the outer wall segmentation of the observer on which it was trained. There was no significant difference for the lumen segmentation. The LBVSC method significantly increased the average lumen overlap for observer 1 whereas it remained the same for observer 2. For the outer wall the LBVSC method has a positive effect on the Dice overlap with respect to both observers.

The difference in effect of the LBVSC method between the training (Table 3.3 and 3.4) and test set (Table 3.6) is explained by the fact that in the former the training set was used to both train the classifier of the LBVSC method and measure the effect of the LBVSC method on the Dice overlap of the resulting segmentation (see also Section 3.4).

Figure 3.6 gives a visual impression of the effect of the LBVSC method on the outer wall segmentation. The LBVSC method (the dashed red contour) here clearly improved

the segmentation of the deformable model fitting method (smallest blue solid contour): it is closer to the manual annotation (solid green contour).

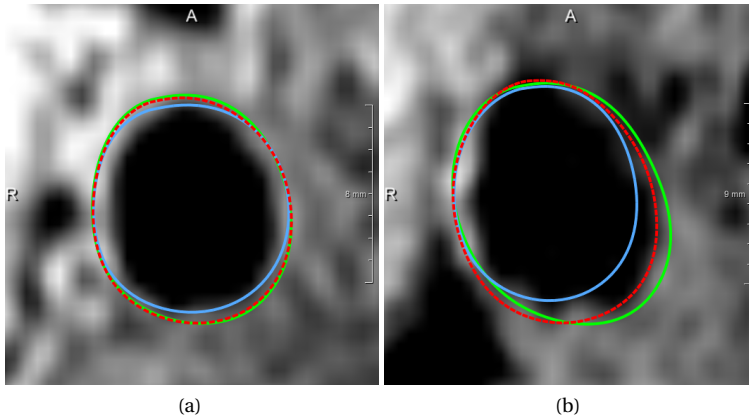


Figure 3.6: Two examples of the effect of the LBVSC method on the outer wall segmentation. The green solid line is the annotation by observer 1, the blue solid line is the segmentation from the deformable model fitting method, the dashed red line is the segmentation after applying the LBVSC method.

In Figure 3.7 the scatter plots of the volume and NWI measurements by observer 1, observer 2 and the automatic method are shown.

The two large markers in the volume measurements indicate two outliers where observer 1 and observer 2 disagree. Figure 3.8 gives an example slice of these outliers where observer 1 and 2 disagreed.

The contours shown in Figure 3.8 are the manual annotations of the outer wall for both observers. It is obvious from these segmentations that in this dataset it is very hard to determine the location of the outer vessel wall and both observers made a different choice on what to include in the vessel wall. In the subsequent analysis we removed these outliers.

Table 3.7 gives the average vessel wall volume and NWI measurements of both observers and the automatic method without applying the segmentation correction and with the LBSC and LBVSC method. As can be seen, the automatic segmentation slightly overestimated the vessel wall volume when compared to observer 1 and underestimated the volume when compared to observer 2. Observer 2 on average made larger volume measurements than observer 1. The average vessel wall volume of the automatic method is between the volumes estimated by observer 1 and observer 2, but was on average closer to observer 1 on which it was trained. The p-values of the differences between the automatic method with and without the LBVSC method are 0.0005 and 0.1 for V_{wall} and NWI respectively.

Table 3.8 shows the differences, Pearson and intra-class correlations of the volume and NWI measurements. The average difference in the wall volume measurements of the automatic method with respect to both observers is smaller than the average difference between the observers. Although the Pearson correlation coefficient of the volume measurements between the observers and the automatic method is not as good as the corre-

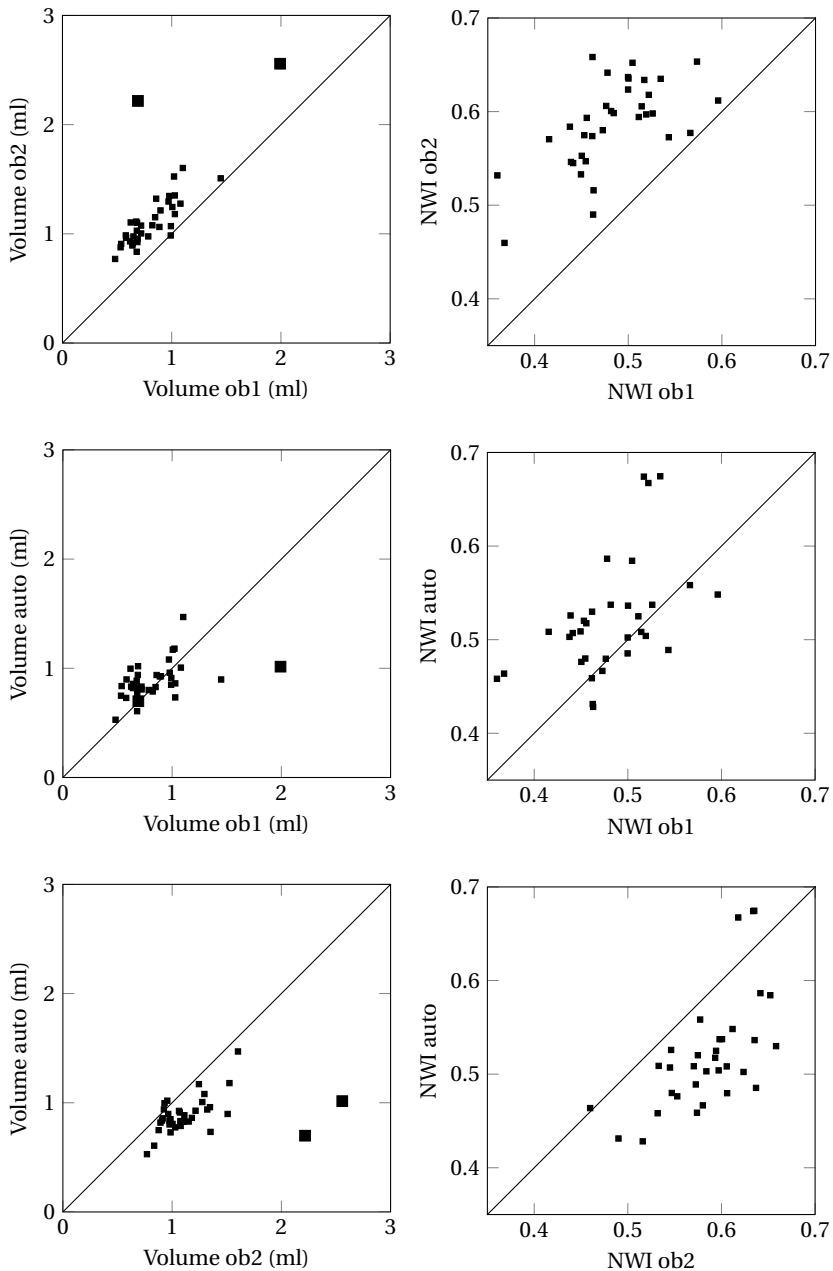


Figure 3.7: Scatter plot of the volume measurements (left column) and normalized wall index (right column) for observer versus observer 2 (top row), observer 1 versus automatic method (middle row) and observer 2 versus automatic method (bottom row). In the volume measurement graphs two outliers are present and shown with big markers. These outliers are not shown in the NWI graphs because they would stretch the scale too much.

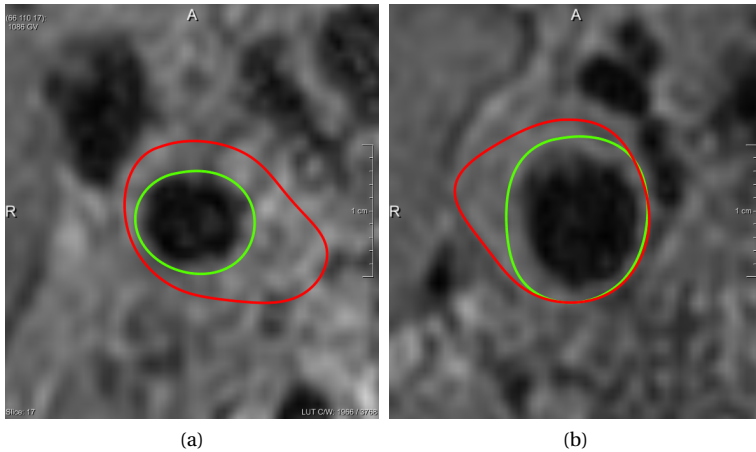


Figure 3.8: Example slice from the two outlier datasets. The green contour is from observer 1 and the red contour from observer 2.

	ob1	ob2	No correction	LBSC	LBVSC
V_{wall} (ml)	0.80 ± 0.21	1.1 ± 0.20	0.78 ± 0.13	0.83 ± 0.11	0.89 ± 0.17
NWI (ml/ml)	0.48 ± 0.05	0.59 ± 0.05	0.51 ± 0.05	0.51 ± 0.05	0.54 ± 0.08

Table 3.7: Average \pm standard deviation of vessel wall volume (ml) and normalized wall index measurements (ml/ml).

	V_{wall}			NWI		
	ΔV_{wall} (ml)	Pearson	icc	ΔNWI (ml/ml)	Pearson	icc
ob2 - ob1	0.30 ± 0.19	0.83	0.58	0.10 ± 0.04	0.51	0.32
auto - ob1	0.08 ± 0.20	0.51	0.62	0.05 ± 0.07	0.50	0.52
auto - ob2	-0.21 ± 0.15	0.57	0.57	-0.05 ± 0.07	0.54	0.56

Table 3.8: The average volume differences, the Pearson and intra-class correlation coefficients of the volume and NWI measurements between the two observers and the automatic method.

lation between the two observers, the intra-class correlation with both observers is better than (observer 1) or almost the same as (observer 2) between the two observers.

Looking at the clinically used NWI, the average difference between the measurements of automatic method and both observers is again smaller than the average difference between the two observers. Also the correlation coefficients between the automatic method and both observers are better than or almost the same as the correlations between the measurements of the two observers.

Table 3.9 shows the Dice overlap between the manual segmentation of the first observer and the automatic method for different size of the training set. The table show that increasing the size of the training set leads to a small increase in overlap.

Number of training sets	10	12	14	16	18
Dice lumen	0.84	0.84	0.84	0.85	0.86
Dice outer wall	0.85	0.84	0.84	0.85	0.86

Table 3.9: Influence of the number of training sets used for training the LBVSC method on the Dice overlap of the lumen and the outer wall, and the NWI

3.6 Discussion

The interobserver measurements presented in this study show that the systematic difference between the outer vessel wall annotations of two observer can be considerable (see the scatter plots in Figure 3.7). As we do not have manual annotations of the second observer on the training set, it is impossible to train the automatic method on both observers, or generate a new reference standard based on the combined annotations of these two observers without compromising the size of the test set. However, the annotation protocol for both observers was the same and the variation between the two observers can also be expected in clinical practice.

The method described in this paper was designed in order to analyze the MRI data acquired in the context of a population study. This population study uses a 1.5 T MRI scanner and a BB sequence which may not be the best possible sequence for imaging the vessel wall. Despite these limitations the described automatic method performs comparable to the observers. In future research it would be interesting to study the effect of different acquisition settings (1.5T vs. 3T, different MR sequences, the use of a head stabilizer) on the vessel wall quantification. The evaluation described in this study was performed on 19 subjects. For the future we plan a quantification of the vessel wall volume and normalized wall index on all 1072 subjects that participated in this study. Manual measurements on this number of subjects becomes infeasible.

The deformable model fitting method enforces a NURBS model on the lumen and wall boundary, and uses a single image feature (the maximum gradient magnitude) to fit the model. For the lumen border this is an adequate image feature. The gradient of the outer wall is less strong, which makes the application of this image feature less successful. The LBVSC method is not limited to the use of a single image feature, but instead uses many features to classify the outer wall voxels. This explains the difference in effect of the LBVSC method on the lumen and outer wall segmentation.

As long as there is a training set on which the LBVSC can be trained, the method described in this paper can easily be adapted to other images, acquired on a higher field MR scanner or using different protocols. If there is a training set consisting of a ground truth definition of multiple observers, these could be combined using existing methods like consensus reading or STAPLE [90], but they can also be used to train multiple classifiers and combine these classifiers into a single stronger classifier using methods described in e.g. [91].

3.7 Conclusion

In conclusion, we presented a method that can automatically quantify the wall volume and normalized wall index of the carotid artery in a region around the bifurcation. The method consists of a deformable model fitting step and a learning-based correction of

systematic errors. Intensity inhomogeneities in the MR images were reduced using a 3D-extended version of the LEMS method. The parameters of both the deformable model fitting and the LBVSC method have been optimized by extensive experiments using the manual annotations of a single observer on a training set. Evaluation was performed with respect to annotations of two observers on a separate test set. Our experiments justify the conclusion that the automatic method performs comparably to the manual annotations in terms of wall volume and normalized wall index measurements and can therefore be used to replace the manual measurements.

All image data, annotations and results from this study are made available through the website <http://ergocar.bigr.nl> (user/pwd: reviewer/PMBVesselWall). We challenge every one to improve our automatic vessel wall volume and normalize wall index measurements on these datasets and publish their results.

Chapter 4

Automated registration of multispectral MR vessel wall images of the carotid artery

This chapter was published in:

R. van 't Klooster, M. Staring, S. Klein, R. M. Kwee, M. E. Kooi, J. H. C. Reiber, B. P. F. Lelieveldt, R. J. van der Geest. Automated registration of multispectral MR vessel wall images of the carotid artery, *Medical Physics*, Volume 40, Issue 12, 121904, 2013.

Abstract

Purpose: Atherosclerosis is the primary cause of heart disease and stroke. The detailed assessment of atherosclerosis of the carotid artery requires high resolution imaging of the vessel wall using multiple MR sequences with different contrast weightings. These images allow manual or automated classification of plaque components inside the vessel wall. Automated classification requires all sequences to be in alignment, which is hampered by patient motion. In clinical practice, correction of this motion is performed manually. Previous studies applied automated image registration to correct for motion using only nondeformable transformation models and did not perform a detailed quantitative validation. The purpose of this study is to develop an automated accurate 3D registration method, and to extensively validate this method on a large set of patient data. In addition, the authors quantified patient motion during scanning to investigate the need for correction.

Methods: MR imaging studies (1.5T, dedicated carotid surface coil, Philips) from 55 TIA/stroke patients with ipsilateral <70% carotid artery stenosis were randomly selected from a larger cohort. Five MR pulse sequences were acquired around the carotid bifurcation, each containing nine transverse slices: T1-weighted turbo field echo, time of flight, T2-weighted turbo spin-echo, and pre- and postcontrast T1-weighted turbo spin-echo images (T1W TSE). The images were manually segmented by delineating the lumen contour in each vessel wall sequence and were manually aligned by applying throughplane and inplane translations to the images. To find the optimal automatic image registration method, different masks, choice of the fixed image, different types of the mutual information image similarity metric, and transformation models including 3D deformable transformation models, were evaluated. Evaluation of the automatic registration results was performed by comparing the lumen segmentations of the fixed image and moving image after registration.

Results: The average required manual translation per image slice was 1.33 mm. Translations were larger as the patient was longer inside the scanner. Manual alignment took 187.5 s per patient resulting in a mean surface distance of 0.271 ± 0.127 mm. After minimal user interaction to generate the mask in the fixed image, the remaining sequences are automatically registered with a computation time of 52.0 s per patient. The optimal registration strategy used a circular mask with a diameter of 10 mm, a 3D B-spline transformation model with a control point spacing of 15 mm, mutual information as image similarity metric, and the precontrast T1W TSE as fixed image. A mean surface distance of 0.288 ± 0.128 mm was obtained with these settings, which is very close to the accuracy of the manual alignment procedure. The exact registration parameters and software were made publicly available.

Conclusions: An automated registration method was developed and optimized, only needing two mouse clicks to mark the start and end point of the artery. Validation on a large group of patients showed that automated image registration has similar accuracy as the manual alignment procedure, substantially reducing the amount of user interactions needed, and is multiple times faster. In conclusion, the authors believe that the proposed automated method can replace the current manual procedure, thereby reducing the time to analyze the images.

4.1 Introduction

Atherosclerosis is the primary cause of heart disease and stroke. These cardiovascular diseases are the leading cause of death in the Western world [63]. Atherosclerosis is a progressive disease which, at an early stage, is characterized by the accumulation of lipids and inflammatory cells in the vessel wall of large arteries, and, at a later stage, by the formation of plaque lesions inside the vessel wall [3]. Identification of vulnerable plaques, lesions with a high risk to rupture which in turn can lead to a cardiovascular event such as stroke, is of high clinical relevance.

Magnetic Resonance Imaging (MRI) of the carotid artery vessel wall is often used to assess atherosclerosis and is one of the most promising imaging modalities for visualizing plaque in the carotid artery. It is noninvasive, does not involve ionizing radiation, and is highly reproducible [92]. Detailed assessment of atherosclerosis in the carotid artery requires high resolution imaging of the vessel wall using multiple MR sequences with different contrast weightings [93]. A MRI examination of the carotid artery usually starts with the acquisition of a time of flight (TOF) magnetic resonance angiography sequence which provides a global overview of the vascular structure. Subsequently, several additional 2D acquisitions can be planned and acquired to obtain information about the vessel wall morphology and plaque composition. These vessel wall images are usually scanned perpendicular to the carotid artery and typically have a high resolution inplane (0.4 mm) and a significantly lower throughplane resolution (3 mm). Manual or automated analysis of the vessel wall images allows identification and quantification of the plaque components inside the vessel wall. Based on this information, the clinically relevant vulnerable plaques can be distinguished from stable plaques.

The duration of a multisequence MRI protocol is between 30 and 60 min. Due to patient movement significant misalignment may occur between the sequences. The effect of patient motion is especially noticeable inplane; a movement of 1 mm by the patient can result in a shift of multiple pixels in the subsequent MR sequence. The effect of movement in the throughplane direction is less obvious due to the lower resolution, but is still present. These translations between different sequences due to patient movement decrease the accuracy of plaque quantification and increase the time needed by a human expert to analyze the images because comparing similar locations between the images is less straightforward due to the inconsistency in the spatial relation between the sequences. Therefore, patient movement should be corrected for.

The current way in clinical research to correct patient movement is manual alignment of the vessel wall images by an expert. First, in one sequence the lumen and outer wall contours are delineated, followed by manual intrascan image alignment by applying a combination of throughplane translation of the complete image stack and inplane translation for individual image slices. The expert takes into account the appearance of the images and uses the lumen and outer wall contours as a reference. Once all images are aligned, regions of plaque can be identified and characterized by evaluating the relative signal intensities in the available imaging sequences. Various schemes for plaque classification have been reported for different imaging protocols, which can be used to identify regions of calcification, lipid core, intraplaque hemorrhage, ulceration, and fibrous tissue [22, 23, 94]. In case the segmentation of the plaque components is performed by an automated method [20, 37, 38], accurate alignment of the images is essential since most of these methods classify pixels in the vessel wall using the signal intensities from the different MR sequences, thereby assuming pixelwise correspondence between the images.

Table 4.1: Literature overview (ROI = region of interest, MI = mutual information).

Study	Dataset description	Image similarity metric	ROI usage	Transformation model	Validation method
Adame et al. [39]	19 patients, two MR sequences	Correlation coefficient	Yes	2D translation	None
Biasioli et al. [40]	Five volunteers + 20 patients, three MR sequences	Correlation ratio MI, Gradient MI	Yes	2D translation + rotation	Five volunteers: quantitative validation. 20 patients: visual validation.
Hofman et al. [37]	25 patients, five MR sequences	Normalized MI	Yes	2D translation + rotation	None
Liu et al. [38]	26 patients, five MR sequences	Active edge map	Yes	2D translation	87% correct, no further details given.
Fei et al. [41]	Two volunteers + one patient, three MR sequences	Normalized MI	Unknown	3D translation + rotation	Visual validation
Tang et al. [42]	48 patients, two MR sequences	MI	Yes	First 3D rigid, then 3D affine	Visual validation

Since manual alignment is a user dependent and a time-consuming procedure, automatic image registration has been applied in a number of studies. An overview of these studies is given in Table 4.1. In previous work, registration was mainly performed in 2D [37–40], ignoring any patient movement in the throughplane direction. In all studies, a region of interest around the carotid artery was used and image similarity metrics based on correlation, mutual information (MI), or gradients in the image were used. Transformation models were limited to translation and rotation. Fei et al. [41] performed image registration in 3D allowing for translation and rotation in all three directions, and Tang et al. [42] used a 3D affine transformation. It is however to be expected that patient motion also results in nonrigid deformation of the carotid vessel wall [95, 96]. Another limitation of the above studies is that the registration results were either assessed visually or no validation was performed. Quantitative validation was performed in only one study on five healthy volunteers [40]. To overcome the limitations of these studies, 3D nonrigid image registration methods should be investigated, optimized, and quantitatively validated on a large set of patient data.

Therefore, the purpose of this study was to investigate patient movement during scanning, to develop an accurate automated 3D registration method, and to perform a quantitative validation. The contribution of this study is threefold: (1) the manual alignments of a large number of studies were analyzed to quantify the average patient movement in MR vessel wall studies, thereby motivating the need for correction; (2) the development of an optimal 3D registration method; and (3) to perform a quantitative validation of the registration results using an independent reference standard on a large population.

4.2 Materials and methods

Image data

Images from 55 TIA or stroke patients with ipsilateral <70% carotid artery stenosis were randomly selected from a larger cohort [97]. MR images of the stenosed artery were obtained on a 1.5T scanner using a dedicated carotid surface coil (both Philips Healthcare, Best, The Netherlands). Five MR pulse sequences were acquired around the carotid bifurcation, each containing nine transverse slices: 3D T1-weighted turbo field echo (T1W TFE), 3D TOF, 2D T2-weighted turbo spinecho (T2W TSE), and pre- and postcontrast 2D T1-weighted turbo spin-echo images (T1W TSE), with precise acquisition parameters as described by Kwee et al [98]. For all sequences, the field of view was 100×80 mm, with a matrix size of 256×205 (inplane resolution, 0.39×0.39 mm), except for the T1W TFE sequence (field of view, 100×80 mm; matrix size, 256×163; inplane resolution, 0.39×0.49 mm). The slice thickness of the T1W TFE and TOF sequences was 3.0 mm with no slice gap. The slice thickness of the T1W TSE and T2W TSE sequences was 2.5 mm with a slice gap of 0.5 mm. All images were reconstructed to a pixel size of 0.20×0.20 mm inplane. This study was approved by the institutional medical ethics committee and all patients gave written informed consent.

Gold standard

An expert observer with four years of experience in vessel wall analysis traced the lumen boundary of the common or the internal carotid artery in each image slice of each MR sequence in all 55 studies. During delineation, all sequences were shown to the expert, so all image information was available to obtain accurate contours. The set of lumen contours form a manual segmentation and are further referred to as the *gold standard* in the remainder of the paper.

Manual alignment

A second expert with two years of experience in MRI plaque analysis performed manual alignment and manual segmentation in all 55 studies. Manual alignment was performed by aligning the images from the different sequences to the precontrast T1W TSE image. This sequence is often used to delineate the vessel wall contours and provides a good visualization of the carotid vessel wall and most plaque components. First, the expert delineated the lumen and outer contours of the common or the internal carotid artery in the precontrast T1W TSE sequence, which were then overlaid on the other sequences. Next, the images of the remaining sequences were inspected and a throughplane translation was applied to the complete image stack if needed. Finally, each image slice was aligned to the lumen and outer contours by applying an inplane translation. The set of throughplane and inplane translations defines the manual alignment. The contours which served as an aid for the alignment were not used in the remainder of this paper. All manual alignments and segmentations were performed using a dedicated software package (VesselMASS; Leiden University Medical Center, Leiden, The Netherlands) [25]. An example of the image data including manual alignment and lumen contour is shown in Fig. 4.1.

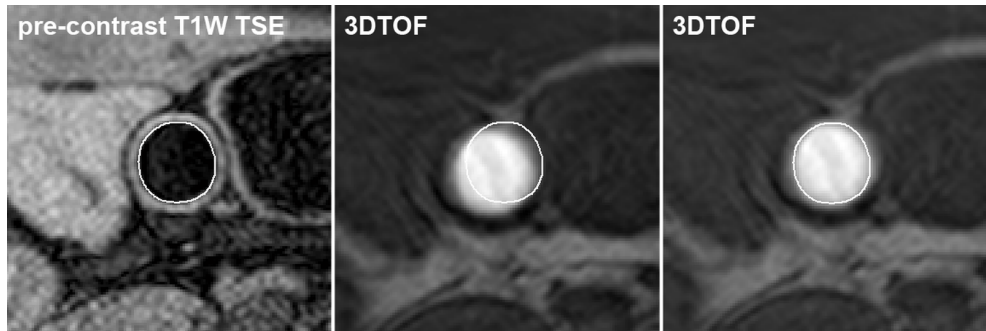


Figure 4.1: T1W TSE image (left) with delineated lumen contour (white), TOF image with the T1W TSE lumen contour overlaid showing misalignment (middle), TOF image after manual alignment (right).

Automatic image registration

The goal of automatic image registration is to determine a spatial transformation that relates positions in one image to corresponding positions in another image. After successful registration, information from the different images can be compared, combined, or analyzed [99]. Registration is the process of finding a coordinate transformation $T(x)$ that makes the moving image $I_M(T(x))$ spatially aligned to the fixed image $I_F(x)$. The degrees of freedom of $T(x)$ determine the types of deformation that can be recovered and these deformations are defined by the choice of the transformation model [85]. The registration problem can be formulated as an optimization problem in which a cost function C , which is negatively related to an image similarity metric S , is minimized with respect to T_μ , where T_μ is a parameterization of transformation T and subscript μ represents a vector that contains the values of the transformation parameters:

$$\mu = \operatorname{argmin}_{\mu} C(T_\mu; I_F, I_M), \quad (4.1)$$

$$C(T; I_F, I_M) = -S(T; I_F, I_M). \quad (4.2)$$

This minimization problem is commonly solved by employing an iterative optimization strategy [100].

There are several choices possible for the transformation model. Performing a 2D translation per image slice is similar to the process of manual alignment by the expert. It provides a 2D translation vector for each image slice. Examples of other transformation models are, in order of increasing flexibility, the rigid, the affine, and the nonrigid B-spline transformation. The rigid transformation treats the image as a rigid body which can translate and rotate. The affine transformation extends the rigid transformation by adding scaling and shearing to the model. The nonrigid transformation is modeled as a weighted sum of B-spline basis functions placed on a uniform control point grid. By moving the control points of the B-spline functions, the underlying image is deformed. The B-spline transformation can model local deformations in the image, produces a smooth transformation, and is computationally efficient [81]. The flexibility of the deformation is defined by the resolution of the control point grid.

In the context of the multisequence MR images of the carotid artery, one of the images is chosen as fixed image and the remaining images will each serve as the moving image. Each MR sequence has a different image contrast and the set of sequences can be considered as a multimodal dataset. Therefore, an image similarity metric should be chosen that is suitable for multimodal image pairs, such as MI (Refs. [101] and [102]) or Normalized Mutual Information (NMI) [103].

The image similarity metric should only be calculated in a region of interest (ROI) around the carotid artery, otherwise the automatic registration algorithm might align the sequences to the dominant neck-air boundary or other structures. The ROI was implemented by defining an image mask centered over the lumen.

In this study, multiple image registration strategies were investigated to find the optimal strategy for MR vessel wall images of the carotid artery. Strategies were created by varying the choice of the fixed image, two different types of the mutual information image similarity metric, the transformation model and the image mask. The following choices were investigated:

- Fixed image: A human expert often uses one sequence as a reference. In this dataset, the precontrast T1W TSE was chosen to be the reference sequence. However, for automated methods this might not be the best sequence, therefore each of the sequences was tested as fixed image.
- Image similarity metric: MI and NMI were tested as image similarity metrics.
- Transformation model: The selected models were 2D translation per image slice, 2D rigid transform per image slice, 3D rigid transform, 3D affine transform, and 3D B-spline transform. For the 3D B-spline transform, different values of the B-spline control point grid spacing were evaluated. The investigated values ranged from 2 to 200 mm.
- Mask shape and size: The mask was centered over the lumen in the fixed image and various mask shapes and sizes were selected. The shape was either a circle or a square and the respective diameter or width varied from 4 to 40 mm.

Determination of the lumen center in each image slice

The image mask was centered over the lumen in each image slice of the fixed image. In each slice, the center of the lumen was derived from the gold standard lumen contours. Additionally, the center of the lumen was derived from automated lumen segmentation [18]. This automated procedure was applied to the MR sequence which was evaluated as the best fixed image in section 4.3. The segmentation procedure was started by manually indicating a point in the lumen center in the first and the last slice, and subsequently the lumen was segmented. In some cases, a third point was indicated around the bifurcation to ensure a correct segmentation.

Quantitative evaluation

Evaluation of the automatic registration was performed by comparing the lumen segmentations of the fixed image and moving image after registration. In the case of successful registration, the lumen segmentations should have a large overlap and a small surface to

surface distance. The gold standard lumen contours were used for this validation. Both the overlap and distance between the segmentations were used to quantify the registration accuracy.

The automatic image registration finds a coordinate transformation which is defined as a mapping from the fixed image to the moving image. Therefore, the lumen contours of the fixed image are transformed to the moving image domain, in which both contours can be compared to each other. Because the transformed contour can move outside the 2D image plane after a 3D registration, it is not possible to compare the contours on a per slice basis. To be able to compare the results of both 2D and 3D registrations, the lumen contours were converted into 3D tubular surface meshes. The surface mesh was created by interpolating a 3D tubular surface through the contours using linear interpolation.

The overlap between the lumen surfaces was calculated using the Dice similarity coefficient (DSC) [87]. The DSC was calculated as follows:

$$DSC = \frac{2|L_{FT} \cap L_M|}{|L_{FT}| + |L_M|}, \quad (4.3)$$

where L_{FT} represents the transformed lumen segmentation of the fixed image, L_M the lumen segmentation of the moving image, and $|\cdot|$ denotes the number of voxels within the segmentation. A DSC of 1 indicates perfect overlap between both lumen surfaces, a value of 0 means that there is no overlap between the surfaces.

The distance between the lumen surfaces was calculated by sampling points on the surface each 0.05 mm. Sampled points on the transformed fixed lumen surface which were positioned outside the moving image domain, points above or below the slice stack of the moving image, were discarded. Then for each point on the transformed fixed lumen surface, the distance to the closest point on the moving lumen surface was calculated. The average of the distances was defined as the mean surface distance (MSD):

$$MSD = \frac{1}{n} \sum_{i=1}^n \min_{q \in L_M} \sqrt{\|p_i - q\|^2}, \quad (4.4)$$

where p_i is a point on the transformed fixed lumen surface, n is the number of points on the transformed fixed lumen surface, and q is a point on the moving lumen surface. A smaller distance indicates a better registration result. The MSD and DSC scores are summarized by using the median including the interquartile range (IQR) indicated by the plus minus sign and boxplots. The IQR is the difference between the 75th and the 25th percentiles. To compare different registration strategies with either the manual alignment or an automated registration strategy, the Wilcoxon signed rank test was applied to the MSD and DSC scores. A p-value smaller than 0.05 was considered to indicate statistical significance.

4.3 Experiments and results

Three experiments were conducted to investigate several aspects of the registration of multispectralMR vessel wall images of the carotid artery. In the first experiment, the need for registration was investigated by analyzing the manual alignments performed by the expert to quantify the amount of patient motion per MR study. In the second experiment, the automatic image registration method was optimized. In the third experiment, we investigated if future improvements of the automated methods are possible. We estimated

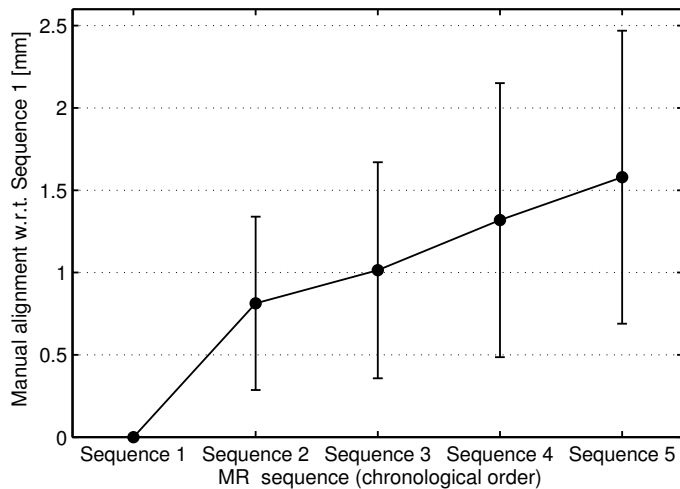


Figure 4.2: Average applied manual alignment based on 55 studies and five sequences. The length of the error bars is two standard deviations.

a lower limit on the registration error by registering the manual lumen segmentations instead of the MR image data.

Manual alignment

The manual alignments applied by the expert were analyzed to investigate the amount of patient movement within one MR study. For each study, the MR sequences were sorted in chronological order. Then, for each MR sequence, the average applied translation with respect to the first acquired MR sequence was measured per slice and averaged over all slices. As a result, the average translation for the first sequence was zero. This calculation was performed for each study generating 55 averages per MR sequence. The average and standard deviation of these 55 averages were calculated for each MR sequence. For the first ten studies, the time needed to perform the manual alignment was recorded.

The analysis results of the manual alignments are shown in Fig. 4.2. In total, 1980 image slices were manually aligned (nine slices per sequence, four MR sequences, 55 studies). The average translation per image slice was 1.33 mm. The translations were larger as the patient was longer inside the scanner. The average duration of the manual alignment procedure was 187.5 ± 12.4 s per patient.

Automatic image registration

To optimize the automatic image registration method, numerous registration strategies were processed. Different masks, choice of the fixed image, image similarity metrics, and transformation models were evaluated. Investigating all permutations of these options was not feasible due to the required amount of computation time. Therefore, a stepwise approach was taken. First, the effect of the mask shape and size was investigated. A 3D rigid body transformation was chosen, MI as metric, and the precontrast T1W TSE image was used as fixed image. Based on the best mask shape and size, all combinations of

fixed and moving images were investigated, again with the same transformation and image metric. Next, the performance of MI and NMI was compared using the optimal fixed image. Then, the optimal value of the B-spline control point grid spacing for the 3D B-spline transformation model was determined. Based on the previously selected registration options, five different transformation models were investigated. For comparison, the MSD of the manual alignments was calculated as well as the MSD in case no registration was applied to the image data. In addition, the DSC was calculated for this experiment. The best registration strategy was evaluated with a mask created using the lumen center extracted from the automated lumen segmentation procedure. Finally, the throughplane translation was quantified for the different 3D registration methods and the amount of volume change was quantified for the 3D B-spline transformation model.

The registration experiments were performed using a speed optimized beta version of the publicly available Elastix software [85]. Elastix is an open source toolbox for rigid and nonrigid registration of images. In this work, a random image sampler, two resolutions of each 1000 iterations, a trilinear image interpolator, and adaptive stochastic gradient descent as optimizer [83], were chosen. The exact registration parameters are available in the parameter file database on the Elastix website with ID Par0018 (<http://elastix.bigr.nl/wiki/index.php/Par0018>).

Masks

In Fig. 4.3, a boxplot is shown for the different shapes and sizes of the mask. The optimal circular image mask had a diameter of 10 mm and a MSD of 0.317 ± 0.148 mm. The optimal square mask had a width of 10 mm and a MSD of 0.324 ± 0.150 mm. In case the mask was too small, such that it did not contain the complete vessel, or when no mask was used, large errors appeared. An oversized mask resulted in a larger MSD and an increase in outliers.

Fixed image

Using the optimal mask, all combinations of fixed and moving images were evaluated. The results are shown using a color matrix in Fig. 4.4. The median MSD and IQR were calculated for each combination of fixed and moving image. The overall score of a fixed image was calculated by accumulating the MSD scores of the four moving image corresponding to the selected fixed image and calculating the median. Using the precontrast T1W TSE as fixed image resulted in the smallest overall MSD while using the TOF as fixed image resulted in the highest MSD. For the further experiments, the precontrast T1W TSE sequence was selected as fixed image.

MI and NMI

Finally, the image similarity metrics MI and NMI were investigated as well as the grid size for the deformable B-spline transformation. MI as image similarity metric performed slightly better than NMI, the MSD was 0.317 ± 0.148 and 0.324 ± 0.156 mm for MI and NMI, respectively.

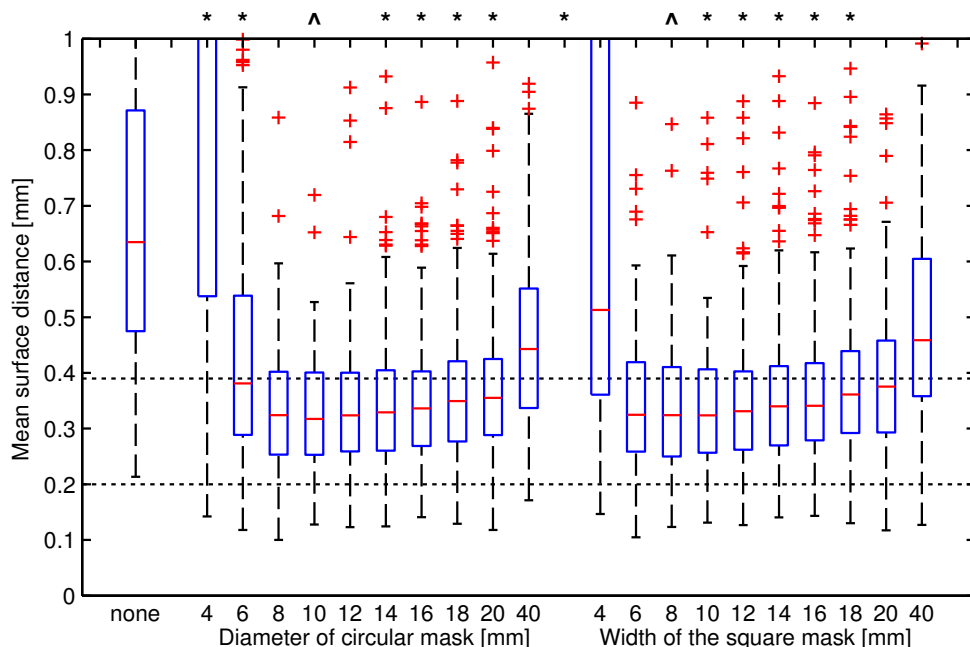


Figure 4.3: Mean surface distance for no mask (“none”), circular and square masks of different sizes. A star on top of a column indicates a significant difference with respect to the optimal score of that shape (lowest median), which is indicated by a hat. The two gridlines show the acquired (0.39 mm) and reconstructed inplane pixel size (0.20 mm).

B-spline control point grid spacing

Different values of the B-spline control point spacing were evaluated using MI as image similarity metric. A control point spacing of 15 mm for the 3D B-spline transformation provided the best results (Fig. 4.5), and the results were quite stable for grid spacings in the range 5-100 mm.

Transformation model

The MSD for the different transformation models using the optimal mask, fixed image, image metric, and control point spacing is shown in Fig. 4.6. The first column of the box-plot shows the distance without applying any form of registration (0.590 ± 0.429 mm). The second column shows the results after manual alignment by the expert (0.271 ± 0.127 mm). The remaining columns show the different transformation models: 2D translation per image slice (0.303 ± 0.276 mm), 2D rigid transformation per image slice (0.308 ± 0.298 mm), 3D rigid transformation (0.317 ± 0.148 mm), 3D affine transformation (0.307 ± 0.149 mm), and the 3D B-spline transformation (0.288 ± 0.128 mm). The last column shows the MSD obtained by the best registration strategy using the optimal mask which was initialized by the automatically segmented lumen contours (0.286 ± 0.144 mm). Similarly, the DSC scores are shown in Fig. 4.7.

The performance of the automated methods increased with an increasing degree of



Figure 4.4: Color matrix showing the median MSD and the interquartile range of the different combinations of fixed and moving images. The rightmost column shows the overall score for each selected fixed image.

freedom of the transformation model. The 3D B-spline registration showed the best registration accuracy and the MSD score was close to the MSD score of the manual alignment procedure. The differences in DSC were smaller compared to the differences in MSD. The 2D models showed substantial more outliers and a higher variation in MSD and DSC scores compared to the 3D models. Visual used to investigate the outliers. The majority of outliers were caused by poor image quality in either the fixed or the moving image, pulsation artifacts, or saturation slabs close to the carotid artery. The saturation slabs were positioned over subcutaneous fat to reduce ghosting artifacts and over the pharynx to reduce swallowing artifacts.

The inplane and throughplane translation as a result of a 3D registration was quantified by calculating the average translation of the lumen segmentation in these directions for each 3D registration. The average inplane translation was 1.093 ± 0.913 mm and the average throughplane translation was 0.738 ± 0.571 mm.

The volume change occurring in the deformable 3D B-spline transformation was quantified by calculating the average determinant of the Jacobian of the deformation field within the fixed mask. A value of 1 indicates no volume change, a value of 1.1 indicates local expansion of 10%, and a value of 0.9 indicates local compression by 10%. The mean and standard deviation of the Jacobian determinant over all patients was 1.00 ± 0.11 , showing no systematic change in volume.

The computation time for the registration of one MR sequence with the precontrast T1W TSE sequence was on average 41.4 s for the 2D translation transform (4.6 s per image slice), 73.8 s for the 2D rigid transformation (8.2 s per image slice), 5.1 s for the 3D rigid transform, 5.0 s for the 3D affine transform, and 13.0 s for the 3D B-spline transform. The

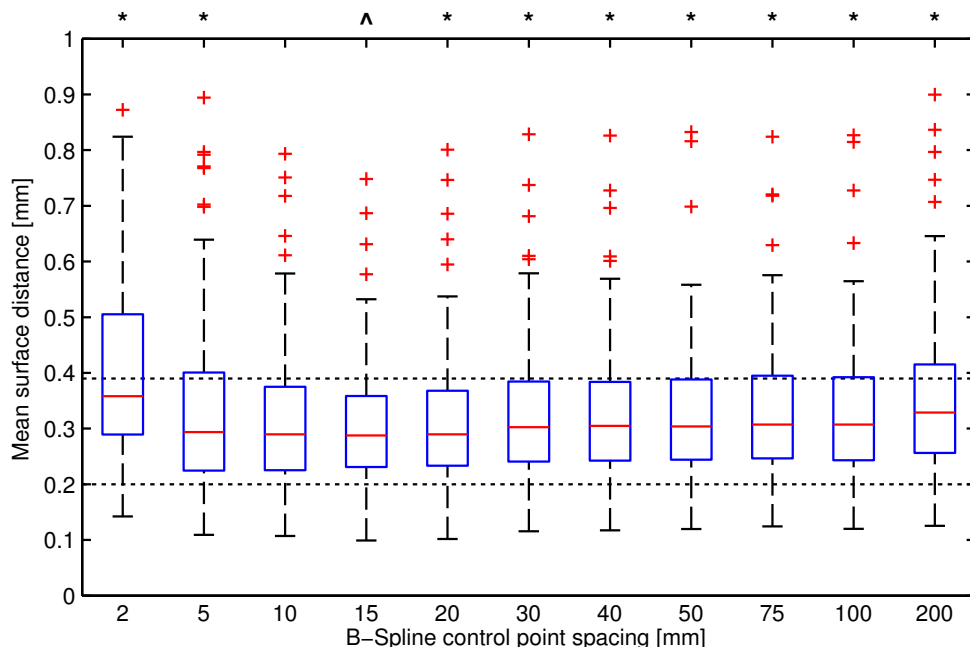


Figure 4.5: Mean surface distance for different values of the control point spacing of the 3D B-spline transform. A star on top of a column indicates a significant difference with respect to the optimal spacing, which is indicated by a hat. The two gridlines show the acquired (0.39 mm) and reconstructed inplane pixel size (0.20 mm).

registration experiments were performed on a standard PC equipped with an Intel Xeon processor with four cores running at 2.4 GHz. An example of a 3D B-spline registration is shown in Fig. 4.8. The postcontrast T1W TSE image shows that throughplane correction is required for correct alignment.

Lower limit registration accuracy

To investigate the lower limit of the registration accuracy, the real image data of each sequence was replaced with a binary mask of the gold standard contours of the lumen of that sequence. Areas within the lumen were set as foreground (intensity value 1), areas outside the lumen as background (intensity value 0). These masks were then used as the fixed and moving images in the registration procedure. Instead of using MI as image similarity metric, the sum of squared differences was used. The automatic image registration was applied on the data to fit the lumen segmentations upon each other. By using the binary lumen masks, perfect image quality is simulated and the results will show an upper bound of the registration accuracy using the current choice of registration parameters.

The lower limit MSD and the regular MSD scores are shown in Fig. 4.9. The values of the lower limit MSD are smaller for transformation models which have more degrees of freedom, but the medians are in all cases larger than the reconstructed pixel size.

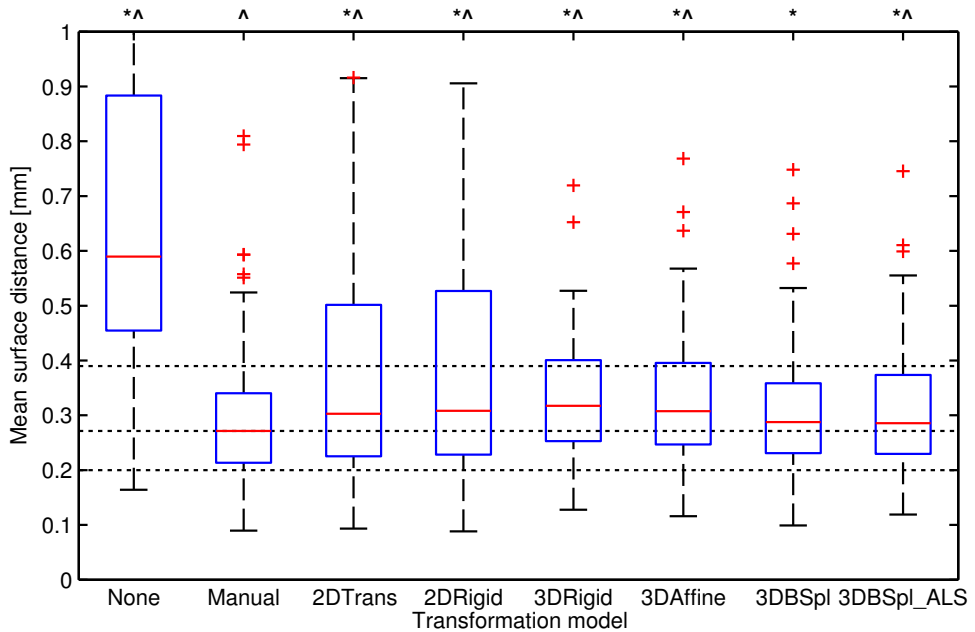


Figure 4.6: Mean surface distance for all transformation models (None: no alignment, Manual: manual alignment by the second expert, 2DTrans: 2D translation per image slice, 2DRigid: 2D rigid transform per image slice, 3DRigid: 3D rigid transform, 3DAffine: 3D affine transform, 3DBspl: 3D B-spline transformation, 3DBspl_ALS: 3D B-spline transformation with a mask based on the automated lumen segmentation). A star on top of a column indicates a significant difference with respect to the manual alignment procedure. A hat on top of the figure indicates a significant difference with the 3D B-spline model. The three gridlines show the acquired (0.39 mm) and reconstructed inplane pixel size (0.20 mm) and the median MSD (0.27 mm) of the manual alignment procedure.

4.4 Discussion

The main observation of this study is that automated image registration of multicontrast MR imaging of the carotid vessel wall using a 3D B-spline transform is almost as accurate as the current clinical practice of manual alignment by an expert, with final accuracy in the order of the inplane voxel size. The required user-interaction to generate the lumen masks to focus the registration was reduced from one mouse-click per image slice to only two or three mouse-clicks per MRI exam. In addition, automated analysis is at least three times faster than manual alignment of the image data and can potentially be an order of magnitude faster if run in parallel. This paper has a number of contributions. First, the need for alignment of multispectral MR vessel wall images of the carotid artery was quantified. Second, an optimized automatic registration strategy was proposed after investigating and optimizing different parameters of the registration method. Third, a validation framework was proposed which allows comparison of registration results with a gold standard. In addition, an estimate of the maximum performance was derived. This is the first study to quantify these aspects on a large set of patients.

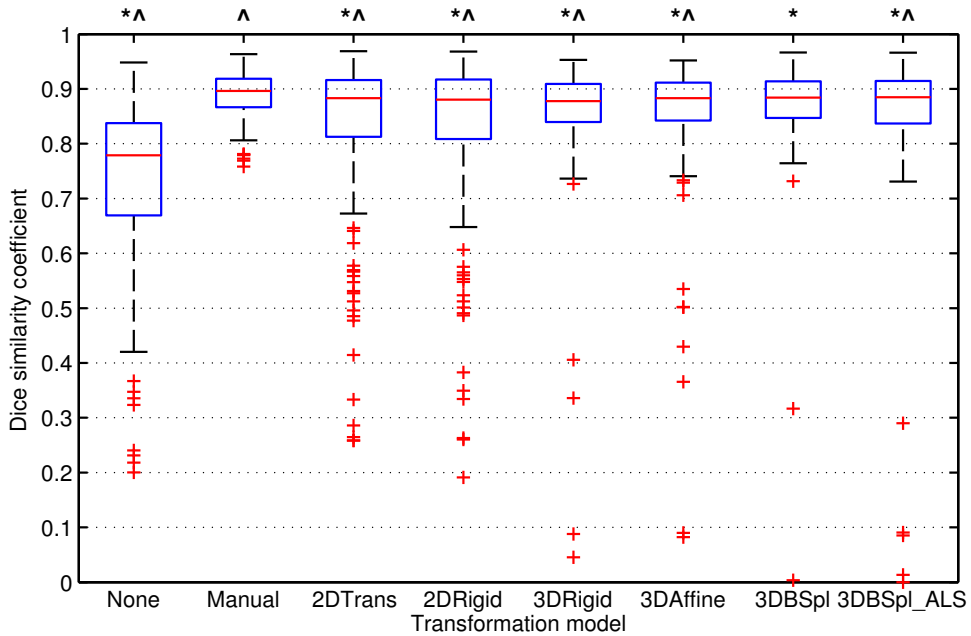


Figure 4.7: Dice similarity coefficient for all transformational models (None: no alignment, Manual: manual alignment by the second expert, 2DTrans: 2D translation per image slice, 2DRigid: 2D rigid transform per image slice, 3DRigid: 3D rigid transform, 3DAffine: 3D affine transform, 3DBSpl: 3D B-spline transformation, 3DBSpl_ALS: 3D B-spline transformation with a mask based on the automated lumen segmentation). A star on top of a column indicates a significant difference with respect to the manual alignment procedure. A hat on top of the figure indicates a significant difference with the 3D B-spline model.

Analysis of the manual alignment by the expert shows the need for registration of carotid MRI studies. The average misalignment per image slice is 1.33 mm, but can be over 2.4 mm, and occurs in all three dimensions. Such a misalignment causes mismatches in pixel correspondence between MR sequences; for example, a location in the vessel wall in one MR sequence can correspond to the lumen area in another MR sequence. If the images are not correctly aligned, manual segmentation of the vessel wall and its components might not be accurate, especially at the boundaries of plaque components. In case an automated plaque segmentation method is applied to the image data, incorrect results are expected, as these methods classify pixels into plaque components according to their signal intensity value in the different MR sequences [20, 37, 38, 104].

The different automatic image registration experiments showed in a stepwise fashion the optimal registration strategy. The building blocks of the registration were optimized to an automated circular mask with a diameter of 10 mm, 3D B-spline transformation model with a control point spacing of 15 mm, MI as image similarity metric, with the precontrast T1W TSE as fixed image. After an indication of the lumen centerline in the T1W image, the other sequences are automatically registered with a median mean surface error of 0.288 ± 0.128 mm. As a reference, the error after manual alignment was 0.271 ± 0.127 mm.

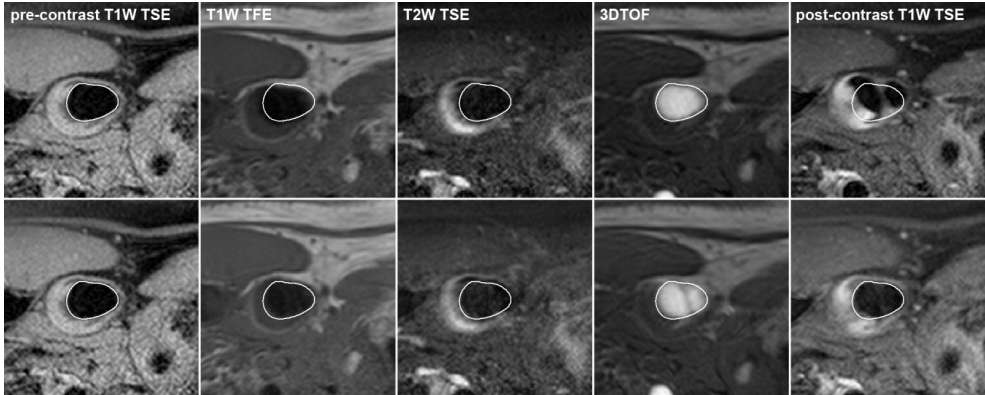


Figure 4.8: Example of MRI images before (top row) and after registration by the optimal 3D B-spline transformation (bottom row). The fixed image is shown in the first column. The lumen contour of the fixed image (white) is overlaid on all images. The post-contrast T1W TSE image shows that throughplane correction, which is achieved by using a 3D transformation model, is required for correct alignment.

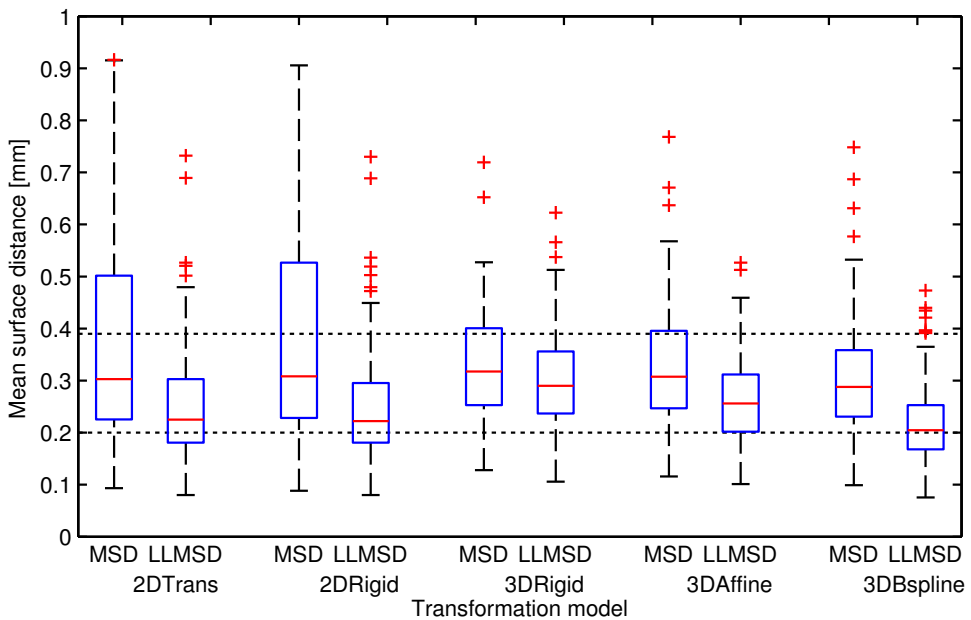


Figure 4.9: MSD and lower limit mean surface distance (LLMSD) of the different transformation models (2DTrans: 2D translation per image slice, 2DRigid: 2D rigid transform per image slice, 3DRigid: 3D rigid transform, 3DAffine: 3D affine transform, 3DBspline: 3D B-spline transformation). The two gridlines show the acquired (0.39 mm) and reconstructed inplane pixel size (0.20 mm).

The computation time for the registration of the MR sequences was 52.0 s per patient. This is much faster than the time needed for manual alignment, which was 187.5 s per patient. Average run time can potentially be further reduced by a factor of 3-4 by running all registrations in parallel.

The shape and size of the optimal image mask should cover the luminal area, the vessel wall, and its direct surrounding. The experiments have shown that most image information necessary for successful registration is contained in this region and that neighboring structures, such as veins and muscles, do not have an important contribution to the registration process. The optimal mask, a circular mask with a diameter of 10 mm, is slightly larger than the dimensions of the carotid artery including the vessel wall. Krejza et al. [105] reported an average internal diameter of the internal carotid artery of 4.89 and 6.31 mm for the common carotid artery. The average vessel wall thickness measured by MRI is 0.92 ± 0.21 mm in elderly subjects with cardiovascular disease [45].

The selection of the fixed image was investigated and the precontrast T1W-TSE sequence was chosen as fixed image. This is the same image that was used by the human expert as reference. The relatively large MSD for the TOF sequence can be explained by the lack of vessel wall depiction in this sequence. Also the selection of the postcontrast T1W TSE sequence as fixed image showed a relatively large MSD. This sequence is always acquired at the end of the study resulting in a higher chance that the subject will move. Moreover, the administration of contrast agent might cause discomfort for the patient and can result in extra patient motion as a reaction to this discomfort. Furthermore, uptake of the contrast agent results in an increase of heterogeneity in the vessel wall intensities which might decrease the performance of the MI image similarity metric. The matrix of MSD scores in Fig. 4.4 shows moderate reflection symmetry. Perfect reflection symmetry matrix was not expected as the used registration framework is not symmetrical.

After comparing MI and NMI as image similarity metric and optimizing the control point grid spacing for the 3D Bspline transformation, all transformation models were compared. The best registration accuracy was achieved by using the 3D B-spline transformation model. Although the medians of the MSD and the Dice overlap do not show a substantial improvement for the 3D transformations compared to the 2D transformations, Figs. 4.6 and 4.7 show that the 3D transformations have substantially less outliers. Clinically, this means that much fewer patients will need manual correction, saving costly reviewing time by the radiologist. Moreover, analysis of the manual segmentations and the 3D registration results showed that patient movement occurs in all three directions and that throughplane translation is in the same order of magnitude as inplane translation. The nonrigid 3D B-spline transformation model showed an improvement over the rigid 3D transformations. A nonrigid model can better handle rotation of the neck which can cause compression and expansion of tissues. Literature indicated that patient movement includes a nonrigid component [95, 96]. Analysis of the deformation fields of the 3D B-spline registrations shows that small local compressions or expansions occur during registration, but on average there was no change in volume. Finally, Fig. 4.5 shows that patient motion can be modeled well with a few degrees of freedom.

While the differences in registration accuracy between the different transformation models are small, a nonrigid 3D transformation model is required to correctly model patient movement and obtain an accurate alignment. The 3D B-spline transformation model has the best registration accuracy and the results show that a 3D model is needed because the throughplane motion is in the same range as the inplane motion. An illustrative example of throughplane motion is shown in Fig. 4.8. The 3D B-spline transformation

model performs slightly worse than the manual alignment procedure. Visual inspection of the results showed that most of the differences can be explained by errors of the automated registration of the 3DTOF sequence caused by the lack of structural information in this sequence. By excluding the 3DTOF sequence from the experiment, the MSD of the 3D B-spline transformation model approaches the MSD of the manual alignment and is no longer significantly different. The 3D B-spline registration with the mask based on the automated lumen segmentation performed similarly to the 3D B-spline registration with the mask that was based on the manual segmentation. This shows that the automatic image registration can be applied with minimal user interaction.

The lower limit MSD was found to be slightly larger than the reconstructed inplane pixel size. The comparison shows that the results of the different registration strategies are close to the lowest possible MSD. Hence, major reductions in MSD are not expected by further optimizing or changing the registration strategies, but improvements might still lead to more accurate registration results possibly beating the manual alignment procedure. The minimum value of the lower limit MSD might be limited by the gold standard contours. These contours will vary slightly between the MR sequences because of possible patient movement and human variation in the delineation process. For example, if the lumen contours in one sequence were drawn slightly larger than in another sequence, it will not be possible to obtain a MSD of zero.

Compared to previously reported studies on automatic registration methods for carotid MR vessel wall imaging, this is the first study in which comprehensive experiments were performed on a large set of patient studies using quantitative validation measures. Only one study performed quantitative validation on simulated neck movements in five volunteers [40]. The authors performed the validation in 2D and assumed that neck movements through the image plane and tissue deformations in the image plane were either absent or negligible. However, patient movement occurs in all directions and as such, a 3D image registration approach has advantages, which is supported by our findings. Also, as the thickness of imaging slices will decrease in the future due to technological advancements, the effects of throughplane motion will have a more prominent effect. Two studies [41, 42] used a 3D-based registration method being a rigid body transformation or affine transformation. Our results show that such a transformation model is insufficient to generate a good result. Our data suggest that deformations, such as bending and stretching [106], should be taken into account when choosing a registration strategy.

This study is subject to a number of limitations. An image mask centered over the lumen is required as input for the automatic image segmentation method. This mask can be created by the application of an automated method to segment the carotid lumen [18, 34], which requires a minimal user interaction of two or three interactions per MRI exam as performed in this study.

Motion between slices, which can occur during a 2D acquisition in which the slices are scanned sequentially, was not investigated. We assume that the effect is small compared to the motion between MR sequences. During the acquisition of one sequence, the patient is instructed not to move and most likely will move after completion of the sequence. The error metrics used in this research cannot detect an erroneous rotation in case the vessel is mostly circular. However, the MRI acquisition is centered on the bifurcation and the error metric is sensitive to the rotation of both bifurcations and ellipsoid-shaped vessels. The registration of the multispectral MR vessel wall images is just one of the steps in the analysis of atherosclerosis in the carotid artery. The final step of the analysis is the assessment

of plaque composition inside the vessel wall. Accurate alignment of the images is beneficial for the analysis of the plaque composition. More research should be conducted to test if there is a difference in outcome of the plaque composition analysis between manual alignment and automatic image registration.

To conclude, the need for image registration using a 3D deformable transformational model was shown, and several carefully selected, critical components of the registration procedure were optimized and quantitatively validated on a large group of patients. The optimal registration strategy was faster than manual alignment by a human expert, and with similar accuracy. These results show that automated image registration can replace the manual alignment, thus reducing the amount of user interactions needed for analyzing carotid vessel wall images and improving the reproducibility of the analysis. The proposed method shows high potential for clinical application. The software and the parameters of the optimal registration strategy are publicly available.

The main findings of this paper, which were acquired with data from a 1.5T scanner, were validated on a more recent 3.0T dataset. The results of the 3.0T dataset are in line with the results of the 1.5T dataset and show that the same registration settings can be applied to newer MRI data. A short report is available in section 4.5.

Acknowledgments

This research was performed within the framework of CTMM, the Center for Translational Molecular Medicine (<http://www.ctmm.nl>), project PARISK (Grant No. 01C-202), and supported by the Dutch Heart Foundation. The authors thank Dirk H. J. Poot, Ph.D. (Biomedical Imaging Group Rotterdam, Department of Radiology and Department of Medical Informatics, Erasmus MC, Rotterdam, The Netherlands) for providing the optimized nearest neighbor search algorithm which was used in the calculation of the mean surface distance, and Martine T. B. Truijman (Department of Radiology, Maastricht University Medical Center, Maastricht, The Netherlands) for supplying the 3.0T dataset which was used in the supplementary material.

4.5 Appendix: 1.5T optimized settings applied to 3.0T data

In the article “Automated registration of multispectral MR vessel wall images of the carotid artery” a large dataset was used for all the experiments. The dataset consisted of vessel wall images of 55 patients acquired with a 1.5T MRI scanner. Although 1.5T scanners are currently the workhorse systems in hospitals and clinics, the use of newer 3.0T scanners in the clinic is increasing. 3.0T imaging offers the advantages such as higher in-plane resolution and thinner images slices (e.g. 2 mm versus 3 mm at 1.5T). To validate the main findings of the article, which were acquired with the 1.5T data, a subset of experiments was performed on 10 patients scanned with a 3.0T MRI scanner.

Ten datasets with a more up-to-date multi-contrast MRI protocol were collected. The datasets are from the ParisK study, which is currently running, and were acquired using a 3.0T MRI scanner. The ParisK study is described at the website: <http://clinicaltrials.gov/ct2/show/NCT01208025>. Relevant study details are:

- Inclusion criteria: patients with neurological symptoms due to ischemia in the carotid artery territory and with a carotid stenosis between 30% and 69% according to the NASCET criteria.
- 3.0T MRI with a multi contrast protocol (T1W pre- and post-contrast, T2W, TOF and IR-TFE).
- Acquired in-plane pixel size: 0.6 mm, reconstructed pixel size: 0.3 mm, slice thickness: 2 mm.

An experiment similar to the experiment described in section 4.3 and Figure 4.6, the comparison of different transformation models, was performed using the T1W pre contrast image as fixed image and the T1W post contrast image as moving image. An observer performed the manual alignment of the images, another observer created the gold standard lumen contours. Automated registrations using different transformation models were performed and evaluated. A circular mask of 10 mm was used, mutual information as image similarity metric, and a B-spline control points spacing of 15 mm for the 3D B-spline transformation model. The results are shown in Figure 4.10.

The mean surface distance (MSD) scores of the different transformation models follow the same trend as the MSD scores in Figure 6 of the paper. The transformation model with the most degrees of freedom, the 3D B-spline transformation model, has the lowest MSD and was very close the MSD of the manual alignment procedure. There was no significant difference between the manual alignment procedure and the 3D B-spline transformation model ($n = 10$). The 2D methods showed low MSD scores but had a large variation. Compared to Figure 6 in the manuscript, the overall MSD is lower, probably due to the lower slice thickness. These findings are in line with the results of the 1.5T dataset and show that the same registration settings can be applied to newer MRI data.

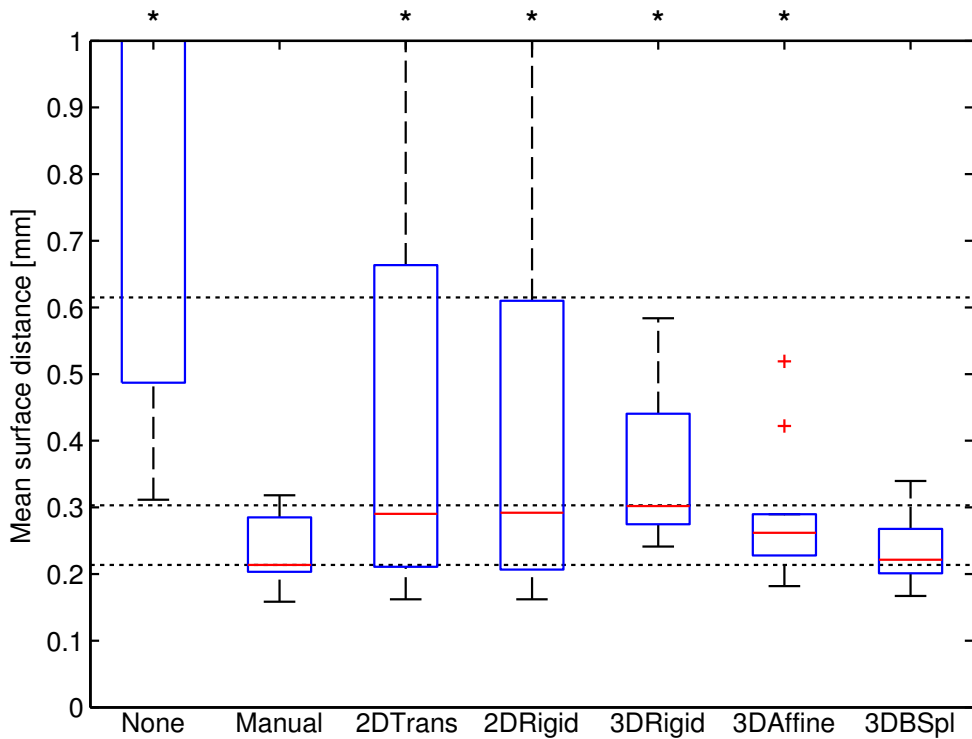


Figure 4.10: Mean surface distance for all transformation models (None: no alignment, Manual: manual alignment by the second expert, 2DTrans: 2D translation per image slice, 2DRigid: 2D rigid transform per image slice, 3DRigid: 3D rigid transform, 3DAffine: 3D affine transform, 3DBSpl: 3D B-spline transformation). A star on top of a column indicates a significant difference with respect to the manual alignment procedure. The three grid-lines show the acquired (0.6 mm) and reconstructed in-plane pixel size (0.3 mm) and the median MSD (0.21 mm) of the manual alignment procedure.

Chapter 5

Visualization of local changes in vessel wall morphology and plaque progression in serial carotid artery MRI

This chapter is in submission:

R. van 't Klooster, M. T. B. Truijman, A. C. van Dijk, F. H. B. M. Schreuder, M. E. Kooi, A. van der Lugt, R. J. van der Geest. Visualization of local changes in vessel wall morphology and plaque progression in serial carotid artery MRI.

5.1 Introduction

Carotid atherosclerosis is an important cause of ischemic stroke. Assessment of plaque composition in addition to degree of luminal stenosis can be used to identify patients with increased risk of stroke and to assess disease progression. Magnetic resonance imaging (MRI) is an excellent non-invasive imaging technique to assess vessel wall morphology and plaque composition, with good accuracy and reproducibility [26]. Serial MRI of the carotid artery is used in several studies which focus on measuring the natural history of carotid artery plaques in symptomatic [26] and asymptomatic [29] patients and effects of lipid-lowering therapy using statins [27, 28]. Current standard to analyze serial MRI scans is to compare volume measurements based on manual segmentations of the vessel wall and plaque components. Before comparing the scans, the scans have to be aligned to each other on a slice level. Different approaches exist to align scans from different time points. One study aligns the scans by centering the image stack at each time point over the plaque [26], another study uses the baseline scan as a reference at the follow-up session to ensure targeting the same arterial segment [28]. Alternatively, post processing can be used to match the axial images from different time points according to their distance to the carotid bifurcation [27, 29]. Furthermore, comparison between time points is hindered by inconsistent repositioning of the artery from scan to scan in conjunction with thick image slices. Balu et al. studied the influence of subject repositioning on measurement precision in serial MRI and identified orientation variability as the most important factor that affected reproducibility [107]. Besides repositioning variability, the current comparison of time points is primarily based on volume measurements, which is a limited representation of the available image data, and no attention is given to local changes or visual presentation of differences between time points.

Therefore, we present a method for analyzing serial MRI scans which employs 3D image registration and visualization techniques to 1) decrease the measurement variability caused by inconsistent repositioning and 2) to enable detailed visual inspection of local differences between time points providing intuitive insight into the disease progression of an individual patient.

5.2 Methods

Patient

A 71 year old male was admitted to the hospital due to loss of strength and sensation of the left arm upon awakening. An MRI of the brain revealed several small cortical ischemic lesions in the region of the right middle cerebral artery. Carotid ultrasound showed an ipsilateral carotid artery plaque with approximately 30% luminal reduction. A minor stroke of the right hemisphere was diagnosed. The patient was included in a large prospective multicenter study to improve diagnosis of mild to moderate carotid plaques (Plaque At RISK study) [108]. The institutional Medical Ethical Committee approved the study and the patient gave written informed consent. The patient was followed up for 2 years, during which he did not experience new ischemic events.

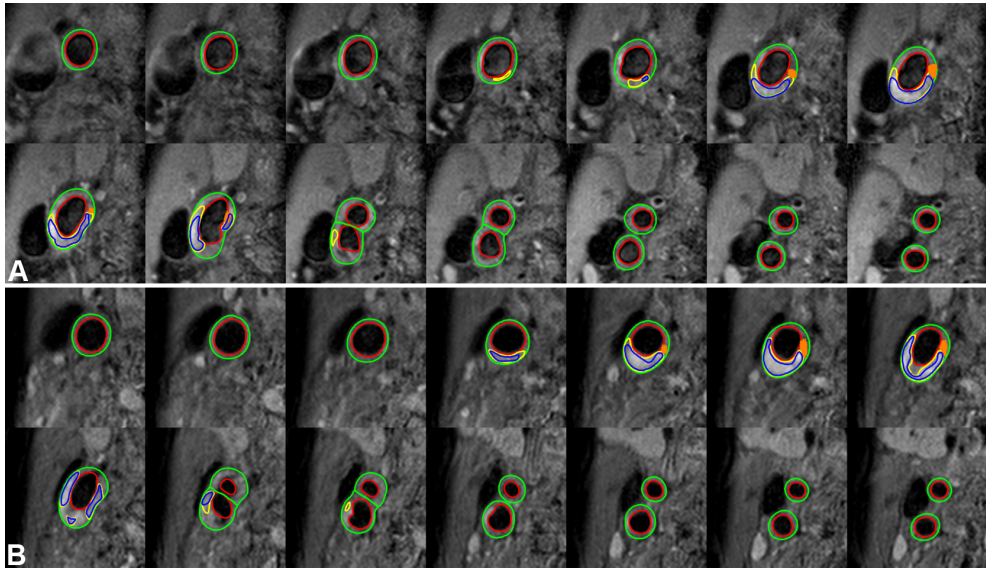


Figure 5.1: a) baseline T1w images, b) 2 year follow-up T1w images (red = lumen, green = outer vessel wall, orange = calcification, yellow = lipid-rich necrotic core, blue = intraplaque hemorrhage).

MRI

Carotid MRI examinations were performed 35 days after the event and after 2 years as previously described [108]. The high-resolution multi-sequence MRI protocol consisted of five MR sequences: 3D time of flight, 2D T1w turbo spin echo (TSE), 2D T2w TSE, 3D inversion recovery-turbo field echo (IR-TFE), and post-contrast 2D T1w TSE. Fifteen transverse adjoining slices of 2 mm each, with an in-plane reconstructed pixel size of 0.3 x 0.3 mm, covering the entire plaque were acquired.

Image analysis

The MR images at baseline and follow-up were manually segmented by delineating the lumen, outer wall, calcifications, lipid-rich necrotic core (LRNC) and intraplaque hemorrhage (IPH) according to previously published criteria [108]. Per definition, IPH was always located within the LRNC. Information from all MRI sequences was taken into account during the delineation process. The pre-contrast T1w images of both time points including segmentations are shown in Figure 5.1 and demonstrate a slice offset between time points at the bifurcation. The offset was manually corrected by applying a through plane translation of one slice to the follow-up image. To reduce the effect of the high anisotropy of the data on the measurements, the T1w images and segmented vessel wall boundaries were interpolated to a slice thickness of 0.5 mm. The vessel wall boundaries were visually inspected and corrected after interpolation. The interpolated vessel wall boundaries are used in the next section for the calculation of the vessel wall thickness and the creation of 3D meshes. The segmentations of the plaque components were not interpolated.

Automated image registration

The baseline and follow-up T1w images were aligned to each other using an automated image registration framework which was optimized for carotid artery MRI scans [109]. After registration, point correspondence between the lumen of the baseline and the follow-up image was obtained, i.e. for each point on the lumen boundary in the baseline image, the corresponding point on the lumen boundary in the follow-up image is known.

Visualization using 3D surface meshes

The interpolated lumen and outer wall segmentation were converted into 3D surface meshes. For each point on the lumen mesh, the distance to the nearest point on the outer wall mesh was calculated resulting in a local vessel wall thickness (VWT) measure. The VWT is color-coded on the lumen mesh to provide a 3D visualization. The VWT analysis was repeated for the follow-up segmentation.

By using the point correspondence between the baseline and follow-up lumen, differences in measurements between baseline and follow-up can be visualized by color coding this difference on the baseline luminal surface mesh. Similarly, increase or decrease of plaque components can be visualized by color coding the lumen surface. Presence of a plaque component was indicated on a lumen mesh point when a plaque component was present between that lumen mesh point and its closest point on the outer vessel wall. Nearest neighbor interpolation was used to extract this information from the manual segmentations.

5.3 Results

First, volume and area-based comparison between baseline and follow-up was performed. Lumen volume at baseline was 1.525 ml and 1.507 ml at follow-up, vessel wall volume 1.634 ml versus 1.577 ml, calcification volume 0.017 ml versus 0.015 ml, and LRNC 0.378 ml versus 0.444 ml. The external carotid artery was excluded from the volume and area-based measurements. Figure 5.2 shows the slice-based area measurements of the lumen, outer vessel wall, calcifications and LRNC. The volume and area measurements demonstrate a mixed result; a consistent increase in LRNC was observed, the other components showed a small decrease and little variation between baseline and follow-up.

Figure 5.3 shows the 3D visualization of VWT at baseline and follow-up, change in VWT and progression or regression of LRNC with or without IPH over time. All metrics were color-coded on the lumen surface and appropriate color maps were chosen. A bipolar color map was chosen for Figure 5.3c in which gray corresponds to no change, blue to a decrease and red to an increase in VWT. The strong red regions indicate a clear increase in VWT. The absence of strong blue regions suggests accurate registration between baseline and follow-up. The increase in VWT is positively correlated with the presence of LRNC (Figure 5.3d). The 3D visualizations are interactive which allows the clinician to explore the results using zoom and rotation.

The change in VWT was quantified for locations inside the vessel wall which were thickened ($VWT > 1$ mm) and grouped into locations without and with LRNC (with or without IPH) (Figure 5.4). The mean change and standard deviation in VWT was -0.02 ± 0.41 mm for thickened vessel wall and 0.36 ± 0.52 mm for the LRNC locations. Wilcoxon

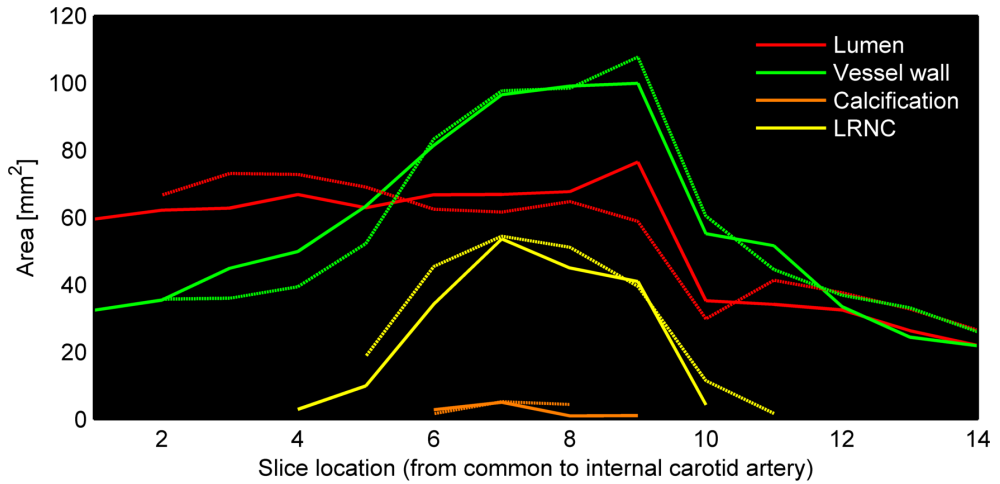


Figure 5.2: slice-based area measurements for baseline (solid line) and 2 years follow-up (dashed line) showing lumen area (red), vessel wall area (green), calcifications (orange) and lipid-rich necrotic core (LRNC) (yellow).

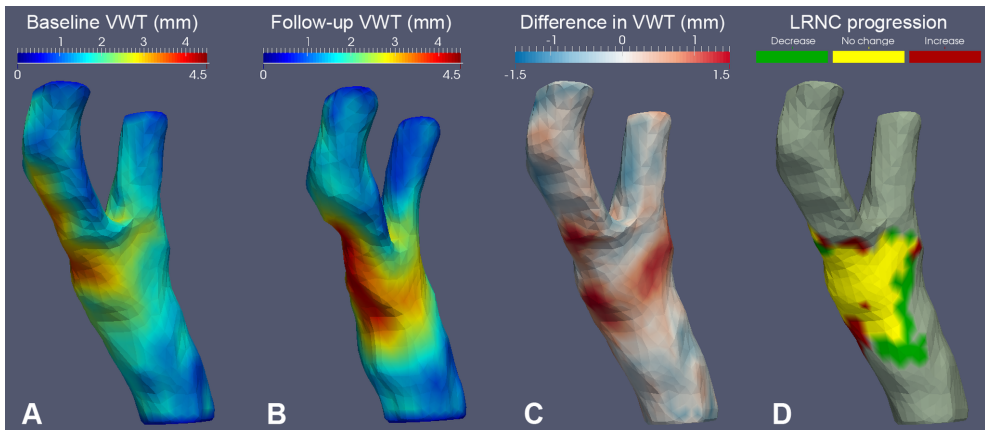


Figure 5.3: a-b) 3D surface meshes showing local vessel wall thickness at baseline and follow-up, respectively; c) difference in vessel wall thickness over time, d) progression or regression of lipid-rich necrotic core (LNRC) with or without intraplaque hemorrhage over time.

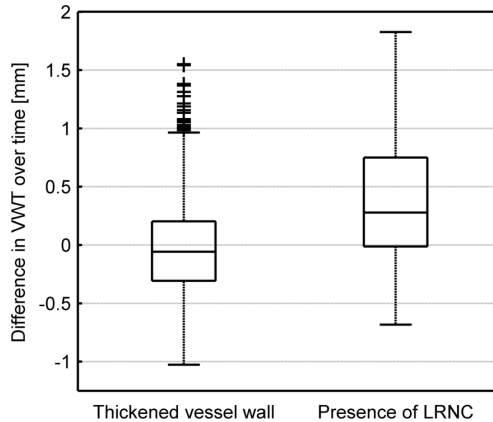


Figure 5.4: boxplot showing difference in VWT between baseline and follow-up for locations with a thickened vessel wall without and with the presence of lipid-rich necrotic core (LRNC).

rank sum test demonstrated a significant difference between both groups (P -value $\ll 0.001$).

5.4 Discussion

A new method was introduced to analyze and present serial MRI data of the carotid artery vessel wall. 3D image registration was used to obtain point correspondence between images from different time points which enables assessment of local changes in plaque morphology. 3D visualization techniques were applied to present changes in vessel wall morphology using difference maps which were color-coded on a mesh of the lumen segmentation of the baseline image and related to the presence of different atherosclerotic plaque components in the vessel wall. The bipolar color map of the difference map in Figure 5.3c allows the clinician to differentiate between small and substantial changes in VWT between time points. Moreover, the tool can be used to demonstrate a significant increase in VWT over time for locations with LRNC with or without IPH. Both observations could not be deduced from the traditional volume or area measurements.

The 3D visualizations provide an interactive and intuitive way to represent measurements extracted from the original image data. In this work visualizations were generated providing insight in the change in VWT and progression or regression of different plaque components. Other measurements, e.g. changes in degree of stenosis, can be visualized using the same methodology. These new visual data analysis tools provide clinicians with a detailed view of atherosclerotic disease progression of individual patients and can potentially improve understanding of the effect of changes in plaque components on local plaque progression/regression.

5.5 Conclusion

The presented method to analyze and visualize changes over time for carotid artery MRI is an improvement over the traditional volume-based analysis as it provides a detailed view

of local differences between baseline and follow-up scans and increased insight into the disease progression of an individual patient.

Acknowledgments

This research was performed within the framework of the Center for Translational Molecular Medicine (www.ctmm.nl), project PARISK (Plaque At RISK; grant 01C-202), and supported by the Dutch Heart Foundation.

Chapter 6

Automated versus manual in vivo segmentation of carotid plaque MRI

This chapter was published in:

R. van 't Klooster, O. Naggara, R. Marsico, J. H. C. Reiber, J. F. Meder, R. J. van der Geest, E. Touzé, C. Oppenheim. Automated Versus Manual In Vivo Segmentation of Carotid Plaque MRI, *American Journal of Neuroradiology*, Volume 33, Pages 1621–1627, 2012.

Abstract

Background and purpose: Automatically identifying carotid plaque composition using MR imaging remains a challenging task in vivo. The purpose of our study was to compare the detection and quantification of carotid artery atherosclerotic plaque components based on in vivo MR imaging data using manual and automated segmentation.

Materials and methods: Sixty patients from a multicenter study were split into a training group (20 patients) and a study group (40 patients). Each MR imaging study consisted of 4 high-resolution carotid wall sequences (T1, T2, PDw, TOF). Manual segmentation was performed by delineation of the vessel wall and different plaque components. Automated segmentation was performed in the study group by a supervised classifier trained on images from the training group of patients.

Results: For the detection of plaque components, the agreement between the visual and automated analysis was moderate for calcifications ($\kappa = 0.59$, CI 95% [0.36-0.82]) and good for hemorrhage (0.65 [0.42-0.88]) and lipids (0.65 [0.03-1.27]). For quantification of plaque volumes, the intraclass correlation was high for hemorrhage (0.80 [0.54-0.92]) and fibrous tissue (0.80 [0.65-0.89]), good for lipids (0.65 [0.43-0.80]), and poor for calcifications.

Conclusions: In 40 patients with carotid stenosis, our results indicated that it was possible to automatically detect carotid plaque components with substantial or good agreement with visual identification, and that the volumes obtained manually and automatically were reasonably consistent for hemorrhage and lipids but not for calcium.

6.1 Introduction

Accurate information of atherosclerotic plaque morphology and composition is necessary to distinguish stable from unstable plaques that are likely to cause embolic events [65]. The vulnerability of an atherosclerotic plaque to rupture is believed to be related to its intrinsic composition, such as the size of the lipid core and presence of intraplaque hemorrhage. In vivo multicontrast high-resolution MR imaging has emerged as a tool capable of identifying and quantifying the main components of the atherosclerotic plaque [110], including hemorrhage, calcifications, lipid core, and fibrous tissue [23, 111, 112]. Most of the current imaging studies of atherosclerotic plaques rely on a human observer's interpretation of MR images with different contrast weightings, producing measurements that have been compared with histology assessment [24]. Manual plaque segmentation requires expertise, is time consuming, and produces results that are subject to interobserver variability [113]. In contrast, automated classification could yield objective and reproducible assessment of plaque composition [37, 114].

Promising work in this field has showed that the composition of atherosclerotic carotid plaques can be objectively determined on ex vivo MR imaging, by means of algorithmic classifiers [104]. Although ex vivo validation is a critical step in the establishment and validation of algorithms, it cannot be directly extrapolated to in vivo material, given the lower image quality and motion artifacts that are inherent to MR images acquired in a clinical setting. Two pilot studies have shown the feasibility of automated plaque analysis in vivo by comparing the accuracy of the classifiers with that attained by human MR imaging readers, using histology as the standard of reference [37, 38]. Both studies reported encouraging results that were comparable with, or possibly more accurate than, manual analysis. However, these previous studies were based on single-center MR imaging data and relied on a small sample of selected patients with high-grade symptomatic carotid stenosis scheduled for carotid endarterectomy.

Therefore, the goal of our work was to extend these results to a larger number of patients for whom markers of plaque instability are essential for therapeutic decision, that is, patients with either symptomatic moderate stenosis or asymptomatic high grade stenosis, using MR images acquired in a multicenter setting.

6.2 Materials and methods

Study population

High-Resolution MR Imaging of Atherosclerotic Stenosis of the Carotid Artery (HIRISC) is an ongoing multicenter prospective study assessing the prognostic value of carotid plaque vulnerability, as defined on MR imaging, for the prediction of cerebral vascular events. Patients are eligible for the study if 1) they have symptomatic stenosis (40% to 69%, according to NASCET criteria) or asymptomatic stenosis (60% NASCET or greater) of the internal carotid artery bifurcation; 2) they are not scheduled for endarterectomy within the next 6 months; and 3) they do not have any other major cause of stroke. The study was approved by the local ethics committee and all patients signed an informed consent form. From the HIRISC imaging data base, we selected 65 consecutive patients who fulfilled the following imaging criteria: of the 4 MR images available, 3 had to be excellent, and the remaining 1 at least good on a subjective 4-level image quality scale (poor, average, good, or excellent), rated by 2 independent readers. Five patients were excluded because man-

ual registration of the 4 MR images was not possible because of severe patient motion. The remaining 60 patients were randomly split into a training group of 20 patients and a study group of 40 patients. For each patient, the carotid artery qualifying for the HIRISC study was analyzed. The training group consisted of 10 men and 10 women (mean age \pm SD of 72.3 ± 12.4 years), 10 right and 10 left carotid stenoses, 11 symptomatic and 9 asymptomatic stenoses, with an overall mean $48.7 \pm 13.2\%$ NASCET degree of stenosis. The study group consisted of 27 men and 13 women (mean age 71.9 ± 10.2 years), 21 right and 19 left carotid stenoses, 25 symptomatic and 15 asymptomatic stenoses, with an overall $44.2 \pm 14.8\%$ NASCET degree of stenosis. There was no significant difference between the training group and the study group for any of these parameters (Student t test for quantitative variables, chi-square test for categorical parameters, level of significance $P < 0.05$).

MR imaging protocol

All patients were imaged on a 1.5-T MR unit using the same 4-channel phased-array carotid surface coil (Machnet BV, Eelde, the Netherlands). Before starting the study, the MR protocol and acquisition parameters were standardized across platforms (Philips, Siemens, GE Healthcare). A fast gradient-echo pulse sequence was used in axial, sagittal, and coronal planes as a localizer. The median sagittal image was used to plan a 2D TOF gradient-echo sequence. Twenty to 30 sections with a thickness of 4 mm were set to cover the neck area using the phased array coil. The z-axis coordinates of the qualifying carotid bifurcation on the 2D TOF images were used to position the following 4 pulse sequences: 3D TOF, T1WI, PDw, and T2WI. The field of view (130 x 130 mm) was identical for all 4 sequences. T1WI, T2WI, and PDw images were obtained with double inversion recovery (ie, black- blood) fast spin-echo sequences with electrocardiographic gating during free breathing using 8 axial sections (3 mm thick, 0.3 mm gap) centered on the qualifying carotid stenosis. PDw and T2WI parameters were as follows: repetition time 2 R-R intervals; effective echo time 16-20 ms for PDw and 50 ms for T2WI; acquisition matrix 256 x 512 (acquired in-plane resolution 508 x 508 μm , interpolated to 254 x 254 μm by zero-filling in k-space); signal intensity averaged 2; fat suppression. T1WI parameters were as follows: repetition time 1 R-R interval; echo time 9-10 ms; acquisition matrix 352 x 256 (acquired in-plane resolution 451 x 508 μm , interpolated to 254 x 254 μm by zero-filling in k-space); signal intensity averaged 3. The 3D TOF sequence used a gradient-echo pulse sequence with repetition time 30 ms; echo time 6.9 ms; flip angle 20° , acquisition matrix 288 x 224, 512 zero-filling (acquired in-plane resolution 451 x 580 μm , interpolated to 254 x 254 μm by zero-filling in k-space); signal intensity averaged 2; 20 sections of 2.2-mm thickness, 1 slab. Total acquisition time was approximately 25 minutes.

Manual image review

For each patient, the images from the 4 vessel wall sequences were visualized using QPlaqueMR software (Medis Medical Imaging Systems BV, Leiden, the Netherlands) and manually coregistered. Two readers, blinded to the results of the automated image analysis, examined, in consensus, all MR images of the qualifying carotid artery using a standardized form and published criteria [23, 24, 115]. For each location, the 4 MR images (PDw, T2WI, T1WI, TOF) were reviewed together. First, the thickness of the vessel wall was reviewed. In the case of a thickened vessel wall, the inner and outer boundaries

were delineated. Next, the vessel wall was segmented as fibrous tissue or as 1 of the different plaque components, namely, calcifications, hemorrhage, or lipid core. All signal intensities were compared with the adjacent sternocleidomastoid muscle. Calcifications were defined as areas of hypointensity on all 4 sequences. Recent and fresh intraplaque hemorrhages (type 1 and 2, as defined previously) [111] were considered together as hyperintensities on T1WI and TOF images. Lipid-rich necrotic core and fibrous components share the same signal intensity on PDw images, that is, signal intensity isointense or slightly hyperintense compared with that of the sternocleidomastoid muscle. PDw and T2WI were compared so as to discriminate between lipids and fibrous component as follows: lipid core was identified as an area in which the signal intensity dropped on T2WI, compared with PDw images, whereas fibrous component corresponded to a relatively high signal intensity area on both sequences.

Calcifications, hemorrhages, and lipid core were considered present if they were observed on at least 1 section. Using the manual drawing features of the QPlaqueMR software, area measurements of vessel, lumen, lipids, hemorrhages, and calcifications were obtained for each location by tracing the boundaries of each component. The fibrous component area was calculated by subtracting lipid core, hemorrhage, and calcium from the plaque area. For each component, volumes per artery were calculated by multiplying the sum of areas from each cross-sectional location by the section thickness plus intersection gap.

Automated image analysis

A pattern recognition system, developed using PRTools [116] and Matlab (2007b; MathWorks, Natick, Massachusetts), was used to automatically classify the pixels inside the vessel wall. Vessel wall pixels were defined by the manually delineated contours of the lumen and outer wall. First, the vessel wall images were normalized based on the median signal intensity within a 4×4 cm region of interest centered at the vessel lumen. This normalization step is required for comparing the different sequences of a single subject as well as for intersubject comparison. Then, for each pixel within the vessel wall, the following features were calculated: normalized signal intensity, zero-, first-, and second-order derivatives at multiple scales from the sequences; distance to the inner and outer wall; and local vessel wall thickness. Based on these features, a linear discriminant classifier was built for classification of each pixel as being calcium, lipid core, hemorrhage, or fibrous tissue. This supervised classifier was trained with the images and manual segmentations from the 20 patients of the training group. During the training phase, the features and their corresponding classes were used to learn statistics describing the data. Subsequently, the trained classifier was used to automatically classify the vessel wall contents of the study group of 40 patients. As in the manual analysis, the presence and volumes of plaque components were determined.

Comparison between automated and manual segmentation

The 2 methods were compared on a per-patient basis. First, the presence and volumes of plaque components in each qualifying artery were determined for the whole dataset. Subsequently, the segmentation results for each patient were assessed by rating whether a plaque component was present or not. Agreement between the automated and manual analysis was assessed for the qualitative segmentation (presence or absence) of each com-

ponent using the κ statistic for dichotomous data and percentage of agreement (similar to accuracy in binary classification). According to Landis and Koch [58], values of κ between 0.8 and 1 indicate almost perfect agreement; 0.6 to 0.8, substantial agreement; 0.4 to 0.6, moderate agreement; 0.2 to 0.4, fair agreement; 0.0 to 0.2, slight agreement; and -1.0 to 0.0, poor agreement.

Quantitative assessment was performed by measuring the volume for each plaque component per artery by both segmentation methods and calculating the intraclass correlation coefficient (ICC) with a 2-way random effect for continuous variables. ICC values over 0.80 were considered excellent. For all agreement parameters, 95% confidence interval (CI) were calculated. Subsequently, scatterplots for plaque volumes in patients were generated to visually compare both methods, and the Pearson correlation coefficient was calculated. A paired Wilcoxon test was used to determine whether the automated and manual analysis method produced different volumes for each plaque component. A P value ≤ 0.05 was considered significant. Bland-Altman analysis [57] was also used to assess any size-dependent bias in the measurements between methods, limits of agreement, and proportional errors.

6.3 Results

Of the 344 sections available in the study group (mean 8.6 per patient), 137 included a thickened wall with atherosclerotic material, according to the visual analysis. Of the 207 remaining sections, only 2 were positive for lipid core with the automated analysis (1.0 and 0.76 mm³, respectively) and 1 was positive for hemorrhage (2.97 mm³).

Qualitative analysis

In the training set of 20 patients, calcium was visually present in 10 cases hemorrhage in 7 cases, while lipids and fibrous tissue were observed in all 20 cases. There were no significant differences in the prevalence of visual detection of each component between the training set and the study group ($P = .65$ for calcium, $P = .12$ for hemorrhage, $P = .31$ for lipids). In the 40 patients of the study group (Fig 6.1), calcium was detected by both methods in 13 patients, hemorrhage in 18 patients, and lipids in all except 2 patients (Table 6.1). The percentage of agreement for calcium and hemorrhage was 80% or higher. The κ values for calcification and hemorrhage indicated moderate and substantial agreement. For identification of lipids, the agreement was almost perfect (97.5%), but because this component was present in almost all plaques, the κ agreement was only substantial ($\kappa = 0.65$ [0.03-1.27]).

Quantitative analysis

The ICC (95% CI) between volumes obtained by the 2 methods was poor for calcifications (0.10 [-0.45-0.60]), excellent for hemorrhage (0.80 [0.54-0.92]), and good for lipids (0.65 [0.43-0.80]). As shown in Fig 6.2, the correlation between volumes was stronger for lipids ($r = 0.88, P < .01$) than for fibrous tissue ($r = 0.80, P < .01$) and hemorrhage ($r = 0.80, P < .01$). For calcifications, the linear correlation coefficient was close to zero ($r = 0.1$, not significant). As shown in Table 6.2, the automated approach overestimated the volume of lipids ($P = .01$). For small volumes of lipids, the Bland-Altman plot showed

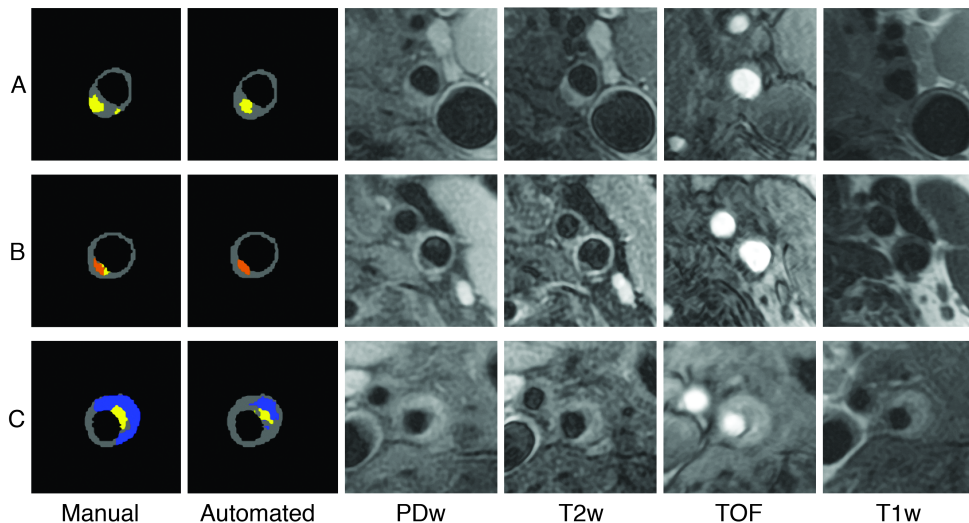


Figure 6.1: Three illustrative examples of manual and automated segmentation. A, Lipid core (yellow) corresponds to an area in which the signal intensity dropped on T2WI compared with PDw images. B, Calcifications (orange) correspond to an area of hypointensity on all 4 sequences. C, Recent hemorrhage (blue) corresponds to an area of hyperintensities on T1WI and TOF images. Note that the automated classifier underestimated the hemorrhage area.

Table 6.1: Percentage of agreement and κ statistic of the plaque components per patient ($n = 40$)

Plaque Component	Manual	Automated		Agreement	κ [95% CI]
		Absence	Presence		
Calcification	Absence	19	3	80.0%	0.59 [0.36-0.82]
	Presence	5	13		
Hemorrhage	Absence	15	4	82.5%	0.65 [0.42-0.88]
	Presence	3	18		
Lipid core	Absence	1	0	97.5%	0.65 [0.03-1.27]
	Presence	1	38		

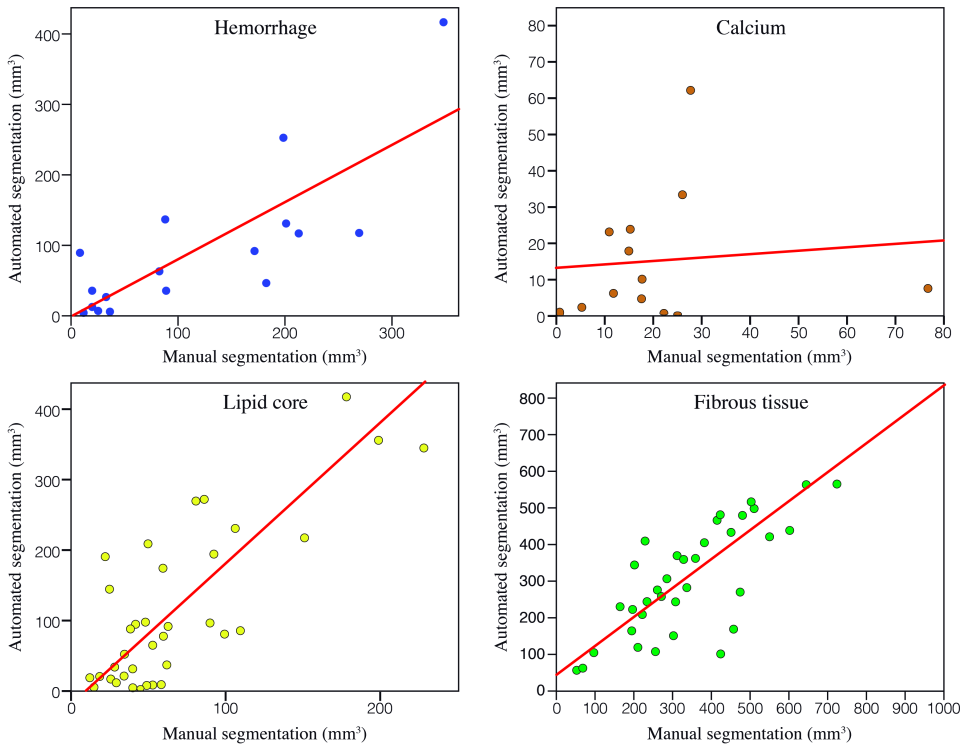


Figure 6.2: Graphs showing scatterplots of the volumes measured with the manual and automated methods for each component. Each dot corresponds to 1 patient.

good agreement between the 2 methods (Fig 6.3). Conversely, for plaques with large volumes of lipids ($> 100 \text{ mm}^3$), the plot indicated a clear overestimation of lipid volumes by automated segmentation compared with manual segmentation. These plaques, in which the automated segmentation overestimated the lipid volumes, were subsequently analyzed visually. They corresponded to carotid arteries curving horizontally after the bifurcation so that the imaging plane was not perpendicular to the arterial wall. This resulted in partial volume effects in the images as well as differences in lumen shape between the MR images, causing low pixel correspondence between the 4 MR images and resulting in classification errors. There were no statistical differences between volumes obtained by the 2 methods for the fibrous component or hemorrhage. For the other plaque components, the Bland-Altman plots did not show any obvious bias according to the size of these components, though differences existed between volumes obtained by the 2 methods.

6.4 Discussion

The purpose of this study was to evaluate the efficacy of automated plaque segmentation for quantifying the main plaque tissue types in carotid arteries on the basis of multicontrast MR imaging. In a population of 40 patients with carotid atherosclerosis and high-resolution MR images acquired in a multicenter setting, our results indicated that 1) it

Table 6.2: Volume of plaque components

Plaque Component	Volume (mm ³)				P value*
	Mean	SD	Median	IQR	
Hemorrhage (n = 18)					
Manual	112	103	86	21-199	0.16
Automated	90	104	58	13-124	
Calcification (n = 13)					
Manual	20	18	18	11-26	0.5
Automated	15	17	7	2-23	
Lipid core (n = 38)					
Manual	73	66	51	33-91	0.01
Automated	125	149	82	19-196	
Fibrous tissue (n = 40)					
Manual	272	176	229	163-344	0.27
Automated	237	162	216	122-340	

Note: IQR indicates interquartile range; n = number of patients for whom a given component was detected by both methods. * Paired Wilcoxon test.

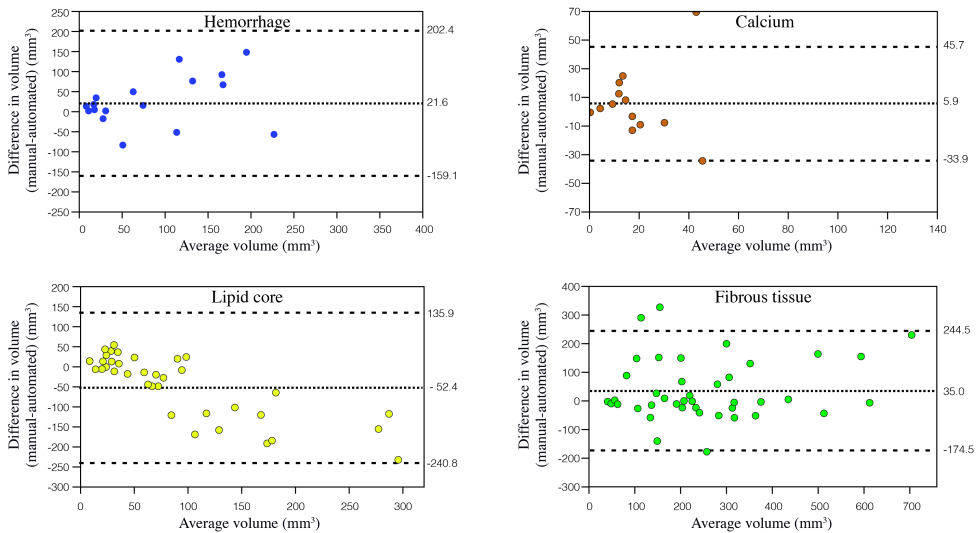


Figure 6.3: Bland-Altman graphics showing the differences between volumes obtained by manual and automated segmentation plotted against the mean of the 2 measurements. Volumes per patient are expressed in mm³. The dotted lines indicate the average bias and the dashed lines show the 95% CI (mean bias ± 1.96 SD). For each component, a negative bias indicates that the automated segmentation overestimates the volumes. A positive bias indicates that the automated segmentation underestimates the volumes.

was possible to automatically detect carotid plaque components with substantial or good agreement with visual identification, and 2) the volumes of plaque components obtained manually and automatically were reasonably consistent for hemorrhage and lipids but not for calcium.

Replacing subjective, time-consuming manual segmentation with an automated segmentation alternative has been a long-time goal. Two studies have tested the possibilities of using supervised classifiers *in vivo* compared with histology [37, 38] and showed encouraging results. In both studies, the algorithm was trained on a small set of patients and then tested on a group of 12 or 13 patients. Both suggested the benefits of supervised classifier algorithms for the detection and the quantification of plaque components. It was even suggested that this approach might be more accurate than manual review of high-resolution MR images for some of the components. All *ex vivo* studies and the 2 *in vivo* studies have focused on patients scheduled for endarterectomy. Our study focused on a different population, composed of patients with moderate symptomatic or severe asymptomatic stenosis and not scheduled for endarterectomy. In this population, the benefit of endarterectomy is still controversial and much is to be expected from markers of plaque instability [117]. To extend the findings of previous “pilot” *in vivo* studies, a larger group of 60 patients was included. Furthermore, these patients were part of a multicenter MR cohort and this should strengthen the generalization of our findings.

Identification of plaque components

Agreement (and κ coefficients) between the manual and automated segmentation method for the detection of calcification, hemorrhage, and lipid core was good and within the range of interobserver variability observed in a previous study dealing with visual analysis on a similar population [113]. The good results observed for hemorrhage can be explained by the high contrast presented by this component on the 4 MR images and by the fact that recent hemorrhage strongly differs from that of other plaque components, especially on T1WI and TOF sequences. This also explains the high sensitivity of the visual detection of hemorrhage on high-resolution MR images compared with histology reported by others [104, 118]. Visual detection of lipid components is based on the comparison of 4 MR images, to eliminate calcification and hemorrhage, and subsequently on a signal intensity loss between PDw and T2WI [115]. This stepwise analysis accounts for the difficulties encountered in both visual and automated analysis. However, the percentage of agreement between the 2 methods for lipids was almost perfect, and the lower κ value can be explained by the high prevalence of this plaque component [119]. Lipid core was detected in almost all the patients by both the automated and manual segmentation methods. Histologic and MR studies have also reported a high prevalence of lipid core, seen in up to two-thirds of plaques [24, 113].

Identifying calcifications using MR imaging is still a difficult task. It relies on differences in magnetic susceptibility between the mineral components and neighboring soft tissues. 3D gradient-echo TOF sequences are theoretically the most sensitive, but they are more affected by artifacts compared with other types of sequences [113]. Moreover, on 3D TOF sequences, calcifications adjacent to the lumen are difficult to separate from other plaque components, such as the fibrous cap, because they share the same signal intensity characteristics [113, 120]. However, these issues affect both manual and automated methods, which could explain why agreement remained reasonable in line with another

group [114]. Finally, these difficulties may not in fact hamper the prediction of vascular risk, because the prognostic value of calcifications for embolic risk is still debated [121].

Quantification of plaque components

Agreement between the automated and manual segmentation methods was high for the quantification of lipid core and hemorrhage and low for calcification, as indicated by the ICC. The same trend appeared when we calculated the Pearson correlation coefficients for the volumes of each component. These correlations lie within the range of previously published values obtained by the only group that distinguished the lipid core from recent hemorrhage [37]. Another group chose to define necrotic core as regions of lipids and intraplaque hemorrhage, and consequently only provided global results [38]. The correlations also compare favorably with results obtained visually by 2 observers. However, the Bland-Altman analysis showed that there is still a considerable discrepancy between the manual and automated outlining. Hofman et al observed that the human eye underestimated the size of hemorrhage and overestimated the size of lipids [37]. This might explain, in part, the discrepancies between our automated and manual segmentations. The Bland-Altman plots additionally showed that the consistency between measurements decreases for plaques with a large lipid core. Large discrepancies were explained by low pixel correspondence between the different sequences, causing errors in the automated classification in patients with a horizontal carotid artery.

Whether calcifications, displayed as a signal intensity loss, should be measured on MR imaging is controversial [122]. Even though our measurements may not be very accurate, the error theoretically applies to both segmentation methods. It does not explain the poor agreement observed between measurements obtained by the 2 methods. In line with this, another group reported a low correlation between manual segmentation and various classifiers, as well as a poor correlation with histology [37]. This may be related to poor performance of the supervised classifier. Performance of a supervised classifier is highly dependent on the training set. The training set should contain sufficient representative examples of each plaque component. The frequency of calcified plaques and volume of calcifications in the data we used were small compared with the other 2 components, explaining, at least in part, the low performance. Indeed, better results were reported in a study with higher frequency of calcified plaques in the training set [114]. The use of the postcontrast T1WI sequence may also improve calcium detection [38].

Limitations

Our study has a number of limitations. First, it lacks an *ex vivo* reference standard to determine absolute accuracy. Even though we found good agreement between the 2 methods, we cannot rule out the possibility that both methods misinterpreted the images. We did, however, use a well-documented manual image review procedure that has been extensively validated against *ex vivo* references [24, 123]. Second, like others [37, 38], we selected MR examinations with good quality images among a larger imaging data base. The results probably depend on image quality and cannot be extrapolated to all high-resolution MR imaging of human carotid plaques, irrespective of the image quality. Third, the classifier was trained on a limited training set of 20 patients. The results would potentially have been better with a larger training set, including more samples of hemorrhage and calcifications. Fourth, given the low interobserver reproducibility for fibrous

cap characterization, previously reported on a similar set of images [113], we chose to exclude automated characterization of the fibrous cap (thick, thin, or ruptured), which is a marker of plaque instability. In our opinion, this goal requires an improvement of the image quality in terms of spatial resolution and contrast. For instance, gadolinium injection could help distinguish between lipid core and fibrous cap [38, 123]. Fifth, we considered fresh (type 1) and recent (type 2) hemorrhage together, given the low prevalence of type 1 hemorrhage [118] and the previously reported moderate agreement between automated and manual segmentations for the identification of these hemorrhage subtypes [114].

Finally, the automated method we used represents one of 4 basic steps in carotid plaque analysis: lumen boundary detection, outer wall boundary detection, multicontrast registration, and plaque segmentation. We have addressed the final step, which is the most critical for automation. Automated methods for the remaining steps have previously been reported [10, 25].

6.5 Conclusions

Once automated methods for atherosclerotic plaque segmentation, such as the one presented here, have been fully validated, a considerable gain in processing time can be expected, together with elimination of interobserver variability. Automated analysis could become a clinical tool for the pretherapeutic assessment of atherosclerotic carotid artery stenoses and, further, could be integrated in longitudinal or transversal studies of large populations. By providing quantitative measurements of lipids and hemorrhage, automated methods could improve the reliability of quantitative markers for plaque instability and ease their use as criteria for assessing the efficacy of treatments stabilizing atherosclerotic plaque.

Acknowledgments

We thank Fatiha Boumaza, Isabelle Laurent, Isabelle Chalmette, all radiographers and collaborators of the Unité de Recherche Clinique, Cochin Port-Royal, Paris. We also thank M. Adame for useful discussions.

Chapter 7

Agreement and reproducibility of automated atherosclerotic carotid artery plaque classification using optimized 3d morphological and intensity features in MR vessel wall images

This chapter is in submission:

S. Gao, R. van 't Klooster, D. F. van Wijk, A. J. Nederveen, B. P. F. Lelieveldt, R. J. van der Geest. Agreement and Reproducibility of Automated Atherosclerotic Carotid Artery Plaque Classification Using Optimized 3D Morphological and Intensity Features in MR Vessel Wall Images.

Abstract

Purpose: To investigate the effect of the choice of the features and training samples to the agreement between manual and automated carotid artery plaque classification in multi-contrast MRI and to evaluate the reproducibility of automated versus manual plaque segmentation.

Materials and methods: Twenty-three patients with 30-70% stenosis underwent two carotid vessel wall MR scans within one month. One reader blindly segmented the data twice to provide the reference standard and training of different classifiers. Three possible improvements to the base classifier, which utilized conventional features, were investigated: 1) 3D morphological features, 2) intensity normalization strategies, 3) refinement of the training set by intersecting the repeated reads. A final classifier was constructed by incorporating the optimal elements from the three improvements.

Results: Compared to the base classifier, the final classifier using the 3D distance to flow divider feature, intensity scaling as normalization and refined training data, had significantly better Dice overlap with manual segmentation. Compared to manual segmentation, automated plaque assessment reproducibility, assessed by the intra-class correlation coefficient, increased from poor to fair for lipid, good to excellent for calcification, and fair to excellent for loose matrix.

Conclusion: Automated plaque classification has great potential for monitoring of treatment and plaque progression.

7.1 Introduction

Rupture of unstable atherosclerotic plaque in the carotid artery is believed to be the primary cause of transient ischemic attack and stroke [124]. Carotid MR imaging is a promising non-invasive tool for identification of plaque vulnerability as it provides direct visualizing of the vessel wall providing information on plaque composition and morphology in addition to lumen dimensions. Numerous studies have shown that multi-contrast weighted MRI can distinguish the major components such as calcification, intra-plaque hemorrhage (IPH) and lipid-rich necrotic core (LRNC) in human carotid atherosclerotic plaque in vivo [23, 24, 94]. Among these components, IPH and LRNC have been reported to be strongly associated with plaque rupture and the occurrence of future cerebrovascular events [65]. Currently, MRI-based plaque characterization heavily relies on manual segmentation, which is a labor-intensive procedure and is prone to intra- and interobserver variability. Reproducible automated plaque detection and classification approaches would greatly increase the clinical applicability of plaque composition quantification from multi-contrast MR imaging protocols.

Several automatic algorithms have been proposed for the segmentation of ex vivo MR images of carotid endarterectomy specimens [43, 104, 125, 126], but translating these methods to in vivo data is hampered by the decreased resolution, motion and flow artifacts typically present in in vivo MR. Recent studies have attempted to develop automated methods for in vivo MR plaque segmentation. Adame et al [25] used an ellipse-fitting approach to detect the outer vessel wall boundaries and used fuzzy clustering to detect the lumen and plaque contours. Liu et al [38] used a maximum-likelihood Bayesian classifier to generate a tissue probability map and used a level set method to define the final plaque regions. Hofman et al [37] compared the performance of four types of supervised classifiers, which included a combined classifier that utilized information of neighboring pixels. Van Engelen et al [127] proposed a supervised classification technique incorporating the labeling uncertainty of the training pixels. Van 't Klooster et al [20] evaluated the efficacy of automatic plaque segmentation on images acquired in a multicenter setting and demonstrated that automatic quantification could provide important information in making the therapeutic decision to recommend endarterectomy for patients with moderate symptomatic and severe asymptomatic stenosis. All these techniques employed pattern recognition, which is based on features being derived from the MR images to aid the separation of the area of interest into plaque components. Generally, signal intensity (SI) features have been used in these algorithms including normalized SI [20, 25, 37, 38, 127] and first and second order derivatives at multiple scales [20, 127] from each of the available contrast weightings (e.g. T1w, T2w, PDw, TOF). In addition, the use of morphological features have been proposed, including distance to the lumen and outer wall [20, 38, 127] and local wall thickness [20].

Useful features can adequately characterize and represent each class in the image, providing relevant information for the classification process. Therefore, the use of critical features aid discrimination by contributing to the separability of spectral classes in both supervised and unsupervised pattern recognition. Despite the wide use of existing intensity and morphological features in this domain, there are still several possible improvements related to the choice of features that have not been considered. First, the reported morphological features are calculated in 2D capturing the location information of components such as being adjacent to the lumen, close to the outer wall boundary or deep within a plaque, but little work has been done in using 3D morphological features. Therefore, it

is unclear whether the addition of 3D morphological features can enhance the discriminative power of a classifier. Second, the region based normalization method proposed by Liu et al [38], in which the image intensity was divided by the median signal intensity within a $4 \times 4 \text{ cm}^2$ region of interest (ROI) centered at the lumen, was found to be the preferred MR signal calibration method applied in most in vivo plaque segmentation studies. However, there is no clear evidence indicating that this normalization approach is also the optimal approach since it has not been compared with other intensity normalization approaches. Furthermore, the quality of the training data can have a large impact on the performance of a supervised classification process and training samples should provide a representative description for the classes. However, in many applications, there is no refinement conducted in the training data to discard unrepresentative samples which may have a negative influence on the classifier in learning spectral signatures of the classes. Additionally, although in vivo studies have demonstrated promising automatic segmentation results indicated by the good agreement between automated plaque classification and manual plaque delineation [20, 25] or histological findings [37, 38, 127], results on interscan reproducibility of automated plaque classification are lacking.

Accordingly, the purpose of this study was to investigate the effect of the following strategies on the classification of atherosclerotic plaque components from in vivo carotid MRI datasets. First, 3D morphological features were incorporated as input to the classifier in addition to the conventional 2D morphological features. Hence, information of plaque distributing along the radial, circumferential and axial direction was considered. Second, several alternative normalized intensity features were evaluated, aiming at mimicking the way an expert is interpreting raw MR signal intensities as relative signal intensities. Third, training samples were obtained from the intersection of the plaque segmentations provided by the repeated reviews of the experienced observer to generate a more reliable classifier. A ground truth provided by histology was not available in this study because the patients, with moderate atherosclerosis, were not scheduled for carotid endarterectomy. In this study, we evaluated the developed automated methods by comparing the agreement between automated classification and manual segmentation by an experienced reader and we evaluated the robustness of the methods by quantifying the scan-rescan reproducibility.

7.2 Materials and methods

Image data

Twenty-five patients, with one or more atherosclerotic events and 30% to 70% carotid artery stenosis, identified by duplex ultrasound measurement, underwent a carotid vessel wall MR exam at baseline and follow-up within one month. No clinical major events were reported in the period between the two exams. Two patients were excluded because of poor image quality. The remaining 23 patients' baseline and follow-up scans, constituting 46 datasets, were used in this study.

All MRI examinations were performed on a 3.0T whole body MR scanner (Intera, Phillips Healthcare, Best, The Netherlands) using an 8 channel bilateral carotid artery coil. Details of the imaging protocol have been described previously [128]. In short, a time of flight (TOF) sequence covering both carotid arteries (FOV = $10 \times 10 \text{ cm}^2$, 40 slices of 2 mm thickness, a segment of 8 cm was scanned) together with ultrasound duplex data were used for localizing the center of the carotid plaque. Subsequently a stack of

ECG-gated unilateral axial TOF, PDw, T1w, T2w images were acquired. The FOV (60×60 mm²), acquisition matrix (120×120), non-interpolated pixel size (0.5×0.5 mm²), number of slices (8), slice thickness (2 mm) and slice gap (0 mm) were identical for all four sequences. The black-blood T1w, T2w, and PDw images were acquired with an identical flip angle (90°). The repetition time was 2 R-R intervals for T2w and PDw, 1 R-R interval for T1w; and echo time was 8 ms for T1w and PDw and 50 ms for T2w. The TOF sequence used the following parameters: flip angle 20° ; echo time 5 ms; repetition time 19 ms. Overview images showing the image stacks superimposed over the carotid artery were saved for planning the acquisition of the follow-up scan.

Manual image review

Images of the 46 exams were examined by an experienced MRI reader, who was fully blinded to the scan session and patient information. To assess the intraobserver agreement, the reader, blinded to the previous annotation result, reanalyzed all the blinded images two months after the initial review. The manual segmentation result of the initial review will be called first read and the results of the second review will be called second read in the remainder of this manuscript. Image sets of each patient obtained from scan and rescan session were randomized and anonymized to prevent any recall bias when repeated reviewing of the same patient. Image review and manual analysis were performed using VesselMass software (Leiden University Medical Center, the Netherlands) [25, 50]. During the procedure, four contrast weighted images of a given slice were simultaneously presented. Next, lumen and outer wall boundaries of the common and the internal carotid artery were manually traced on the T1w image and propagated to the images of other weightings. T2w, PDw and TOF images were manually registered to the T1w image by translating each image stack in through-plane direction and each slice in the x and y direction to match the contours of inner and outer wall, such that patient motion between acquisitions was corrected, resulting in an aligned set of multi-contrast images. Contours of lipid, calcification, ulceration, hemorrhage and loose matrix were delineated according to previously described and validated plaque classification criteria [24], and was based on relative intensities observed in the four sequences, such as lower, higher, or equal to adjacent sternocleidomastoid muscle. To enable the intensity normalization based on the sternocleidomastoid muscle during the automatic classification, muscle contours were traced by another reader with over 4 years of experience in carotid MRI image review.

To enable assessment of the scan-rescan reproducibility of plaque classification at a slice level, registration between scan and rescan sessions was performed. The alignment of the transverse slices in the repeat scans was performed manually using the T1w series. First, the corresponding slice in the follow-up scan was found to match the bifurcation slice in the baseline scan, which was imaged at the location crossing or just next to the flow divider. This matching procedure was then applied to the other slices from proximal to distal relative to the carotid bifurcation in the caudo-cranial direction.

Automatic plaque classification

The base classifier

The base classifier was constructed according to the description in a previous study [20]. In brief, a supervised pattern recognition system was trained using the available manual

segmentation results to automatically classify the plaque contents by using the intensity and morphological features extracted from multi-contrast MRI. For the 23 patients a total of 46 datasets were included in the automated analysis. Twelve MRI slices were excluded because not all contrast weightings were available which resulted in 7 ± 1 (range 3-8) MRI slices per dataset for which information from all 4 sequences (T1w, T2w, PDw, TOF) was available. In each slice, the pixels in the carotid artery vessel wall, as defined by lumen and outer wall boundaries, were extracted to create datasets. For each pixel, the following features were calculated: normalized SI of the four sequences, distance to the vessel lumen, distance to the outer wall and local wall thickness. A linear discriminant classifier (LDC) that modeled each class as a multivariate Gaussian distribution with an equal covariance matrix was trained based on the above intensity and morphological features. The classifier was evaluated by using a leave-one-patient out cross-validation approach, in which all pixel samples in one dataset from baseline or follow-up scan of one patient were used for testing and all pixel samples in the baseline and follow-up exams of the remaining 22 patients (44 datasets) were used for training. The segmentation provided by the first read was used to train the classifier, from which the features and a priori probability were calculated; the reference standard was set by the same read. Each vessel wall pixel was classified to be one of the six classes: fibrous tissue, lipid, calcification, ulceration, hemorrhage, and loose matrix according to the highest posterior probability. A post processing step was implemented to eliminate isolated pixels. Isolated pixels were relabeled to the majority class of its neighboring pixels (within a 3×3 window). A pixel was considered to be isolated if it was the only pixel of a given plaque component in a slice. The automatic classification experiments were performed using MATLAB 2011b (Mathworks, Natick, US) and the pattern recognition toolbox PRTools (version 4.2.0) [129].

Strategies for improving the classifier

Three different strategies to improve the base classifier were investigated.

Strategy 1: Incorporation of 3D morphological features

Atherosclerotic plaque predominantly develops at the carotid bifurcation in regions with relatively low wall shear stress [130]. To explore the effect of adding information about the axial and circumferential position into the automated plaque classification, we propose two 3D morphological features: 1) distance to the flow divider and 2) angle to the external carotid artery to describe the location of a pixel within the vessel wall relative to the carotid bifurcating structure. The 3D distance feature (as illustrated in Figure 7.1) is computed as the vertical distance with respect to the flow divider, the location where the common carotid artery (CCA) separates into the internal carotid artery (ICA) and the external carotid artery (ECA). The 3D angular feature (as illustrated in Figure 7.2) is computed as the cosine of the angular position of a pixel with respect to the ECA.

Strategy 2: Intensity normalization approaches

One of the major difficulties associated with MR image segmentation is that image intensities do not have a tissue specific meaning. MR signal intensities may vary significantly even between images obtained from the same tissue of the same patient at the same scanner with the same imaging protocol. Consequently, a classifier trained based on unprocessed raw MR image intensities may yield poor classification results, as intensities of the

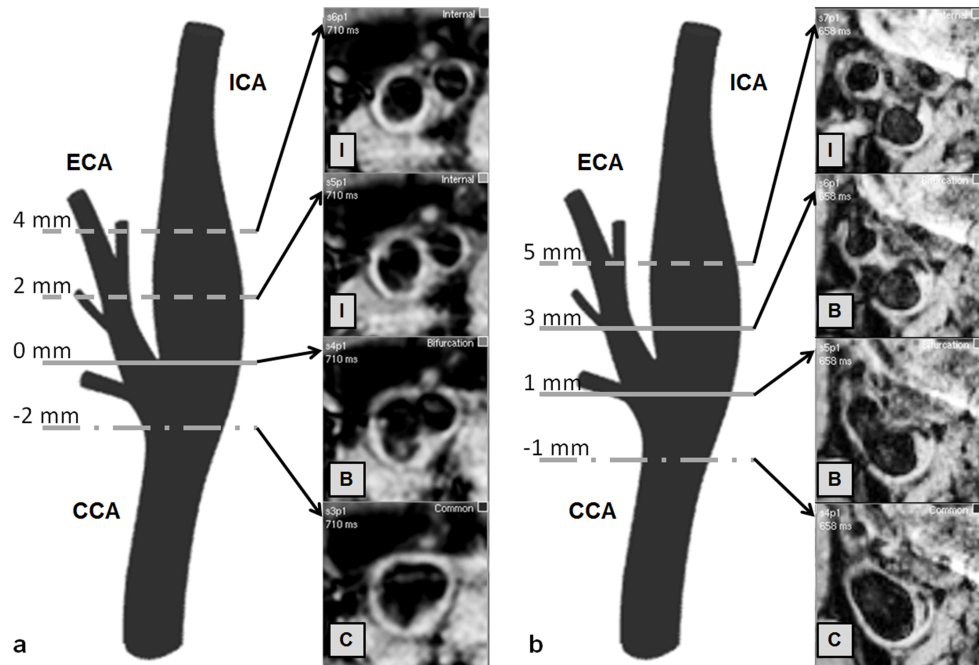


Figure 7.1: An example of the 3D distance to flow divider feature calculation. Each image slice is labeled as Common (C), Bifurcation (B), or Internal (I) on the T1w image. The dashed line, solid line and dash dot line show the imaging slice center located at ICA, bifurcation and CCA. The 3D distance feature is calculated by subtracting the z-coordinate of the bifurcation slice from the z coordinate of current slice, and multiplying resulting difference by the slice thickness. Therefore, locations at the ICA have a positive distance and locations at the CCA have a negative distance. (a) Example of a single bifurcation slice in one artery. The bifurcation slice (slice 4) crosses the flow divider, resulting in z coordinate equal to 4. (b) Example of two bifurcation slices in one artery. The bifurcation slices are above (slice 6) and below (slice 5) the flow divider, resulting in z-coordinate equals to 5.5.

same tissue may differ considerably between the images used for training and testing. Therefore, raw MRI data must undergo intensity normalization prior to automatic classification. Intensity normalization for in vivo MR carotid plaque imaging data remains a challenging problem. The following approaches were evaluated, in which the normalization was performed slice by slice, and their efficacy on plaque tissue classification was compared.

Normalization based on a square Region of Interest: nROI

Liu et al suggested that the median intensity of $4 \times 4 \text{ cm}^2$ square region of interest (ROI) closely agreed with that of the sternocleidomastoid muscle which is used as the reference by the human observer [38]. Accordingly, the signal intensity of each image slice was divided by the median signal intensity of the $4 \times 4 \text{ cm}^2$ ROI centered at lumen in the current

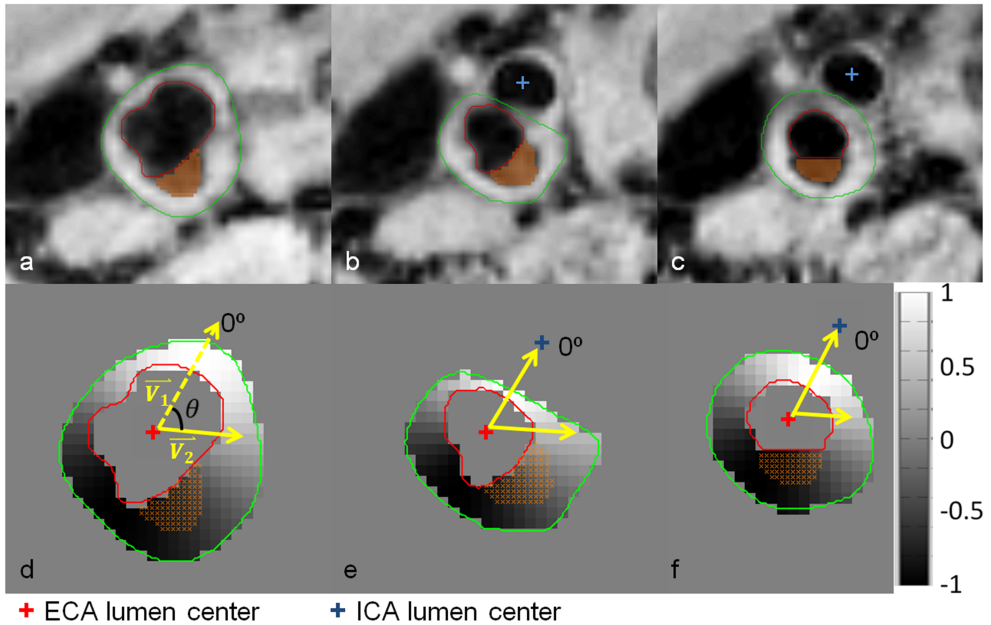


Figure 7.2: An example of angle to ECA feature calculation. The top panel (a, b, and c) shows three consecutive T1w images at the level of the common carotid artery (a), carotid bifurcation (b) and internal carotid artery (c) and manually annotated contours of lumen (red), outer wall (green) and region of calcified tissue (orange). The center of the lumen of the ECA is indicated by a reference point (blue cross). The bottom panel (d, e, and f) shows the angular feature map calculated from the corresponding slice. The vector v_1 (yellow arrow) indicates the direction from the ICA lumen center towards the ECA lumen and represents the 0 degree angle. The vector v_2 (yellow arrow) is pointing from the ICA lumen center to a vessel wall pixel of interest. The angle θ is the angle between v_1 and v_2 . In slices where the ECA is not visible in the field of view (a), v_1 is derived from the nearest bifurcation slice. Pixel intensity values of the angular feature map are computed as $\cos\theta$, ranging from -1 to +1, resulting in a low value for pixels far away from the ECA and a value close to 1 for pixels near the ICA.

slice (Figure 7.3a). This was repeated for all four contrast weightings.

Normalization based on a donut-shaped Region of Interest: nDonut

A circular ROI with a diameter of 4 cm contains relatively more relevant information than the 4×4 cm² squared ROI. Moreover, the presence of pathology may potentially distort the normalization result since plaque composition and lumen size varies from patient to patient. The lumen and vessel wall area were removed from the circular ROI in each slice, which resulted in a donut-shaped ROI. MR images of all contrast weightings were divided by the median signal intensity of the donut shaped ROI centered at the lumen (Figure 7.3b).

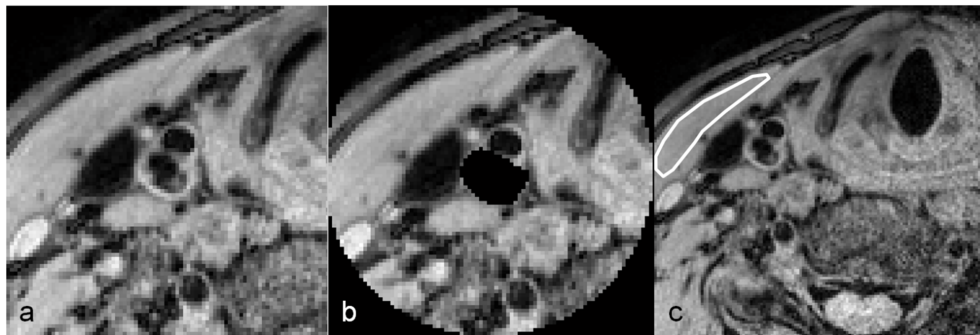


Figure 7.3: (a) The $4 \times 4 \text{ cm}^2$ ROI centered at ICA lumen of a T1w image slice. (b) The 4 cm diameter donut shaped ROI centered at the ICA lumen of a T1w image slice. (c) Manually traced SCM contour (white) on T1w image.

Normalization based on the sternocleidomastoid muscle: nSCM

Normalization of the signal intensities based on the signal intensity of the nearby sternocleidomastoid muscle is commonly reported as the preferred approach when performing manual plaque classification [24]. T1w, T2w and PDw images were divided by the median signal intensity of the manually traced sternocleidomastoid muscle (SCM) (Figure 7.3c). In this approach the TOF images were normalized using the nROI method because of the poor depiction of the SCM in the TOF images.

Normalization based on intensity scaling: nScaling

Intensity scaling is a common practice for MR intensity standardization in brain segmentation studies [131]. The T1w, T2w, PDw and TOF images were linearly scaled according to Equation 7.1, in which the 2.5 and 97.5 percentile of the intensity histogram in the donut-shaped region were mapped to 0 and 1000.

$$SI_{scaled} = \frac{(|SI| - 2.5\%DonutImage) \times 1000}{(97.5\%DonutImage - 2.5\%DonutImage)} \quad (7.1)$$

Normalization based on manually annotated fibrous tissue: nManuFibrous

This normalization approach is mimicking the human observer who compares the SI of a location of interest to the surrounding fibrous tissue when segmenting plaque components. T1w, T2w and PDw images were normalized by dividing all intensities by the median value of the manually identified fibrous tissue region. In this approach the TOF images were normalized using the nROI method because of the poor depiction of the vessel wall in the TOF images.

Normalization based on automatically detected fibrous tissue: nAutoFibrous

In practice, it is not possible to know the regions of fibrous tissue prior to the automated plaque classification. To simulate the procedure of nManuFibrous, we performed a step-wise normalization. In the first step the nROI normalization was used to perform an initial

classification of fibrous tissue. In the second step the initial fibrous tissue classification was used to generate the normalization factor for the T1w, T2w and PDw images. As in the nManuFibrous method, the TOF images were normalized using the nROI method.

Strategy 3: Refinement of the training samples

In supervised classification, spectral signatures of each class are derived from representative samples in the training phase. The performance of a classifier can be significantly influenced by the training data. In this study, a histology guided manual segmentation was not available. Therefore, to train a more reliable classifier the training samples were generated from the intersection of the segmentations provided by the two repeated reads by the reader (first read and second read), which discarded the pixels with unequal labels between both segmentations. In this trial, the priori probability, morphological and intensity features were calculated from the first read and the second read. Then the priors and features were averaged respectively and were used to train the classifier. Both sets of manual segmentations were used as reference standard.

Evaluation of the automated classification results

Agreement

To evaluate the effects of the three proposed strategies including 3D morphology features, different intensity normalization procedures, and the training set refinement on the automated plaque classification, the results from different classifiers were compared to the result from the experienced observer. The agreement between automated and manual segmentation was assessed using the 2D Dice overlap measure, which is defined as the area of overlap between the manual and automatic segmentation divided by their mean area. The 2D Dice was calculated and averaged for the slices in which both the observer and the classifier detected a given type of tissue. To compare the performance of the base classifier and the final classifier which incorporated the selected optimal elements from the three proposed strategies based on the highest automated-manual agreement, we calculated the average 2D Dice. The experimental design is listed in Table 1. To compare the agreements obtained by different classifiers, the Mann-Whitney test was applied to the 2D Dice scores. A p-value smaller than 0.05 was considered to be statistically significant.

Reproducibility

To assess the scan-rescan plaque classification reproducibility of the manual and the automated methods, the intraclass correlation coefficient (ICC) was used. For each plaque type, areas were measured in all baseline slices and the corresponding follow-up slices. The ICC was calculated between the baseline areas of all patients and the follow-up areas. Pixel-wise analysis was not an option because the registration between baseline and follow up images is not accurate at a pixel level, due to variations in patient position. According to Cichetti et al [132], ICC values between 0.75 and 1 indicate an excellent agreement; 0.69 to 0.74 a good agreement; 0.40 to 0.59 a fair agreement; and below 0.40 a poor agreement.

Table 7.1: Experimental setup.

Experiment for evaluation	Variables	Constants
3D Morphologic features	distance to flow divider; angle to ECA;	Intensity and 2D morphologic features; nROI; train by manual segmentation of first read; evaluate on the test set of first read;
Intensity normalization approaches	nROI; nDonut; nSCM; nScaling; nManuFibrous; nAutoFibrous;	Intensity and 2D morphologic features; train by manual segmentation of first read; evaluate on the test set of first read
Training set refinement	train by manual segmentation of first read; train by manual segmentation of second read; train by intersection of two reads (first read and second read);	Intensity and 2D morphologic features; nROI; evaluate on the first read and second read separately then take average from these two results.
Final classifier	3D feature which introduces highest improvement; Normalization approach which introduce highest improvement; train by best training set;	Intensity and 2D morphologic features; evaluate on the first read and second read separately then take average from these two results.

Table 7.2: The presence of particular plaque components in 46 datasets based on the manual segmentation provided by the first read.

	Lipid	Calcification	Ulceration	Hemorrhage	Loose Matrix
Number of datasets that a given plaque component was detected	20	42	9	3	29
Number of patients that a given component was detected in both scan and rescan	6	17	1	1	10

7.3 Results

The results of automated atherosclerotic plaque classification experiments are presented in Figure 7.4-7.8. In total 304 slices from unilateral carotid arteries ($n = 46$) from 23 patients were included in the final analysis. Table 7.2 lists the presence of particular plaque types in the complete data set based on the manual segmentation of the first read. It shows that for ulceration and hemorrhage, the number of cases was small and the manual segmentation reproducibility was poor, which was not sufficient for training the classifier to classify ulceration and hemorrhage. Therefore, no analysis was performed for these two types of tissue in this study.

3D morphological features

The agreement between manual segmentation and automated classification based on the different feature combinations are shown in Figure 7.4. The base classifier using the conventional set of features yielded an average Dice of 0.27 for lipid, 0.34 for calcification,

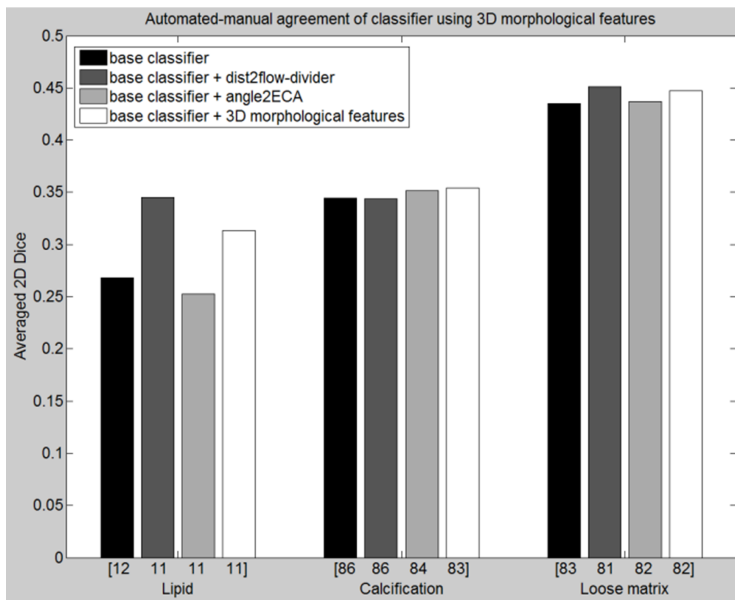


Figure 7.4: Results of automated-manual segmentation agreement obtained by classifiers with different feature combinations. The values between brackets are the number of slices in which both the manual and automated methods detected a given plaque component.

and 0.43 for loose matrix. After adding the distance to flow divider feature to the base classifier, the classification agreement improved to an average Dice of 0.35, 0.34 and 0.45 respectively. A substantial improvement in average Dice was observed for lipid. Including the angle to ECA feature to the base classifier did not result in an improvement in agreement. Including both 3D morphology features to the base classifier resulted in a minor increase in classification accuracy. No statistical significant difference in the classification accuracy was found between the base classifier and the classifiers incorporating 3D morphological features.

Intensity normalization

Figure 7.5 shows the agreement between manual segmentation and automated classification using different intensity normalization methods. The result shows that the effectiveness of normalization methods ranks in the following order: nScaling \approx nManuFibrous > nDonut > nROI > nSCM > nAutoFibrous. The classifier using normalization by linear scaling (nScaling) yielded a comparable accuracy to the one using the nManuFibrous method. Compared to the result of the base classifier which used nROI method, the highest increase in average Dice provided by the proposed normalization methods was found for lipid and loose matrix. Application of the nScaling intensity normalization resulted in a significant increase ($p < 0.05$) in Dice for loose matrix, but no significant increase in Dice for lipid was found. The classifier using normalization by the automatic classified fibrous tissue (nAutoFibrous) produced the lowest average Dice for these two components. The different normalization methods showed only small differences in average Dice for

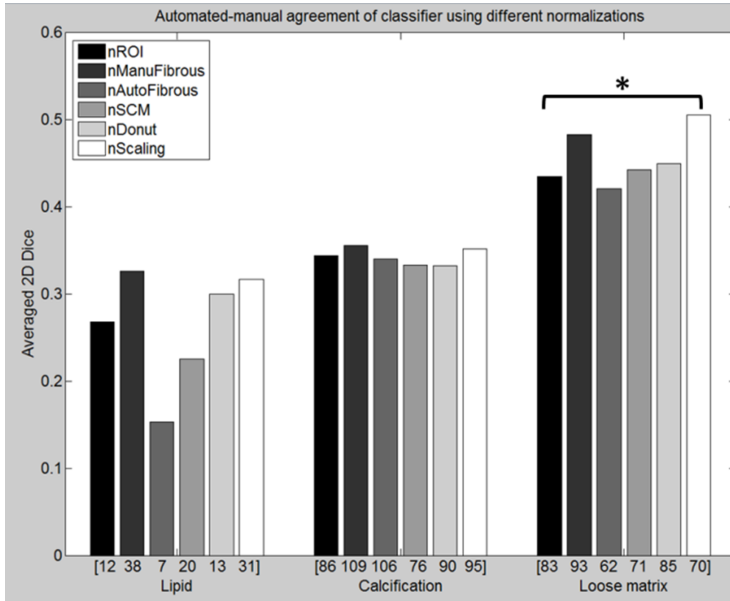


Figure 7.5: Results of automated-manual segmentation agreement obtained by classifiers with different intensity normalization approaches. The values between brackets indicate the number of slices in which both the manual and automated methods detected a given plaque component. The classifier using linear intensity scaling (nScaling) for image normalization resulted in the highest Dice overlap with manual segmentation. * indicates statistically significant difference ($p < 0.05$) between methods.

calcification.

Training set refinement

Figure 7.6 shows the performance of two classifiers in which the first was trained using the segmentation of either the first or the second read (black bars), while the second classifier was trained using the intersection of both reads (white bars). Both classifiers were tested on the first read and the second read. The final result for each classifier was calculated by taking the average of the results on the first and the second read. The classifier using the training data from the intersection of both reads provided better agreement with manual plaque classification than the one using the training data from a single read. No statistical significant difference in the classification agreement was found between the classifiers without and with training set refinement.

Base classifier versus the final classifier

The 3D distance to flow divider feature, the image normalization based on linear intensity scaling (nScaling), and the training set using the intersection of two reads were integrated into a final classifier. The result in Figure 7.7a shows the improvement of the final classifier (red bar) compared to the base classifier (blue bar) in average Dice. The final classifier achieved a significantly higher Dice for lipid ($p < 0.01$) and loose matrix ($p < 0.01$), and a

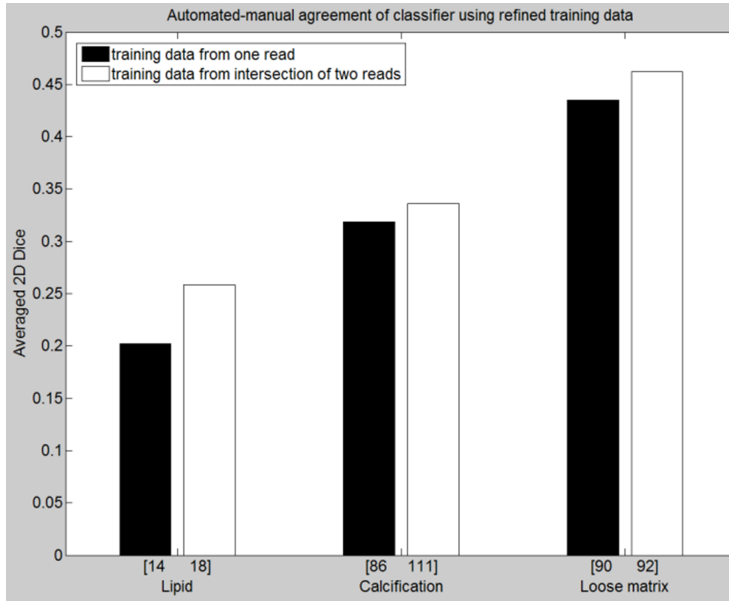


Figure 7.6: Results of automated-manual segmentation agreement obtained by classifiers without and with training set refinement. The values between brackets are the number of slices in which the both manual and automated methods detected a given plaque component.

higher Dice for calcification which was not statistically significant. The higher Dice for all three plaque components demonstrates that the final classifier is in better agreement with the manual observer at a pixel level. Figure 7.7a shows that the agreement between automatic and manual segmentation was lower than the agreement between the repeated manual delineations (green bar). Figure 7.7b shows three typical examples. In each example, a slice was classified by manual analysis, the base and the final classifier. The classification result from the final classifier showed more overlap with manual analysis than the classification result from the base classifier for lipid, calcification and loose matrix. Although the improvements provided by the three proposed strategies were not significant in most of the separate experiments, the final classifier which integrated the optimal elements resulted in a significant improvement over the base classifier.

Scan-rescan plaque segmentation reproducibility

The interscan plaque segmentation reproducibility for the base classifier, the final classifier and the experienced reader, assessed by ICC of area for the major plaque components, is shown in Figure 7.8. The ICC demonstrates that the final classifier obtained similar reproducibility as the base classifier and both classification methods achieved a higher reproducibility in segmenting the scan-rescan images compared to manual segmentation. Compared to manual analysis, automated plaque component area measurement reproducibility increased from poor to fair for lipid, increased from good to excellent for calcification and increased from fair to excellent for loose matrix.

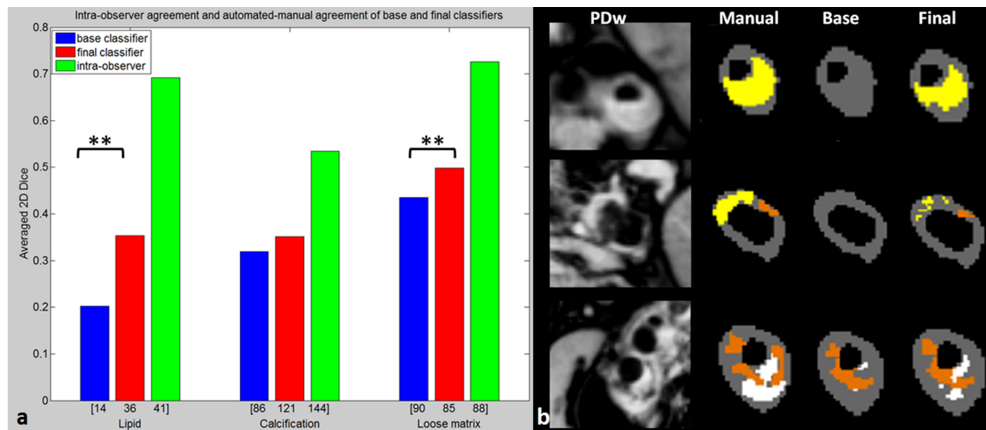


Figure 7.7: Results of automated-manual agreement obtained by the base classifier (blue bar), and the final classifier (red bar) and results of intra-observer agreement obtained by the experienced reader (green bar). (a) Measurement of averaged Dice, the values between brackets are the number of slices in which both the manual and automated methods detected a given plaque component. Stars ** in the figure of Dice indicate statistically significant differences with $p < 0.01$. (b) Typical examples of manual and automated classification in one slice for lipid (yellow), calcification (orange), loose matrix (white) and fibrous tissue (gray). PDw images show the anatomical information of the corresponding slice.

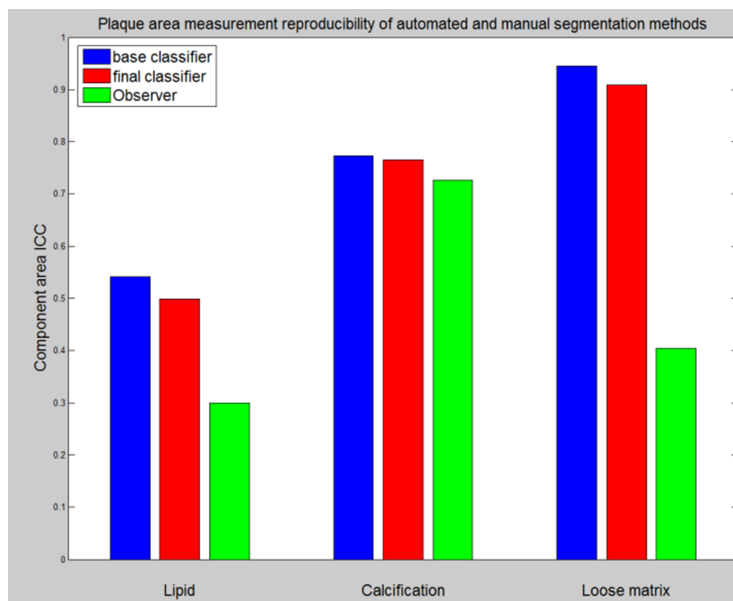


Figure 7.8: Results of scan-rescan plaque segmentation reproducibility, which were assessed by plaque area ICC, obtained by the base classifier (blue bar), the final classifier (red bar) and the observer (green bar)

7.4 Discussion

In this study, we evaluated several methods for automated classification of plaque components in the carotid vessel wall from in vivo multispectral MRI. We compared the agreement between automated and manual segmentation and compared the reproducibility of the proposed methods with the reproducibility of manual segmentation. Our findings show that the performance of automated classification, in terms of agreement with manual delineation, was improved by 1) using a new 3D morphological feature, the distance to the flow divider, 2) using linear intensity scaling for the normalization of the images, and 3) using a refined training data based on the intersection of two manual reads. Based on scan-rescan data and image analysis, it was demonstrated that automated plaque analysis was more reproducible than manual image review.

Two 3D morphological features, distance to the flow divider and the angle to the ECA, were introduced in this study. These features provide spatial information of a pixel inside the vessel with respect to the bifurcating structure of the carotid artery. The aim of these features is to mimic the behavior of a radiologist. An expert radiologist is able to combine the image contrast and the prior knowledge of the predilection sites where atherosclerotic lesions frequently develop to determine the plaque composition. The performance of the classifier was improved by the addition of the 3D distance to the flow divider feature. This result shows that plaque formation occurs more frequently near the area of the flow divider. This observation is in line with our expectation from literature. The performance of the classifier did not improve by adding the other 3D feature, the angle to the ECA, indicating that plaque was not concentrating at a particular location along the circumferential direction. This observation is inconsistent with our expectation, which might be associated with the presence of a considerable amount of small plaques in addition to large plaques in the current data. It can be observed from the annotated carotid images that large plaques are located far away (at around 180°) from the ECA in most cases, however, for small plaques, no angular preference of location is observed.

The choice of intensity normalization plays an important role in in vivo atherosclerotic plaque segmentation. Intensity normalization is needed to allow comparison of signal intensities from different images. We compared the classification agreements resulting from several normalization approaches applied to the same dataset. It was shown that using the nScaling approach, rather than the nROI approach which is often used in other studies, resulted in the best agreement, which was indicated by the highest Dice of lipid, calcification and loose matrix.

The nROI approach [38] is based on the assumption that the median signal intensity of a 4×4 cm² ROI centered at the carotid artery is similar to the signal intensity of the adjacent SCM. This signal intensity of the muscle is frequently used as reference value during the manual segmentation procedure. The nROI might therefore be a reliable surrogate for the SI of the SCM. To test this assumption, Liu et al [38] calculated the ratio between the SI of the SCM and the median SI of the ROI, and took the average in five contrast weightings: T1w, T2w, PDw, TOF and T1w post contrast. The mean ratio was equal to 1.07 (± 0.11). In our data, the ratio between the median SI of SCM, obtained using the SCM contours, and ROI was 1.40 (± 0.32) in T1w, 1.15 (± 0.22) in T2w, 1.49 (± 0.37) in PDw, and 1.01 (± 0.18) in TOF, showing that for the T1w and PDw images, the median SI of the nROI was not similar to the SI of the SCM. The difference in SI ratios between our study and Liu's study might be explained by the differences in the MRI protocol and differences in intensity inhomogeneity correction by the MRI scanner. We would expect that the classifier based on nSCM

would provide a better result of Dice in comparison with the nROI approach, which was not the case for our data. Therefore, using only the muscle as reference might not be sufficient for manual segmentation, and possibly, the radiologist compares the intensity of the lesion to that of the muscle and the surroundings (such as fibrous tissue in the vessel wall) to characterize plaque composition.

The Dice for nDonut was higher than the Dice for nROI, which was in agreement with our expectation. Compared to nROI, the donut region contains more anatomical information, and more importantly, the region of the diseased vessel was removed, so the normalization would not be affected by different degrees of pathology. The nManuFibrous approach performed better than nDonut, as shown in Figure 7.5. The higher score for nManuFibrous suggests that during image review, the observer uses the intensity of the normal vessel wall as reference for determining the component type of a suspect lesion according to its relative intensity (e.g. hyper-, hypo-, or iso- intensity compared to the fibrous tissue). However, in practice, the nManuFibrous approach is not feasible as it requires prior knowledge of the regions of fibrous tissue. Instead we evaluated the nAutoFibrous approach in which the automated classification of fibrous tissue obtained in an initial processing step was used for normalization. The nAutoFibrous however resulted in the lowest Dice of all normalization approaches, which was most likely due to inaccuracies in the fibrous region detection in the initial multiclass classification and the usage of misclassified fibrous tissue containing multiple plaque components to generate the normalization factor for reclassification in the second step.

The best Dice was obtained using nScaling which used the same ROI as the nDonut approach but used a range scaling process based on mapping the lower and higher percentiles of the ROI intensity histogram to a standard minimum and a maximum instead of dividing all signal intensities by the median value.

Another improvement in agreement was achieved by using the refined training data. The refinement was performed by taking the intersection of the manual segmentations of the first read and second read to generate the training samples. Using this approach unreliable training samples were discarded. These samples were pixels that had a different class label between reads and were mostly located near the lumen or outer wall contour or at the boundaries of issue types. As pixels near region boundaries may suffer from partial volume effect, they are not representative of any single tissue type and will have a negative impact on deriving the spectral characteristics of the classes. Similarly, pixels that are labeled as different plaque components in the repeated reads are atypical of the class they are supposed to represent. By training the classifier on the intersection of the segmentation of two reads, the result produced by the automatic classification would not be biased towards the opinion of any single interpretation.

The final classifier, which used the improved algorithm through integration of the most effective elements: 3D distance to the flow divider feature, linear intensity scaling for image normalization and refined training data, significantly outperformed the base classifier.

Previous studies [37, 38] used the correlation coefficient between the absolute (or relative) component areas segmented by the classifier and the observer to evaluate the segmentation agreement, which provided the measurement of the size differences but not the difference in location. Instead, we utilized the 2D Dice to quantify the classification agreement on a pixel-by-pixel basis within a slice. We were not able to compare our scores to the results in other studies [37, 38] which calculated the component area ICC. Nevertheless, our scores were calculated based on metrics which were more sensitive to reflect

improvements in classified regions on a slice level.

To be able to perform a comprehensive validation of the automatic classification method not only the classifier's automated-manual agreement but also the classifier's reproducibility should be assessed. Manual segmentation was considered to be the gold standard for evaluating the automatic classification method as histology was not available. Therefore, the measurement of the agreement of the classifier was also dependent on the manual segmentation. Figure 7.7 shows that the agreement between the repeated manual delineations was higher than the agreement between the manual and automatic segmentation. However, Figure 7.8 shows that the automatic classification method was more reproducible than the manual annotation in the setting on the analysis of scan-rescan image data. Although the observer was reproducible in repeatedly segmenting the same images, the reproducibility of manual segmentation on the scan-rescan images was much lower. The automatic classifier, which learned from the expert's experience and strictly follows the classification rules based on the multi-contrast properties of the classes, was more robust to changes in the rescan image. As such, the classifier was more reproducible in scan-rescan area measurements of tissue components.

One limitation of this study is that there is no histology information to train and evaluate the automated classifier. The performance of the supervised classification is compromised by the limited accuracy of the manual segmentation. However, we used the well-documented manual plaque segmentation criteria which have been validated against histology, and we also assessed the reproducibility of automated classifier.

In conclusion, this study demonstrates that the agreement of automatic atherosclerotic plaque classification can be significantly improved by using a 3D morphological feature, normalization based on intensity scaling within a donut-shaped region, and refined training data. Furthermore, we showed that automatic classification can be more reproducible than the manual segmentation of the scan-rescan images. Therefore, automatic atherosclerotic plaque classification is a promising technique to provide anatomical and morphological clinical data complementary information to improve risk stratification, evaluate treatment strategies and monitor disease progression.

Acknowledgements

This study was funded by the Dutch Technology Foundation STW, which is the applied science division of NWO as part of project CARISMA 11631 "Automated carotid plaque analysis from quantitative MR imaging".

Chapter 8

Evaluation of multicontrast MRI including fat suppression and inversion recovery spin echo for identification of intra-plaque hemorrhage and lipid core in human carotid plaque using the mahalanobis distance measure

This chapter was published in:

B. C. te Boekhorst, R. van 't Klooster, S. M. Bovens, K. W. van de Kolk, M. J. Cramer, M. F. van Oosterhout, P. A. Doevendans, R. J. van der Geest, G. Pasterkamp, C. J. van Echteld. Evaluation of multicontrast MRI including fat suppression and inversion recovery spin echo for identification of intra-plaque hemorrhage and lipid core in human carotid plaque using the mahalanobis distance measure, *Magnetic Resonance in Medicine*, Volume 67, Issue 6, Pages 1764–1775, 2012.

Abstract

Intra-plaque hemorrhage (IPH) and lipid core, characteristics of rupture prone carotid plaques, are often visualized *in vivo* with MRI using T1 weighted gradient and spin echo, respectively. Increasing magnetic field strength may help to identify IPH and lipid core better. As a proof of concept, automatic segmentation of plaque components was performed with the Mahalanobis distance (MD) measure derived from image contrast from multicontrast MR images including inversion recovery spin echo and T1 weighted gradient echo with fat suppression. After MRI of nine formaldehyde-fixated autopsy specimens, the MDs and Euclidean Distances between plaque component intensities were calculated for each MR weighting. The distances from the carotid bifurcation and the size and shape of calcification spots were used as landmarks for coregistration of MRI and histology. MD between collagen/cell-rich area and IPH was largest with inversion recovery spin echo (4.2/9.3, respectively), between collagen/cell-rich area/foam cells and lipid core with T1 weighted gradient echo with fat suppression (26.9/38.2/4.6, respectively). The accuracy of detection of IPH, cell-rich area, and collagen increased when the MD classifier was used compared with the Euclidean Distance classifier. The enhanced conspicuity of lipid core and IPH in human carotid artery plaque, using *ex vivo* T1 weighted gradient echo with fat suppression and inversion recovery spin echo MRI and MD classifiers, demands further *in vivo* evaluation in patients.

8.1 Introduction

Clinically, the degree of stenosis, which is generally identified by angiography, is often used as a marker for plaques that may give rise to clinical symptoms. However, lumenography is regarded to be insufficient for identification of vulnerable plaques for two reasons. Outward remodeling with preservation of lumen size is a characteristic of vulnerable plaques but cannot be identified with lumenography [133]. Second, plaque composition rather than lumen size appears to determine plaque vulnerability. For identification of high-risk carotid artery plaque not only the classical markers of plaque vulnerability—large lipid core (LC), a thin fibrous cap [134], and abundance of macrophages [135] but also intra-plaque hemorrhage (IPH) has been recognized as an important predictor of major clinical events, e.g., transient ischemic attack or stroke [111, 118, 136]. MRI is the most promising technique for visualization of these plaque markers, because each plaque component generates unique MR contrast in various MR acquisitions, the technique is noninvasive and depicts the anatomy of the vessel. A substantial number of studies have been reported on carotid artery plaque MRI both *ex vivo* [104, 115, 137–139] and *in vivo* [118, 123, 136, 140–142]. In most studies, multicontrast weighted MRI is used for characterization of carotid atherosclerotic plaque. In particular, reports have stressed the importance of T2 weighted (T2w) spin echo (SE) sequences for differentiation between LC and fibrous tissue [115]. More recently, T1 weighted fast SE and gradient echo (GE) imaging have gained interest, because these sequences may lead to better visualization and bright depiction of IPH [111, 118, 136] and LC [11, 23, 140].

With the advent of clinical high field magnets (7 T), interest in the possibilities for *in vivo* carotid artery imaging at high field strength has grown. Higher field magnets bring the advantage of increased SNR or the possibility to increase resolution. Unfortunately, adjustments to MR sequences or development of novel methods are necessary, as T1 of a particular tissue increases with increasing field strength, while T2 decreases, necessitating adjustment of MR sequences to generate optimized contrast. Inversion Recovery Spin Echo (IR-SE) has a larger potential for visualization of T1 differences than nonprepared T1 weighted SE or GE [143]. Possibly, sharp delineation of IPH, characterized by short T1, and differentiation from adjacent stable plaque components at higher field will be better with the IR-SE technique than with the nonprepared SE or GE technique.

Additionally, early studies have revealed that chemical shift imaging of lipid, aimed at the narrow frequency range of methylene protons within adipose tissue, could visualize LC [144, 145]. At 9.4 T, T1 weighted GE with chemically selective fat suppression (FS), aimed at the same frequency range as in the mentioned studies, allowed for better delineation of LC than T1 weighted GE without this FS [146].

To objectively compare the image contrast between different plaque components amongst different MR sequences, techniques are needed that can quantify image contrast, based on absolute signal levels, which may vary across platforms and with coil configurations. Moreover, such statistical measures can be used in conjunction with pattern recognition techniques to enable automatic segmentation of plaque components based on their signal characteristics. In a number of studies, the Euclidean Distance (ED) measure is used for identification of plaque components (9). An important drawback of the ED is that the measure cannot be used to compare differently scaled signals from different domains (in this particular case: contrast weightings). The Mahalanobis Distance (MD) measure is scale-invariant and takes into account correlation of the data [147, 148], enabling comparison of image contrast between different MR sequences.

Table 8.1: MR acquisition parameters

MR weighting	T1w	T1wFS	PDw	T2w FSE		IR-SE	IR-SE	IR-SE
	GE	GE	FSE	(intermediate TE)	(long TE)	(TI = 400 ms)	(TI = 1000 ms)	(TI = 1300 ms)
TR (ms)	300	300	3500	3500	3500	5000	5000	5000
TE (ms)	2.14	2.14	8.53	19.76	37.97	3.10	3.10	3.10
ETL	-	-	8	16	16	-	-	-
Flip angle (°)	60	60	90/180	90/180	90/180	90/180	90/180	90/180
Inversion time (ms)	-	-	-	-	-	400	1000	1300
FOV (mm x mm)	10 x 10	10 x 10	10 x 10	10 x 10	10 x 10	10 x 10	10 x 10	10 x 10
Matrix	256 x 256	256 x 256	256 x 256	256 x 256	256 x 256	256 x 256	256 x 256	256 x 256
Resolution ($\mu\text{m} \times \mu\text{m}$)	39 x 39	39 x 39	39 x 39	39 x 39	39 x 39	39 x 39	39 x 39	39 x 39
Thickness (mm)	0.5	0.5	0.5	0.5	0.5	0.5	0.5	0.5
Number of slices	20	20	20	20	20	1	1	1
Bw (kHz)	152	152	152	152	152	200	200	200
Fat suppression	-	+	-	-	-	-	-	-
NEX	50	50	50	50	50	6	6	6
AT (h:mm:ss)	1:04:00	1:04:00	1:33:20	0:46:40	0:46:40	2:08:00	2:08:00	2:08:00

ETL: echo train length; FOV: field of view; Bw: bandwidth; NEX: number of excitations; AT: acquisition time.

The first objective of this study is to investigate the added value of IR-SE and T1 weighted GE with FS (T1wFS) to multicontrast weighted MRI at high field for identification of unstable plaque components.

The second objective of this study is to compare the MD to the ED between various human carotid plaque components on various MR weighted images. We hypothesize that automated plaque classification using a MD measure may result in improved assessment of plaque components, when compared with the ED measure.

8.2 Materials and methods

MRI

Nine carotid artery specimens (including bifurcation), obtained at autopsy, were 4% formaldehyde fixated and stored at 4°C for at least 48 h. Samples were rewarmed to 37°C before and kept at 37°C during imaging. This set of carotid artery specimens was used as the study set.

The artery samples were imaged in a vertical 9.4 T, 89 mm bore size magnet equipped with 1500 mT/m gradients and connected to an Avance 400 MR system (Bruker BioSpin, Ettlingen, Germany) using a quadrature-driven birdcage coil with an inner diameter of 10 mm. Care was taken to remove any air bubbles.

During a couple of pilot experiments at 9.4 T inversion time (TI) was varied and contrast between regions which were assumed to contain collagen (fibrous cap) and regions which were assumed to contain IPH was optimized, while nulling the regions which were assumed to contain collagen. After some cycles of optimization, these imaging results corresponded with histology. The same holds true for the chosen pulse repetition time (TR) for the T1w GE and the echo time (TE) for the T2w fast spin-echo sequence. During these pilot experiments, we found that contrast on T1w fast spin echo (FSE) showed no contrast difference, when compared with T2w FSE with intermediate TE. Therefore, we performed T1w GE which showed apparently different contrast. Eventually, we came up with the next panel of six MR sequences: T1 weighted GE with (T1wFS) and without FS (T1w), proton density weighted (PDw), FSE, T2w FSE with intermediate and long TE and IR-SE. For all acquisition parameters, see Table 8.1.

T1 and T2 measurements of fresh and formaldehyde 4%-fixated femoral artery plaque

The T1 and T2 measurements were arranged to compare T1 and T2 values of plaque components of fresh plaque to formaldehyde-fixated plaque and because of the large differences between reported plaque component T1 and T2 values. Thus, we aimed at useful application of sequences to the clinical in vivo situation at ultra-high field. Adjustment of in vitro protocols to the in vivo situation could be based on the differences in T1 and T2 between fresh and formaldehyde-fixated material. For this reason, we performed T1 and T2 measurements on fresh femoral artery plaque components both before and after formaldehyde fixation. Three diseased femoral arteries were freshly obtained following surgery, immediately warmed to 37°C and imaged. T1 was obtained from a series of IR images with increasing TIs (20 ms-8000 ms) and a TR of 9500 ms. T2 was obtained from a series of images obtained with a single-slice multiecho imaging sequence with incremented TEs (4-100 ms) and a TR of 5000 ms. After T1 and T2 measurements (duration 2 h), samples were formaldehyde 4% fixated, stored at 4°C. Forty-eight hours later, T1 and T2 measurements were repeated at exactly the same slice position using visual landmarks based on plaque and wall morphology.

Histology

Carotid and femoral artery specimens were decalcified by submersion in ethylenediamine tetra-acetic acid for 24 h and embedded in paraffin. A total of 10 μ m axial sections were cut at 0.5 mm intervals. Hematoxylin & eosin and collagen stainings with Picrosirius red were performed. Photographs of stained slices (jpeg format) and MR data (ParaVision 4.0 (Bruker Biospin, Ettlingen, Germany) converted to DICOM format) were manipulated with ImageJ software (W. Rasband, version 1.29, National Institutes of Health, Bethesda, Maryland, USA). On every histological slice for each recognizable plaque component, a region of interest (ROI) was traced. All histological slices were evaluated by a research physician experienced in histopathology, and unambiguous ROIs representing the following plaque components (“truth regions”), were delineated: LC, IPH, collagen, cell-rich area, foam cells, and calcification. Necrotic areas with cholesterol crystals were identified as LC. Areas with (remnants of) erythrocytes and fibrin strands on Hematoxylin & eosin staining were identified as IPH. Closely packed spindle-shaped cells and high densities of nuclei (both smooth muscle cells and fibroblasts) in the fibrous cap of plaque were identified as cell-rich areas. Closely packed purple/red strands on Picrosirius Red staining were identified as collagen. Lipid-laden round cells on Hematoxylin & eosin staining were identified as foam cells.

Image processing and manual image segmentation

Image segmentation was performed using histology assisted tracing with VesselMass software (LKEB, Leiden, Netherlands) and subsequently statistical analysis was performed using Matlab (The Mathworks, Natick, Massachusetts, USA). The truth regions served as user input and represent the various “classes” or plaque components.

We used the distance from the carotid bifurcation and the luminal shape and unique morphology and size of calcification spots as visual landmarks for longitudinal matching of MRI with histology. The luminal shape and morphology and size of calcification spots

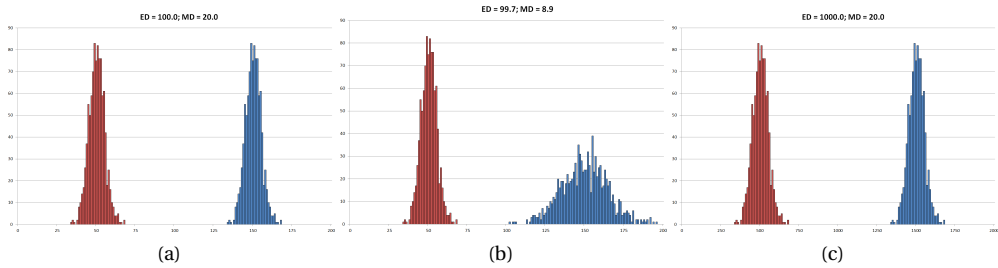


Figure 8.1: The influence of the distribution width (a versus b) and scaling (a versus c) of artificial data with a normal distribution on MD and ED.

were used for correction of orientation and axial matching of MRI with histology. Twenty-three histological carotid artery sections and six femoral artery sections could be matched to MR images. After correction of orientation, ROIs were copied from histological images to longitudinally matching MRI slices and proportionately up-scaled to MR images, accounting for both deformation in the x and y direction in the axial plane. For MR images of femoral artery plaque representing the T1 and T2 measurement data sets, the mean absolute signal intensities of the ROIs were plotted against TI or TE. Mono-exponential recovery functions were fitted to the T1 data sets and mono-exponential decay functions were fitted to the T2 data sets to obtain the T1 and T2 values, respectively.

Calculation of MD

Quantification of image contrast between different plaque components can be achieved by calculating the intensity-based distance between the two classes. For each MR sequence, the signal intensities of the various plaque components were determined, and the distance was calculated for all available pairs of plaque components. In this study, the MD metric is used. MD measures the separation of two groups of objects and takes into account correlations of the data set (Fig. 8.1a,b). Moreover, it is scale-invariant (Fig. 8.1a,c), so tissue-independent variation of the MR signal will not affect MD and MD may allow for differentiation of classes based on variably scaled parameters created by different imaging modalities.

The plaque region is described by a group of image locations (pixels). For each pixel, the signal intensities of multiple MR sequences are available. So, each image pixel x corresponds to a vector containing the signal intensities of the different MR sequences. The MD between two plaques, i.e., groups X_i and X_j with group means \bar{x}_i and \bar{x}_j , is given as a matrix calculation in Eq. 8.1 X_i contains all image pixels x of group i .

$$MD_{ij} = \sqrt{(\bar{x}_i - \bar{x}_j)^T S^{-1} (\bar{x}_i - \bar{x}_j)} \quad (8.1)$$

where:

T = matrix transpose

S^{-1} = Inverse of the pooled covariance matrix of the two groups; this matrix is computed as the weighted average of the two covariance matrices.

As a reference, the equation of the ED between two groups is given:

$$ED_{ij} = \sqrt{(\bar{x}_i - \bar{x}_j)^2} \quad (8.2)$$

MDs of all selected ROIs were pooled per weighting and per pair of components. The MR weighting leading to the highest pooled MD was determined for pairs of plaque components including both an established stable and unstable plaque component (lipid core-cell rich area, lipid core-collagen, IPH-cell rich area, IPH-collagen, foam cells-cell rich area, and foam cells-collagen) and for the pair lipid core-foam cells.

Automatic segmentation of plaque components

Three carotid artery samples were used to perform two segmentation experiments. In these experiments, a MD classifier and an ED classifier were used to segment plaque areas. The classifier was trained by the histology assisted traced truth regions.

1. Each carotid artery sample consisted of four slices. A Mahalanobis [147] and an Euclidean classifier were trained on three slices and then applied to the fourth slice for automatic segmentation of the plaque components on a pixel-by-pixel basis. This process was repeated for each carotid artery sample resulting in three automatically segmented slices (one for each carotid artery sample).
2. The slices of the three carotid arteries, in total 12 slices, were pooled to create a training set of 11 slices and a test set of one slice. Again, a Mahalanobis and an Euclidean classifier were trained and applied on the test set. For each carotid artery sample, the slice of the test set was chosen to be the same slice as used in experiment one, but the training set consisted of the other 11 slices. This experiment also resulted in three automatically segmented slices.

An automatic plaque classification experiment with a training set that is fully independent of the test set was not possible due to the limited number of carotid samples containing sufficient plaque components. Segmentation results from both experiments were compared because in both experiments, the same slices were used as test set.

These procedures were executed for various relevant combinations of MR weightings, including T1w/T2w/PDw, (T1wFS/T2w/PDw), T1w/T2w/PDw/IR-SE, T1w/T2w/PDw/T1wFS, and T1w/T1wFS/T2w/PDw/IR-SE.

Sensitivity, specificity, accuracy

The results of the automatic segmentation were compared on a pixel-by-pixel basis to the truth regions of the corresponding slice. Segmentation results from the three carotid artery samples were averaged for each experiment to determine the sensitivity and specificity of the classifier for each plaque component. Sensitivity is defined as: the number of pixels correctly labeled by the classifier as tissue x (true positive pixels) divided by the total number of pixels labeled tissue x as determined by histological review. The percentage false negative pixels is $(100 - \text{sensitivity}(\%))$. Specificity is defined as the number of pixels correctly excluded by the classifier from tissue x (true negative pixels) divided by the total number of pixels excluded from tissue x as determined by histological review. The percentage false positive pixels is $(100 - \text{specificity}(\%))$. The accuracy was calculated as the total number of pixels correctly labeled by the classifier divided by the total number of pixels analyzed.

Table 8.2: T1 and T2 values of fresh and 4% formaldehyde-fixed atherosclerotic human femoral artery plaque components at 9.4 T and at 37°C

Plaque component	Fresh in PBS	4% formaldehyde-fixed	Fresh in PBS	4% formaldehyde-fixed
	T1 (ms)	T1 (ms)	T2 (ms)	T2 (ms)
IPH (old)	827 ± 296	793 ± 158	4.6 ± 0.11	10.9 ± 2.30
IPH (recent)	982 ± 246	833 ± 139	12.1 ± 1.05	15.0 ± 2.15
Lipid core	1110 ± 171	1035 ± 105	10.6 ± 1.97	13.3 ± 2.40
Foam cells	1230 ± 300	1150 ± 62	12.4 ± 1.88	17.4 ± 2.91
Cell rich area	1538 ± 386	1446 ± 41	28.9 ± 3.81	33.4 ± 4.72
Collagen	1578 ± 440	1548 ± 88	25.6 ± 5.82	30.3 ± 3.12

PBS: phosphate buffered saline.

Data are expressed as mean ± SD of three measurements of three sets of components from three plaques.

Thrombus was only encountered in one of these plaques.

8.3 Results

T1 and T2 Measurements of Fresh and 4% Formaldehyde Fixed Plaque

T1 and T2 values measured in fresh and 4% formaldehyde fixed plaque are listed in Table 8.2. T2 values of all components in freshly obtained plaque were shorter when compared with 4% formaldehyde fixed plaque. T1 values of all components in freshly obtained plaque were longer when compared with 4% formaldehyde fixed plaque.

Visual inspection of mri of carotid plaque

LC and IPH are visualized best with T1wFS and IR-SE, respectively (Figs. 8.2 and 8.3). T1wFS creates largest contrast between LC (dark) and other plaque components including foam cells (brighter). IR-SE shows largest contrast between IPH (bright) and other plaque components (darker).

Calculation of the MD

Figure 8.4 shows the mean absolute signal intensities of the ROIs corresponding with plaque components for various carotid artery samples. Samples show large variations of intensities per plaque component and per MR weighting. The diversity of composition of an agreed distinct plaque component like LC or IPH, additional to day-to-day differences of shim settings may cause these variations. However, the relative intensity differences between plaque components are similar per MR weighting (Fig. 8.4).

Calcification has low signal intensity on all MR weightings. IPH has high signal intensity on IR-SE (TI = 1000 ms) images, while other plaque components show lower signal intensities on these images. Cell-rich areas have high signal intensity on PDw images, while other plaque components have lower signal intensities on these images.

On every histological slice for each recognizable plaque component, a ROI (truth region) was traced, and the mean signal intensities for the ROIs were calculated for each of the different MR contrast weightings. By calculating the MD for each pair of plaque components per MR weighting, a characteristic signature for each plaque component could be determined. Pooled MDs are shown in Figure 8.5. IR-SE with TI = 1000 ms leads to larger MD between collagen or cell-rich area and IPH (4.2 and 9.3, respectively), when compared with other MR sequences. T1wFS appears to lead to larger MD between LC and foam cells

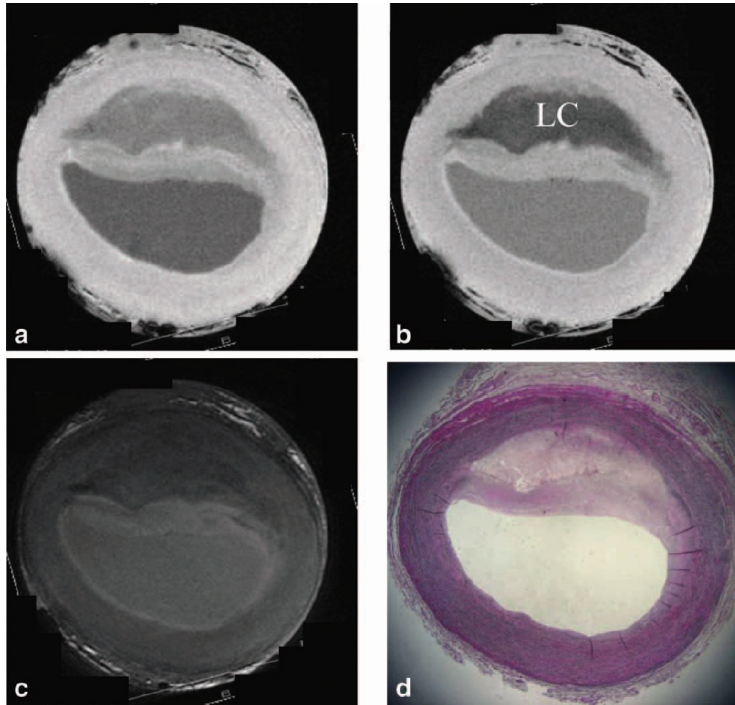


Figure 8.2: MRI and histology of carotid artery plaque with a large LC: (a) T1w, (b) T1wFS, (c) T2w, and (d) EVG staining. Conspicuity of LC is enhanced on T1wFS, when compared with T1w.

or cell rich areas or collagen (4.6, 38.2, and 26.9, respectively), when compared with the other sequences (Fig. 8.5).

An example of discrimination between lipid, cell rich area, and collagen using both the ED and the MD is shown in Fig. 8.6. In the presented case, the MD is better able to discriminate between different plaque components than the ED. Consequently, in this particular case, the MD metric is preferred to the ED.

Figure 8.7 shows the correspondence of truth regions and automatically segmented regions in one carotid artery sample after training on three, the first segmentation experiment, and after training on 11 pooled slices, the second segmentation experiment.

The sensitivity/specificity/accuracy of detection of various plaque components (LC, IPH, cell rich area, and collagen) achieved with various sets of MR weightings is reported in Table 8.3 for the first segmentation experiment, and Table 8.4 for the second segmentation experiment, using both the MD- and ED-based classifier.

Segmentation results; First experiment

Large LC in the absence of IPH was easily distinguished with T1w, T2w, and PDw imaging, while the sensitivity of the detection of LC in the presence of IPH was greatly improved by replacement of T1w with T1wFS and addition of IR-SE to the standard clinical set of MR

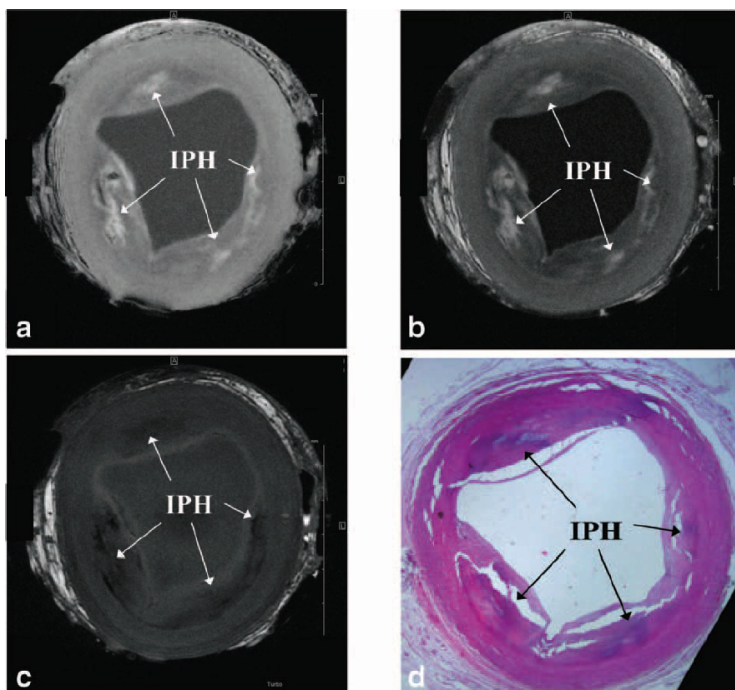


Figure 8.3: MRI and histology of human carotid atherosclerotic plaque with multiple regions of IPH: (a) T1w, (b) IR-SE (TI = 1000 ms), (c) T2w with intermediate TE, and (d) Hematoxylin & eosin staining. Arrows indicate IPH. T1w and IR-SE image show bright regions in the plaque corresponding with IPH. IPH on T2w image is dark. IR-SE image shows highest contrast of IPH.

Table 8.3: Sensitivity, specificity, and accuracy of the first segmentation experiment (see text for details) of various plaque components achieved with various sets of mr weightings using a mahalanobis distance- and an euclidean distance-based classifier

Plaque component	Set of MR weightings	Mahalanobis distance			Euclidean distance		
		Sensitivity (%)	Specificity (%)	Accuracy (%)	Sensitivity (%)	Specificity (%)	Accuracy (%)
Lipid core in	T1w/PDw/T2w	75	99	95	76	99	95
presence of IPH	T1wFS/PDw/T2w/IRSE	81	98	95	81	98	95
Large lipid core in	T1w/PDw/T2w	100	99	100	99	99	99
absence of IPH	T1wFS/PDw/T2w/IRSE	100	99	100	99	99	99
IPH	T1w/PDw/T2w	56	97	82	56	97	82
	T1w/PDw/T2w/IRSE	57	97	82	57	97	82
Cell-rich area	T1w/PDw/T2w	87	92	91	89	94	94
	T1wFS/PDw/T2w	89	92	92	91	95	94
Collagen	T1w/PDw/T2w	82	79	80	87	86	86
	T1w/PDw/T2w/IRSE	82	81	82	86	87	87

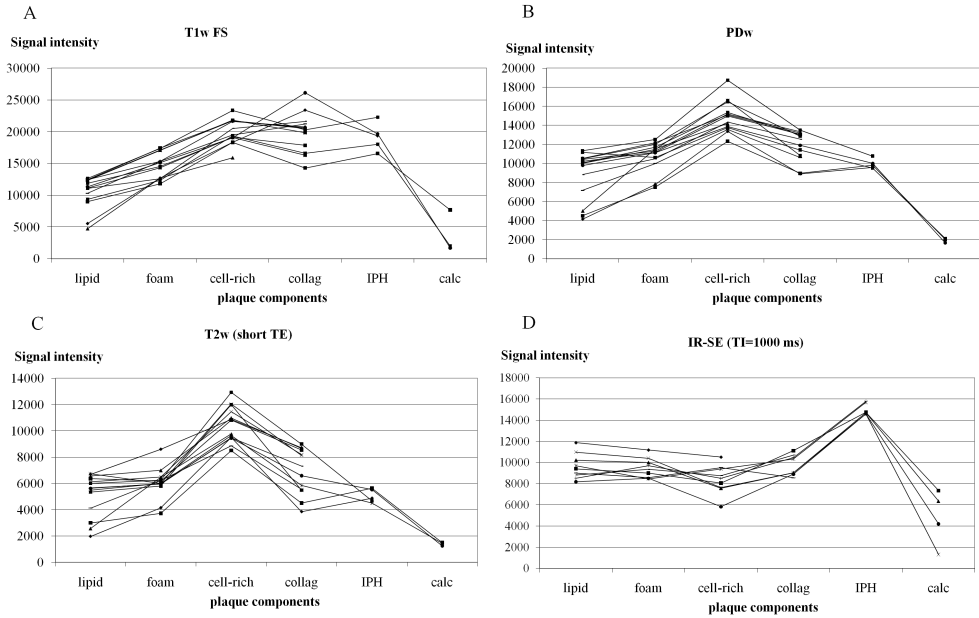


Figure 8.4: Absolute signal intensities (y-axis) of various components (x-axis) on T1wFS (a), PDw images (b), T2w with intermediate TE (c), and IR-SE (with TI = 1000 ms) (d) images.

Table 8.4: Sensitivity, specificity, and accuracy of the second segmentation experiment (see text for details) of various plaque components achieved with various sets of mr weightings using a mahalanobis distance- and an euclidean distance-based classifier

Plaque component	Set of MR weightings	Mahalanobis distance			Euclidean distance		
		Sensitivity (%)	Specificity (%)	Accuracy (%)	Sensitivity (%)	Specificity (%)	Accuracy (%)
Lipid core	T1w/PDw/T2w	79	82	83	63	97	90
	T1wFS/T2w	91	90	91	66	99	93
IPH	T1w/PDw/T2w	49	71	65	50	55	56
	T1w/PDw/T2w/IRSE	50	78	70	50	61	60
Cell-rich area	T1w/PDw/T2w	45	98	84	35	100	84
	T1wFS/PDw/T2w/IRSE	75	95	91	33	100	84
Collagen	T1w/PDw/T2w	44	88	84	65	77	77
	T1w/T1wFS/PDw/T2w/IRSE	55	90	86	65	82	81

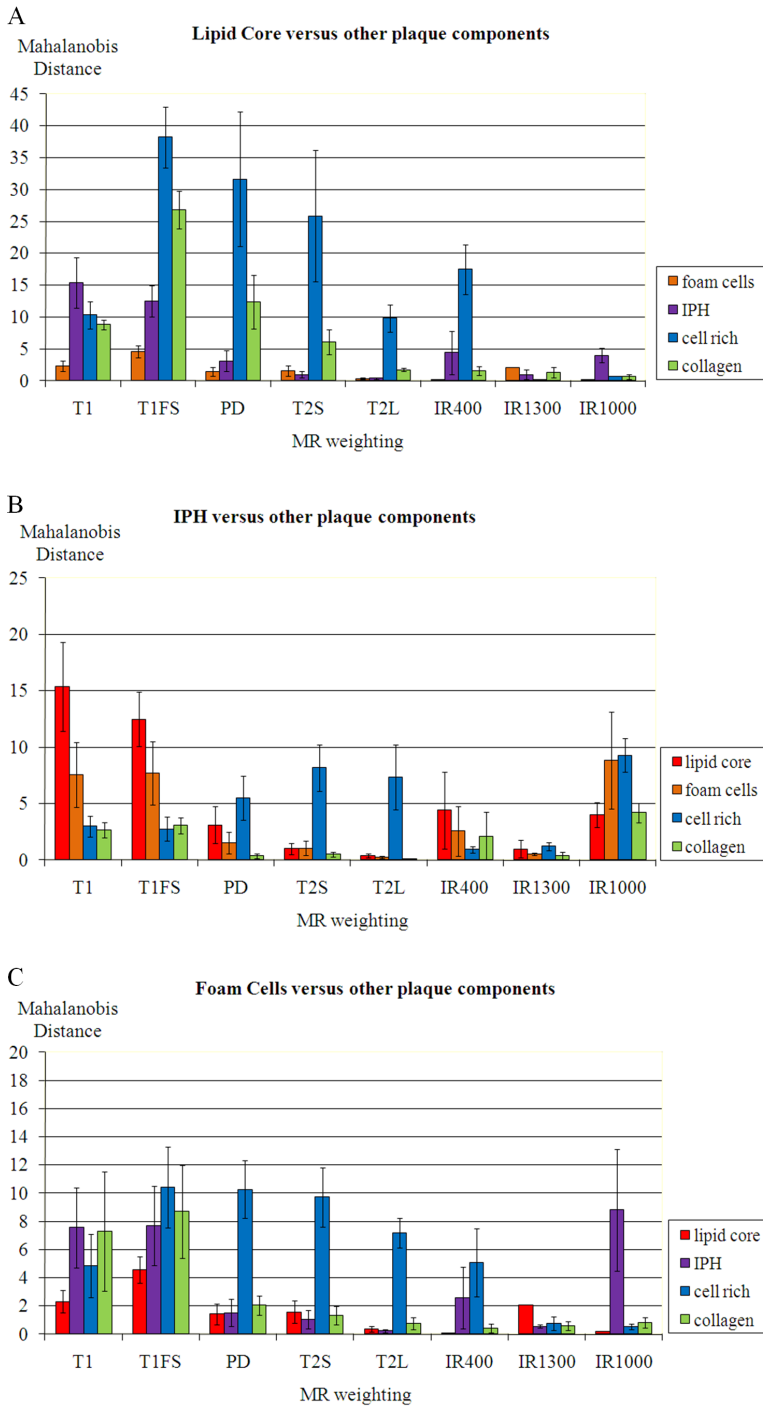


Figure 8.5: MD between vulnerable carotid plaque components and stable plaque components. a) MD between LC and IPH, foam cells, cell rich areas, collagen. b) MD between IPH and LC, foam cells, cell rich areas, collagen. c) MD between foam cells and LC, IPH, cell rich areas, collagen.

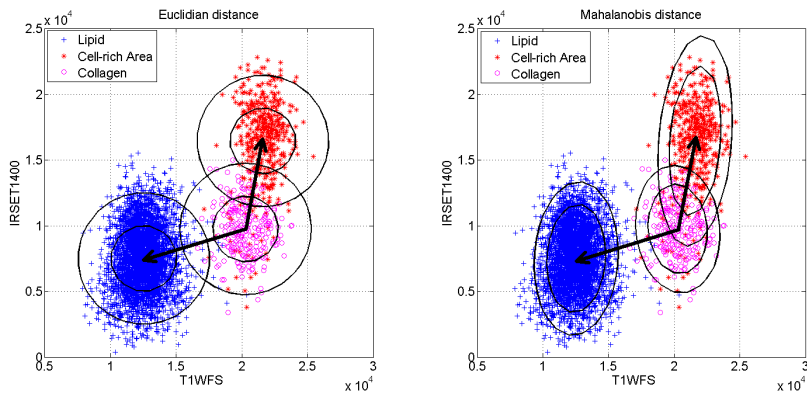


Figure 8.6: ED versus MD of a cloud of data points representing collagen. Each data point represents a pixel. The ED does not take into account the correlation of the data points according to the circular form of the iso-distance lines (a), whereas MD does take into account the correlation of the data points according to the ellipse form of the iso-distance lines (b). The distances between the group centers of collagen and cell rich area and between the group centers of collagen and LC (arrows) represent EDs (a and b). The two EDs measured from collagen to LC and from collagen to cell rich area are nearly similar (a). However, the MD between collagen and LC is larger than the MD between collagen and cell rich area as can be observed from the iso-distance lines in b.

weightings (T1w, PDw, and T2w) (Table 8.3). No differences between results of the first segmentation experiment obtained with ED and MD classifiers were found (Table 8.3).

Segmentation results; Second experiment

Combination of T1wFS with T2w improved the sensitivity, specificity, and accuracy of the detection of LC, when compared with the standard clinical set. The specificity and accuracy of the detection of IPH were improved by the combination of T1w, T2w, PDw, and IR-SE, when compared with the standard clinical set. Sensitivity was improved by replacement of T1w with T1wFS and addition of IR-SE to the standard set of MR weightings. Sensitivity and accuracy were improved by replacement of T1w with T1wFS and addition of IR-SE to the standard set of MR weightings (T1w, PDw, and T2w), with only a minor decrease of specificity. Sensitivity of the detection of collagen was improved by addition of both T1wFS and IR-SE to the standard set of MR weightings (T1w, PDw, and T2w) (Table 8.3).

When the MD classifier in combination with the novel sequence panels was used, the accuracies of detection of IPH, cell-rich area, and collagen were greatly improved with comparable accuracy of detection of LC, when compared with application of the ED classifier (Table 8.3).

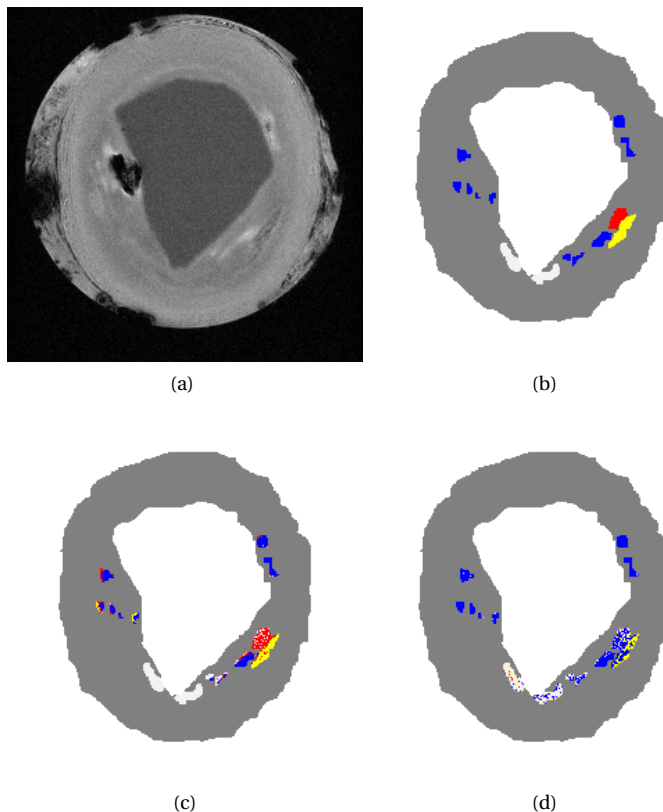


Figure 8.7: a) MR image at one slice level of a carotid artery sample. b) Truth regions drawn on histology and projected to the MR image in a. c) Plaque components assigned to same regions based on the first automatic segmentation experiment. d) based on the second segmentation experiment on a pixel-by-pixel basis by a trained classifier (see text for additional information). Each color represents a different plaque component. Blue: IPH; red: collagen; white: cell rich area; yellow: LC.

8.4 Discussion

With respect to the first objective of this study, we show that addition of IR-SE to a panel of MR weighted sequences (T1w GE, PDw FSE, and T2w FSE) leads to better discrimination between IPH and stable plaque components of formaldehyde-fixed human carotid artery plaque. The addition of FS to T1w GE leads to better discrimination between LC and stable plaque components, including foam cells, when compared with T1w GE without FS.

With respect to the second objective, we have performed two segmentation experiments to compare the MD to the ED between various human carotid plaque components on various MR weighted images. The first experiment shows no superiority of the MD classifier over the ED classifier. Taking into account the advantage of scale-invariance, it will not be a surprise that when the training set belonged to the same carotid artery sam-

ple as the test set, no differences between using MD or ED were found.

The second segmentation experiment reveals that, in case of a partially independent training set, the suggested novel panels of sequences show higher accuracies of detection of IPH, cell-rich area, and collagen using the MD classifier than using the ED classifier. No difference in accuracy was found for the detection of LC.

To our knowledge, a head-to-head comparison between MD and ED classifiers for plaque classification from multicontrast MRI has not been reported. Automated segmentation with the “Mahalanobis distance-based classifier” provides the possibility to categorize characteristics of atherosclerotic plaques in six components. This MD-based classifier is a supervised classification algorithm, which calculates in this study the MD from multicontrast weighted *ex vivo* MR images. Two segmentation experiments were performed. In general, the results for the segmentation based on a training set of three slices from the same carotid artery were slightly better than the experiment where 11 slices from three carotid artery samples were pooled. However, except for the sensitivity of detection of IPH and collagen, results of segmentation using the pooled training set approximate the high values obtained with the first segmentation experiment closely.

T1 and T2 of plaque components

The increase of T1 of tissues with increasing field strength increases the challenge to visualize T1 differences between plaque components at high field. Adjustment of MR sequences to increased field strengths should be based on T1 and T2 values of tissues of interest at those field strengths. However, there are some conflicting data from various reports on the T1 and T2 values of atherosclerotic plaque components at 9.4 T ([115, 149]). Second, previous reports have shown that room temperature and formaldehyde fixation lead to important T2 changes of fibrous plaque ([148]). Unfortunately, for this study, fresh atherosclerotic plaque material was not sufficiently available. We compared T1 and T2 values of femoral plaque components obtained from surgery, measured at 37°C before and after 4% formaldehyde fixation. The large range of T2 values found in literature for a particular plaque component may relate to differences in definition of plaque components on histology and the procedure of T1 and T2 measurement (spectroscopic or using MR imaging) ([11, 138, 150, 151]).

IPH

Differentiation between IPH and stable plaque components, though possible when using T1 weighted MR imaging without inversion-preparation, remains difficult according to the moderate specificity of 74% for the *in vivo* identification of recent IPH in literature [118] which is comparable with this study (specificity 71%) when using the standard set of MR weightings (T1w, PDw, and T2w). However, combination of T1w with inversion recovery SE in this study resulted in an improvement of the specificity by 14%. At 9.4 T, thrombus (= old IPH) T1 was reported to be 1180 ms, whereas T1 of fibrous tissue was reported to be ~ 1800 ms [149]. Application of a method, which is more heavily T1 weighted, like inversion recovery SE could identify IPH with higher specificity. We achieved in this study clear identification of thrombus with inversion recovery SE, as a result of efficient nulling of the signal from stable plaque components. *In vivo* thrombus imaging has been achieved previously with a T1w inversion recovery 3D GE sequence at 1.5 T [14, 152]. However, choices which are made in the *in vivo* situation will be different when compared to

the *ex vivo* situation and the TI in those studies was chosen to null the blood signal at 1.5 T [14, 152], leaving suboptimal contrast between IPH and stable plaque components.

Lipid core

The second component of interest in this study was LC. MRI of LC has shifted from direct lipid imaging with spectroscopic techniques [144, 145] to MRI of the water signal of LC [153]. T1/T2w GE (TR = 35 ms) images at 1.5 T have been reported to show iso- to hyper-intensity of LC [23, 154], but T1w GE images (TR = 300 ms) at 9.4 T have been reported to show iso- to hypo-intensity of LC [146] as is confirmed in this study. The T2 decrease of LC with increasing field, may explain the low signal intensity of LC on T1w images at 9.4 T. Despite the chosen short TE (2.14 ms), LC has lowest signal, when compared with all other components except calcification. Therefore, TE appears to be more signal limiting than TR for T1w GE images, acquired at 9.4 T. The less efficient depiction of LC with T2w and PDw imaging at 9.4 T may be explained by an increase of T1 for both fibrous tissue and LC at higher field strength, resulting in increased saturation of the fibrous tissue when using TR = 3500 ms.

In carotid artery imaging, FS is generally applied to remove strong signals from peri-adventitious fat which could lead to chemical shift artifacts. We showed that LC was visualized more accurately using GE including FS, when compared with GE without FS. FS is thought to have little impact on tissue contrast within atherosclerotic plaque, because lipids found in atherosclerotic plaque consist primarily of cholesteryl esters and free cholesterol and not triglycerides as in perivascular fat [155]. Suppression of the small number of triglycerides in LC with a saturation pulse aimed at the resonant frequency of methylene protons, was surprisingly effective in increasing conspicuity of LC, suggesting an effect on relaxation of nearby water protons.

Contrast-enhanced MRI using small gadolinium chelates has shown capability to differentiate between LC and fibrous cap. Differentiation was evenly possible or better than with T2w imaging [142, 156]. However in these studies, difference in enhancement between fibrous tissue (~80%) and LC (~30%) occurred by virtue of presence of neovascularity in fibrous tissue [142], which may vary among plaques.

Effect of resolution on image segmentation

There is a relation between resolution of MRI and segmentation results. Some plaque components use little space or are mixed up mostly with another component (area of lipid mingled with fibroblasts). At low resolution, these plaque components cannot be distinguished from each other due to partial volume effects. However, at higher resolution, the partial volume effects will be smaller. Due to the trade-off between signal to noise ratio and resolution, and the lower signal to noise per unit of acquisition time at lower field, prolonged scan times are needed to achieve high resolution at lower field. So, differentiation between small foam cell areas, potentially evolving in LC in near future, and LC, and cell-rich areas may be more practical at higher field strength.

One report suggests that an *in vivo* in-plane resolution between 156 and 1250 μm per pixel does not impair classification accuracy of human carotid artery plaque components with MRI [157]. However, the authors also stated that degradation in resolution is most detrimental to plaques with large numbers of components [157]. The thicknesses of tissue layers should at least span one pixel, to differentiate them visually [150]. To prevent over-

estimation of the surface of spot-like plaque components, the diameter should at least span five pixels [150]. Most importantly, one should keep in mind that the classification accuracy depends also on the sizes of component areas delineated on histology. If the delineation of the truth regions has been done in a coarse way, the quality of MR images will also be less demanding.

However, although we have chosen very small truth regions, we have put a mask on the other regions of the carotid plaque and wall layers. We have done this because it would be very time-consuming to categorize the whole plaque and wall area at the resolution of the truth regions. However, higher specificity, sensitivity, and accuracy are easier to achieve this way than for the whole area including more ambiguous regions.

MD-based classifier

In this study, segmentation of plaque components was done with a supervised classification algorithm, the “Mahalanobis Distance classifier”. Validated automated classification algorithms help in achieving maximum reproducibility and reliability in longitudinal in vivo plaque characterization studies. Variation in shim settings and coil configuration may cause differences in raw signal intensity of the same plaque component between carotid artery samples and modify contrast between two plaque components. Furthermore, display of the image data may vary due to variety of window level settings and will determine the size of the image contrast between two plaque components. Moreover, postprocessing software often applies contrast stretching or normalization which prevents direct comparison of contrast between various MR weightings. Instead of visual assessment, statistics can be applied to the image data which provide a reproducible and quantitative assessment of the image contrast. The slightly better performance of the MD over the ED with respect to detection accuracies of IPH, cell-rich area, and collagen, using the novel panels of MR sequences suggested in this study, suggests the MD classifier to be preferred over the ED classifier for identification of plaque components by MRI.

When the ED was used in earlier reports, the measured distance was largely influenced by contrast weightings with high average signal intensity instead of contrast weightings with highest image contrast [104]. Earlier reported automatic plaque segmentation methods using a Gaussian classifier have been successfully applied but needed preprocessing which included rescaling of all pixels values to a baseline “iso-intensity” [38]. Others have used specially enhanced cluster analysis [125] or predictive models [158] composed RGB images out of three ex vivo MR sequences by stretching the image contrast of each sequence to an eight-bit color channel. Such a preprocessing step, which can cause loss of data, is not needed in case the MD is used because it is invariant to scaling. However, the segmentation algorithm based on the MD classifier is not as mature as the algorithms that amongst others also take spatial information into account [38, 125, 158].

However, the basic segmentation algorithm showed that the MD is preferred over the ED because it is invariant to scaling and takes into account the covariance among the variables. Therefore, it could be a better metric for comparison of outcomes of various MR weightings than the ED and may compare the same MR weightings obtained at another MR laboratory without influencing classification results. Therefore, classification algorithms based on MD may be used for multicenter trials focused on longitudinal plaque characterization and MD is even suitable for comparison of different imaging modalities [159, 160].

Limitations

There are a number of limitations to this study. Clinical *in vivo* MRI of carotid arteries is complicated by decreased resolution, motion artifacts, signals from flowing blood, and greater spatial variability in MR signal due to the use of surface coils. The automated classification method for detection of plaque components has not been applied to *in vivo* data in this study.

The acquisition time of the IR-SE sequence was very long and can certainly be shortened by a multislice FSE instead of a single-slice SE approach and the use of phased-array surface coils and multiple receivers. The IR-SE sequence was not compared with the direct thrombus imaging method of Moody et al. [14]. For *in vivo* experiments, incorporation of a double IR module into the IR-SE used in this study will lead to dark blood images. This method might stand the competition with the direct thrombus imaging method of Moody et al. [14] in the *in vivo* situation; however, this has yet to be studied.

Performance of the classifier needs to be checked for MR images with lower SNR or lower resolution, obtained within clinically realistic acquisition times. Lower resolution will come with shorter acquisition times at the same SNR. At the high in-plane resolution in this study, the truth regions chosen with scrutinized microscopy were also very small. Perfect matching between histology and MRI is always difficult, but with the small truth regions used in this study it even became more challenging. Furthermore, the sample size was limited and so was the number of carotid artery sections with IPH. Only old IPH and not fresh/recent IPH were found in this data set because the carotid artery samples were not obtained from surgery but from autopsy. Second, due to the small number of carotid artery sections, a real classification experiment using an independent training set and test set could not be performed. Instead, automatic segmentation based on adjacent slices of the same carotid artery sample and segmentation based on a combination of slices from different carotid artery samples was performed. Third, because of the use of novel sequences and the small number of carotid samples, automatic segmentation was only performed for small regions corresponding to histological truth regions and not for the entire plaque. To verify the ability of the automated classification method to characterize also regions with ambiguity with respect to the type of plaque component, additional research is needed using a larger number of carotid artery samples.

8.5 Conclusions

In conclusion, identification of LC and IPH in human carotid artery plaque was improved *ex vivo* at 9.4 T with two clinically not commonly used MRI techniques, T1w GE with FS and IR-SE (TI = 1000 ms). Results of *in vivo* application of these MRI techniques will have to be awaited. Automatic plaque segmentation using a supervised classification algorithm based on the MD was feasible and led to slightly better accuracy of identification of IPH, cell-rich area, and collagen, showing promise for the MD metric in multicenter trials on longitudinal plaque characterization.

Chapter 9

An objective method to optimize the MR sequence set for carotid plaque classification using automated image segmentation

This chapter was published in:

R. van 't Klooster, A.J. Patterson, V.E. Young, J.H. Gillard, J.H.C. Reiber, R.J. van der Geest. An Objective Method to Optimize the MR Sequence Set for Plaque Classification in Carotid Vessel Wall Images Using Automated Image Segmentation, *PLOS ONE*, DOI: 10.1371/journal.pone.00784922013, 2013.

Abstract

A typical MR imaging protocol to study the status of atherosclerosis in the carotid artery consists of the application of multiple MR sequences. Since scanner time is limited, a balance has to be reached between the duration of the applied MR protocol and the quantity and quality of the resulting images which are needed to assess the disease. In this study an objective method to optimize the MR sequence set for classification of soft plaque in vessel wall images of the carotid artery using automated image segmentation was developed. The automated method employs statistical pattern recognition techniques and was developed based on an extensive set of MR contrast weightings and corresponding manual segmentations of the vessel wall and soft plaque components, which were validated by histological sections. Evaluation of the results from nine contrast weightings showed the tradeoff between scan duration and automated image segmentation performance. For our dataset the best segmentation performance was achieved by selecting five contrast weightings. Similar performance was achieved with a set of three contrast weightings, which resulted in a reduction of scan time by more than 60%. The presented approach can help others to optimize MR imaging protocols by investigating the tradeoff between scan duration and automated image segmentation performance possibly leading to shorter scanning times and better image interpretation. This approach can potentially also be applied to other research fields focusing on different diseases and anatomical regions.

9.1 Introduction

A multi-sequence MRI protocol is widely used to investigate the status of atherosclerosis in the carotid artery. Atherosclerosis is a progressive disease which, at an early stage, is characterized by vessel wall thickening causing outward remodeling, followed by narrowing of the lumen, and at a later stage by the formation of different plaque lesions inside the vessel wall [161]. Identification of vulnerable plaques, lesions with a high risk to rupture, before the development of cardiovascular events, is of high clinical relevance. These lesions are typically soft and contain a large lipid-rich necrotic core (LR/NC) or intraplaque hemorrhage (IPH) [23], which can both be identified by in-vivo MRI [65]. A typical MR imaging protocol for assessment of the carotid artery vessel wall consists of the application of multiple MR sequences to obtain information about the lumen morphology and a detailed characterization of the vessel wall [92].

An optimal in-vivo MR imaging protocol should incorporate contrast weightings that can separate the tissue of interest from surrounding structures, have a sufficiently high spatial resolution and have a short acquisition time. Since scanner time is limited, a balance has to be reached between the number of applied MR sequences and how well different plaque components can be distinguished from each other on the resulting images. Latest developments in this field include the design of new MR pulse sequences, adaptation of existing MR sequences to higher field strength, design of specialized carotid coils and development of 3D isotropic imaging [162]. Consequently, objective evaluation of the resulting images is needed in order to determine the benefits of these continuous technological developments and the corresponding increase or decrease in scan time.

In an earlier work, Zhao et al. [163], presented a method to minimize the number of MR sequences and its impact on manual quantification of plaque lesions in vessel wall MR imaging studies. However, the proposed method has several drawbacks as the method is subjective because sets of different MR sequences are evaluated by the same readers introducing bias of the readers to their previous segmentation result. Also, the number of combinations of sequences that could be evaluated was limited. Cappendijk et al. [94] used a logistic regression model to determine the optimal MR weighting combination for plaque assessment enabling objective assessment of different combinations of sequences. However, assessment was limited to plaque identification; plaque volume was not taken into account. In addition, no relation was shown between the selected combination of MR sequences and the total scan duration. In another study by Liu et al. [38] an automated segmentation algorithm using pattern recognition techniques was applied. In that study the training of the classifier was performed on the same data as for which it was tested rendering subsequent results unreliable. Again, no relation was shown between the selected combination of MR sequences and the total scan duration.

Accordingly, the purpose of this study was to develop an objective method to optimize the MR sequence set for classification of soft plaque in vessel wall MR images of the carotid artery with respect to segmentation accuracy and total scan duration. Instead of using a human observer to investigate different sets of MR sequences and their impact on plaque classification, automated image segmentation was employed which is inherently exhaustive and objective. The method was developed based on an extensive set of MR contrast weightings and corresponding manual segmentations of the vessel wall and soft plaque components, which were validated by histological sections. The proposed method is generic and can also be applied to other fields of research in which multi-spectral image data, such as multi-sequence MRI, is acquired and automated segmentation algorithms

are available.

9.2 Materials and methods

Ethics statement

The study was approved by The Cambridgeshire Three Research Ethics Committee. Written forms of informed consent were obtained from all subjects before imaging. Sharing of image data into the public domain was not permitted in the approved study protocol.

Image data

Fifteen patients (11 male, age range 50-89 years), scheduled for carotid endarterectomy, were pre-operatively scanned using MRI. Color Doppler ultrasound was used for surgical screening to confirm the presence of stenosis >70%. Carotid specimens were retrieved after carotid endarterectomy. The endarterectomy specimens were fixed and cryosectioned to preserve the plaque components. Histological staining was performed with haematoxylin and eosin, elastic Van Gieson and Nile red. The sections were digitized using a conventional microscope at 5X magnification (Leica DM LB2, Leica Microsystems, Wetzlar, Germany). The histological sections were visually matched with the MRI image data. For each patient at least one histological section was available which matched the imaging data. The matching sections served as ground truth for the manual image segmentation.

MR imaging was performed on a 1.5T scanner (Signa HDx, GE Healthcare, Waukesha, WI) using a bilateral four-channel phased-array carotid coil (PACC, Machnet, Eelde, The Netherlands). The subject was positioned in the scanner with the carotid coils placed superficially over the anterior neck to cover the carotid artery centering on the carotid bifurcation. A vacuum constraining pillow system (Vac Lok Cushion, Oncology Systems Ltd, UK) was used to restrict head and neck movement.

In total six MR sequences were acquired from which nine contrast weightings were extracted. A 2D time-of-flight (TOF) angiography sequence was employed to identify the diseased segment and the position of the bifurcation. High-resolution multi-contrast axial images were obtained through the disease-affected section of the artery. The protocol included fat suppressed T1-weighted (T1W), dual echo T2/proton density-weighted (T2W/PDW) and short-tau inversion recovery (STIR) fast spin echo sequences using cardiac gated double inversion recovery preparation for blood suppression. Direct Thrombus Imaging (MRDTI) was performed using an inversion recovery T1 weighting prepared 3D fast spoiled gradient echo sequence [14]. The MRDTI sequence was acquired in the coronal plane to negate blood flow effects. A single-shot diffusion-weighted echo-planar imaging sequence was used to obtain T2W ($b = 0 \text{ s/mm}^2$) and diffusion-weighted (DW) images ($b = 500 \text{ s/mm}^2$) [16]. T2W and DW images were subsequently used to compute apparent diffusion coefficient (ADC) maps. The three resulting images are further labeled as DWT2, DWI, and ADC throughout the text. The image slices had a minimum coverage of 21 mm of the disease-affected section of the artery. A full list of the imaging parameters is shown in Table 9.1. The MR imaging protocol and subsequent post processing resulted in nine contrast weightings (TOF, T1W, T2W, PDW, STIR, MRDTI, DWT2, DWI, and ADC) which were used for further analysis.

Table 9.1: Carotid MR imaging pulse sequence parameters.

	TOF	T1W	T2W/PDW	STIR	MRDTI	DWT2/DWI
Acquisition	2D TOF	2D FSE	2D FSE	2D FSE	3D FSPGR	2D EPI
	- Axial	- Axial	- Axial	- Axial	- Coronal	- Axial
FOV (cm)	22x22	10x10	10x10	10x10	10x10	16x16
pFOV	1	1	1	1	1	0.5
Matrix	512x512	256x256	256x256	256x256	160x160	128x128
NEX	1	2	2	2	1	16
TR (ms)	16.6	1R-R	2R-R	2R-R	5.7	2200
TE (ms)	4.1	7.7	99.7/7.7	99.7	2.6	75
TI (ms)	-	-	-	150	19.0	-
Slice thickness (mm)	2	3	3	3	1	3
ETL	-	12	16	24	1	-
Fat suppression	No	Yes	Yes	Yes	No	Yes
In-plane resolution (mm)	0.86	0.39	0.39	0.39	0.625	1.25
Scan Time (min:sec) ¹	0:48	5:22	8:24	5:36	2:09	4:42

¹Scan times for either a 3D slab or multiple consecutive 2D slices comprising 21mm of carotid/plaque (assumes heart rate of 60bpm)

Reference standard determined by manual image analysis

An experienced radiologist manually segmented the MR image data using the matching histological sections as ground truth to form the reference standard. The images from the nine contrast weightings were processed and manually segmented using the following steps:

1. T1W images were defined as reference images.
2. The other contrast weightings were processed to match the reference images resolution and geometry using multiplanar reconstruction.
3. The histological sections were visually matched with the image data. For each patient at least one matching histology section was available.
4. The lumen and outer contours were manually delineated on the T1W images by an experienced radiologist using CMRtools (Cardiovascular Imaging Solutions, London, UK). This software was also used, for subsequent steps 5 & 6, for the manual alignment of image slices and the delineation of plaque components.
5. The other MR sequences were manually aligned to the T1W image by translating the image slices in-plane to match the lumen and outer contours resulting in a set of aligned multi-contrast images.
6. The segmentation of the plaque components was performed by evaluating the images in the aligned set assisted by the available histology data. The plaque component contours were defined on the image where they could be seen most clearly. The expert manually delineated IPH, LR/NC and calcium regions.

Finally, the contours of IPH and LR/NC were combined and labeled as soft plaque. The manual image analysis resulted in an aligned set of vessel wall images including manual segmentations based on histology. The manual segmentation is further referred to as the *reference standard* in the remainder of the manuscript.

Automated image segmentation using statistical pattern recognition

Several methods for segmentation of plaque components in the carotid artery have been described in literature, the majority employing statistical pattern recognition techniques [25, 37, 38, 43]. Similarly, a pattern recognition system, developed using PRTTools [116] and MATLAB (2009b, The MathWorks, Natick, MA, USA), was used to automatically classify the pixels within the vessel wall based on the different MR signal intensities. Vessel wall pixels were defined by the reference standard; the manually delineated contours of the lumen and outer wall. A standard PC was used to run the pattern recognition system software.

A pattern recognition system consists of a sensor that gathers the observations to be classified, a feature extraction mechanism that computes numeric or symbolic information from these observations, and a classifier that, based on these features, can classify the observations into different classes. In this study, the observations included the image slices of the nine contrast weightings and the manually segmented vessel wall contours. For each vessel wall pixel a number of features were extracted. These features contained normalized MR signal intensities and image gradient information. Based on these features, each observation was classified as soft plaque, defined as being LR/NC and/or IPH, or not being soft plaque. Calcium was not identified since the calcium regions were relatively small and the number of examples in the available image data was low.

Feature extraction

Prior to feature extraction, the vessel wall images were normalized by dividing the signal intensities by the median value of a 4 by 4 cm region of interest located at the lumen center [38]. This normalization step is required for comparing the different sequences of a single subject, as well as for inter-subject comparison. Subsequently, for each pixel inside the vessel wall the following features were extracted: the normalized signal intensity, zero-, first and second order derivatives at multiple scales (0.25, 0.5, 1.0 and 2.0 mm) from each of the vessel wall images. The zero-, first and second order derivative features were calculated using the RecursiveGaussianImageFilter of the open-source Insight Segmentation and Registration Toolkit (<http://www.itk.org>). The zero order derivatives are equivalent to blurred versions of the normalized signal intensities, the first and second order derivatives contain edge and texture information of the images.

Training and testing a classifier

The features of each observation served as input for a classifier. The classifier used is a Mahalanobis distance classifier, which is a type of Bayes classifier. A similar segmentation algorithm with a Bayes classifier was presented by Hofman et al. [37]. This is a supervised classifier that needs example observations and its corresponding classes in order to train the classifier. During the training phase, the features and the classes were used to learn statistics describing the example data. Once trained, the classifier can assign a class to unseen observations. Because of the relatively low number of patients, leave one out cross validation was used for training and testing the classifier. Data from one patient is used as the testing set, and the remaining patients are used as the training data. This is repeated such that each patient in the population is used once as the testing set.

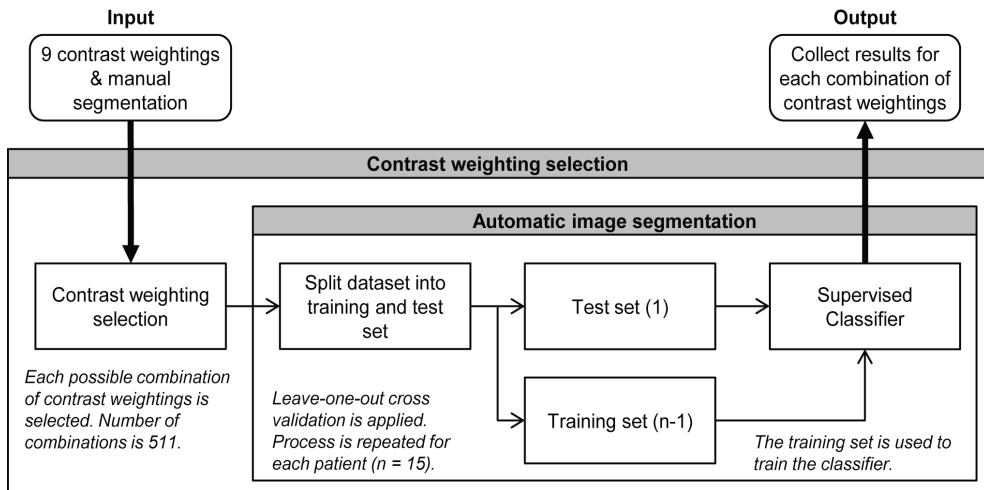


Figure 9.1: Scheme of the contrast weighting selection and the automatic image segmentation procedure. The procedure is started by the selection of a combination of contrast weightings. The automated image segmentation method is applied to that combination of contrast weightings and the reference standard which is based on the manual segmentation. The automated segmentation results are compared with the reference standard. This automated image segmentation procedure is then repeated for each contrast weighting selection and results of each combination are collected.

Evaluation of each combination of contrast weightings

In this study nine contrast weightings from six different MR sequences were available. Each possible combination of contrast weightings was investigated by selecting a combination of weightings and applying the automated image segmentation method as shown in Figure 9.1. Besides the selection of the set of contrast weightings, no further feature selection was applied.

For each combination of contrast weightings the automatically segmented soft plaque volume per patient was compared to the reference standard using Pearson's correlation. The correlation coefficient, P -value and confidence interval (CI) were calculated for each combination of contrast weightings. In addition, the time needed to acquire the MR sequences corresponding to the set of contrast weightings, was calculated.

9.3 Results

Image data from 15 patients was analyzed by the manual observer and the automated image segmentation method. The presence and volumes of the plaque components in the patient population obtained by manual image analysis are given in Table 9.2.

In total 75 vessel wall slices (five slices per patient) were analyzed using the automated image segmentation method. The automated segmentation method was repeated for each combination of contrast weightings. The number of combinations which were tested was 511 ($2^9 - 1$). The selected contrast weightings, correlations, CIs, p -values and corre-

Table 9.2: Plaque composition of patient population ($n = 15$).

Plaque component	Average volume \pm SD (mm^3)
Calcium ($n = 5$)	26.5 (\pm 15.5)
Hemorrhage ($n = 4$)	75.6 (\pm 48.3)
Lipid ($n = 14$)	142.0 (\pm 115.8)

SD = Standard Deviation.

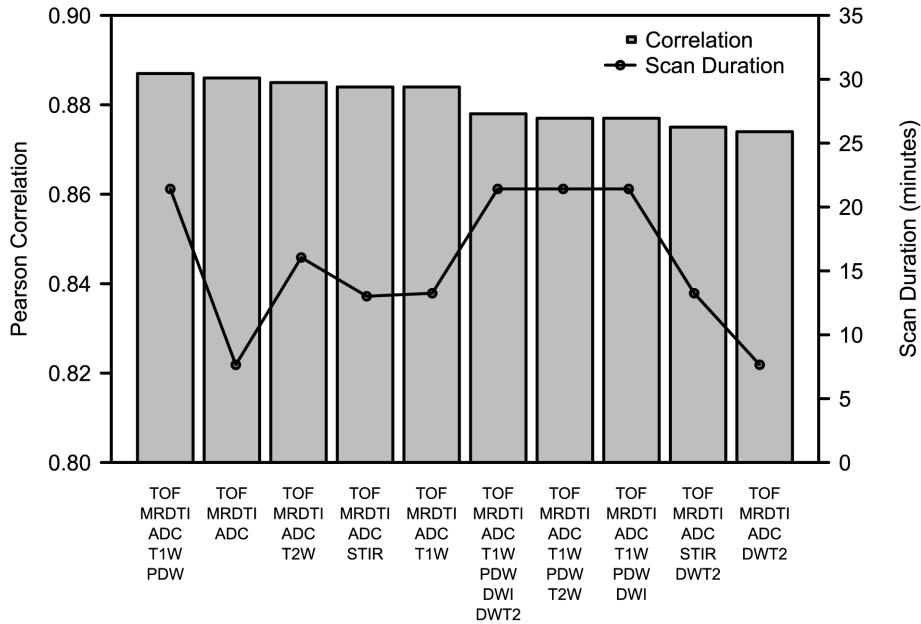


Figure 9.2: Comparison between automated segmentation performance, contrast weighting combinations and scan duration. The ten best contrast weighting combinations ranked by the correlation between the automated image segmentation and the reference standard are shown using a bar plot. Each bar represents one set of contrast weightings (contrast weightings are tiled horizontally on the horizontal axis). The total MR scan duration of each set is superimposed using a line plot.

sponding scan durations are available in the Table S1. Figure 9.2 shows the correlation and total MR scan duration for the ten best contrast weighting combinations.

In Table 9.3 the results are ordered based on the number of contrast weightings used. The highest correlation is achieved by selecting five weightings. However, while using the combination of TOF, MRDTI and ADC weightings, the correlation is almost similar to the highest correlation and the scan time is reduced by more than 60%. Figure 9.3 shows the difference in plaque segmentation result between using 3 and 5 weightings for one image slice of the dataset.

Table 9.3: Correlation between the automated image segmentation and the reference standard ranked by number of contrast weightings.

Contrast weightings	Number of weightings	Pearson Correlation [CI]	P-value	MR scan duration [min]
TOF	1	0.711 [0.312-0.897]	p = 0.003	0.8
TOF-MRDTI	2	0.860 [0.622-0.953]	p < 0.001	3.0
TOF-MRDTI-ADC	3	0.886 [0.683-0.962]	p < 0.001	7.7
TOF-MRDTI-ADC-T2W	4	0.885 [0.682-0.961]	p < 0.001	16.1
TOF-MRDTI-ADC-PDW-T1W	5	0.887 [0.688-0.962]	p < 0.001	21.4
TOF-MRDTI-ADC-PDW-T1W-T2W	6	0.877 [0.663-0.959]	p < 0.001	21.4
TOF-MRDTI-ADC-PDW-T1W-DWI- DWT2	7	0.878 [0.665-0.959]	p < 0.001	21.4
TOF-MRDTI-ADC-PDW-T1W-DWI-DWT2-T2W	8	0.855 [0.611-0.951]	p < 0.001	21.4

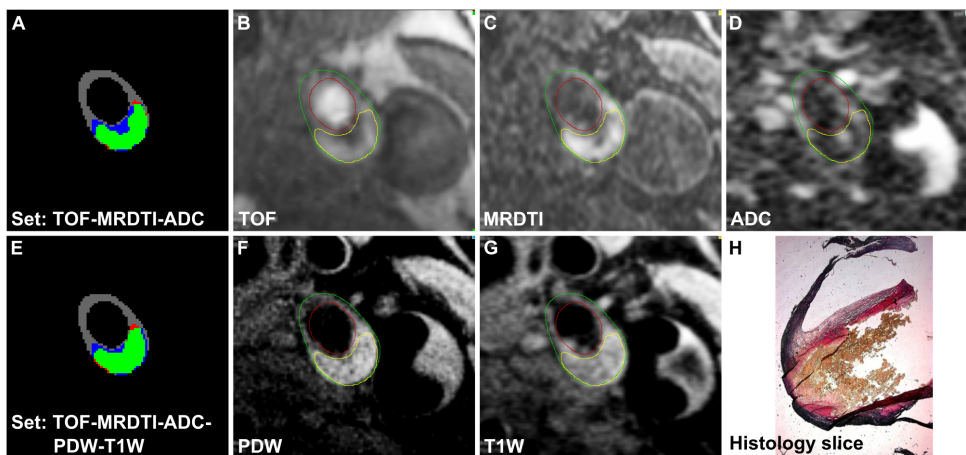


Figure 9.3: Automated segmentation results for two sets of contrast weightings including MR images and histology. A) segmentation result for the contrast weighting set TOF-MRDTI-ADC showing the overlap between the automated segmentation method and the reference standard (green: true positive lesion, blue: false negative lesion, red: false positive lesion), B) TOF image, C) MRDTI image, D) ADC image, E) segmentation result for the set TOF-MRDTI-ADC-PDW-T1W, F) T1W image, G) PDW image, and H) the matching histological slice with elastic Van Gieson staining. The contours of the reference standard are overlaid on the different MR images (panels B,C,D,E,G). The lumen and vessel wall are depicted by the red and green contour, soft plaque is depicted by the yellow contour. The yellow colour in the histological slice in panel H is consistent with the presence of lipid.

9.4 Discussion

An objective method to optimize the MR imaging protocol for plaque classification in vessel wall images using an automated classifier was presented. Evaluation of the results from nine contrast weightings showed the tradeoff between scan duration and automated segmentation performance. The presented method has potential for application in a clinical setting, or may be of value when developing new imaging protocols for clinical research.

The automated image segmentation method is based on pattern recognition and uses only the vessel wall images and histology based manual segmentations in order to achieve a direct interpretation of the informational content of these images and the segmentation performance. While morphology was used to delineate the boundaries of the vessel wall, no morphological features were used in the automated image segmentation algorithm to ensure that the segmentation results are directly related to the image information of the contrast weightings. Also, no feature selection or post processing was used. The performance of the algorithm was in line with previous studies [37, 38]. Furthermore, our approach is free of the constraints imposed by previous studies which sought to define a minimal number of sequences using manual segmentation [38, 163], specifically the number of combinations that could be evaluated, observer bias and the lack of an independent training set.

Performance of the automated segmentation method increased by the number of selected contrast weightings with an optimum at five weightings. Selection of more than five weightings showed a decrease in performance. Such a behavior is typical for a pattern recognition system; adding information to the system by selecting more features increases the performance, but at a certain point the performance stabilizes or decreases because the extra features do not contain relevant or contradicting information. The first selected contrast weighting was the TOF image. Both LR/NC and IPH can be identified from this weighting [23] explaining why this weighting was the first one to be selected by the presented method. Next, the MRDTI weighting was added to the set; the MRDTI weighting was reported to be sensitive for the detection of IPH [14]. The third selected weighting was the ADC image, which can be used to distinguish LR/NC [16] from other plaque components and fibrous tissue. Addition of the other contrast weightings provided only a small improvement which, in our opinion, was not relevant.

This study is subject to a number of limitations. No distinction was made between IPH and LR/NC. However, if more image data is available, the method can be extended by either applying the method to each plaque component independently or by pooling the segmentation results for the different plaque components. In the first case, the optimal sequence set for a single plaque component can be investigated. In the second case, the set of sequences is evaluated with respect to all plaque components. The reference standard was acquired using manual segmentation by a radiologist and is therefore not completely objective. The manual segmentation process was assisted by histology reducing the effect of human variability in the reference standard. There were no matching histology sections for all image slices. In cases where no matching histology section was available, the nearest histology section was interpreted in order to perform the delineation of the vessel wall and plaque components combining the standard assumptions of the relative contrast weighting of plaque components [92]. Due to the limited size of the dataset, leave-one-out cross validation was used for the training and testing of the automated segmentation algorithm. This method provides an approximately unbiased estimate of the classification performance. A larger dataset, which can be split into a training set and an independent

testing set, can provide a more reliable estimate of the classification performance. The presented soft plaque correlation measurements have wide confidence intervals. Because of these wide intervals it is not possible to indicate whether or not a particular set of vessel wall images is significantly better than another set of images. However, the different correlations can still be compared and the scan duration should be considered in the interpretation of the results.

In conclusion, a method was presented to objectively evaluate the MR sequence protocol for the detection of the soft plaque in MR vessel wall images of the carotid artery. The presented approach allows development and optimization of MR imaging protocols by investigating the tradeoff between scan duration and automated segmentation performance possibly leading to shorter scanning times and better image interpretation. This approach can potentially also be applied to other research fields focusing on different diseases and anatomical regions.

Acknowledgments

This study was funded by the Dutch Technology Foundation STW, which is the applied science division of NWO, and the Technology Programme of the Ministry of Economic Affairs. Project number LGT.6454. <http://www.stw.nl>.

Chapter 10

Summary and conclusions

10.1 Summary

In this thesis we developed and evaluated several methods for the automated analysis of the carotid artery vessel wall using multi-sequence MR vessel wall images to assess atherosclerosis. **Chapter 1** provides a general introduction into atherosclerosis and different stages of the disease were described including the importance to differentiate between stable and vulnerable plaques. Several non-invasive imaging techniques were discussed and the advantages of multi-sequence MRI were highlighted. A standard workflow for the manual analysis of these images was presented and existing methods for the automated analysis of these images were discussed.

A new method to segment the vessel wall boundaries was presented in **chapter 2**. The segmentation method uses a 3D deformable vessel model requiring only minimal user interaction by combining 3D MRA and 2D vessel wall images. Comparison of the automated method with manual segmentation showed substantial agreement with slight underestimation and a proportional error of the vessel wall thickness and volume. However, the automated method demonstrated improved interobserver agreement, improved inter-scan reproducibility and was substantially faster. Advantages over existing methods were that the method uses a true 3D model, which can be applied to both isotropic and non-isotropic image data, instead of segmenting the vessel wall boundaries in each image slice independently, as was done in other methods. This property is especially helpful in areas where the edges of the vessel wall are vague or poorly defined as in the bifurcation area. In case of a vague or missing edge in an image slice, edge information from neighboring slices is taken into account to guide the model to the correct location. The same effect applies to the bifurcation area, where most segmentation methods have the tendency to expand into the ECA, but this effect is limited for the 3D vessel model as edge information from neighbouring image slices is used during the model fitting.

In **chapter 3**, the underestimation of the 3D deformable vessel model segmentation method was addressed by adding a postprocessing step in which systematic segmentation errors were corrected by using a learning-based vessel segmentation correction method. This method can correct systematic errors caused by differences in image characteristics when using different MR acquisition parameter settings or different scanning equipment, and can correct for the limited flexibility of the 3D segmentation model. The application of the learning-based vessel segmentation correction method showed a small improve-

ment for the segmentation of the lumen boundary and a major improvement for the outer wall. After adding the learning-based segmentation correction step, the segmentation results were comparable to the manual annotations in terms of vessel wall dimensions and can therefore be used to replace the manual measurements speeding up the current analysis. Additionally, this development opens up possibilities for population studies with a large number of subjects where manual measurements becomes infeasible. Moreover, the learning-based segmentation correction method is potentially a powerful tool which can be applied to other automated segmentation problems. It can be used to adapt an automated segmentation result to an observer (e.g. the observer draws the contours on the rise of the edge, while the automated method searches for the strongest edge), or to adapt an existing method to different images.

The main theme of **chapters 4 and 5** is image registration, the automated alignment, of the multi-sequence MR images within one scan session and between scan sessions. In **chapter 4**, the need for image registration was shown by quantification of patient motion during one scan session. This quantification showed that the average misalignment is considerable and that patient movement occurs in all three dimensions. Different automated image registration experiments were performed in which several carefully selected, critical components of the registration procedure were optimized and quantitatively validated on a large group of patients. The optimal registration strategy was faster than manual alignment by a human expert, and provided similar accuracy. The results showed that automated image registration can replace the manual alignment procedure. This is the first study in which patient motion was quantified, a 3D deformable transformation model was used, and the registration experiments were validated on a large set of patient studies using quantitative measures. Additionally, the optimal registration strategy was validated on a more recent 3.0T dataset. The results of the 3.0T dataset were in line with the results of the 1.5T dataset showing that the same registration strategy can be applied to newer MRI data.

In **chapter 5** image registration is used to improve the comparison of baseline and follow-up images in serial MRI studies. Traditionally, observers either visually match each image slice of the baseline study with an image slice of the follow-up study and compare area measurements of the vessel wall and plaque components, or do not perform any matching and compare volume metrics based on the whole vessel. In both cases, only a small part of the available image information is used in the analysis. In our approach, 3D image registration was used to obtain point correspondence between images from different timepoints. Using this correspondence, measurements in the baseline study can be related to measurements in the follow-up study in high detail. Additionally, 3D visualization techniques were applied to present local changes in vessel wall morphology using difference maps which were color-coded on a mesh of the lumen segmentation of the baseline image. This approach is an improvement over the traditional volume-based image comparison and provides a detailed view of local differences over time improving insight into the disease progression of an individual patient.

In **chapters 6 to 9** pattern recognition techniques were applied for the analysis of atherosclerotic plaque components in MR vessel wall images. In **Chapter 6**, a study was presented in which an automated segmentation method was used to classify plaque components based on in vivo MRI from a multicenter study. The automated segmentation method employed a supervised classifier which was trained using intensity and gradient information from the MR sequences and morphological information such as local vessel wall thickness. The results indicated that it was possible to automatically detect carotid

plaque components with substantial or good agreement with visual identification, and that the volumes obtained manually and automatically were reasonably consistent for hemorrhage and lipids but not for calcium. The current results show that automated segmentation in a multicenter study is feasible provided MR protocols and acquisition parameters are standardized between centers. The results are promising, but improvements are still needed as the agreement between automated and manual segmentation was reasonable. The current results can serve as an initial segmentation to speed up the manual segmentation procedure.

In **chapter 7** the effect of 3D morphological features, image normalization strategies and composition of the training set on the accuracy and reproducibility of supervised plaque classification was investigated. Image normalization is often performed using the median signal intensity value of a $4 \times 4 \text{ cm}^2$ square region of interest around the lumen, which is a surrogate measure for the signal intensity of the sternocleidomastoid muscle which is used as reference during manual segmentation of plaque components. Our results showed that a normalization approach using intensity scaling provided better results than the region of interest based approach. Interestingly, our results also showed a low agreement between the median value of the $4 \times 4 \text{ cm}^2$ region of interest and the median value of the sternocleidomastoid muscle. The agreement between manual and automated segmentation was significantly improved by using the 3D distance to the flow divider feature, normalization based on intensity scaling and a training set based on the intersection of two repeated reads. Finally, the results showed that automated segmentation is more reproducible than manual segmentation.

In **chapter 8** pattern recognition techniques were applied to investigate the added value of two MR sequences at high field, inversion recovery spin echo and T1 weighted gradient echo with fat suppression, for identification of unstable plaque components. Instead of using the Euclidean distance measure, the Mahalanobis distance measure was used to quantify contrast between plaque components in MR sequences. The Mahalanobis distance measure is scale-invariant and takes into account the covariance between the samples, enabling comparison of image contrast between different MR sequences which is not possible while using the Euclidean distance measure. As a proof of concept, two automated segmentation experiments were performed using an Euclidean distance classifier and a Mahalanobis distance classifier. The experiments showed a better performance for the Mahalanobis classifier.

Chapter 9 presents another application of pattern recognition techniques for multi-sequence vessel wall imaging. In this chapter, automated segmentation was used to objectively evaluate an MR sequence protocol for the detection of soft plaque in the carotid artery. The approach allows development and optimization of an MR imaging protocol by investigating the tradeoff between scan duration and automated segmentation performance possibly leading to shorter scanning times and better image interpretation. This approach can be easily generalized and can therefore potentially be applied to other research fields focusing on different diseases and anatomical regions.

10.2 Conclusion

The main goal of this thesis was to develop methods for automated segmentation, registration and classification of the carotid artery vessel wall and plaque components using multi-sequence MR vessel wall images.

Several novel automated image segmentation and registration techniques have been developed. For each technique, existing methods were discussed to identify the need for developing a new method. Subsequently, the results of the new method were compared to existing methods where possible. All techniques were developed and validated using relevant patient data and reference standards. Manual segmentations created by experienced observers were used as reference standard and were in some cases based on histology data. At the end of each chapter, clinical implications were discussed by answering questions such as; what is the required user interaction to initialize the segmentation method?, how do the results compare to manual segmentation?, what is the decrease in analysis time?, and how does the technique fit into the current clinical research workflow?

To conclude, novel automated methods were developed which contributed to each step in the analysis of multi-contrast MR vessel wall images. Therefore, the main goal of this thesis has been realized.

10.3 Future directions

The work presented in this thesis is an important contribution to the automated analysis of multi-sequence MR vessel wall imaging of the carotid artery. However, given the current methodology, fully automated image analysis is not yet feasible, therefore motivating future research. Several possibilities exist to expand the current work: 1) The automated segmentation of the vessel wall boundaries is currently performed based on edge information of one contrast weighting. This method can be extended to include edge information from multiple contrast weightings possibly improving segmentation performance. 2) The 3D vessel model should be extended towards a full 3D bifurcation model to obtain a comprehensive description of this important region without having to correct for errors caused by the external carotid artery. 3) Another challenge is the automated segmentation of plaque components. The segmentation results are highly dependent on the choice of MR sequences and the quality of the acquired images. As these two factors are often difficult to control, a semi-automated approach should be investigated which speeds up the analysis time while preserving the segmentation performance of the observer. Additionally, the latest developments in T1, T2 and T2* mapping techniques should be closely monitored. These techniques allow the measurement of absolute T1, T2 and T2* relaxation times which are tissue specific biophysical MR properties. The quantitative properties, as opposed to working with relative signal intensities, promise a major contribution to automated classification of plaque components. 4) Develop a new workflow which is not analogue to the manual segmentation workflow. This might result in a different ordering of the segmentation steps or in hybrid approaches. Potential examples of hybrid approaches are the simultaneous segmentation of the vessel wall boundaries and registration of the multi-contrast images, and the simultaneous detection of the vessel wall boundaries and plaque components.

The availability of “good” datasets is currently limited. A good dataset should include a large number of MRI scans, preferably over 50, with sufficient image quality. Ideally, histology should be obtained and used as gold standard to assist the manual segmentation process. Alternatively, in case no histology is available, the image data should be analyzed by multiple trained observers who score the data individually and also perform a consensus reading. Acquiring such a dataset takes time as patients have to be recruited, scanned, and all data needs to be manually segmented. It would be helpful to the community to cre-

ate such as dataset and make it available to other research groups. A possible vehicle to do so is to organize a “challenge”. A challenge allows different research groups to develop and test algorithms on a standardized set of data using a common evaluation framework.

A future direction on a higher level is to focus on treating the image data as a 3D volume instead of processing each image slice independently. As thinner image slices and isotropic datasets are becoming more popular, 2D segmentation methods will become computationally more intensive and can only take advantage of image information within the slice. Moreover, the analysis of patient movement and the automated registration results from chapter 4 showed the importance of a 3D approach. In the process of developing 3D segmentation methods, one has to be vigilant as a typical vessel wall imaging dataset is highly anisotropic and extensive use of interpolation can degrade the reliability of the results. Finally, as isotropic datasets are becoming more popular, manual segmentation becomes impractical, motivating the need for automated 3D segmentation methods.

Researchers developing image processing methods should work in close collaboration with MR pulse sequence developers and the clinicians who perform the MRI scanning. Various parameters, such as design choices in the MR pulse development, choice of applied MR sequences, setup of the scan protocol and slice planning, can have a substantial impact on the manual or automated analysis result of the image data. For example, an MR pulse sequence developer can focus on increasing the in-plane image resolution, which has a positive impact on the manual segmentation result, or put his effort into decreasing the slice thickness, which is more favorable from an image processing point of view. A good collaboration between the different parties will greatly contribute to a good end result.

Finally, the importance of a good software tool, which supports both the manual segmentation and automated analysis including correction of intermediate results, should not be underestimated. A good tool allows clinicians to efficiently view the image data and perform manual segmentations. These segmentations can then be used for the development and validation of new segmentation methods, which, in turn, can be added to the software tool to support the clinician. And, although the ultimate goal is to develop fully automated segmentation methods, results of newly developed segmentation methods will always need thorough visual verification and ideally limited manual corrections.

Samenvatting en conclusies

Samenvatting

In dit proefschrift zijn verschillende methoden ontwikkeld en geëvalueerd voor de automatische analyse van de vaatwand van de halsslagader op basis van multi-sequentie MRI beelden van patiënten met de ziekte atherosclerose. **Hoofdstuk 1** geeft een algemene introductie van de ziekte atherosclerose en bespreekt verschillende stadia van deze ziekte waaronder het belang om onderscheid te maken tussen stabiele en kwetsbare plaques ("vulnerable plaques"). Verschillende niet-invasieve beeldvormingstechnieken zijn besproken en de voordelen van multi-sequentie MRI zijn toegelicht. Een standaard workflow voor de handmatige analyse van deze beelden werd gepresenteerd en bestaande methoden voor de geautomatiseerde analyse zijn besproken.

Een nieuwe methode voor de segmentatie van de vaatwandcontouren is gepresenteerd in **hoofdstuk 2**. De segmentatiemethode maakt gebruik van een 3D-vertormbaar vaatwandmodel en vereist slechts minimale gebruiksinteractie door het combineren van de 3D MRA en 2D vaatwandbeelden. Vergelijking van de automatische methode met manuele segmentaties toonde een substantiële overkomst met een lichte onderschatting en proportionele fout van de dikte en het volume van de vaatwand. De geautomatiseerde methode toonde echter een betere interobserver overeenkomst, een betere inter-scan reproduceerbaarheid en was aanzienlijk sneller. Ten opzichte van bestaande methoden biedt de nieuwe methode het voordeel dat er een volwaardig 3D-model gebruikt wordt dat kan worden toegepast op isotrope en niet-isotrope beelden in plaats van het segmenteren van de vaatwandcontouren in elke slice (2D beeldplak) afzonderlijk, zoals bij andere methoden gebeurt. Deze eigenschap is vooral krachtig in gebieden waar de grenzen van de vaatwand vaag of slecht gedefinieerd zijn zoals in het bifurcatiegebied. Bij een vage of ontbrekende gradiënt in een slice, wordt informatie uit naburige slices gebruikt om het model naar de juiste locatie te sturen. Dit effect heeft ook toegevoegde waarde in het bifurcatiegebied, waar de meeste segmentatiemethoden de neiging hebben om een deel van de arteria carotis externa te segmenteren. Dit wordt beperkt doordat het 3D-vaatmodel informatie uit naburige slices gebruikt tijdens het fitten van het model.

In **hoofdstuk 3** wordt een techniek beschreven waarmee de onderschatting van de segmentatiemethode uit hoofdstuk 2 gecorrigeerd wordt middels een postprocessing stap waarbij systematische segmentatie fouten worden gecorrigeerd met behulp van patroonherkenningstechnieken. Deze techniek kan systematische fouten corrigeren die worden veroorzaakt door verschillen in beeldkenmerken zoals het gebruik van verschillende MRI acquisitie parameterinstellingen of andere scanapparatuur, en kan corrigeren voor de beperkte flexibiliteit van het 3D-vaatwandmodel. De toepassing van de correctiestap toonde een kleine verbetering van de segmentatie van de lumen contouren en een aanzienlijke

verbetering voor de contouren van de buitenwand. Toepassing van de correctiestap resulteerde in segmentatieresultaten met gelijke nauwkeurigheid aan die van handmatige annotaties. De verbeterde methode kan worden gebruikt om handmatige metingen te vervangen en zodoende de huidige analyse te versnellen. Bovendien biedt deze ontwikkeling mogelijkheden voor bevolkingsonderzoek met een groot aantal personen waar handmatige segmentatie niet haalbaar is. Ook is de correctiestap potentieel een krachtig hulpmiddel dat kan worden toegepast op andere automatische segmentatieproblemen. De methode kan worden gebruikt om automatische segmentatieresultaten aan te passen aan een expert (bijv. de expert tekent de contouren op de start van de gradiënt, terwijl de geautomatiseerde methode zoekt naar de sterkste gradiënt), of om een bestaande methode aan te passen aan andere beelden.

Het thema van **hoofdstukken 4 en 5** is beeldregistratie, het automatisch op elkaar passen van beelden, van multi-sequentie MRI beelden binnen een scansessie en tussen scansessies. In **hoofdstuk 4** wordt de noodzaak van beeldregistratie aangetoond door de beweging van de patiënt gedurende een scan sessie te kwantificeren. Hieruit bleek dat de gemiddelde fout in uitlijning van de beelden aanzienlijk is en dat beweging van de patiënt in alle drie dimensies plaatsvindt. Verschillende automatische beeldregistratie experimenten werden uitgevoerd waarbij zorgvuldig geselecteerde kritische componenten van de registratieprocedure werden geoptimaliseerd en kwantitatief geëvalueerd op een grote groep patiënten. De optimale beeldregistratie strategie was sneller dan handmatige uitlijning van de beelden door een expert en was even nauwkeurig. Deze resultaten tonen aan dat automatische beeldregistratie de handmatige uitlijning procedure kan vervangen. Dit is de eerste studie waarin de mate van beweging van de patiënt is gekwantificeerd, een 3D-vertormbaar transformatie model is gebruikt en waarbij de registratie-experimenten gevalideerd zijn op een grote set patiëntstudies met behulp van kwantitatieve metrieken. Daarnaast werd de optimale registratiestrategie gevalideerd op een recentere 3.0T dataset. De resultaten van de 3.0T dataset waren in overeenstemming met de resultaten van de 1.5T dataset en laten zien dat dezelfde registratiestrategie ook kan worden toegepast op nieuwere MRI beelden.

In **hoofdstuk 5** wordt beeldregistratie toegepast om de vergelijking van baseline en follow-up beelden in longitudinale MRI studies te verbeteren. Experts proberen de slices van de baseline studie visueel naast de slices van de follow-up studie te leggen en vergelijken vervolgens oppervlakte metingen van de vaatwand en plaquecomponenten, of ze voeren geen correctie uit en vergelijken volumemetingen van het gehele bloedvat. In beide gevallen wordt slechts een klein deel van het beschikbare beeldinformatie gebruikt in de analyse. In de voorgestelde aanpak wordt gebruik gemaakt van 3D-beeldregistratie om puntcorrespondentie tussen beelden van verschillende tijdstippen te verkrijgen. Met behulp van de deze correspondentie kunnen metingen in het baseline beeld worden gekoppeld aan metingen in het follow-up beeld op een gedetailleerd niveau. Vervolgens worden 3D-visualisatie technieken toegepast om lokale wijzigingen in vaatwandmorfologie te presenteren door de gevonden verschillen in kleur te coderen op een maas van de lumen segmentatie van het baseline beeld. Deze aanpak is een verbetering ten opzichte van de traditionele volume gebaseerde metingen en biedt een gedetailleerde weergave van lokale vaatwandveranderingen tussen twee tijdstipmomenten. Deze aanpak kan het inzicht in de progressie van de ziekte van een individuele patiënt verbeteren.

In **hoofdstukken 6 tot en met 9** worden patroonherkenningstechnieken toegepast voor het analyseren van atherosclerotische plaquecomponenten in MRI vaatwandbeelden. **Hoofdstuk 6** beschrijft een studie waarbij automatische segmentatie is gebruikt om

plaquecomponenten te classificeren op basis van in-vivo MRI beelden in een multicenter studie. De automatische segmentatiemethode maakt gebruik van een lineaire classifier die wordt getraind met intensiteit en de gradiënt informatie van de MRI beelden en morfologische informatie zoals de lokale vaatwanddikte. De resultaten tonen aan dat het mogelijk is om plaquecomponenten in de vaatwand automatisch te detecteren met substantiële of goede overeenstemming met visuele identificatie en dat de handmatig en automatisch verkregen volumes redelijk consistent zijn voor bloeding en lipiden, maar niet voor kalk. De huidige resultaten laten zien dat automatische segmentatie in een multicenter studie haalbaar is mits de MRI protocollen en acquisitie parameters gestandaardiseerd worden tussen de centra. De resultaten zijn veelbelovend, maar verbeteringen zijn nog steeds nodig aangezien de overeenkomst tussen automatisch en handmatig gesegmenteerde volumes nog niet goed genoeg is. De huidige resultaten kunnen dienen als een initiële segmentatie om de handmatige segmentatie procedure te versnellen.

In **hoofdstuk 7** wordt het effect van 3D morfologische kenmerken, beeldnormalisatie strategieën en de samenstelling van de training dataset op de nauwkeurigheid en de reproduceerbaarheid van de automatische plaqueclassificatie onderzocht. Beeldnormalisatie wordt vaak uitgevoerd met behulp van de mediaan van de signaalintensiteiten in een vierkant gebied van $4 \times 4 \text{ cm}^2$ gecentreerd rondom het lumen. Deze waarde dient als surrogaat voor de signaalintensiteit van de musculus sternocleidomastoideus, welke als referentie wordt gebruikt tijdens de handmatige segmentatie van plaquecomponenten. Onze resultaten toonden dat normalisatie middels het schalen van de intensiteiten betere resultaten gaf dan de mediaan gebaseerde aanpak. Interessant is ook dat onze resultaten een slechte overeenkomst toonden tussen de mediaanwaarde van het $4 \times 4 \text{ cm}^2$ gebied en de mediaan van de musculus sternocleidomastoideus. De overeenkomst tussen handmatige en geautomatiseerde segmentatie werd aanzienlijk verbeterd door het gebruik van de 3D-afstand-tot-het-bifurcatiepunt informatie, normalisatie gebaseerd op het schalen van de intensiteiten en een training set gebaseerd op de intersectie van twee herhaalde manuele segmentaties. Tenslotte toonden de resultaten aan dat automatische segmentatie reproduceerbaarder is dan handmatige segmentatie.

In **hoofdstuk 8** worden patroonherkennings technieken toegepast om de toegevoegde waarde van twee MRI sequenties bij hoge veldsterkte, *inversion recovery spin echo* en *T1 gewogen gradiënt echo met vet onderdrukking*, te onderzoeken voor de identificatie van instabiele plaquecomponenten. In plaats van de Euclidische afstandsmaat, wordt de Mahalanobis afstandsmaat gebruikt om het contrast tussen plaquecomponenten in MRI sequenties te kwantificeren. De Mahalanobis afstandsmaat is schaal-invariant en houdt rekening met de covariantie tussen de datapunten, waardoor het, in tegenstelling tot de Euclidische afstandsmaat, mogelijk is om het contrast tussen plaquecomponenten in verschillende MRI sequenties met elkaar te vergelijken. Als proof of concept, werden twee geautomatiseerde segmentatie experimenten uitgevoerd met een classifier die de Euclidische afstandsmaat gebruikt en een classifier die de Mahalanobis afstandsmaat gebruikt. De experimenten toonden betere resultaten voor de classifier gebruikmakend van Mahalanobis afstandsmaat.

Hoofdstuk 9 geeft nog een toepassing van patroonherkennings technieken op multi-sequentie vaatwandbeelden. In dit hoofdstuk wordt automatische segmentatie gebruikt om een MRI sequentie protocol ten behoeve van de detectie van *soft plaque* in de halsslagader objectief te evalueren. De aanpak maakt het mogelijk om een MRI-protocol te optimaliseren door het onderzoeken van de afweging tussen de duur van de scan en de

geautomatiseerde segmentatieresultaten. Dit kan potentieel leiden tot kortere scantijden en betere beeldinterpretatie. Deze aanpak kan eenvoudig worden gegeneraliseerd en kan mogelijk worden toegepast op andere onderzoeksgebieden die zich richten op andere ziekten en anatomische gebieden.

Conclusie

De doelstelling van dit proefschrift was het ontwikkelen van methoden voor de automatische segmentatie, registratie en classificatie van de vaatwand van de halsslagader en plaquecomponenten op basis van multi-sequentie MRI vaatwandbeelden.

Er zijn verschillende nieuwe geautomatiseerde segmentatie- en registratietechnieken ontwikkeld. Voor elke techniek werden bestaande, veelal handmatige, methoden besproken om de noodzaak aan te tonen voor het ontwikkelen van een nieuwe methode. Vervolgens werden de resultaten van de nieuwe methode vergeleken met bestaande methoden waar mogelijk. Alle technieken werden ontwikkeld en gevalideerd met behulp van relevante patiëntgegevens en referentiestandaarden. Manuele segmentaties, gemaakt door ervaren experts, werden gebruikt als referentiestandaard en waren in een aantal gevallen gebaseerd op histologische informatie. Aan het eind van elk hoofdstuk, werden klinische implicaties besproken door vragen te beantwoorden zoals: Wat is de vereiste interactie van de gebruiker om de segmentatiemethode te starten; hoe vergelijken de resultaten zich met de handmatige segmentatieresultaten; is er een afname van de analysetijd; en hoe past de nieuwe techniek in de workflow van het huidige klinisch onderzoek?

In dit proefschrift zijn nieuwe geautomatiseerde methoden ontwikkeld die hebben bijgedragen aan elke stap in de analyse van multi-contrast MRI vaatwandbeelden. Samenvattend kan gesteld worden dat hiermee de doelstelling van dit proefschrift is behaald.

Toekomstperspectief

Het werk gepresenteerd in dit proefschrift vormt een belangrijke bijdrage aan de automatische analyse van multi-sequentie MRI vaatwandbeelden van de halsslagader. Volledig automatische beeldanalyse is echter nog niet haalbaar gezien de huidige stand van de techniek en motiveren vervolgonderzoek. Er zijn verschillende mogelijkheden om het huidige werk uit te breiden: 1) De geautomatiseerde segmentatie van de vaatwandcontouren wordt momenteel uitgevoerd op basis van gradiënt informatie van een enkele MRI sequentie. De methode kan worden uitgebreid door gebruik te maken van de gradiënt informatie uit meerdere contrast wegingen, dit leidt mogelijk tot betere segmentatieresultaten. 2) Het 3D-vaatmodel kan worden uitgebreid naar een volledig 3D-bifurcatiemodel om een betere beschrijving van deze belangrijke regio te verkrijgen zonder te hoeven corrigeren voor fouten die worden veroorzaakt door het negeren van de aanwezigheid van de arteria carotis externa. 3) Een andere uitdaging is de automatische segmentatie van plaquecomponenten. De segmentatieresultaten zijn sterk afhankelijk van de keuze van MRI sequenties en de kwaliteit van de verkregen beelden. Omdat deze twee factoren vaak lastig onder controle zijn te krijgen, dient een semi-automatische aanpak, die de analysetijd reduceert en de segmentatieprestaties van de expert behoudt, te worden onderzocht. Bovendien is het belangrijk om de laatste ontwikkelingen in T1, T2 en T2* mapping technieken nauwlettend te volgen. Deze technieken maken het mogelijk om de absolute T1, T2 en T2* relaxatietijden te meten. Dit zijn weefselspecifieke magnetische biofysische ei-

enschappen. Deze kwantitatieve eigenschappen, in tegenstelling tot het werken met relatieve signaal intensiteiten, beloven een belangrijke stap in de automatische classificatie van plaquecomponenten. 4) Het ontwikkelen van een nieuwe workflow die niet analoog is aan de handmatige segmentatie workflow. Dit kan resulteren in een andere volgorde van de segmentatie stappen of in een hybride aanpak. Mogelijke voorbeelden van een hybride aanpak zijn de simultane segmentatie van de vaatwandcontouren en registratie van de multi-contrast beelden of de simultane detectie van de vaatwandcontouren en plaquecomponenten.

De beschikbaarheid van “goede” datasets is momenteel beperkt. Een goede dataset bevat een groot aantal MRI-scans, bij voorkeur meer dan 50, van voldoende beeldkwaliteit. Idealiter wordt histologie verkregen en gebruikt als gouden standaard om het handmatig segmentatie proces te ondersteunen. Indien er geen histologie beschikbaar is, moeten de beelden worden geanalyseerd door meerdere getrainde experts die de beelden individueel scoren en gezamenlijk een consensus analyse uitvoeren. Het verwerven van een dergelijke dataset kost veel tijd omdat er patiënten geïncludeerd en gescand moeten worden, en alle beelden manueel gesegmenteerd moeten worden. Het zou waardevol zijn voor de gemeenschap om een goede dataset te verzamelen en deze beschikbaar te maken voor onderzoeksgroepen. Een mogelijke manier om dit te bewerkstelligen is het organiseren van een *challenge*, een wedstrijd. Door een challenge te organiseren kunnen verschillende onderzoeksgroepen algoritmes ontwikkelen en testen aan de hand van een gestandaardiseerde set van beelden met behulp van een gemeenschappelijk evaluatie framework.

Een aanbeveling voor toekomstig onderzoek op een hoger niveau is om de beelden als een 3D volume te behandelen in plaats elke slice afzonderlijk. Aangezien de slice-dikte steeds dunner wordt en het gebruik van isotrope datasets toeneemt, zullen 2D-segmentatiemethoden steeds meer rekenkracht vereisen en kunnen deze methoden alleen gebruik maken van beeldinformatie aanwezig in de desbetreffende slice. Bovendien is het belang van een 3D-benadering gedemonstreerd met de analyse van de beweging van de patiënt en met de geautomatiseerde registratieresultaten uit hoofdstuk 4. Tijdens het ontwikkelen van 3D-segmentatiemethoden, moet men in het achterhoofd houden dat een typische MRI vaatwand dataset zeer anisotroop is en dat bij veelvuldig gebruik van interpolatie de betrouwbaarheid van de resultaten achteruit kan gaan. Tenslotte wordt manuele segmentatie door de toename van het gebruik van het isotrope datasets onpraktisch, welke de behoefte motiveert voor automatische 3D-segmentatiemethoden.

Onderzoekers die werken aan beeldverwerkingsmethoden moeten nauw samenwerken met MRI pulssequentie ontwikkelaars en de artsen die de MRI-scans uitvoeren. Verschillende parameters, zoals ontwerpkeuzes in de MRI puls-ontwikkeling, de keuze van toegepaste MRI sequenties, opzet van het scanprotocol en de sliceplanning, kunnen een aanzienlijke impact hebben op de resultaten van de manuele of automatische beeldanalyse. Zo kan bijvoorbeeld een MRI pulssequentie ontwikkelaar zich richten op het verhogen van de beeldresolutie in het beeldvlak, hetgeen een positieve invloed heeft op het manuele segmentatieresultaat, of zich richten op het verminderen van de slice dikte, hetgeen gunstiger is vanuit een beeldverwerkings perspectief. Een goede samenwerking tussen de verschillende partijen zal sterk bijdragen aan een beter eindresultaat.

Tenslotte moet het belang van een goede software tool, welke zowel manuele segmentatie als automatische analyse ondersteund inclusief het corrigeren van tussenresultaten, niet worden onderschat. Een goede tool geeft klinici de mogelijkheid om efficiënt beelden te bekijken en manuele segmentaties uit te voeren. Deze segmentaties kunnen ver-

volgens worden gebruikt voor de ontwikkeling en validatie van nieuwe segmentatiemethoden, die op hun beurt kunnen worden toegevoegd aan de software tool om de arts te ondersteunen. En, hoewel het uiteindelijke doel is om volledig geautomatiseerde segmentatiemethoden ontwikkelen, vereisen de resultaten van nieuw ontwikkelde segmentatiemethoden altijd een grondige visuele verificatie en idealiter slechts beperkte handmatige correcties.

References

- [1] I. Vaartjes, I. van Dis, F. L. J. Visseren, and M. L. Bots. *Hart- en vaatziekten in Nederland 2011, cijfers over leefstijl- en risicofactoren, ziekte en sterfte*. Hartstichting, Den Haag, 2011.
- [2] A. Blokstra, M. J. J. C. Poos, and E. A. van der Wilk. *Volksgezondheid Toekomst Verkenning, Nationaal Kompas Volksgezondheid*. RIVM, Bilthoven, 2012.
- [3] A. J. Lusis. Atherosclerosis. *Nature*, 407(6801):233–241, Sep 2000.
- [4] G. Pasterkamp, D. P. de Kleijn, and C. Borst. Arterial remodeling in atherosclerosis, restenosis and after alteration of blood flow: potential mechanisms and clinical implications. *Cardiovasc. Res.*, 45(4):843–852, Mar 2000.
- [5] M. R. Ward, G. Pasterkamp, A. C. Yeung, and C. Borst. Arterial remodeling. Mechanisms and clinical implications. *Circulation*, 102(10):1186–1191, Sep 2000.
- [6] A. V. Finn, M. Nakano, J. Narula, F. D. Kolodgie, and R. Virmani. Concept of vulnerable/unstable plaque. *Arterioscler. Thromb. Vasc. Biol.*, 30(7):1282–1292, Jul 2010.
- [7] R. M. Kwee, R. J. van Oostenbrugge, L. Hofstra, G. J. Teule, J. M. van Engelshoven, W. H. Mess, and M. E. Kooi. Identifying vulnerable carotid plaques by noninvasive imaging. *Neurology*, 70(24 Pt 2):2401–2409, Jun 2008.
- [8] G. L. ten Kate, E. J. Sijbrands, D. Staub, B. Coll, F. J. ten Cate, S. B. Feinstein, and A. F. Schinkel. Noninvasive imaging of the vulnerable atherosclerotic plaque. *Curr Probl Cardiol*, 35(11):556–591, Nov 2010.
- [9] H. R. Underhill, T. S. Hatsukami, Z. A. Fayad, V. Fuster, and C. Yuan. MRI of carotid atherosclerosis: clinical implications and future directions. *Nat Rev Cardiol*, 7(3):165–173, Mar 2010.
- [10] W. Kerwin, D. Xu, F. Liu, T. Saam, H. Underhill, N. Takaya, B. Chu, T. Hatsukami, and C. Yuan. Magnetic resonance imaging of carotid atherosclerosis: plaque analysis. *Top Magn Reson Imaging*, 18(5):371–378, Oct 2007.
- [11] T. Saam, T. S. Hatsukami, N. Takaya, B. Chu, H. Underhill, W. S. Kerwin, J. Cai, M. S. Ferguson, and C. Yuan. The vulnerable, or high-risk, atherosclerotic plaque: non-invasive MR imaging for characterization and assessment. *Radiology*, 244(1):64–77, Jul 2007.
- [12] Z. A. Fayad and V. Fuster. Clinical imaging of the high-risk or vulnerable atherosclerotic plaque. *Circ. Res.*, 89(4):305–316, Aug 2001.

- [13] C. Yuan, W. S. Kerwin, V. L. Yarnykh, J. Cai, T. Saam, B. Chu, N. Takaya, M. S. Ferguson, H. Underhill, D. Xu, F. Liu, and T. S. Hatsukami. MRI of atherosclerosis in clinical trials. *NMR Biomed*, 19(6):636–654, Oct 2006.
- [14] A. R. Moody, R. E. Murphy, P. S. Morgan, A. L. Martel, G. S. Delay, S. Allder, S. T. MacSweeney, W. G. Tennant, J. Gladman, J. Lowe, and B. J. Hunt. Characterization of complicated carotid plaque with magnetic resonance direct thrombus imaging in patients with cerebral ischemia. *Circulation*, 107(24):3047–3052, Jun 2003.
- [15] H. Ota, V. L. Yarnykh, M. S. Ferguson, H. R. Underhill, J. K. Demarco, D. C. Zhu, M. Oikawa, L. Dong, X. Zhao, A. Collar, T. S. Hatsukami, and C. Yuan. Carotid intraplaque hemorrhage imaging at 3.0-T MR imaging: comparison of the diagnostic performance of three T1-weighted sequences. *Radiology*, 254(2):551–563, Feb 2010.
- [16] V. E. Young, A. J. Patterson, U. Sadat, D. J. Bowden, M. J. Graves, T. Y. Tang, A. N. Priest, J. N. Skepper, P. J. Kirkpatrick, and J. H. Gillard. Diffusion-weighted magnetic resonance imaging for the detection of lipid-rich necrotic core in carotid atheroma in vivo. *Neuroradiology*, 52(10):929–936, Oct 2010.
- [17] H. C. Stary, A. B. Chandler, R. E. Dinsmore, V. Fuster, S. Glagov, W. Insull, M. E. Rosenfeld, C. J. Schwartz, W. D. Wagner, and R. W. Wissler. A definition of advanced types of atherosclerotic lesions and a histological classification of atherosclerosis. A report from the Committee on Vascular Lesions of the Council on Arteriosclerosis, American Heart Association. *Circulation*, 92(5):1355–1374, Sep 1995.
- [18] R. van 't Klooster, P. J. de Koning, R. A. Dehnavi, J. T. Tamsma, A. de Roos, J. H. Reiber, and R. J. van der Geest. Automatic lumen and outer wall segmentation of the carotid artery using deformable three-dimensional models in MR angiography and vessel wall images. *J Magn Reson Imaging*, 35(1):156–165, Jan 2012.
- [19] R. M. Kwee, J. M. van Engelshoven, W. H. Mess, J. W. ter Berg, F. H. Schreuder, C. L. Franke, A. G. Korten, B. J. Meems, R. J. van Oostenbrugge, J. E. Wildberger, and M. E. Kooi. Reproducibility of fibrous cap status assessment of carotid artery plaques by contrast-enhanced MRI. *Stroke*, 40(9):3017–3021, Sep 2009.
- [20] R. van 't Klooster, O. Naggara, R. Marsico, J. H. Reiber, J. F. Meder, R. J. van der Geest, E. Touze, and C. Oppenheim. Automated versus manual in vivo segmentation of carotid plaque MRI. *AJNR Am J Neuroradiol*, 33(8):1621–1627, Sep 2012.
- [21] V. C. Cappendijk, S. Heeneman, A. G. Kessels, K. B. Cleutjens, G. W. Schurink, R. J. Welten, W. H. Mess, R. J. van Suylen, T. Leiner, M. J. Daemen, J. M. van Engelshoven, and M. E. Kooi. Comparison of single-sequence T1w TFE MRI with multisequence MRI for the quantification of lipid-rich necrotic core in atherosclerotic plaque. *J Magn Reson Imaging*, 27(6):1347–1355, Jun 2008.
- [22] J. F. Toussaint, G. M. LaMuraglia, J. F. Southern, V. Fuster, and H. L. Kantor. Magnetic resonance images lipid, fibrous, calcified, hemorrhagic, and thrombotic components of human atherosclerosis in vivo. *Circulation*, 94(5):932–938, Sep 1996.
- [23] C. Yuan, L. M. Mitsumori, M. S. Ferguson, N. L. Polissar, D. Echelard, G. Ortiz, R. Small, J. W. Davies, W. S. Kerwin, and T. S. Hatsukami. In vivo accuracy of

- multispectral magnetic resonance imaging for identifying lipid-rich necrotic cores and intraplaque hemorrhage in advanced human carotid plaques. *Circulation*, 104(17):2051–2056, Oct 2001.
- [24] T. Saam, M. S. Ferguson, V. L. Yarnykh, N. Takaya, D. Xu, N. L. Polissar, T. S. Hatsukami, and C. Yuan. Quantitative evaluation of carotid plaque composition by in vivo MRI. *Arterioscler. Thromb. Vasc. Biol.*, 25(1):234–239, Jan 2005.
- [25] I. M. Adame, R. J. van der Geest, B. A. Wasserman, M. A. Mohamed, J. H. Reiber, and B. P. Lelieveldt. Automatic segmentation and plaque characterization in atherosclerotic carotid artery MR images. *MAGMA*, 16(5):227–234, Apr 2004.
- [26] R. M. Kwee, M. T. Truijman, R. J. van Oostenbrugge, W. H. Mess, M. H. Prins, C. L. Franke, A. G. Korten, J. E. Wildberger, and M. E. Kooi. Longitudinal MRI study on the natural history of carotid artery plaques in symptomatic patients. *PLoS ONE*, 7(7):e42472, 2012.
- [27] X. Q. Zhao, L. Dong, T. Hatsukami, B. A. Phan, B. Chu, A. Moore, T. Lane, M. B. Neradilek, N. Polissar, D. Monick, C. Lee, H. Underhill, and C. Yuan. MR imaging of carotid plaque composition during lipid-lowering therapy a prospective assessment of effect and time course. *JACC Cardiovasc Imaging*, 4(9):977–986, Sep 2011.
- [28] C. T. Sibley, A. L. Vavere, I. Gottlieb, C. Cox, M. Matheson, A. Spooner, G. Godoy, V. Fernandes, B. A. Wasserman, D. A. Bluemke, and J. A. Lima. MRI-measured regression of carotid atherosclerosis induced by statins with and without niacin in a randomised controlled trial: the NIA plaque study. *Heart*, 99(22):1675–1680, Nov 2013.
- [29] J. Sun, H. R. Underhill, D. S. Hippe, Y. Xue, C. Yuan, and T. S. Hatsukami. Sustained acceleration in carotid atherosclerotic plaque progression with intraplaque hemorrhage: a long-term time course study. *JACC Cardiovasc Imaging*, 5(8):798–804, Aug 2012.
- [30] I. M. Adame Valero. *Automated segmentation of atherosclerotic arteries in MR Images*. PhD thesis, Leiden University Medical Center, 2007.
- [31] C. Yuan, E. Lin, J. Millard, and J. N. Hwang. Closed contour edge detection of blood vessel lumen and outer wall boundaries in black-blood MR images. *Magn Reson Imaging*, 17(2):257–266, Feb 1999.
- [32] W. Kerwin, C. Han, B. Chu, D. Xu, Y. Luo, J. Hwang, T. Hatsukami, and C. Yuan. A quantitative vascular analysis system for evaluation of atherosclerotic lesions by mri. In WiroJ. Niessen and MaxA. Viergever, editors, *Medical Image Computing and Computer-Assisted Intervention - MICCAI 2001*, volume 2208 of *Lecture Notes in Computer Science*, pages 786–794. Springer Berlin Heidelberg, 2001.
- [33] H. R. Underhill, W. S. Kerwin, T. S. Hatsukami, and C. Yuan. Automated measurement of mean wall thickness in the common carotid artery by MRI: a comparison to intima-media thickness by B-mode ultrasound. *J Magn Reson Imaging*, 24(2):379–387, Aug 2006.

- [34] I. M. Adame, P. J. de Koning, B. P. Lelieveldt, B. A. Wasserman, J. H. Reiber, and R. J. van der Geest. An integrated automated analysis method for quantifying vessel stenosis and plaque burden from carotid MRI images: combined postprocessing of MRA and vessel wall MR. *Stroke*, 37(8):2162–2164, Aug 2006.
- [35] A. Arias Lorza, D. D. B. Carvalho, J. Petersen, A. C. van Dijk, A. van der Lugt, W.J. Niessen, S. Klein, and M. de Bruijne. Carotid artery lumen segmentation in 3d free-hand ultrasound images using surface graph cuts. In *MICCAI 2013*. Erasmus MC, University of Copenhagen, 2013.
- [36] E. Ukwatta, J. Yuan, M. Rajchl, W. Qiu, D. Tessier, and A. Fenster. 3-D carotid multi-region MRI segmentation by globally optimal evolution of coupled surfaces. *IEEE Trans Med Imaging*, 32(4):770–785, Apr 2013.
- [37] J. M. Hofman, W. J. Branderhorst, H. M. ten Eikelder, V. C. Cappendijk, S. Heeneman, M. E. Kooi, P. A. Hilbers, and B. M. ter Haar Romeny. Quantification of atherosclerotic plaque components using in vivo MRI and supervised classifiers. *Magn Reson Med*, 55(4):790–799, Apr 2006.
- [38] F. Liu, D. Xu, M. S. Ferguson, B. Chu, T. Saam, N. Takaya, T. S. Hatsukami, C. Yuan, and W. S. Kerwin. Automated in vivo segmentation of carotid plaque MRI with Morphology-Enhanced probability maps. *Magn Reson Med*, 55(3):659–668, Mar 2006.
- [39] I. M. Adame, R. J. van der Geest, B. A. Wasserman, M. Mohamed, J. H. C. Reiber, and B. P. F. Lelieveldt. Automatic plaque characterization and vessel wall segmentation in magnetic resonance images of atherosclerotic carotid arteries. *Proc. SPIE*, 5370:265–273, 2004.
- [40] L. Biasioli, J. A. Noble, and M. D. Robson. Multicontrast mri registration of carotid arteries in atherosclerotic and normal subjects. *Proc. SPIE*, 7623:76232N–76232N–8, 2010.
- [41] B. Fei, J. S. Suri, and D. L. Wilson. Three-dimensional volume registration of carotid MR images. *Stud Health Technol Inform*, 113:394–411, 2005. PMID: 15923750.
- [42] H. Tang, T. van Walsum, R. S. van Onkelen, R. Hameeteman, S. Klein, M. Schaap, F. L. Tori, Q. J. van den Bouwhuijsen, J. C. Witteman, A. van der Lugt, L. J. van Vliet, and W. J. Niessen. Semiautomatic carotid lumen segmentation for quantification of lumen geometry in multispectral MRI. *Med Image Anal*, 16(6):1202–1215, Aug 2012.
- [43] C. Karmonik, P. Basto, K. Vickers, K. Martin, M. J. Reardon, G. M. Lawrie, and J. D. Morrisett. Quantitative segmentation of principal carotid atherosclerotic lesion components by feature space analysis based on multicontrast MRI at 1.5 T. *IEEE Trans Biomed Eng*, 56(2):352–360, Feb 2009.
- [44] L. A. Crowe, B. Ariff, J. Keegan, R. H. Mohiaddin, G. Z. Yang, A. D. Hughes, S. A. McG Thom, and D. N. Firmin. Comparison between three-dimensional volume-selective turbo spin-echo imaging and two-dimensional ultrasound for assessing carotid artery structure and function. *J Magn Reson Imaging*, 21(3):282–289, Mar 2005.

- [45] R. Duivenvoorden, E. de Groot, B. M. Elsen, J. S. Lameris, R. J. van der Geest, E. S. Stroes, J. J. Kastelein, and A. J. Nederveen. In vivo quantification of carotid artery wall dimensions: 3.0-Tesla MRI versus B-mode ultrasound imaging. *Circ Cardiovasc Imaging*, 2(3):235–242, May 2009.
- [46] E. de Groot, G. K. Hovingh, A. Wiegman, P. Duriez, A. J. Smit, J. C. Fruchart, and J. J. Kastelein. Measurement of arterial wall thickness as a surrogate marker for atherosclerosis. *Circulation*, 109(23 Suppl 1):I33–38, Jun 2004.
- [47] P. R. de Sauvage Nolting, E. de Groot, A. H. Zwinderman, R. J. Buirma, M. D. Trip, and J. J. Kastelein. Regression of carotid and femoral artery intima-media thickness in familial hypercholesterolemia: treatment with simvastatin. *Arch. Intern. Med.*, 163(15):1837–1841, 2003.
- [48] J. A. Lima, M. Y. Desai, H. Steen, W. P. Warren, S. Gautam, and S. Lai. Statin-induced cholesterol lowering and plaque regression after 6 months of magnetic resonance imaging-monitored therapy. *Circulation*, 110(16):2336–2341, Oct 2004.
- [49] R. Corti, Z. A. Fayad, V. Fuster, S. G. Worthley, G. Helft, J. Chesebro, M. Mercuri, and J. J. Badimon. Effects of lipid-lowering by simvastatin on human atherosclerotic lesions: a longitudinal study by high-resolution, noninvasive magnetic resonance imaging. *Circulation*, 104(3):249–252, Jul 2001.
- [50] R. Alizadeh Dehnavi, J. Doornbos, J. T. Tamsma, M. Stuber, H. Putter, R. J. van der Geest, H. J. Lamb, and A. de Roos. Assessment of the carotid artery by MRI at 3T: a study on reproducibility. *J Magn Reson Imaging*, 25(5):1035–1043, May 2007.
- [51] P. J. de Koning, J. A. Schaap, J. P. Janssen, J. J. Westenberg, R. J. van der Geest, and J. H. Reiber. Automated segmentation and analysis of vascular structures in magnetic resonance angiographic images. *Magn Reson Med*, 50(6):1189–1198, Dec 2003.
- [52] P. Makowski, P. J. H. Koning, E. Angelie, J. J. M. Westenberg, R. J. Geest, and J. H. C. Reiber. 3d cylindrical b-spline segmentation of carotid arteries from mri images. In Matthias Harders and Gábor Székely, editors, *Biomedical Simulation*, volume 4072 of *Lecture Notes in Computer Science*, pages 188–196. Springer Berlin Heidelberg, 2006.
- [53] Les Piegl and Wayne Tiller. *The NURBS book (2nd ed.)*. Springer-Verlag New York, Inc., New York, NY, USA, 1997.
- [54] R. Manniesing, M. A. Viergever, and W. J. Niessen. Vessel axis tracking using topology constrained surface evolution. *IEEE Trans Med Imaging*, 26(3):309–316, Mar 2007.
- [55] J. P. Janssen, G. Koning, P. J. de Koning, J. C. Tuinenburg, and J. H. Reiber. Validation of a new method for the detection of pathlines in vascular x-ray images. *Invest Radiol*, 39(9):524–530, Sep 2004.
- [56] E. Angelie, E. R. Oost, D. Hendriksen, B. P. Lelieveldt, R. J. Van der Geest, and J. H. Reiber. Automated contour detection in cardiac MRI using active appearance models: the effect of the composition of the training set. *Invest Radiol*, 42(10):697–703, Oct 2007.

- [57] J. M. Bland and D. G. Altman. Statistical methods for assessing agreement between two methods of clinical measurement. *Lancet*, 1(8476):307–310, Feb 1986.
- [58] J. R. Landis and G. G. Koch. The measurement of observer agreement for categorical data. *Biometrics*, 33(1):159–174, Mar 1977.
- [59] Y. Zhang, Y. Bazilevs, S. Goswami, C. L. Bajaj, and T. J. Hughes. Patient-Specific Vascular NURBS Modeling for Isogeometric Analysis of Blood Flow. *Comput Methods Appl Mech Eng*, 196(29-30):2943–2959, May 2007.
- [60] M. K. Makhijani, H. H. Hu, G. M. Pohost, and K. S. Nayak. Improved blood suppression in three-dimensional (3D) fast spin-echo (FSE) vessel wall imaging using a combination of double inversion-recovery (DIR) and diffusion sensitizing gradient (DSG) preparations. *J Magn Reson Imaging*, 31(2):398–405, Feb 2010.
- [61] N. Balu, B. Chu, T. S. Hatsukami, C. Yuan, and V. L. Yarnykh. Comparison between 2D and 3D high-resolution black-blood techniques for carotid artery wall imaging in clinically significant atherosclerosis. *J Magn Reson Imaging*, 27(4):918–924, Apr 2008.
- [62] Z. Fan, Z. Zhang, Y. C. Chung, P. Weale, S. Zuehlsdorff, J. Carr, and D. Li. Carotid arterial wall MRI at 3T using 3D variable-flip-angle turbo spin-echo (TSE) with flow-sensitive dephasing (FSD). *J Magn Reson Imaging*, 31(3):645–654, Mar 2010.
- [63] V. L. Roger, A. S. Go, D. M. Lloyd-Jones, R. J. Adams, J. D. Berry, T. M. Brown, M. R. Carnethon, S. Dai, G. de Simone, E. S. Ford, C. S. Fox, H. J. Fullerton, C. Gillespie, K. J. Greenlund, S. M. Hailpern, J. A. Heit, P. M. Ho, V. J. Howard, B. M. Kissela, S. J. Kittner, D. T. Lackland, J. H. Lichtman, L. D. Lisabeth, D. M. Makuc, G. M. Marcus, A. Marelli, D. B. Matchar, M. M. McDermott, J. B. Meigs, C. S. Moy, D. Mozaffarian, M. E. Mussolino, G. Nichol, N. P. Paynter, W. D. Rosamond, P. D. Sorlie, R. S. Stafford, T. N. Turan, M. B. Turner, N. D. Wong, and J. Wylie-Rosett. Heart disease and stroke statistics—2011 update: a report from the American Heart Association. *Circulation*, 123(4):e18–e209, Feb 2011.
- [64] S. Glagov, E. Weisenberg, C. K. Zarins, R. Stankunavicius, and G. J. Kolettis. Compensatory enlargement of human atherosclerotic coronary arteries. *N. Engl. J. Med.*, 316(22):1371–1375, May 1987.
- [65] N. Takaya, C. Yuan, B. Chu, T. Saam, H. Underhill, J. Cai, N. Tran, N. L. Polissar, C. Isaac, M. S. Ferguson, G. A. Garden, S. C. Cramer, K. R. Maravilla, B. Hashimoto, and T. S. Hatsukami. Association between carotid plaque characteristics and subsequent ischemic cerebrovascular events: a prospective assessment with MRI—initial results. *Stroke*, 37(3):818–823, Mar 2006.
- [66] A. Varghese, L. A. Crowe, R. H. Mohiaddin, P. D. Gatehouse, G. Z. Yang, D. N. Firmin, and D. J. Pennell. Inter-study reproducibility of 3D volume selective fast spin echo sequence for quantifying carotid artery wall volume in asymptomatic subjects. *Atherosclerosis*, 183(2):361–366, Dec 2005.
- [67] S. Zhang, J. Cai, Y. Luo, C. Han, N. L. Polissar, T. S. Hatsukami, and C. Yuan. Measurement of carotid wall volume and maximum area with contrast-enhanced 3D MR imaging: initial observations. *Radiology*, 228(1):200–205, Jul 2003.

- [68] X. Kang, N. L. Polissar, C. Han, E. Lin, and C. Yuan. Analysis of the measurement precision of arterial lumen and wall areas using high-resolution MRI. *Magn Reson Med*, 44(6):968–972, Dec 2000.
- [69] C. Yuan, K. W. Beach, L. H. Smith, and T. S. Hatsukami. Measurement of atherosclerotic carotid plaque size in vivo using high resolution magnetic resonance imaging. *Circulation*, 98(24):2666–2671, Dec 1998.
- [70] H. Wang, S. R. Das, J. W. Suh, M. Altinay, J. Pluta, C. Craige, B. Avants, and P. A. Yushkevich. A learning-based wrapper method to correct systematic errors in automatic image segmentation: consistently improved performance in hippocampus, cortex and brain segmentation. *Neuroimage*, 55(3):968–985, Apr 2011.
- [71] Y. Freund and R. E. Schapire. A decision-theoretic generalization of on-line learning and an application to boosting. *Journal of Computer and System Sciences*, 55(1):119 – 139, 1997.
- [72] Z. Tu, S. Zheng, A. L. Yuille, A. L. Reiss, R. A. Dutton, A. D. Lee, A. M. Galaburda, I. Dinov, P. M. Thompson, and A. W. Toga. Automated extraction of the cortical sulci based on a supervised learning approach. *IEEE Trans Med Imaging*, 26(4):541–552, Apr 2007.
- [73] J. H. Morra, Z. Tu, L. G. Apostolova, A. E. Green, A. W. Toga, and P. M. Thompson. Automatic subcortical segmentation using a contextual model. *Med Image Comput Comput Assist Interv*, 11(Pt 1):194–201, 2008.
- [74] A. Hofman, C. M. van Duijn, O. H. Franco, M. A. Ikram, H. L. Janssen, C. C. Klaver, E. J. Kuipers, T. E. Nijsten, B. H. Stricker, H. Tiemeier, A. G. Uitterlinden, M. W. Vernooij, and J. C. Witteman. The Rotterdam Study: 2012 objectives and design update. *Eur. J. Epidemiol.*, 26(8):657–686, Aug 2011.
- [75] Q. J. van den Bouwhuisen, M. W. Vernooij, A. Hofman, G. P. Krestin, A. van der Lugt, and J. C. Witteman. Determinants of magnetic resonance imaging detected carotid plaque components: the Rotterdam Study. *Eur. Heart J.*, 33(2):221–229, Jan 2012.
- [76] J. G. Sled, A. P. Zijdenbos, and A. C. Evans. A nonparametric method for automatic correction of intensity nonuniformity in MRI data. *IEEE Trans Med Imaging*, 17(1):87–97, Feb 1998.
- [77] N. J. Tustison, B. B. Avants, P. A. Cook, Y. Zheng, A. Egan, P. A. Yushkevich, and J. C. Gee. N4ITK: improved N3 bias correction. *IEEE Trans Med Imaging*, 29(6):1310–1320, Jun 2010.
- [78] B. H. Brinkmann, A. Manduca, and R. A. Robb. Optimized homomorphic unsharp masking for MR grayscale inhomogeneity correction. *IEEE Trans Med Imaging*, 17(2):161–171, Apr 1998.
- [79] M. S. Cohen, R. M. DuBois, and M. M. Zeineh. Rapid and effective correction of RF inhomogeneity for high field magnetic resonance imaging. *Hum Brain Mapp*, 10(4):204–211, Aug 2000.

- [80] O. Salvado, C. Hillenbrand, S. Zhang, and D. L. Wilson. Method to correct intensity inhomogeneity in MR images for atherosclerosis characterization. *IEEE Trans Med Imaging*, 25(5):539–552, May 2006.
- [81] D. Rueckert, L. I. Sonoda, C. Hayes, D. L. Hill, M. O. Leach, and D. J. Hawkes. Non-rigid registration using free-form deformations: application to breast MR images. *IEEE Trans Med Imaging*, 18(8):712–721, Aug 1999.
- [82] P. Thevenaz and M. Unser. Optimization of mutual information for multiresolution image registration. *IEEE Trans Image Process*, 9(12):2083–2099, 2000.
- [83] S. Klein, J. P. W. Pluim, M. Staring, and M. A. Viergever. Adaptive stochastic gradient descent optimisation for image registration. *International Journal of Computer Vision*, 81(3):227–239, 2009.
- [84] L. Ibanez, W. Schroeder, L. Ng, and J. Cates. *The ITK Software Guide*. Kitware, Inc. ISBN 1-930934-15-7, <http://www.itk.org/ItkSoftwareGuide.pdf>, second edition, 2005.
- [85] S. Klein, M. Staring, K. Murphy, M. A. Viergever, and J. P. Pluim. elastix: a toolbox for intensity-based medical image registration. *IEEE Trans Med Imaging*, 29(1):196–205, Jan 2010.
- [86] K. Hameeteman, M. A. Zuluaga, M. Freiman, L. Joskowicz, O. Cuisenaire, L. F. Valencia, M. A. Gulsun, K. Krissian, J. Mille, W. C. Wong, M. Orkisz, H. Tek, M. H. Hoyos, F. Benmansour, A. C. Chung, S. Rozie, M. van Gils, L. van den Borne, J. Sosna, P. Berman, N. Cohen, P. C. Douek, I. Sanchez, M. Aissat, M. Schaap, C. T. Metz, G. P. Krestin, A. van der Lugt, W. J. Niessen, and T. van Walsum. Evaluation framework for carotid bifurcation lumen segmentation and stenosis grading. *Med Image Anal*, 15(4):477–488, Aug 2011.
- [87] L.R. Dice. Measures of the amount of ecologic association between species. *Ecology*, 26(3):297–302, July 1945.
- [88] F. Heckel, O. Konrad, H. K. Hahn, and H. O. Peitgen. Interactive 3d medical image segmentation with energy-minimizing implicit functions. *Computers & Graphics*, 35(2):275 – 287, 2011.
- [89] P. E. Shrout and J. L. Fleiss. Intraclass correlations: uses in assessing rater reliability. *Psychol Bull*, 86(2):420–428, Mar 1979.
- [90] S. K. Warfield, K. H. Zou, and W. M. Wells. Simultaneous truth and performance level estimation (STAPLE): an algorithm for the validation of image segmentation. *IEEE Trans Med Imaging*, 23(7):903–921, Jul 2004.
- [91] D. M. J. Tax, M. van Breukelen, R. P. W. Duin, and J. Kittler. Combining multiple classifiers by averaging or by multiplying? *Pattern Recognition*, 33(9):1475 – 1485, 2000.
- [92] C. Yuan, M. Oikawa, Z. Miller, and T. Hatsukami. MRI of carotid atherosclerosis. *J Nucl Cardiol*, 15(2):266–275, 2008.

- [93] C. Yuan, W. S. Kerwin, M. S. Ferguson, N. Polissar, S. Zhang, J. Cai, and T. S. Hatsukami. Contrast-enhanced high resolution MRI for atherosclerotic carotid artery tissue characterization. *J Magn Reson Imaging*, 15(1):62–67, Jan 2002.
- [94] V. C. Cappendijk, K. B. Cleutjens, A. G. Kessels, S. Heeneman, G. W. Schurink, R. J. Welten, W. H. Mess, M. J. Daemen, J. M. van Engelshoven, and M. E. Kooi. Assessment of human atherosclerotic carotid plaque components with multisequence MR imaging: initial experience. *Radiology*, 234(2):487–492, Feb 2005.
- [95] T. Ohya, T. Iwai, K. Luan, T. Kato, H. Liao, E. Kobayashi, K. Mitsudo, N. Fuwa, R. Kohno, I. Sakuma, and I. Tohnai. Analysis of carotid artery deformation in different head and neck positions for maxillofacial catheter navigation in advanced oral cancer treatment. *Biomed Eng Online*, 11:65, 2012.
- [96] S. W. Robertson, C. P. Cheng, and M. K. Razavi. Biomechanical response of stented carotid arteries to swallowing and neck motion. *J. Endovasc. Ther.*, 15(6):663–671, Dec 2008.
- [97] R. M. Kwee, R. J. van Oostenbrugge, M. H. Prins, J. W. Ter Berg, C. L. Franke, A. G. Korten, B. J. Meems, J. M. van Engelshoven, J. E. Wildberger, W. H. Mess, and M. E. Kooi. Symptomatic patients with mild and moderate carotid stenosis: plaque features at MRI and association with cardiovascular risk factors and statin use. *Stroke*, 41(7):1389–1393, Jul 2010.
- [98] R. M. Kwee, G. J. Teule, R. J. van Oostenbrugge, W. H. Mess, M. H. Prins, R. J. van der Geest, J. W. Ter Berg, C. L. Franke, A. G. Korten, B. J. Meems, P. A. Hofman, J. M. van Engelshoven, J. E. Wildberger, and M. E. Kooi. Multimodality imaging of carotid artery plaques: 18F-fluoro-2-deoxyglucose positron emission tomography, computed tomography, and magnetic resonance imaging. *Stroke*, 40(12):3718–3724, Dec 2009.
- [99] W. R. Crum, T. Hartkens, and D. L. Hill. Non-rigid image registration: theory and practice. *Br J Radiol*, 77 Spec No 2:S140–153, 2004.
- [100] S. Klein, M. Staring, and J. P. Pluim. Evaluation of optimization methods for nonrigid medical image registration using mutual information and B-splines. *IEEE Trans Image Process*, 16(12):2879–2890, Dec 2007.
- [101] Paul Viola and William M. Wells III. Alignment by maximization of mutual information. *International Journal of Computer Vision*, 24(2):137–154, 1997.
- [102] F. Maes, A. Collignon, D. Vandermeulen, G. Marchal, and P. Suetens. Multimodality image registration by maximization of mutual information. *IEEE Trans Med Imaging*, 16(2):187–198, Apr 1997.
- [103] C. Studholme, D.L.G. Hill, and D.J. Hawkes. An overlap invariant entropy measure of 3d medical image alignment. *Pattern Recognition*, 32(1):71 – 86, 1999.
- [104] S. E. Clarke, R. R. Hammond, J. R. Mitchell, and B. K. Rutt. Quantitative assessment of carotid plaque composition using multicontrast MRI and registered histology. *Magn Reson Med*, 50(6):1199–1208, Dec 2003.

- [105] J. Krejza, M. Arkuszewski, S. E. Kasner, J. Weigele, A. Ustymowicz, R. W. Hurst, B. L. Cucchiara, and S. R. Messe. Carotid artery diameter in men and women and the relation to body and neck size. *Stroke*, 37(4):1103–1105, Apr 2006.
- [106] N. D. Nanayakkara, B. Chiu, A. Samani, J. D. Spence, J. Samarabandu, and A. Fenster. A "twisting and bending" model-based nonrigid image registration technique for 3-D ultrasound carotid images. *IEEE Trans Med Imaging*, 27(10):1378–1388, Oct 2008.
- [107] N. Balu, W. S. Kerwin, B. Chu, F. Liu, and C. Yuan. Serial MRI of carotid plaque burden: influence of subject repositioning on measurement precision. *Magn Reson Med*, 57(3):592–599, Mar 2007.
- [108] M. T. Truijman, M. E. Kooi, A. C. van Dijk, A. A. de Rotte, A. G. van der Kolk, M. I. Liem, F. H. Schreuder, E. Boersma, W. H. Mess, R. J. van Oostenbrugge, P. J. Koudstaal, L. J. Kappelle, P. J. Nederkoorn, A. J. Nederveen, J. Hendrikse, A. F. van der Steen, M. J. Daemen, and A. van der Lugt. Plaque At RISK (PARISK): prospective multicenter study to improve diagnosis of high-risk carotid plaques. *Int J Stroke*, Oct 2013.
- [109] R. van 't Klooster, M. Staring, S. Klein, R. M. Kwee, M. E. Kooi, J. H. Reiber, B. P. Lelieveldt, and R. J. van der Geest. Automated registration of multispectral MR vessel wall images of the carotid artery. *Med Phys*, 40(12):121904, Dec 2013.
- [110] C. Oppenheim, E. Touze, X. Leclerc, E. Schmitt, F. Bonneville, P. Vandermarcq, E. Gerardin, J. F. Toussaint, J. L. Mas, and J. F. Meder. [High resolution MRI of carotid atherosclerosis: looking beyond the arterial lumen]. *J Radiol*, 89(3 Pt 1):293–301, Mar 2008.
- [111] N. Takaya, C. Yuan, B. Chu, T. Saam, N. L. Polissar, G. P. Jarvik, C. Isaac, J. McDonough, C. Natiello, R. Small, M. S. Ferguson, and T. S. Hatsukami. Presence of intraplaque hemorrhage stimulates progression of carotid atherosclerotic plaques: a high-resolution magnetic resonance imaging study. *Circulation*, 111(21):2768–2775, May 2005.
- [112] B. D. Coombs, J. H. Rapp, P. C. Ursell, L. M. Reilly, and D. Saloner. Structure of plaque at carotid bifurcation: high-resolution MRI with histological correlation. *Stroke*, 32(11):2516–2521, Nov 2001.
- [113] E. Touze, J. F. Toussaint, J. Coste, E. Schmitt, F. Bonneville, P. Vandermarcq, J. Y. Gaurvit, F. Douvrin, J. F. Meder, J. L. Mas, and C. Oppenheim. Reproducibility of high-resolution MRI for the identification and the quantification of carotid atherosclerotic plaque components: consequences for prognosis studies and therapeutic trials. *Stroke*, 38(6):1812–1819, Jun 2007.
- [114] W. S. Kerwin, F. Liu, V. Yarnykh, H. Underhill, M. Oikawa, W. Yu, T. S. Hatsukami, and C. Yuan. Signal features of the atherosclerotic plaque at 3.0 Tesla versus 1.5 Tesla: impact on automatic classification. *J Magn Reson Imaging*, 28(4):987–995, Oct 2008.
- [115] J. F. Toussaint, J. F. Southern, V. Fuster, and H. L. Kantor. T2-weighted contrast for NMR characterization of human atherosclerosis. *Arterioscler. Thromb. Vasc. Biol.*, 15(10):1533–1542, Oct 1995.

- [116] R. P. W. Duin, P. Juszczak, P. Paclik, E. Pekalska, D. de Ridder, D. M. J. Tax, and S. Verzakov. PR-Tools4.1, a matlab toolbox for pattern recognition, 2007. <http://prtools.org>.
- [117] B. A. Wasserman, R. J. Wityk, H. H. Trout, and R. Virmani. Low-grade carotid stenosis: looking beyond the lumen with MRI. *Stroke*, 36(11):2504–2513, Nov 2005.
- [118] B. Chu, A. Kampschulte, M. S. Ferguson, W. S. Kerwin, V. L. Yarnykh, K. D. O'Brien, N. L. Polissar, T. S. Hatsukami, and C. Yuan. Hemorrhage in the atherosclerotic carotid plaque: a high-resolution MRI study. *Stroke*, 35(5):1079–1084, May 2004.
- [119] P. E. Crewson. Reader agreement studies. *AJR Am J Roentgenol*, 184(5):1391–1397, May 2005.
- [120] C. Yuan, L. M. Mitsumori, K. W. Beach, and K. R. Maravilla. Carotid atherosclerotic plaque: noninvasive MR characterization and identification of vulnerable lesions. *Radiology*, 221(2):285–299, Nov 2001.
- [121] J. L. Hunt, R. Fairman, M. E. Mitchell, J. P. Carpenter, M. Golden, T. Khalapyan, M. Wolfe, D. Neschis, R. Milner, B. Scoll, A. Cusack, and E. R. Mohler. Bone formation in carotid plaques: a clinicopathological study. *Stroke*, 33(5):1214–1219, May 2002.
- [122] R. L. Wolf, S. L. Wehrli, A. M. Popescu, J. H. Woo, H. K. Song, A. C. Wright, E. R. Mohler, J. D. Harding, E. L. Zager, R. M. Fairman, M. A. Golden, O. C. Velazquez, J. P. Carpenter, and F. W. Wehrli. Mineral volume and morphology in carotid plaque specimens using high-resolution MRI and CT. *Arterioscler. Thromb. Vasc. Biol.*, 25(8):1729–1735, Aug 2005.
- [123] J. Cai, T. S. Hatsukami, M. S. Ferguson, W. S. Kerwin, T. Saam, B. Chu, N. Takaya, N. L. Polissar, and C. Yuan. In vivo quantitative measurement of intact fibrous cap and lipid-rich necrotic core size in atherosclerotic carotid plaque: comparison of high-resolution, contrast-enhanced magnetic resonance imaging and histology. *Circulation*, 112(22):3437–3444, Nov 2005.
- [124] C. Yuan, S. X. Zhang, N. L. Polissar, D. Echelard, G. Ortiz, J. W. Davis, E. Ellington, M. S. Ferguson, and T. S. Hatsukami. Identification of fibrous cap rupture with magnetic resonance imaging is highly associated with recent transient ischemic attack or stroke. *Circulation*, 105(2):181–185, Jan 2002.
- [125] V. V. Itskovich, D. D. Samber, V. Mani, J. G. Aguinaldo, J. T. Fallon, C. Y. Tang, V. Fuster, and Z. A. Fayad. Quantification of human atherosclerotic plaques using spatially enhanced cluster analysis of multicontrast-weighted magnetic resonance images. *Magn Reson Med*, 52(3):515–523, Sep 2004.
- [126] B. Sun, D. P. Giddens, R. Long, W. R. Taylor, D. Weiss, G. Joseph, D. Vega, and J. N. Oshinski. Automatic plaque characterization employing quantitative and multicontrast MRI. *Magn Reson Med*, 59(1):174–180, Jan 2008.
- [127] A. van Engelen, W. J. Niessen, S. Klein, H. C. Groen, H. J. M. Verhagen, J. J. Wentzel, A. van der Lugt, and M. de Bruijne. Supervised in-vivo plaque characterization incorporating class label uncertainty. In *Biomedical Imaging (ISBI), 2012 9th IEEE International Symposium on*, pages 246–249, 2012.

- [128] D. F. van Wijk, A. C. Strang, R. Duivenvoorden, D. J. Enklaar, R. J. van der Geest, J. J. Kastelein, E. de Groot, E. S. Stroes, and A. J. Nederveen. Increasing spatial resolution of 3T MRI scanning improves reproducibility of carotid arterial wall dimension measurements. *MAGMA*, Sep 2013.
- [129] R. P. W. Duin, P. Juszczak, P. Paclik, E. Pekalska, D. de Ridder, D. M. J. Tax, and S. Verzakov. PR-Tools4.1, a matlab toolbox for pattern recognition, 2012. <http://prtools.org>.
- [130] D. N. Ku, D. P. Giddens, C. K. Zarins, and S. Glagov. Pulsatile flow and atherosclerosis in the human carotid bifurcation. Positive correlation between plaque location and low oscillating shear stress. *Arteriosclerosis*, 5(3):293–302, 1985.
- [131] M. Shah, Y. Xiao, N. Subbanna, S. Francis, D. L. Arnold, D. L. Collins, and T. Arbel. Evaluating intensity normalization on MRIs of human brain with multiple sclerosis. *Med Image Anal*, 15(2):267–282, Apr 2011.
- [132] D. V. Cicchetti. Guidelines, criteria, and rules of thumb for evaluating normed and standardized assessment instruments in psychology. *Psychological Assessment*, 6(4):284–290, 1994.
- [133] G. Pasterkamp, A. H. Schoneveld, A. C. van der Wal, C. C. Haudenschild, R. J. Clarijs, A. E. Becker, B. Hillen, and C. Borst. Relation of arterial geometry to luminal narrowing and histologic markers for plaque vulnerability: the remodeling paradox. *J. Am. Coll. Cardiol.*, 32(3):655–662, Sep 1998.
- [134] E. Falk, P. K. Shah, and V. Fuster. Coronary plaque disruption. *Circulation*, 92(3):657–671, Aug 1995.
- [135] R. Ross. Atherosclerosis is an inflammatory disease. *Am. Heart J.*, 138(5 Pt 2):S419–420, Nov 1999.
- [136] A. Kampschulte, M. S. Ferguson, W. S. Kerwin, N. L. Polissar, B. Chu, T. Saam, T. S. Hatsukami, and C. Yuan. Differentiation of intraplaque versus juxtaluminal hemorrhage/thrombus in advanced human carotid atherosclerotic lesions by in vivo magnetic resonance imaging. *Circulation*, 110(20):3239–3244, Nov 2004.
- [137] J. F. Toussaint, J. F. Southern, V. Fuster, and H. L. Kantor. Water diffusion properties of human atherosclerosis and thrombosis measured by pulse field gradient nuclear magnetic resonance. *Arterioscler. Thromb. Vasc. Biol.*, 17(3):542–546, Mar 1997.
- [138] S. E. Clarke, V. Beletsky, R. R. Hammond, R. A. Hegele, and B. K. Rutt. Validation of automatically classified magnetic resonance images for carotid plaque compositional analysis. *Stroke*, 37(1):93–97, Jan 2006.
- [139] W. J. Rogers, J. W. Prichard, Y. L. Hu, P. R. Olson, D. H. Benckart, C. M. Kramer, D. A. Vido, and N. Reichel. Characterization of signal properties in atherosclerotic plaque components by intravascular MRI. *Arterioscler. Thromb. Vasc. Biol.*, 20(7):1824–1830, Jul 2000.
- [140] J. M. Cai, T. S. Hatsukami, M. S. Ferguson, R. Small, N. L. Polissar, and C. Yuan. Classification of human carotid atherosclerotic lesions with in vivo multicontrast magnetic resonance imaging. *Circulation*, 106(11):1368–1373, Sep 2002.

- [141] L. M. Mitsumori, T. S. Hatsukami, M. S. Ferguson, W. S. Kerwin, J. Cai, and C. Yuan. In vivo accuracy of multisequence MR imaging for identifying unstable fibrous caps in advanced human carotid plaques. *J Magn Reson Imaging*, 17(4):410–420, Apr 2003.
- [142] C. Yuan, W. S. Kerwin, M. S. Ferguson, N. Polissar, S. Zhang, J. Cai, and T. S. Hatsukami. Contrast-enhanced high resolution MRI for atherosclerotic carotid artery tissue characterization. *J Magn Reson Imaging*, 15(1):62–67, Jan 2002.
- [143] D. G. Mitchell and M. S. Cohen. *Mri Principles*. W. B. Saunders, 2004.
- [144] S. Vinitiski, P. M. Consigny, M. J. Shapiro, N. Janes, S. N. Smullens, and M. D. Rifkin. Magnetic resonance chemical shift imaging and spectroscopy of atherosclerotic plaque. *Invest Radiol*, 26(8):703–714, Aug 1991.
- [145] T. P. Trouard, M. I. Altbach, G. C. Hunter, C. D. Eskelson, and A. F. Gmitro. MRI and NMR spectroscopy of the lipids of atherosclerotic plaque in rabbits and humans. *Magn Reson Med*, 38(1):19–26, Jul 1997.
- [146] B. C. Te Boekhorst, Cramer M. J., Van Oosterhout M. E., Pasterkamp G., Doevendans P. A., and Van Echteld C. J. High-resolution MRI for identification of various components of human carotid artery plaque using different weightings and fat suppression. In *J Cardiovasc Magn Reson*, volume 9, pages 252–253, 2007.
- [147] F. Babiloni, L. Bianchi, F. Semeraro, J. del R Millan, J. Mouriño, A. Cattini, S. Salinari, M. G. Marciani, and F. Cincotti. Mahalanobis distance-based classifiers are able to recognize eeg patterns by using few eeg electrodes. In *Engineering in Medicine and Biology Society, 2001. Proceedings of the 23rd Annual International Conference of the IEEE*, volume 1, pages 651–654. IEEE, 2001.
- [148] S. Dalager-Pedersen, E. Falk, S. Ringgaard, I. B. Kristensen, and E. M. Pedersen. Effects of temperature and histopathologic preparation on the size and morphology of atherosclerotic carotid arteries as imaged by MRI. *J Magn Reson Imaging*, 10(5):876–885, Nov 1999.
- [149] J. Morrisett, W. Vick, R. Sharma, G. Lawrie, M. Reardon, E. Ezell, J. Schwartz, G. Hunter, and D. Gorenstein. Discrimination of components in atherosclerotic plaques from human carotid endarterectomy specimens by magnetic resonance imaging ex vivo. *Magn Reson Imaging*, 21(5):465–474, Jun 2003.
- [150] M. Schar, W. Y. Kim, M. Stuber, P. Boesiger, W. J. Manning, and R. M. Botnar. The impact of spatial resolution and respiratory motion on MR imaging of atherosclerotic plaque. *J Magn Reson Imaging*, 17(5):538–544, May 2003.
- [151] M. Shinnar, J. T. Fallon, S. Wehrli, M. Levin, D. Dalmacy, Z. A. Fayad, J. J. Badimon, M. Harrington, E. Harrington, and V. Fuster. The diagnostic accuracy of ex vivo MRI for human atherosclerotic plaque characterization. *Arterioscler. Thromb. Vasc. Biol.*, 19(11):2756–2761, Nov 1999.
- [152] R. E. Murphy, A. R. Moody, P. S. Morgan, A. L. Martel, G. S. Delay, S. Alder, S. T. MacSweeney, W. G. Tennant, J. Gladman, J. Lowe, and B. J. Hunt. Prevalence of complicated carotid atheroma as detected by magnetic resonance direct thrombus

- imaging in patients with suspected carotid artery stenosis and previous acute cerebral ischemia. *Circulation*, 107(24):3053–3058, Jun 2003.
- [153] J. F. Toussaint, M. Pachot-Clouard, and H. L. Kantor. Tissue characterization of atherosclerotic plaque vulnerability by nuclear magnetic resonance. *J Cardiovasc Magn Reson*, 2(3):225–232, 2000.
- [154] M. Honda, N. Kitagawa, K. Tsutsumi, I. Nagata, M. Morikawa, and T. Hayashi. High-resolution magnetic resonance imaging for detection of carotid plaques. *Neurosurgery*, 58(2):338–346, Feb 2006.
- [155] C. Yuan and W. S. Kerwin. MRI of atherosclerosis. *J Magn Reson Imaging*, 19(6):710–719, Jun 2004.
- [156] B. A. Wasserman, W. I. Smith, H. H. Trout, R. O. Cannon, R. S. Balaban, and A. E. Arai. Carotid artery atherosclerosis: in vivo morphologic characterization with gadolinium-enhanced double-oblique MR imaging initial results. *Radiology*, 223(2):566–573, May 2002.
- [157] R. R. Ronen, S. E. Clarke, R. R. Hammond, and B. K. Rutt. Resolution and SNR effects on carotid plaque classification. *Magn Reson Med*, 56(2):290–295, Aug 2006.
- [158] R. W. Anderson, C. Stomberg, C. W. Hahm, V. Mani, D. D. Samber, V. V. Itskovich, L. Valera-Guallar, J. T. Fallon, P. B. Nedanov, J. Huizenga, and Z. A. Fayad. Automated classification of atherosclerotic plaque from magnetic resonance images using predictive models. *BioSystems*, 90(2):456–466, 2007.
- [159] L. Silveira, S. Sathaiyah, R. A. Zangaro, M. T. Pacheco, M. C. Chavantes, and C. A. Pasqualucci. Correlation between near-infrared Raman spectroscopy and the histopathological analysis of atherosclerosis in human coronary arteries. *Lasers Surg Med*, 30(4):290–297, 2002.
- [160] G. V. Nogueira, L. Silveira, A. A. Martin, R. A. Zangaro, M. T. Pacheco, M. C. Chavantes, and C. A. Pasqualucci. Raman spectroscopy study of atherosclerosis in human carotid artery. *J Biomed Opt*, 10(3):031117, 2005.
- [161] C. Pasterkamp and E. Falk. Atherosclerotic plaque rupture: an overview. *Journal of Clinical and Basic Cardiology*, 3(2):81–86, 2000.
- [162] N. Balu, V. L. Yarnykh, B. Chu, J. Wang, T. Hatsukami, and C. Yuan. Carotid plaque assessment using fast 3D isotropic resolution black-blood MRI. *Magn Reson Med*, 65(3):627–637, Mar 2011.
- [163] X. Zhao, H. R. Underhill, C. Yuan, M. Oikawa, L. Dong, H. Ota, T. S. Hatsukami, Q. Wang, L. Ma, and J. Cai. Minimization of MR contrast weightings for the comprehensive evaluation of carotid atherosclerotic disease. *Invest Radiol*, 45(1):36–41, Jan 2010.

Publications

Journal publications

R. van 't Klooster, P. J. H. de Koning, R. A. Dehnavi, J. T. Tamsma, A. de Roos, J. H. C. Reiber, R. J. van der Geest. Automatic lumen and outer wall segmentation of the carotid artery using deformable three-dimensional models in MR angiography and vessel wall images. *Journal of Magnetic Resonance Imaging*, 2012 Jan;35(1):156-65.

B. C. te Boekhorst, **R. van 't Klooster**, S. M. Bovens, K. W. van de Kolk, M. J. Cramer, M. F. van Oosterhout, P. A. Doevendans, R. J. van der Geest, G. Pasterkamp, C. J. van Echteld. Evaluation of multicontrast MRI including fat suppression and inversion recovery spin echo for identification of intra-plaque hemorrhage and lipid core in human carotid plaque using the mahalanobis distance measure. *Magnetic Resonance in Medicine*, 2012 Jun;67(6):1764-75.

R. van 't Klooster, O. Naggara, R. Marsico, J. H. C. Reiber, J. F. Meder, R. J. van der Geest, E. Touzé, C. Oppenheim. Automated versus manual in vivo segmentation of carotid plaque MRI. *American Journal of Neuroradiology*, 2012 Sep;33(8):1621-7.

K. Hameeteman, **R. van 't Klooster**, M. Selwaness, A. van der Lugt, J. C. M. Witteman, W. J. Niessen, S. Klein. Carotid wall volume quantification from magnetic resonance images using deformable model fitting and learning-based correction of systematic errors. *Physics in Medicine and Biology*, 2013 Mar 7;58(5):1605-23.

R. van 't Klooster, A. J. Patterson, V. E. Young, J. H. Gillard, J. H. C. Reiber, R. J. van der Geest. An objective method to optimize the MR sequence set for plaque classification in carotid vessel wall images using automated image segmentation. *PLOS ONE*, 2013 Oct 23;8(10):e78492.

R. van 't Klooster, M. Staring, S. Klein, R. M. Kwee, M. E. Kooi, J. H. C. Reiber, B. P. F. Lelieveldt, R. J. van der Geest. Automated registration of multispectral MR vessel wall images of the carotid artery. *Medical Physics* 2013; 40, 121904.

S. Gao*, **R. van 't Klooster***, D. F. van Wijk, A. J. Nederveen, B. P. F. Lelieveldt, R. J. van der Geest. Accuracy and reproducibility of automated atherosclerotic carotid artery plaque classification in MR vessel wall images. *Submitted*.

*Shared first authorship.

R. van 't Klooster, M. T. B. Truijman, A. C. van Dijk, F. H. B. M. Schreuder, M. E. Kooi, A. van der Lugt, R. J. van der Geest. Visualization of local changes in vessel wall morphology and plaque progression in serial carotid artery MRI. *Submitted*.

Abstracts and presentations

J. H. C. Reiber, I. M. Adame, P. J. H. de Koning, **R. van 't Klooster**, I. Isgum, K. DeMarco, R. J. van der Geest. Magnetic resonance angiography and vessel wall imaging: great tools for assessing atherosclerosis. *North American Society for Cardiovascular Imaging Annual Meeting*, 2007.

I. Isgum, **R. van 't Klooster**, P. J. H. de Koning, F. Jabi, K. DeMarco, J. H. C. Reiber, R. J. van der Geest. Automatic Detection of Atherosclerotic Carotid Plaque From Combined Magnetic Resonance Angiography and Vessel Wall Images. *European Congress of Radiology*, 2008.

R. van 't Klooster, A. J. Patterson, V. E. Young, J. H. Gillard, J. H. C. Reiber, R. J. van der Geest. Histology Assisted Validation of Automatic Detection of Soft Plaque in Vessel Wall Images by Using Optimal Number of MR Sequences. *International Society for Magnetic Resonance in Medicine Annual Meeting*, 2010.

R. van 't Klooster, P. J. H. de Koning, R. A. Dehnavi, J. T. Tamsma, A. de Roos, J. H. C. Reiber, R. J. van der Geest. Automatic lumen and outer wall segmentation of the carotid artery using a deformable 3D model in MR angiography and vessel wall images. *European Society of Cardiology Congress*, 2010.

C. Oppenheim, **R. van 't Klooster**, R. Marsico, O. Naggara, O. Eker, R. J. van der Geest, I. M. Adame, E. Touze, J. F. Meder. Automated Versus Human In Vivo Segmentation of Carotid Plaque MRI. *XIX Symposium Neuroradiologicum*, 2010.

R. van 't Klooster, M. Staring, S. Klein, R. M. Kwee, M. E. Kooi, J. H. C. Reiber, B. P. F. Lelieveldt and R. J. van der Geest. Automatic Registration of Multispectral MR Vessel Wall Images of the Carotid Artery. *International Society for Magnetic Resonance in Medicine Annual Meeting*, 2012.

Book chapters

R. J. van der Geest, P. H. Kitslaar, P. J. H. de Koning, **R. van 't Klooster**, W. J. Jukema, G. Koning, H. A. Marquering, J. H. C. Reiber. Advanced three-dimensional postprocessing in computed tomographic and magnetic resonance angiography. In: V. B. Ho and G. P. Reddy, *Cardiovascular Imaging*, St Louis, MO, 2011:1128-1143.

Acknowledgments

With great pleasure and excitement I look back on the past years as a researcher of the Laboratorium voor Klinische en Experimentele Beeldverwerking (LKEB). I would like to start by thanking all my colleagues for their help, constructive work-related discussions, fun conversations and open-door atmosphere.

I would like to thank my two promotors, Prof. Hans Reiber and Prof. Boudewijn Lelieveldt, for the opportunity to become a PhD candidate within the LKEB. The LKEB is a strong and diverse medical image processing group. Both Hans and Boudewijn can be proud of their group and their ability to acquire funding in these financially difficult times.

Rob, you have been a kind supervisor, co-promotor and colleague. I value the freedom I had during your supervision and I was surprised by your ability to quickly switch between subjects, especially when one colleague left your room and I entered with a question on a completely different subject. During the last two years we grew towards equal colleagues and I enjoyed working as such.

Dear roommates, I feel blessed to have shared so much time with you in the Terminaalzaal, you have been like a second family to me. There has never been a moment in which I did not feel at home in the office. I value the openness and willingness to share more than work-related matters. Alize, Emmanuelle, Dennis, Roald, Luca, Ece, Qian, Trung, Baldur, Paulien, it was a pleasure!

Berend, you ignited my fascination for medical image processing. You were an excellent supervisor during my master's graduation project and are a great teacher. My initial thought: a project on 2D hand radiographs does not seem too exciting, proved to be naive. It was a pity that we could not pursue this work into a PhD project. Still, I am very happy with the results we achieved with the graduation project and the papers we were able to publish afterwards.

Patrick, we started as buddies within the STW project and stayed buddies when we both started working on different projects. You helped out many times when I was frustrated with compiler errors and managed to stay patient and calm, thanks! Jasper, volleyball was the common denominator, but I am sure that without these discussions I would have also mentioned you in this part of this paragraph. Patrick and Jasper, you were two constant factors for the past seven years, I am really glad that both of you agreed to become my paranymphs. Marius, thanks for all your kind help and critical attitude towards my work. Pieter, I wish we could have spend more time on our Friday afternoon project, still we managed to achieve a lot. Thanks for all your MeVisLab help and I would like to see those subdivision surfaces on the cover of a PhD thesis somewhere in the future (no pressure!). Julien, thanks for all the out-of-the-box conversations during lunch. Michèle, thanks for all your IT support and random chats. Shan, I enjoyed working together on the

challenging image data for the past two years, thank you!

The work described in this thesis would not have been possible without the following collaborations. I worked closely together with the Biomedical Imaging Group Rotterdam from the Erasmus MC and joining the R-vip each Thursday turned out to be a wise decision. I would like to thank Arna, Diego, Hui, Reinhard, Andres, Henk, Stefan, Marleen and Wiro for the nice work within the PARISk project and all the R-VIP meetings. Anouk, we were a good team and we bridged the gap between image processing and the clinic effectively. My visits to the Maastricht University Medical Center were less frequent but it was always worth the trip. Eline, Robert, Martine, Bernard and Floris thank you for the fruitful collaboration and sharing of the image data. Furthermore, I would like to thank Aart and Diederick from the Academic Medical Center in Amsterdam, Andrew and Vicky from Addenbrooke's Hospital, and Catherine from Centre Hospitalier Sainte Anne for being constructive and insightful co-authors, and Sabine en Alexander from Philips Technologie GmbH Innovative Technologies for the nice collaboration.

Finally, I would like to thank my all friends, especially my closest friends and my brother, for being there and making life a lot of fun. I would like to thank my parents for all their support and opportunities they have given me.

Lieve Yvonne, je slaat je heldhaftig door je onregelmatige en roerige baan en je staat altijd voor me klaar. Ik ben trots op je! Ik kijk met veel plezier terug op de afgelopen jaren en krijg een glimlach op mijn gezicht als ik terugdenk aan de vele mooie vakanties. Met veel enthousiasme kijk ik uit naar de spannende tijd die voor ons ligt.

Curriculum Vitae

Ronald van 't Klooster was born on the 9th of March, 1981 in Laren. After graduation at the Willem de Zwijger College in Bussum in 1999, he started studying Electrical Engineering at Delft University of Technology. He chose the specialisation Media and Knowledge Engineering and the minor Biomedical Engineering. His graduation project was carried out at the Division of Image Processing of the Leiden University Medical Center, on the subject of the automatic quantification of osteoarthritis in hand radiographs. After graduation in 2006, he accepted a research position in the same lab and worked on the automated evaluation of vascular MR image data.

In 2010, he started his PhD research on the segmentation and registration of multi-sequence MR vessel wall images of the carotid artery in cross-sectional, dynamic and longitudinal studies for the assessment of atherosclerosis. The research was carried out within the framework of CTMM, the Center for Translational Molecular Medicine, project PARISK "Plaque At Risk" in close collaboration with the Biomedical Imaging Group Rotterdam, several medical centers, and industrial partners. A number of the developed methods were successfully transferred to the industrial partners.

Currently, Ronald is working at Quantib B.V. in Rotterdam as Research & Development Engineer. Quantib B.V. is a medical technology company that develops innovative software in the field of quantitative MRI and CT image analysis.